The Role of Anticyclonic Transient Eddies in Atmospheric Blocking Dynamics

Charlie Suitters

Department of Meteorology

University of Reading

A thesis presented for the degree of

Doctor of Philosophy

October 2024

Declaration

I confirm that this is my own work and the use of all material from other sources has been properly and fully acknowledged.

Charlie Suitters

Abstract

Atmospheric blocks are large, quasi-stationary anticyclones with a lifetime from several days to multiple weeks. While blocks are relatively common in mid-latitudes, their dynamics are not completely understood, contributing to their unpredictability in medium-range numerical weather prediction (NWP). This study quantifies the role of anticyclonic (AC) synoptic-scale eddies towards blocking through a combined Eulerian and Lagrangian technique for block and AC eddy identification, respectively.

It is shown for the first time that there is a statistically significant relationship between the mean number of block-AC eddy interactions and block persistence. Longer blocks absorb more AC eddies than shorter blocks, due to the associated increase in area and/or strength of the block after an AC eddy-block interaction, preventing dissipation or downstream advection of the block. However, for blocks with a particular persistence, there is large variability around the mean in the number of AC eddies it absorbs.

In analysis of three blocks with similar persistence but different numbers of AC eddy interactions, AC eddies are only important towards the PV budget of a block when they first enter. Furthermore, the relative importance of diabatic processes varies spatially and temporally in each block, but there is no robust relationship between the relative importance of diabatic processes and AC eddies towards blocking dynamics.

Accurate forecasts of block-AC eddy interactions are shown to be important for accurate blocking forecasts in medium-range NWP. Forecast errors in AC eddy speed, size, or strength can result in errors in block size, position, strength, or persistence. Conversely, forecasts that better represent AC eddies are more accurate in their forecasts of blocking.

These results help to further the understanding of the role of AC eddies towards blocking dynamics, and show that poor AC eddy representation is one of the key reasons medium-range NWP performs so poorly for blocking.

Acknowledgements

Firstly, I would like to thank my supervisors Oscar, Kevin, Reinhard and Duncan for their guidance and expertise throughout the PhD - it goes without saying that this work would not have been possible without you. I have thoroughly enjoyed working with the four of you and really appreciate the warmth, support, and time you have given me for the past four years. Also, thanks to my monitoring committee, Bryan and John, for your invaluable input to improve my work and keeping me on the right track.

Thank you to all of my amazing friends for the memories made over PhD. To all of my office mates, especially Natalie, special thanks must go to you for putting up with all of my nonsensical rants over the past few years. Natalie, it turns out that the answer to the question "what can I actually achieve in 15 minutes?" is a lot...if those 15 minutes accumulate over the space of four years!

Hannah, Izzy, and Harriet, completing the journey from fresh-faced undergraduates to tired, old PhD candidates with you has been a pleasure, and I am so proud of all of us for getting to this point! Also, Blair, Brian, Isabelle, and others, thank you for making the PhD experience so enjoyable and I have been so lucky to have met such a lovely group of people. To Ravi, Kathryn, and Ellie, your support from afar has been much appreciated, and thank you for pretending to understand the ins and outs of atmospheric blocking! And of course my housemate Alanna, we might have both gone insane during the PhD but thank you for the support and good times we have shared.

Last but certainly not least, I need to thank my parents, who have given me their never-ending support and encouragement through the good times and the bad throughout the PhD. I would not be here today without you, and I know I have made you so proud. I love you lots!

Contents

Declaration iii

Abstract v

Acknowledgements vii

Contents ix

Mathematical Symbols xv

Abbreviations xix

List of Figures xxi

List of Tables xxv

1 Introduction 1

1.1 Motivation 1

1.2 Thesis Aims 3

1.3 Thesis Outline 6

2 Literature Review 9

2.1 Introduction to Anticyclones 9

2.2 Blocking Characteristics 10

2.2.1 Blocking Morphology 11

2.2.2 Blocking Climatology 12

2.3 Impacts from Atmospheric Blocking 14

2.3.1 Impacts on Surface Temperature 15

2.3.2 Hydrological Impacts from Blocking 17

2.3.3 Other Impacts from Blocking . . . 19
2.4 Block Identification . . . 20
2.4.1 Weather Regimes . . . 21
2.4.2 Z500 Gradient Reversals . . . 24
2.4.3 θ Gradient Reversals . . . 26
2.4.4 Z500 Anomalies . . . 27
2.4.5 PV Anomalies . . . 29
2.5 Blocking Dynamics . . . 30
2.5.1 Block-Eddy Interactions . . . 30
2.5.2 Diabatic Processes . . . 36
2.5.3 Other Mechanisms . . . 39
2.6 Objective Feature Tracking of Anticyclones . . . 41
2.6.1 Anticyclone Climatologies . . . 41
2.6.2 Tracking Blocking Anticyclones . . . 43
2.6.3 Combining Anticyclone Tracking with Block Detection . . . 44
2.7 Blocking in Numerical Weather Prediction . . . 47
2.7.1 Block Representation . . . 47
2.7.2 Improving Block Representation: Meteorology . . . 49
2.7.3 Improving Block Representation: Model Configuration . . . 51

3 Data and Methods **53**
3.1 Data . . . 53
3.1.1 ERA5 . . . 53
3.1.2 Met Office Unified Model . . . 53
3.1.3 MOGREPS-G . . . 55
3.2 Methods . . . 55
3.2.1 Z'_* Definition . . . 56
3.2.2 $\overline{Z_*}$ Background State Climatology . . . 56
3.2.3 Tracking AC Eddies . . . 57
3.2.4 Block Events . . . 58
3.2.5 Attributing Tracks to Events . . . 60
3.2.6 Comparison of AGP, ANOM, and Z'_* Indices . . . 61

4 Transient Anticyclonic Eddies and Their Relationship to Atmospheric Block Persistence 65

4.1 Motivation . . . 65
4.2 ERA5 Details . . . 65
4.3 Case Study of a Block and its Transient Eddies . . . 66
4.4 Northern Hemisphere Z'_* Index Blocking Climatology . . . 69
4.4.1 59-Day PAC Block . . . 72
4.5 Relationship between Block Persistence AC Transient Eddies . . . 72
4.5.1 Number of AC Eddies . . . 72
4.5.2 AC Eddy Strength and Speed . . . 75
4.6 Discussion . . . 79
4.7 Conclusions . . . 81
4.8 Supplementary Material . . . 84
4.8.1 Block Persistence Distribution for MAM and SON . . . 84
4.8.2 Number of AC Eddies Contributing to MAM and SON Blocks 84
4.8.3 AC Eddy Strength and Speed for Blocks in MAM and SON 85
4.8.4 AC Eddy Strength and Speed for Blocks of Different Lengths in MAM and SON . . . 86

5 Dynamics of Blocks with Different Numbers of AC Eddies 89

5.1 Introduction . . . 89
5.2 Methods . . . 91
5.2.1 Block Definitions . . . 91
5.2.2 q'_* Definition . . . 91
5.2.3 Defining q'_* AC and Spawned Eddies . . . 94
5.2.4 PV Equation . . . 95
5.2.5 Dry Dynamics Data Source . . . 97
5.2.6 Model Setup . . . 97
5.2.7 PV Budget . . . 101
5.3 February 2019 (2 AC Eddies) . . . 101
5.3.1 Event Synopsis . . . 101
5.3.2 Dry Dynamics . . . 104
5.3.3 Diabatic Dynamics . . . 109

5.4 March 2021 (1 AC Eddy) . . . 119
5.4.1 Event Synopsis . . . 119
5.4.2 Dry Dynamics . . . 121
5.4.3 Diabatic Dynamics . . . 125
5.5 August 2021 (0 AC Eddies) . . . 129
5.5.1 Event Synopsis . . . 129
5.5.2 Dry Dynamics . . . 131
5.5.3 Diabatic Dynamics . . . 135
5.6 PV Budget Analysis for All Cases . . . 138
5.6.1 Comparison of PV Budgets . . . 138
5.6.2 Comparison of MetUM Components . . . 140
5.6.3 Comparison of Blocking Dynamics . . . 141
5.7 Summary and Conclusions . . . 142

6 Forecasts of Anticyclonic Eddies and their Impacts on Block Forecasts 147
6.1 Introduction . . . 147
6.2 Methods and Data . . . 148
6.2.1 Data Source . . . 148
6.2.2 Forecast Skill: The ZAL Metric . . . 149
6.2.3 Predictability Barriers . . . 150
6.2.4 Summary of Methods . . . 153
6.3 February 2019 . . . 154
6.3.1 Mean ZAL . . . 154
6.3.2 Block Onset Predictability Barrier . . . 155
6.3.3 Block Decay Predictability Barrier . . . 163
6.4 March 2021 . . . 171
6.4.1 Mean ZAL . . . 171
6.4.2 Block Onset Predictability Barrier . . . 172
6.5 Discussion and Conclusions . . . 180
6.5.1 Predictability Barrier Characteristics . . . 181
6.5.2 AC Eddy Representation and Block Forecasts . . . 182

7 Conclusions **185**

7.1 Research Questions 186

7.1.1 Is there a Relationship between AC Eddies and Block Persistence? 186

7.1.2 For blocks with similar persistence but different AC eddy interactions, are their dynamics different? 187

7.1.3 Do errors in the forecasting of AC eddies lead to errors in forecasts of blocks? 188

7.2 Key Results from this Thesis 189

7.3 Open Questions and Possible Future Research 190

Appendices **193**

A Appendix **195**

A.1 Comparison of Δq_{PC2} and Δq_{LW} under the Original and Updated PC2 Scheme 195

A.2 MOGREPS-G Blocking Tool 197

Bibliography **201**

Mathematical Symbols

	Coordinates
t	Time
λ	Longitude
ϕ	Latitude
λ_0	Reference longitude
ϕ_0	Reference latitude
θ	Potential temperature
y	Meridional distance
	Operators, Means, and Anomalies
∇	3D gradient operator in Cartesian coordinates
∇_θ	3D gradient operator in isentropic coordinates
$\langle\gamma\rangle$	Quantity γ averaged only within a block
$\overline{\gamma}$	Time mean of variable γ
γ'	Anomaly in γ from the time mean
$[\gamma]$	Zonal mean of variable γ
γ_*	Anomaly in γ from the zonal mean
$\overline{\gamma_*}$	Monthly climatological anomaly in γ from the zonal mean
	Winds
$\mathbf{u}$	3D wind vector, (u, v, w)
$\mathbf{u_\theta}$	3D wind vector in isentropic coordinates
	Geopotential Height
Z_{500}	500 hPa geopotential height (Z500)

Z'_*	Z500 anomaly used to define the blocking index and anticyclonic (AC) eddies

Block and AC Eddy Characteristics

N_{eddies}	Total number of anticyclonic eddies
$N_{spawned}$	Number of spawned eddies
$N_{internal}$	Number of internal tracks
P_{block}	Block persistence
A_{block}	Block area, with 5-day persistence criterion applied
A_{inst}	Area of instantaneous blocking
v_{east}	AC eddy eastward velocity
v_{north}	AC eddy northward velocity
r	Pearson correlation

Potential Vorticity (PV)

q	PV
S_q	Sources and sinks of PV
q'_*	PV anomalies, analogous to Z'_*

Diabatic Tracers

q_0	Conserved potential vorticity
Δq_i	PV diabatic tracer, due to parameterisation i
$\Delta\theta_i$	Potential temperature diabatic tracer, due to parameterisation i
ε_q	Error term when balancing PV diabatic tracers
Δq	Total diabatic change to PV
$\Delta\theta$	Total diabatic change to potential temperature
Δq_I	PV inconsistency tracer

Forecasts of Blocks

Z, A, L	Block intensity, area, location metric
D	Cartesian distance of forecast from origin in ZAL space

N_{mem}	Number of ensemble members
γ_f	Forecast of quantity γ
γ_r	Renanalysis of quantity γ
$\mathbf{x}$	Block centre of mass position
d	Longest great circle distance in a domain
t_{val}	Forecast validity time
t_{in}	Forecast initialisation time
h	Forecast lead time
Z_{mean}, A_{mean}, L_{mean}	Mean Z, A, L of all ensemble members

Existing Blocking Indices

GHG	Meridional geopotential height gradient
γ_e	Equatorward value of γ
γ_p	Poleward value of γ
ϕ_{cen}	Central blocking latitude
$\Delta\phi$	Meridional scale of blocking
θ_{PV2}	Potential temperature on the dynamical tropopause

Governing Equations

ρ	Air density
σ	Pseudo-density in isentropic coordinates
$\mathbf{\Omega}$	Earth's rotation rate
c_p	Specific heat capacity of dry air at constant pressure
Π	Exner pressure
p	Pressure
p_0	Reference pressure, 1000 hPa
R	Specific gas constant of dry air
$\mathbf{g}$	Gravitational vector
$\mathbf{S_u}$	Sources of momentum
S_θ	Sources of heat
$\mathbf{F}$	Friction
$\dot{\theta}$	Heating rate

ζ	Vertical component of absolute vorticity
β	Meridional rate of change of Coriolis parameter
α	Dissipation constant

Abbreviations

AC	Anticyclonic
AS	August, September
ATL	Euro-Atlantic domain
AWB	Anticyclonic wave breaking
CAPE	Convective available potential energy
CBL	Central blocking latitude
CMIP5	Coupled Model Intercomparison Project Phase 5
CWB	Cyclonic wave breaking
DJF	December, January, February (boreal winter)
DOY	Day of year
EBMM	Eddy-Block Matching Mechanism
ECMWF	European Centre for Medium-Range Weather Forecasts
EOF	Empirical orthogonal function
EPVA	Eulerian potential vorticity anomaly
Eq.	Equation
ESM	Eddy Straining Mechanism
EVF	Eddy vorticity forcing
Fig.	Figure
FM	February, March
GCM	General circulation model
IFS	Integrated Forecast System
JJA	June, July, August (boreal summer)
LHB	Latent heating burst
MAM	March, April, May (boreal spring)
MCS	Mesoscale convective system

MetUM	Met Office Unified Model
MSLP	Mean sea level pressure
NAO	North Atlantic Oscillation
NH	Northern Hemisphere
NMI	Nonlinear multiscale interaction
NWP	Numerical weather prediction
PAC	North Pacific domain
PB	Predictability barrier
PV	Potential vorticity
pvu	Potential vorticity unit
QLPVA	Quasi-Lagrangian potential vorticity anomaly
Q1, Q2, Q3, Q4	First, second, third, and fourth quartile
RQ	Research question
RWB	Rossby wave breaking
SAM	Selective Absorption Mechanism
Sect.	Section
SH	Southern Hemisphere
SON	September, October, November (boreal autumn)
UK	United Kingdom
USA	United States of America
UTC	Coordinated Universal Time
WCB	Warm conveyer belt
ZAL	Block intensity, area, and location metric
Z500, Z700	500 hPa and 700 hPa geopotential height

List of Figures

1.1 Schematic of omega and dipole blocks 1
1.2 Haweswater Reservoir showing very low levels in September 2003 after the summer 2003 heatwave 2
1.3 Heavy snowfall in East Dunbartonshire on 1 March 2018 2

2.1 The five typical blocking shapes 11
2.2 Conceptual model of block evolution 13
2.3 Example Northern Hemisphere block frequency climatology 14
2.4 Euro-Atlantic weather regimes according to Ferranti et al. (2015) . . 22
2.5 Schematic of Z500 and potential temperature gradients reversals in a block 25
2.6 Schematic of the eddy straining mechanism 32
2.7 Schematic of the selective absorption mechanism 33
2.8 Schematic of omega and dipole blocks attracting/repelling eddies . 35
2.9 Schematic of the eddy-block matching mechanism 36
2.10 Block characteristics according to degree of diabatic heating 38

3.1 Climatological $\overline{Z_*}$ 57
3.2 Difference between grid point persistence and the persistence of a block event 59
3.3 Scenarios where anticyclonic eddy tracks contribute to blocking . . 61
3.4 Comparison of three blocking indices 62

4.1 Example event showing blocked grid points and anticyclonic eddies 67
4.2 Example time series of block area and intensity, in relation to time of anticyclonic eddy interactions 68
4.3 Climatological blocking frequency according to the Z'_* index 70

4.4 Block persistence distribution for winter and summer 71
4.5 Relationships between block persistence, area, and number of anticyclonic eddies, in winter and summer 73
4.6 Anticyclonic eddy strength and speed for winter blocks 75
4.7 Anticyclonic eddy strength and speed for summer blocks 76
4.8 Block persistence distribution for spring and autumn 84
4.9 Relationships between block persistence, area, and number of anticyclonic eddies, in spring and autumn 85
4.10 Anticyclonic eddy strength and speed for spring blocks 86
4.11 Anticyclonic eddy strength and speed for autumn blocks 87

5.1 $\overline{q_*}$ and $\overline{Z_*}$ comparison 93
5.2 Synopsis of the February 2019 event 102
5.3 Area and strength time series of the February 2019 event 103
5.4 PV flux convergence time series for the February 2019 block 105
5.5 PV flux convergence maps for the February 2019 block 106
5.6 Contribution of anticyclonic eddies towards PV flux convergence for the February 2019 event 108
5.7 PV inconsistency tracer analysis for the February 2019 event 110
5.8 Δq and $\Delta\theta$ maps at selected stages of the February 2019 case 112
5.9 Δq and $\Delta\theta$ vertical cross-sections at selected stages of the February 2019 case 113
5.10 PV tracer component maps for the February 2019 block 115
5.11 PV tracer component vertical cross-sections for the February 2019 block 116
5.12 Diabatic PV tracer accumulation time series in the February 2019 case study 118
5.13 Synopsis of the March 2021 event 119
5.14 Area and strength time series of the March 2021 event 120
5.15 PV flux convergence time series for the March 2021 block 122
5.16 PV flux convergence maps for the March 2021 block 123
5.17 Contribution of anticyclonic eddies towards PV flux convergence for the March 2021 event 124

5.18 PV inconsistency tracer analysis for the March 2021 event 126
5.19 Diabatic PV tracer accumulation time series in the March 2021 case study 127
5.20 Δq and $\Delta\theta$ maps and vertical cross-sections at onset of the March 2021 case 128
5.21 Synopsis of the August 2021 event 129
5.22 Area and strength time series of the August 2021 block 130
5.23 PV flux convergence time series for the August 2021 event 132
5.24 PV flux convergence maps for the August 2021 case 133
5.25 Contribution of spawned eddies towards PV flux convergence for the August 2021 case 134
5.26 PV inconsistency tracer analysis for the August 2021 block 135
5.27 Diabatic PV tracer accumulation time series in the August 2021 block event 136
5.28 Cross-sections and maps of diabatic tracers in the early stages of the August 2021 block 137
5.29 PV budget analysis of all three block events 139

6.1 Schematic of predictability barriers 150
6.2 Schematic of a "ZAL diagram" 152
6.3 Predictability barriers in the February 2019 block 155
6.4 Ensemble mean RMSE and spread in the February 2019 block . . . 156
6.5 ZAL for each member, at each initialisation time, for the February 2019 block onset predictability barrier 156
6.6 February 2019 ZAL diagram, for the onset predictability barrier . . 158
6.7 Group Z'_*, q'_*, and anticyclonic eddy comparison, valid 12 UTC 19 February 2019, examining the onset predictability barrier 160
6.8 Group Z'_*, q'_*, and anticyclonic eddy comparison, valid 06 UTC 20 February 2019, examining the onset predictability barrier 161
6.9 Group Z'_*, q'_*, and anticyclonic eddy comparison, valid 00 UTC 23 February 2019, examining the onset predictability barrier 162
6.10 ZAL for each member, at each initialisation time, for the block decay predictability barrier in the February 2019 case 163

6.11 ZAL diagram for the February 2019 block decay predictability barrier 164
6.12 Group Z'_*, q'_*, and anticyclonic eddy comparison, valid 00 UTC 28 February 2019, examining the decay predictability barrier 166
6.13 Group Z'_*, q'_*, and anticyclonic eddy comparison, valid 18 UTC 1 March 2019, examining the decay predictability barrier 167
6.14 Group Z'_*, q'_*, and anticyclonic eddy comparison, valid 06 UTC 2 March 2019, examining the decay predictability barrier 168
6.15 Predictability barriers in the March 2021 block 171
6.16 ZAL for each member, at each initialisation time, for the March 2021 block predictability barrier 172
6.17 ZAL diagram for the predictability barrier in the March 2021 block 173
6.18 Group Z'_*, q'_*, and anticyclonic eddy comparison, valid 12 UTC 14 March 2021, examining the predictability barrier 175
6.19 Group Z'_*, q'_*, and anticyclonic eddy comparison, valid 00 UTC 13 March 2021, examining the predictability barrier 176
6.20 Group Z'_*, q'_*, and anticyclonic eddy comparison, valid 12 UTC 12 March 2021, examining the predictability barrier 177
6.21 Group Z'_*, q'_*, and anticyclonic eddy comparison, valid 18 UTC 11 March 2021, examining the predictability barrier 178

A.1 Comparison of Δq_{SW} and Δq_{PC2} under the original and updated PC2 cloud scheme. 196
A.2 Postage stamps example from the blocking tool 199

List of Tables

2.1 Description of the Euro-Atlantic weather regimes according to Ferranti et al. (2015) 22
2.2 A summary of the main similarities and differences between the work in this thesis, and the work of Hauser et al. (2022) and Hauser et al. (2023). 47

5.1 Description of the three case studies analysed in the thesis 91
5.2 The PV tracers analysed in this work 99

6.1 Groups of members for the onset predictability barrier in the February 2019 case 157
6.2 Groups of members for the decay predictability barrier in the February 2019 block 165
6.3 Groups of members for the March 2021 predictability barrier 174

Chapter 1

Introduction

1.1 Motivation

The term "atmospheric blocking" typically describes mid-latitude circulation patterns that are characterised by the presence of a persistent, almost stationary, high pressure system, that disrupts the eastward progression of other weather systems. Around such blocks, the polar front jet stream deviates from its usual west-east orientation, and large-amplitude waves develop where flow is diverted around the high pressure instead (Rex, 1950). In a sense, atmospheric blocks literally "block" the downstream progress of the jet stream, and the result is that the storm track is removed from its usual location (Fig. 1.1).

Due to the persistent anomalous flow patterns brought about by blocking events, surface weather during blocking episodes is also often anomalous and sometimes severe. The stalling or diversion of extratropical cyclones by blocks can bring excessive precipitation and strong winds to regions for days or weeks at a time, with hazards from this ranging from flooding (Grams et al., 2014) to

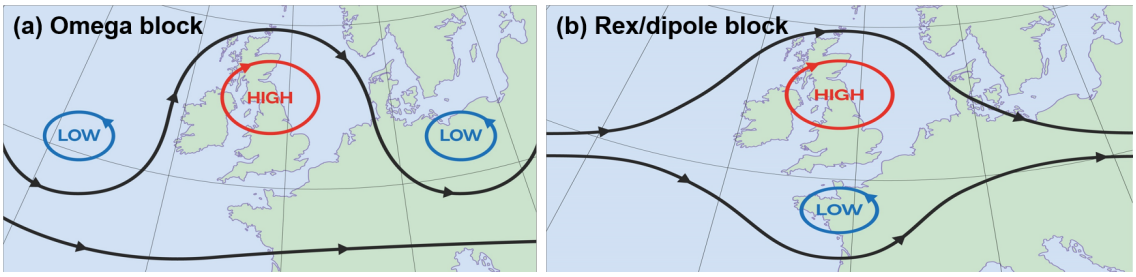

Figure 1.1: Schematic of the storm track (black arrows) around (a) an omega block, and (b) a Rex/dipole block, and the associated surface pressure systems during blocking over the UK (Met Office, 2024a).

Figure 1.2: Haweswater Reservoir showing very low levels in September 2003 after the summer 2003 heatwave (UK Centre for Ecology and Hydrology, 2024).

wind damage (Pfahl, 2014). Conversely, the prolonged high pressure can lead to diverse impacts beneath it that depend on the season (Kautz et al., 2022). The European summer heatwave of 2003 (Black et al., 2004) coincided with an atmospheric blocking event, and led to many forest fires, droughts (Fig. 1.2), and more than 20,000 deaths (Met Office, 2024b). Blocking also led to the infamous "Beast from the East" event in February–March 2018 (Karpechko et al., 2018), which brought widespread snowfall (Fig. 1.3) and freezing temperatures to the UK and other parts of Europe. This event was also responsible for two rare Red Weather Warnings for severe, dangerous weather issued by the Met Office (Met Office,

Figure 1.3: Heavy snowfall in East Dunbartonshire on 1 March 2018 (BBC Weather, 2019).

2018).

Because of the large range of impacts that blocking can be associated with, it is vital that it is forecasted accurately to allow for adequate preparation and mitigation against any severe weather. Unfortunately, weather and climate models have struggled for some time in forecasting atmospheric blocks at the medium-range and beyond (Davini and D'Andrea, 2016). The particular issue with simulations of blocking is that often, their persistence is underestimated and consequently forecasts initialised in a state of blocking are the least skillful over Europe (Ferranti et al., 2015).

One of the potential reasons explaining why blocks are not forecasted as well as other weather regimes is that their dynamical behaviour is still not fully understood (Woollings et al., 2018). Many different processes are known to be important for blocking dynamics, such as eddy-block interactions (Yamazaki and Itoh, 2013a), upstream diabatic heating (Steinfeld and Pfahl, 2019), and Rossby wave breaking (RWB) (Masato et al., 2012). However, the relevance of each process can vary depending on season and location (Miller and Wang, 2022), which means that the blocking lifecycle is complex and difficult to model accurately in weather and climate models. A relationship between some of these dynamical processes and block persistence is investigated in this thesis. In particular, the role of eddy-block interactions and diabatic heating towards the persistence of a block are examined, since the main issue when it comes to forecasting blocks comes from the underestimation of their longevity.

1.2 Thesis Aims

Of the dynamical mechanisms listed in Sect. 1.1, the climatological roles of both diabatic heating (Steinfeld and Pfahl, 2019) and RWB (Drouard et al., 2021) for blocking have already been established, with Drouard et al. (2021) also being able to directly link RWB to the persistence of a blocking event. However, while there have been a few theoretical and case study works on the importance of transient synoptic eddies for blocking (Shutts, 1983; Yamazaki and Itoh, 2013a; Luo et al., 2014), to this author's knowledge there has yet to be a climatological investigation

on the link between synoptic-scale anticyclonic (AC) eddies and block persistence (the role of cyclonic eddies and blocking has been examined in Maddison et al. (2019)). Furthermore, the expertise and experience at the University of Reading in tracking synoptic-scale systems in space and time (using TRACK, (Hodges, 1994, 1995, 1999)) enables the identification of such eddies in a large dataset with ease.

The decision to focus on the role of transient synoptic-scale anticyclonic eddies (i.e. synoptic-scale anticyclones; "AC eddies" hereafter), rather than cyclonic eddies (synoptic-scale cyclones), is now motivated further. Though blocking patterns as a whole can have both an anticyclonic and a cyclonic circulation associated with them (see Sect. 2.2.1), often when "blocks" are studied in detail, it is the blocking high that is considered to be the most important aspect due to the way in which blocks are detected in datasets (Sect. 2.4). Therefore, it is beneficial to know what processes contribute to the structure and dynamical behaviour of blocking highs so that more knowledge can be gained about the blocking lifecycle.

It has been demonstrated that though both synoptic cyclones and anticyclones provide indirect anticyclonic forcing on the northern (i.e. anticyclonic) portion of dipole-like blocking (Shutts, 1983), only the AC eddies actually enter and mix with the blocking anticyclone (Yamazaki and Itoh, 2013a) (more details are given in Sect. 2.5.1). Thus, to obtain a better insight into the processes that govern the dynamics of blocking highs, it is sufficient to only focus on the interactions of blocks with AC eddies, rather than cyclonic ones. Additionally, recent research has given far more attention to tracking the behaviour of synoptic cyclones, rather than anticyclones, so this study provides the opportunity to perform objective feature tracking on AC eddies to add to the wealth of knowledge already known about cyclonic eddies.

Therefore in this thesis, the role of AC transient synoptic-scale eddies towards the persistence of a block is studied. This topic is examined through the following three main research questions, each of which is decomposed into a series of more specific sub-questions:

RQ1 Is there a relationship between AC eddies and block persistence?

- Is there an association between block persistence and the *number* of AC eddies a block interacts with?
- Are block persistence and the *strength* of AC eddies a block interacts with related?
- What happens to block area and intensity when AC eddies interact with a block?

RQ2 For blocks with similar persistence but different AC eddy interactions, are their dynamics different?

- How does potential vorticity (PV) flux convergence vary in space and time in blocks?
- What role do AC eddies play in the convergence of PV flux in the block?
- Are diabatic processes more or less influential in blocks with fewer or more AC eddies?
- Do the principal sources of diabatic PV modification differ between block events?

RQ3 Do errors in the forecasting of AC eddies lead to errors in forecasts of blocks?

- Which periods (onset/maintenance/decay) of blocking are the least certain?
- Do these periods coincide with AC eddy interactions with the block?
- Can errors in forecasted block characteristics be traced back to errors in forecasted AC eddy characteristics?

The answers to these questions are sought in the following ways. Firstly, research question 1 (RQ1) is investigated through a climatological analysis of Euro-Atlantic and North Pacific blocks in reanalysis, and the AC eddies that overlap with a blocking index. A novel definition, based on anomalously high 500 hPa geopotential height (Z500), is used in both a Eulerian sense (for block identification) and a Lagrangian perspective (for AC eddy tracking). Statistical relationships are found between the persistence of block events and the number and

strength of AC eddies that enter a block, and the validity of the selective absorption mechanism (SAM, Yamazaki and Itoh (2013a), see Sect. 2.5.1) is explored.

The examination of RQ2 is achieved through two different perspectives. The dynamics of three blocks, with similar persistence but differing numbers of AC eddies, are analysed in detail. Firstly, the role of PV flux convergence in blocks, and the importance of AC eddies for this quantity, are analysed using reanalysis. Second, the role of diabatic dynamics in these blocks is also quantified through simulations including diagnostics of diabatic processes in the Met Office Unified Model (MetUM). Results for the three blocks are compared and contrasted to see where and when PV flux convergence and diabatic processes are most active, and whether or not diabatic processes are more important in blocks with fewer eddy interactions.

Finally, RQ3 is explored by examining multiple forecasts from the operational global ensemble issued by the Met Office for two of the same three blocks analysed for RQ2. Periods of increased forecast uncertainty in block area, intensity, and location are identified by comparing to reanalysis, for multiple combinations of forecast initialisation and lead times. Any periods of reduced predictability that coincide with AC eddy interactions are then analysed further. Ensemble members are grouped together based upon their performance in simulating the block, and maps of these groups are compared to determine whether the error in the blocking forecast arises from errors in representation of the AC eddies.

1.3 Thesis Outline

Here, the thesis structure is summarised.

Section 2 provides the background to the thesis from the existing literature. The section begins (Sect. 2.2) by describing the typical characteristics of a block, including the five canonical configurations that a block can take, a qualitative description of how they are identified meteorologically, and where and when they are climatologically found. Common impacts from atmospheric blocking are discussed in Sect. 2.3, which highlight the importance of studying them further and the need for accurate weather forecasting to better prepare for such hazards. A

more objective description of block identification techniques is outlined in Sect. 2.4. Section 2.5 describes the dynamics behind blocking events, with a focus on block-eddy interactions and diabatic processes. Sect. 2.6 gives an overview of previous studies that have tracked both blocking and non-blocking anticyclones. Finally, the performance of current weather and climate models in simulating blocking is discussed in Sect. 2.7, and highlights ways in which block representation can be improved.

The datasets and block and AC eddy definitions used throughout this thesis are then discussed in Sect. 3. Brief background descriptions of the models and datasets used are given in Sect. 3.1, while more specific information on details such as the forecast setup, tools, and analysis to be performed on them are given in the appropriate sections in later working chapters. The methodology and rationale behind the calculations to define blocks and AC eddies are described in Sect. 3.2, while again more specific methodology relevant to each working chapter is given later in the thesis.

RQ1 is examined in Sect. 4, and consists of the results presented in Suitters et al. (2023), where statistical relationships are derived between block persistence and AC eddies. Analysis of RQ2 is presented in Sect. 5 through the study of both PV flux convergence and the diabatic processes in three blocks with similar persistence and differing numbers of contributing AC eddies. RQ3 is explored in Sect. 6 through the analysis of ensemble forecasts of unpredictable periods in blocks that coincide with AC eddy interactions. More details on RQ1-3 are given in the previous section.

Finally, the thesis is concluded in Sect. 7, where the RQs are repeated and answered, and scope for future work is also discussed.

Chapter 2

Literature Review

2.1 Introduction to Anticyclones

Before examining the literature on blocks and AC eddies, some brief background is provided into the structure of mid-latitude anticyclones: both those that cause blocking and those that do not. At the surface, anticyclones are distinct regions of surface high pressure, marked by surface divergence and winds that spiral outwards from the centre of the high in a clockwise direction in the Northern Hemisphere (NH). Unlike with extratropical cyclones where two air masses meet at weather fronts, anticyclones normally consist of only one air mass with near-uniform properties throughout the high.

Non-blocking (i.e. transient) anticyclones can be considered as ridges within a baroclinic Rossby wave. This means that, like extratropical cyclones, transient anticyclones have a westward tilt with height, with the upper-level ridge centred slightly upstream and to the west of the surface high. Since they are embedded within the Rossby wavetrain, transient anticyclones generally progress eastward with the jet stream. In a comprehensive climatological study of anticyclones (Ioannidou and Yau, 2008), transient anticyclones are described as cold-core and generated as the result of longwave cooling over snow-covered land, or orographic lift (both processes which generate lower-level negative relative vorticity). Such anticyclones are referred to as "anticyclonic (AC) eddies" throughout the rest of this thesis, since they can be considered as anticyclonic perturbations from the mean flow. AC eddies can also be generated downstream of regions of cyclogenesis (Colucci, 1985).

On the other hand, blocking anticyclones (hereafter "blocks", unless otherwise specified) are not transient features found along the Rossby wave guide. They are much larger and persist for longer in a particular location than AC eddies, and also have a warm-core thermal structure, in contrast to AC eddies. Unlike the ridges and troughs along a baroclinic Rossby wave, blocks do not tilt with height and are instead considered to be equivalent barotropic in nature. In other words, the upper-level ridge is positioned vertically above the surface anticyclone in a blocking system and the system is "vertically-stacked", like a mature extratropical cyclone or tropical cyclone. Despite their stationarity, blocks are not Lagrangian coherent features, with the air within them being constantly replaced by both eddy (Sect. 2.5.1) and diabatic sources (Sect. 2.5.2); however the relative importance of each source in blocking is still unclear.

2.2 Blocking Characteristics

Atmospheric blocks are all identifiable by their anticyclonic circulation, large size, persistence, and quasi-stationarity. The anticyclonic nature of blocks is marked by a surface anticyclone, high geopotential heights, low PV on a height or potential temperature surface, or high potential temperature on a height or PV surface (see Sect. 2.2.1). More details on how blocks are identified objectively in datasets are given in Sect. 2.4. Despite these common characteristics, the exact configuration of each individual block can vary greatly from one another, and a single blocking event can undergo many changes to its orientation, shape, and intensity throughout its lifetime (Sousa et al., 2021). This means that often, it is easier for synopticians to subjectively identify blocks by looking at weather maps, rather than using a small set of objective criteria that cannot capture their full variability. This has led to a variety of different techniques for identifying blocks (Sect. 2.4), but in this section of the Literature Review, the focus will be on the typical characteristics that an atmospheric block can have.

2.2.1 Blocking Morphology

Blocks are anticyclonic systems that "block" the passage of mid-latitude westerly winds. They can be identified as persistent, large-scale, mid-latitude regions of:

- Relatively high mean sea level pressure (MSLP),
- A maximum in geopotential height, typically chosen to be at the 500 hPa level, or positive geopotential height anomaly,
- A maximum in potential temperature on a quasi-horizontal surface (normally on the PV = 2 pvu surface), or
- A minimum in PV, or negative PV anomaly, on a quasi-horizontal surface (usually isobars or isentropes), or between two such surfaces.

These characteristics are long-lasting, with lifetimes ranging from several days to multiple weeks (e.g. Woollings et al., 2018).

Due to the mostly barotropic nature of blocks, the listed features are often coincident, and thus any one of the above methods can be used to detect a blocking event (see Sect. 2.4). Figure 2.1 shows example blocks in terms of their Z500 and potential temperature on the 2 pvu level. High geopotential heights coincide with high potential temperatures (and vice versa), confirming that either metric could be used to identify blocks in these cases. Figure 2.1 also shows the five typical

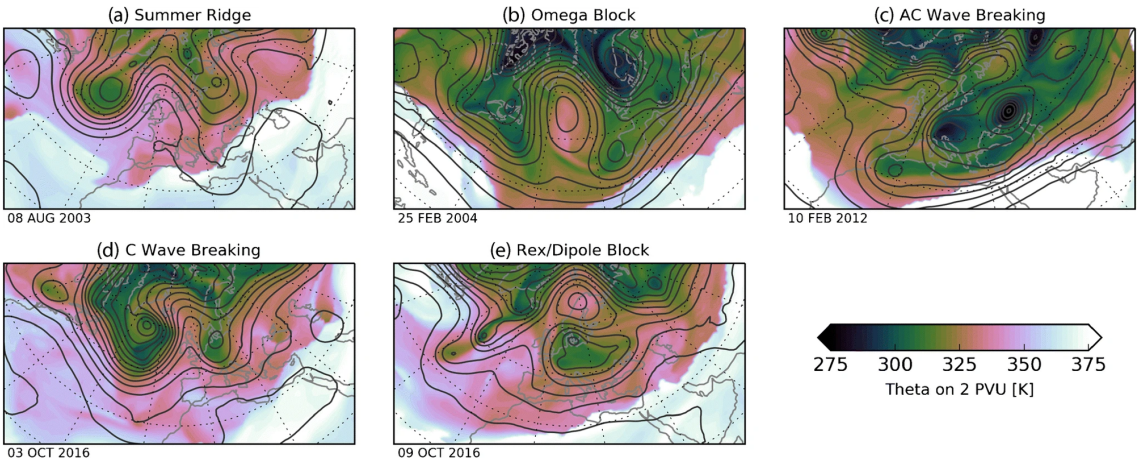

Figure 2.1: Examples of the five typical blocking shapes using data from ERA-Interim: (a) a stationary ridge, (b) an omega block, (c) anticyclonic wave breaking, (d) cyclonic wave breaking, and (e) a Rex/dipole block. Black contours show the 500 hPa geopotential height (60 m intervals), and shading shows the potential temperature on the 2 pvu surface. Taken from Fig. 1 in Woollings et al. (2018).

configurations that a block can have. The simplest is a stationary ridge (Fig. 2.1a) which occurs when a large-amplitude Rossby wave has a near-zero phase speed, preventing its propagation downstream thereby building stationary anticyclonic conditions. The large-scale flow around this ridge is diverted poleward, and if this diversion becomes amplified enough, a closed circulation can develop inside the ridge. The effect of this is to cause an Ω-shaped pattern in the upper-level streamlines or Z500 contours, and thus this blocking shape is called an omega block. RWB (see Sect. 2.5.3) can also lead to blocking, and is illustrated by the anticyclonic (Fig. 2.1c) and cyclonic (Fig. 2.1d) overturning of Z500 contours. Mature blocks often take the shape of a Rex or dipole block (Fig. 2.1e), where a north-south dipole of an anticyclone and cut-off low develops and the large-scale mean flow is diverted to the north and south of the systems.

Sousa et al. (2021) introduced a conceptual model describing how a block can cycle through various configurations throughout its lifetime, shown in Fig. 2.2. In this model, the stationary ridges shown in Fig. 2.1a arise from temporary poleward excursions of the subtropical high pressure belt (Fig. 2.2a, b) which can sometimes form mid-latitude blocking events. If RWB occurs, mid-latitude blocking can begin and an omega block can form within the subtropical high intrusion as the mid-latitude jet stream amplifies (Fig. 2.2c). At this stage, the block is still connected to the subtropical high belt, but if the anticyclone becomes secluded from it at a later stage, a Rex block can form as shown in Fig. 2.2d, e. It is worth noting that not all blocks go through this lifecycle (see examples in Sect. 5), but the model proposed by Sousa et al. (2021) demonstrates blocking behaviour that is commonly seen.

2.2.2 Blocking Climatology

Many studies have presented a climatology of blocking according to various different methods (e.g. Scherrer et al., 2006; Tyrlis and Hoskins, 2008; Schiemann et al., 2017; Liu et al., 2018; Suitters et al., 2023), see also Sect. 2.4. All these climatologies vary slightly in their absolute magnitudes and precise locations of blocking frequency maxima, but most of them demonstrate similar qualitative characteristics (Barnes et al., 2012), which will be discussed here. An example

Northern Hemisphere (NH) blocking frequency climatology for winter (DJF) and summer (JJA) from Woollings et al. (2008) is shown in Fig. 2.3. Blocking is most frequent in DJF and least common in JJA. In both seasons, two blocking centres of action are present, slightly downstream and poleward of the storm track regions (Tyrlis and Hoskins, 2008) in the Northeast Pacific and the Euro-Atlantic. The JJA Euro-Atlantic blocking frequency maximum is located over Scandinavia whereas in DJF the maximum is over the Northeast Atlantic south of Iceland; the Northeast Pacific blocking maximum location does not have as much seasonality. In this climatology, other well-documented blocking regions of Greenland (e.g.

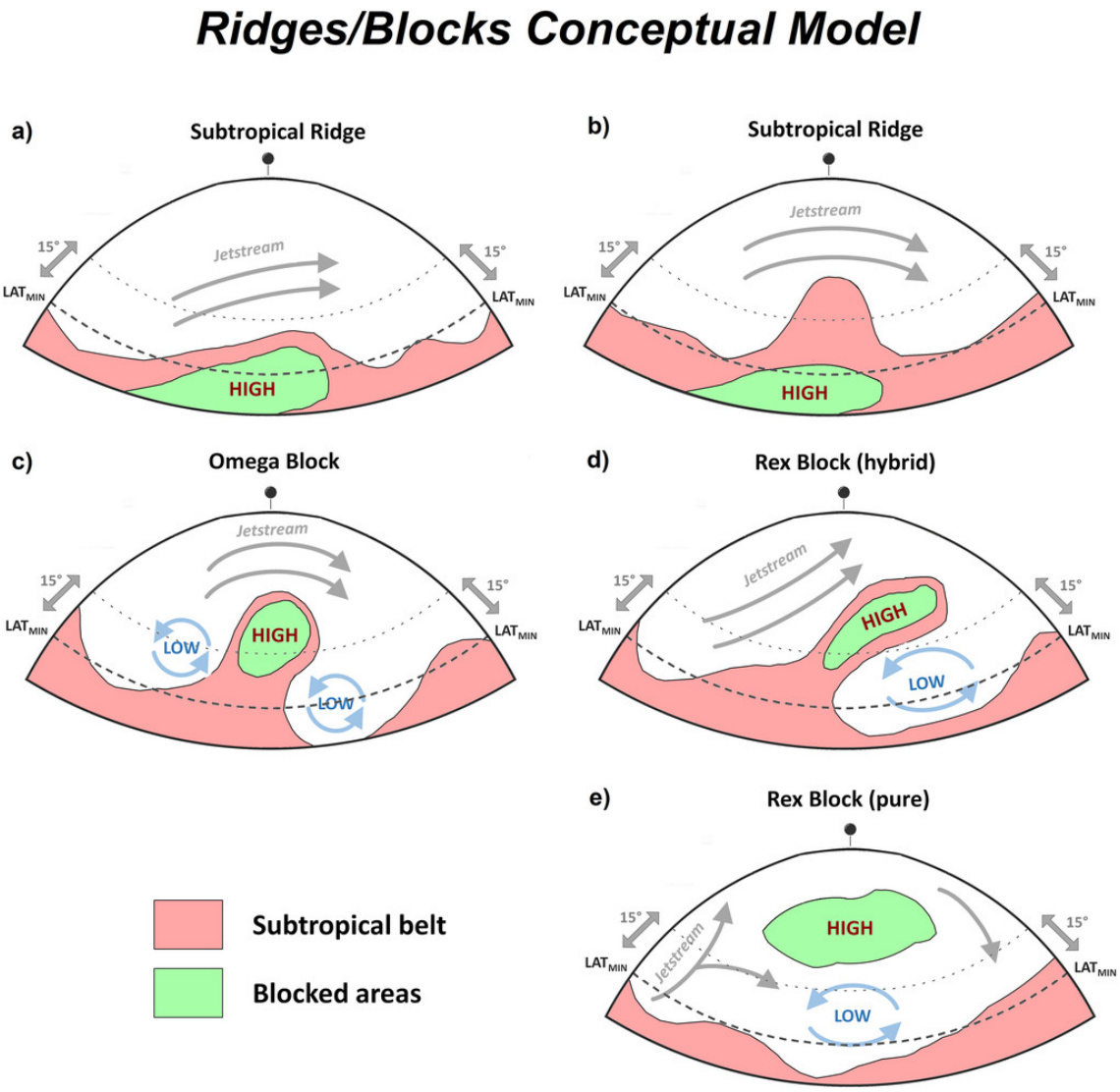

Figure 2.2: Conceptual model, from Fig. 1 in Sousa et al. (2021), demonstrating how a block may evolve from the extension of a subtropical ridge (a) to eventually taking the form of a dipole block (e). Red shading shows the location of the subtropical high belt (with mean location LAT_{MIN}), and green shading shows blocked areas.

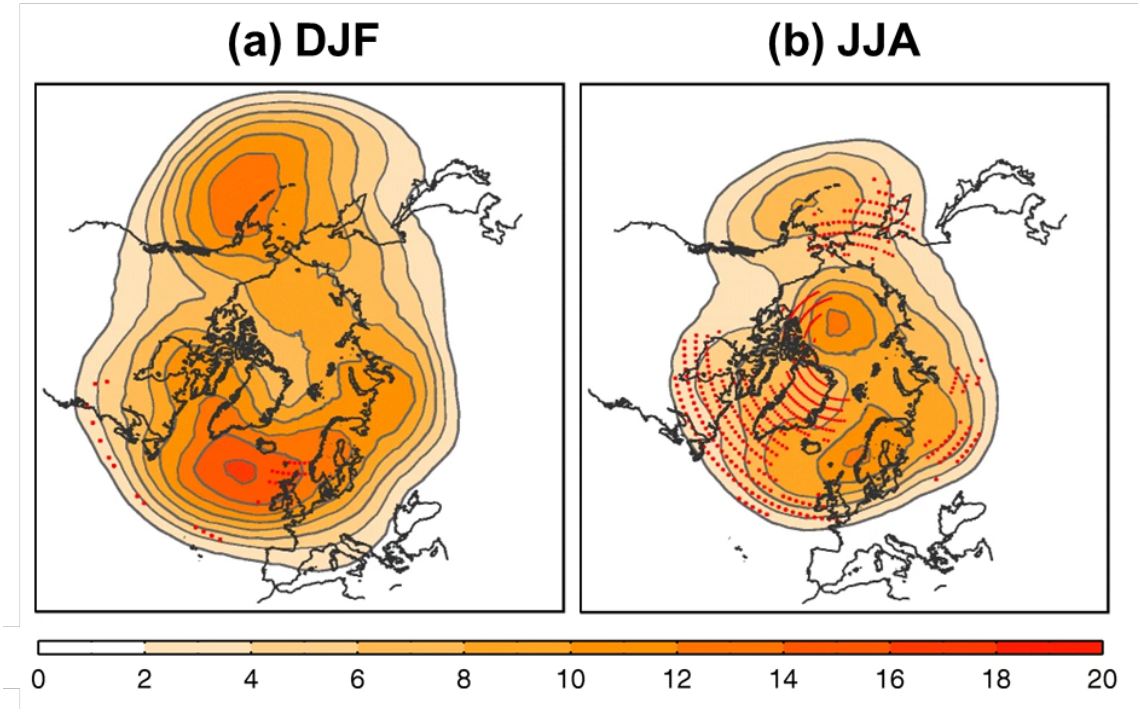

Figure 2.3: Northern Hemisphere Blocking climatology, in terms of percentage of days blocked according to the ANOM blocking index (see Sect. 2.4.4 for more details) for (a) December–February (winter, DJF), and (b) June–August (summer, JJA). Red stippling shows regions where there has been an increase in blocking tendency in recent decades, but this will not be discussed further in this thesis. Figure adapted from Fig. 2 in Woollings et al. (2008).

Davini et al., 2012; Hanna et al., 2016; Hauser et al., 2023) and the Urals (e.g. Wang et al., 2010; Peings, 2019; Luo et al., 2021) do not have their own maxima, and are instead part of a broader Euro-Atlantic maximum. There is also a maximum in high-latitude blocking in JJA that is not present in DJF.

It is also worth noting that while less common, less persistent, and less intense than NH blocking, blocking also occurs in the Southern Hemisphere (SH). The majority of SH blocking occurs over the South Atlantic basin (Toulabi Nejad et al., 2022), but blocking can also be found over the Australia-New Zealand sector in austral winter (Patterson et al., 2019). However, the focus for the rest of the thesis will be on NH blocking.

2.3 Impacts from Atmospheric Blocking

The anomalous surface circulation patterns brought on by atmospheric blocking can bring impacts both beneath and around the blocking high itself (e.g. Kautz

et al., 2022). However, the severity and spatial coverage of these hazards depends on the time of year, shape, and position of the blocking circulation (Sousa et al., 2021). Both the persistence of an individual blocking event, and the accumulation of blocked days following successive blocking events, have been shown to be important for surface impacts (Drouard and Woollings, 2018). This section summarises the most common hazards that can be associated with blocking events (more detail on blocking impacts, the dynamics behind them, and case studies can be found in the review by Kautz et al. (2022)).

2.3.1 Impacts on Surface Temperature

Warm Season

The sustained high surface pressure within a block results in the suppression of cloud formation and clear-sky conditions. This results in enhanced diabatic heating of near-surface air from larger sensible heat flux and incoming shortwave radiation, and increased adiabatic warming due to the subsidence of air under the anticyclone. Therefore under the block itself, surface temperatures are expected to rise, and indeed the two aforementioned mechanisms account for the majority of the heating beneath a block in the summer, rather than horizontal temperature advection (Bieli et al., 2015; Zschenderlein et al., 2019). The build-up of heat under a block can also enter a positive feedback loop with soil moisture (Fischer et al., 2007; Miralles et al., 2019), whereby the decreased precipitation associated with the block decreases soil moisture and latent heating, thus resulting in increased sensible heat flux and further heating.

Naturally this increase of heat beneath a persistent block can therefore lead to a prolonged period of above-average temperatures, known as a heatwave. When blocking occurs over Europe in summer, a heatwave beneath the blocking anticyclone is common (Kautz et al., 2022). Pfahl and Wernli (2012) found that more than four-fifths of 6-hourly high extreme temperatures in mid- and high-latitudes coincide with a blocked pattern, but the relationship between blocking and summer heatwaves varies according to location. Brunner et al. (2018) found a strong positive correlation between northern European blocks and northern European

heatwaves in every season except winter (e.g. 80% of summer Scandinavian heatwaves coincide with a block), but blocking is less likely to cause a heatwave in southern Europe (only 10% of all heatwaves). As a result of the strong relationship in Western, Northern, and Central Europe between anomalously anticyclonic circulation and heatwaves (e.g. Meehl and Tebaldi, 2004; Zschenderlein et al., 2019), blocking is strongly related to extreme summer heat, and it has been shown that heatwaves persist longer when they coincide with a block (Röthlisberger and Martius, 2019). Heatwaves can have a marked effect on human comfort and mortality (Robine et al., 2008), as well as impacts on the natural world including drought (Sousa et al., 2017) and wildfires (e.g. Sun et al., 2019) (see Sect. 2.3.2). Many examples of heatwaves resulting from a block have been previously studied in detail, for example Europe, summer 2003 (Black et al., 2004); Russia, summer 2010 (Trenberth and Fasullo, 2012); and China, summer 2018 (Li et al., 2019).

Cold Season

Cold season blocking can result in periods of anomalously low surface temperatures. The continued adiabatic and diabatic warming within the core of the block mentioned above means that the daytime surface temperatures beneath the blocking anticyclone are often not extreme. However, the long nights combined with increased outgoing longwave radiation due to clear-sky conditions can lead to very cold minimum temperatures instead (Sousa et al., 2018). The most extreme cold conditions induced by blocking are most often found on the downstream and equatorward flanks of the block, and are associated with the advection of negative temperature anomalies from higher latitudes (Bieli et al., 2015; Sousa et al., 2018; Kautz et al., 2022), also known as cold air outbreaks (Smith and Sheridan, 2020). This is in contrast with summer blocking, where the most extreme temperatures are driven by local processes, rather than by thermal advection from non-local sources. However like with heatwaves, the majority (70%) of European cold spells correspond with a Euro-Atlantic blocking event (Brunner et al., 2018). Therefore winter blocking can also be detrimental to society through cold weather-related health impacts (Charlton-Perez et al., 2019). Both cold spells

and heatwaves can also have important implications for renewable energy (e.g. Bloomfield et al., 2020), infrastructure (e.g. Forzieri et al., 2018), and agriculture (e.g. Vogel et al., 2019) (Sect. 2.3.3). Previous studies have examined case studies of extreme cold waves brought about by blocking, for example in Western Europe in winter 2009-10 (Cattiaux et al., 2010) and March 2018 (Karpechko et al., 2018), and the Balkans in January 2017 (Anagnostopoulou et al., 2017).

2.3.2 Hydrological Impacts from Blocking

Hydrological extremes (drought and floods) are also common meteorological hazards associated with blocking events. The presence of a block causes the jet stream to be diverted to the north and south around it (Rex, 1950). When this happens, the position and orientation of the mid-latitude storm track is also changed, bringing precipitation anomalies underneath the block, on its flanks, and further downstream. These are discussed below.

Beneath the Blocking High

First, the hydrological extremes beneath the blocking high itself are described. Prolonged subsidence in a blocking anticyclone suppresses cloud development and therefore precipitation. Furthermore, the presence of the block prevents the usual passage of extratropical cyclones in the region, and thus this dominant source of precipitation in mid-latitudes (Hawcroft et al., 2012) is also lacking beneath a block. Naturally, dry spells can lead to drought beneath the block, given appropriate antecedent conditions and longevity of the block. For example, Sousa et al. (2017) found that during Central European blocking, only one-quarter of the normal daily precipitation amounts fall, and low-latitude blocking is the primary source of water scarcity in Southern Europe. If precipitation deficits associated with blocking occur during the wet season (when a location gets the majority of its annual rainfall, for example October–March in Iberia), the effects of drought can be even more severe and long-lasting (Kautz et al., 2022). The shape of blocking can also affect the severity of precipitation anomalies (Sousa et al., 2021). Drought is problematic because it results in the availability of less high-quality water, and the impacts caused by this are diverse and affect a wide range of sec-

tors, including human (e.g. hosepipe bans (Chappells et al., 2011)), economic (e.g. agricultural (Brunner et al., 2017)), and natural (e.g. wildfires (Antokhina et al., 2023)).

Block Edges

The edges of the blocks are also associated with hydrological impacts. The deflection and potentially splitting of the mid-latitude jet stream means that extratropical cyclones take a less-typical track when a block is present. Lenggenhager and Martius (2020) showed that blocking affects the location and intensity of regional-scale rainfall in Europe. The western and northern flanks of atmospheric blocks are often home to enhanced moisture transport (Lenggenhager and Martius, 2020) from warm conveyer belts (WCBs) and atmospheric rivers (Pasquier et al., 2019), which can lead to heavy precipitation and impacts such as flooding (Grams et al., 2014). Blocks can also lead to the stalling of cut-off lows and PV streamers that bring heavy precipitation to an area. For example, all of the worst summer floods in Switzerland between 1868 and 2005 were caused by a stalling of such systems upstream of a Russian block (Stucki et al., 2012). In cases where the storm track is diverted to the south during an atmospheric block, enhanced precipitation and flooding can be found to the south of the block instead. During European blocking, heavy rainfall often occurs in Southern Europe, south of the blocking anticyclone (Sousa et al., 2017).

Thunderstorms are also a hazard that can become more or less likely on the flanks of blocking events, depending on the time of year. In the warmer months, very warm and moist air can be advected from the south to the block's west, which can promote thunderstorm development. Mohr et al. (2019) found that more thunderstorms were present in Western and Central Europe when blocking was situated over the Baltics. However, advection of cooler, more stable air from the northeast can suppress thunderstorm development around the eastern flank of European blocks (Mohr et al., 2019), while the cold conditions advected towards this region in winter can lead to snowstorms (Kautz et al., 2022).

Further Up-/Downstream

Since blocks modulate the position of the storm track, blocking can also result in significant weather changes further downstream. For example, Lenggenhager and Martius (2020) found that summertime central or eastern North Atlantic blocking increases the likelihood of heavy precipitation events further downstream over much of the Europen continent, as a result of the shifted storm track position. The amount of North American and European spring and summer snow cover was also shown to correlate with the amount of North Atlantic blocking, which then goes on to affect subsequent snow cover for the following seasons (García-Herrera and Barriopedro, 2006).

2.3.3 Other Impacts from Blocking

This section describes some of the other impacts from atmospheric blocking aside from those to temperature and precipitation. Firstly, blocking can lead to both increased demand and reduced supply of renewable energy in Europe. A study by van der Wiel et al. (2019) found that atmospheric blocking results in long periods (7–14 days or more) of low renewable energy production that peaks in late summer due to weak winds beneath the high. This agrees with the finding that Europe-wide wind energy generation decreases during a European, Scandinavian, or Greenland blocking regime (Grams et al., 2017). More details are given on weather regimes in Sect. 2.4.1. Bloomfield et al. (2020) found that European peak energy demand occurs during periods of high pressure, where anomalously cold air is advected towards Europe from Russia and Scandinavia, however these are also the periods where the shortfall in energy generation is largest (van der Wiel et al., 2019). Therefore, atmospheric blocks are responsible for the problematic combination of increased energy demand but also reduced renewable energy generation from wind. While solar energy generation increases underneath sunny blocks, the current installed capacity means that the loss of generation from wind power is a far more important factor (Bloomfield et al., 2020).

The increased subsidence and reduced wind speeds under a block also has implications for air quality, where pollutants become trapped in the boundary layer.

It has been demonstrated that both boundary layer ozone and PM10 concentrations increase under European blocks (Garrido-Perez et al., 2017; Ordóñez et al., 2017), meaning that in blocked weather, it is less likely that air quality meets safe levels. Winter blocks can also lead to what is sometimes known as "anticyclonic gloom" (Li et al., 2021), where prolonged periods of fog and low stratus cloud persist beneath the block as a result of the strong temperature inversion.

While surface winds underneath a block are typically very light, blocks can indirectly cause strong winds on its flanks. Pfahl (2014) found that for northwestern and northeastern Europe, periods of extreme maximum wind gusts are associated with a higher-than-climatology blocking frequency in southern Europe. The presence of a blocking anticyclone combines with a surface cyclone in northern Europe to create a stronger pressure gradient and therefore increase surface wind speeds. An example of this occurred during January 2007, where Storm Kyrill brought strong winds to Western, Northern, and Eastern Europe, which were exasperated by a blocking anticyclone over southern Europe (Fink et al., 2009).

To conclude this section of the Literature Review, blocking can cause various diverse severe weather conditions at the surface. Examples of these impacts range from severe heat or cold, drought, flooding, renewable energy generation challenges, poor air quality, and strong winds (Kautz et al., 2022). Therefore, it is crucial that our understanding of blocking is improved in order to better prepare for the hazards that they may bring.

2.4 Block Identification

As described in Sect. 2.2.1, all blocks are identified by their anticyclonic circulation pattern, persistence, and large spatial extent. However, quantifying these measures in gridded datasets is not simple and has led to a large variety of methods for defining a block. The purpose of this section is to describe the main techniques of identifying a block in datasets, as well as to discuss some of their advantages and disadvantages. Further details of some of the block identification techniques mentioned here, and their benefits and drawbacks, are given in Bar-

riopedro et al. (2010), but the discussion in this thesis will include these as well as other methods developed since.

2.4.1 Weather Regimes

One method to classify a blocked weather configuration is through the classification of weather regimes. Weather regimes by their nature lend themselves to identifying certain blocking situations, because they are designed to capture common weather patterns that are recognisable for their recurrence, persistence, and quasi-stationarity (Michelangeli et al., 1995). To do this, a large dataset of MSLP (James, 2007; Neal et al., 2018), or geopotential height at either 700 hPa (Z700, Vautard (1990)) or 500 hPa (Ferranti et al., 2015; Grams et al., 2017; Lee et al., 2023) is required. Then, a sufficient number of empirical orthogonal functions (EOFs) are computed and retained, and k-means clustering is used to identify the most common weather patterns that a region experiences. This subsection of the Literature Review summarises and evaluates some of the most notable examples of weather regime definitions in previous studies.

One of the earliest studies into defining weather regimes for northwestern Europe and the North Atlantic was performed by Vautard (1990). In this study, two-daily Z700 obtained from National Meteorological Center data, for extended winter (November–March) 1949–1986 is used. These data are projected onto the first nine EOFs and a low-pass filter is applied to remove temporal fluctuations smaller than 10 days. Vautard (1990) found there to be four common weather regimes around the Euro-Atlantic sector: European blocking (BL), the zonal regime (ZO), Greenland anticyclone (GA), and an Atlantic ridge (AR). A later study by Ferranti et al. (2015) using reanalysis from the European Centre for Medium Range Weather Forecasts (ECMWF) of Z500 from October–April 1980–2008 and 10 EOFs found the same four fundamental regimes to be most common. The zonal and Greenland anticyclone regimes from Vautard (1990) are the positive and negative phases respectively of the North Atlantic Oscillation (NAO, e.g. Visbeck et al. (2001)), and are therefore denoted as NAO+ and NAO- in the work by Ferranti et al. (2015). The regimes are depicted in Fig. 2.4 and briefly described in Table 2.1.

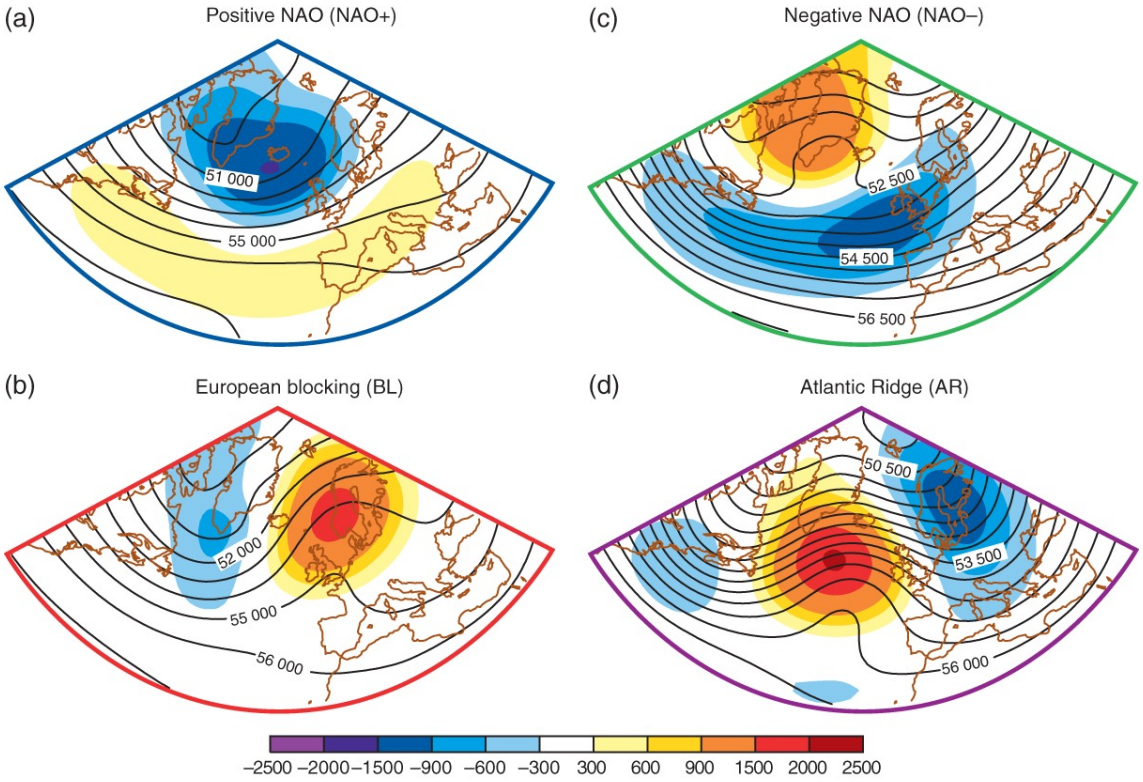

Figure 2.4: The four winter weather regimes in the Euro-Atlantic sector. Black contour lines show the average Z500 and the filled contours show the anomalous Z500 during each regime (both in metres, see Ferranti et al. (2015) for more details on the calculations of the average and anomalous Z500). Taken from Fig. 1 of Ferranti et al. (2015).

Name	**Description**
Positive NAO (NAO+)	Anomalously low Z500 over Iceland and the northeast Atlantic, and slightly higher than normal Z500 south of approximately 45°N throughout the North Atlantic. Conditions across Western Europe are very zonally-driven.
European blocking (BL)	Blocking anticyclone positioned over northern Europe, with a slightly deeper trough than climatology south of Greenland.
Negative NAO (NAO-)	Anomalously high Z500 over Greenland and the northwest Atlantic, with anomalously low Z500 over much of the rest of the North Atlantic and Western and Northern Europe.
Atlantic ridge (AR)	Strong ridging in the North Atlantic southeast of Greenland, and anomalous troughing over Northern Europe, bringing northwesterly winds to Western Europe.

Table 2.1: The four winter Euro-Atlantic weather regimes as defined in Ferranti et al. (2015) and Fig. 2.4.

Due to weather regimes requiring persistence by construction, it is easy to deduce that three of the four regimes defined by Ferranti et al. (2015) depict blocking of some sort somewhere in the Euro-Atlantic sector. The NAO- regime is associated (and sometimes considered synonymous) with Greenland blocking (e.g. Woollings et al., 2008; Davini et al., 2012), the BL regime is named after a blocking event over Europe, and the AR regime has a persistent blocking anticyclone over the northeastern Atlantic. Therefore, when a particular synoptic situation is described as fitting best into one of these three regimes, it is likely that blocking is occurring somewhere nearby. However, because the regime patterns are averages, individual events that are classed as having a BL regime, for example, may look rather different synoptically than the mean pattern, so therefore may not best describe the surface conditions. Secondly, these regime definitions are only applicable for October to April, so are not valid for year-round regime classification. Finally, these regimes only apply to Euro-Atlantic weather conditions, and using this technique to find blocking elsewhere requires new clusters and regimes to be defined (for example, see Lee et al. (2023) for North Pacific-North American weather regimes).

Some of the issues described above were addressed by Grams et al. (2017), where Euro-Atlantic weather regimes were defined using year-round Z500 rather than just extended winter, and seven regimes (rather than four) were devised to differentiate a little more between different synoptic situations. Three cyclonic (Atlantic trough, AT; zonal, ZO; and Scandinavian trough, ScTr) and four anticyclonic (Atlantic ridge, AR; European blocking, EuBL; Scandinavian blocking, ScBL; and Greenland blocking, GL) weather regimes were defined using this method. The AR, EuBL and GL regimes are qualitatively similar to the AR, BL and NAO- regimes found in Ferranti et al. (2015), but the addition of the ScBL regime, where the blocking anticyclone is positioned over Scandinavia instead of further south in Europe allows for slightly more distinction between weather types. In addition to the fact that these regimes apply all year, these seven weather patterns can describe more of the synoptic situations that lead to blocking over Europe, but still lack the precision of other metrics as to exactly how the block might be positioned. More detail as to the exact position of a

block (or cyclone) could be achieved by clustering over a much smaller region and including many more clusters, for example the 30 patterns over northwestern Europe used for forecasting at the Met Office (Neal et al., 2018), or the 29 "Grosswetterlagen" devised by the Deutche Wetterdienst (James, 2007)). However, the issue remains that these regimes are only valid for a particular area, and thus the use of weather regimes for an entire hemisphere is not practical.

2.4.2 Z500 Gradient Reversals

The methods for detecting a block described in the following (Sects. 2.4.2-2.4.5) can be applied anywhere and do not require a fixed location to work, unlike weather regimes. One of the most common ways to identify blocking is to use the concept of a reversal in the meridional Z500 gradient. Climatologically, Z500 is largest closest to the equator and gradually decreases in the poleward direction, leading to an equatorward meridional gradient in Z500 (Fig. 2.5a). However under a block, anticyclonic conditions generate a local maximum in Z500 and thus lead to a local reversal in the meridional Z500 gradient, with locally high Z500 poleward of a region of lower Z500 (Fig. 2.5b). This is especially true in dipole blocks where a cut-off low develops on the equatorward side, resulting in a local minimum in Z500.

A very simple implementation of this idea was introduced by Lejenäs and Økland (1983). Here, a "zonal index" of Z500 (Z_{500}) is used to characterise blocking, in 10° intervals of longitude. The zonal index is given as the difference in Z500 between 40 and 60°N. Blocking is then identified in areas where this index is negative, i.e. when Z500 is lower to the south than the north (a reversal of climatology). This idea of a reversal in Z500 was taken further in the study by Tibaldi and Molteni (1990). In their blocking index, the *gradient* of Z500 in the meridional direction had to be reversed. Blocking anticyclones are identified where there are sufficient westerly winds to the north (i.e. the jet), and easterly winds to the south. These calculations are the the basis for the AGP blocking index (Scherrer et al., 2006), which defines a block using the following geopotential height gradients (GHG) around a grid point's latitude (ϕ_0) in both the equatorward (e) and

poleward (p) directions (with longitude λ_0):

$$GHG_e = \frac{Z_{500}(\lambda_0, \phi_0) - Z_{500}(\lambda_0, \phi_e)}{\phi_0 - \phi_e} \tag{2.1}$$

$$GHG_p = \frac{Z_{500}(\lambda_0, \phi_p) - Z_{500}(\lambda_0, \phi_0)}{\phi_p - \phi_0} \tag{2.2}$$

ϕ_p and ϕ_e are usually taken to be 15° north/south of ϕ_0, since these are the typical latitudinal size of mid-latitude blocks (Tibaldi and Molteni, 1990). Blocking occurs at grid points where the following conditions are met for five or more days:

$$GHG_e > 0 \tag{2.3}$$

$$GHG_p < -10 \text{ m/°lat} \tag{2.4}$$

The condition shown in Eq. 2.3 asserts that the equatorward Z500 gradient must be positive, i.e. 15° in the equatorward direction, Z500 must be lower than at the reference point. Additionally, Eq. 2.4 states that on the poleward side of the reference point, Z500 must be sufficiently lower such that strong westerly winds are present.

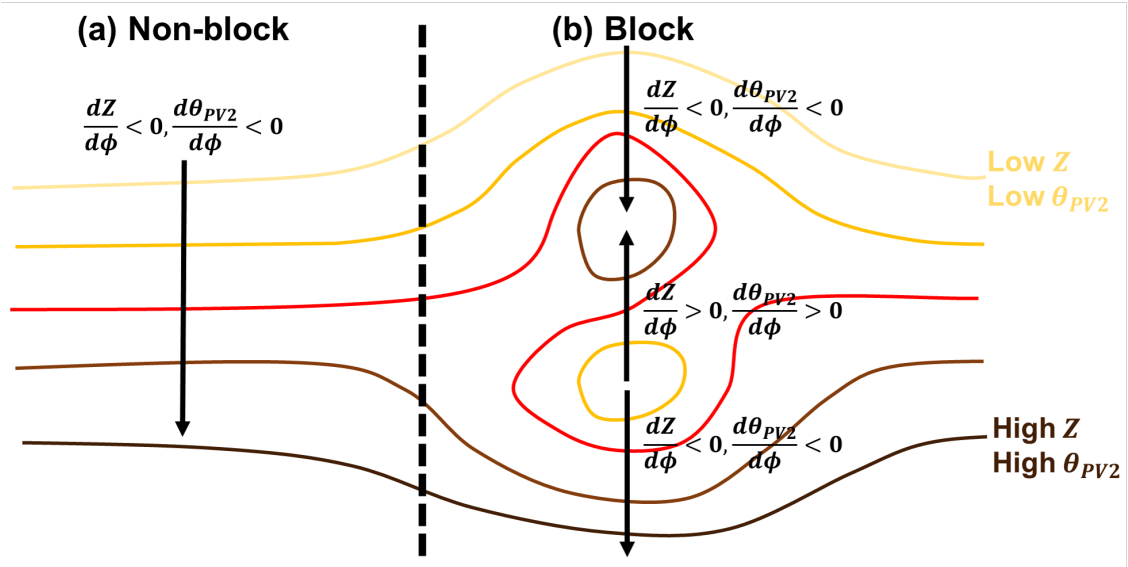

Figure 2.5: Schematic of the meridional Z500 and potential temperature gradients ($\frac{dZ}{d\phi}$ and $\frac{d\theta_{PV2}}{d\phi}$ respectively) for (a) zonal flow and (b) a blocked flow. Lighter (darker) contour lines indicate lower (higher) Z500 or potential temperature. The poleward direction is upward in this diagram such that the mean flow in (a) is westerly.

Due to its simplicity, the AGP index is a quick way computationally to identify blocks in reanalysis or other datasets, and as such has been a popular choice for many studies of blocking (e.g. Barriopedro et al., 2006; Scherrer et al., 2006; Diao et al., 2006; Davini et al., 2012; Dunn-Sigouin et al., 2013; Azizi et al., 2015). However, AGP-like indices have a few well-known problems (Barriopedro et al., 2010). These indices do not perform particularly well at the identification of stationary ridge-like blocks, or weak omega blocks, since the reversal in meridional Z500 gradient is much weaker in these cases and the criterion in Eq. 2.3 is not met. The AGP index also has preference for detecting low-latitude blocking events (e.g. Schiemann et al., 2017). Conversely, high-latitude blocking is underestimated using Z500 gradient reversal-based methods (e.g. Tyrlis et al., 2021).

The latter two problems can be improved by imposing additional criteria or modifying the thresholds in the calculations of Z500 gradients. Firstly, a second equatorward Z500 gradient condition was introduced by Davini et al. (2012), and adapted in other studies such as Sousa et al. (2021). Here, it is also imposed that on the equatorward side of the block, there should be westerly winds (as well as on the poleward side) to indicate the splitting of the jet around blocks, which is not seen around low-latitude blocks:

$$GHG_{e2} = \frac{Z_{500}(\lambda_0, \phi_e) - Z_{500}(\lambda_0, \phi_e - 15^\circ)}{15^\circ} < -5 \text{ m}/^\circ \text{ lat} \tag{2.5}$$

The original AGP index may also be modified in order to better capture high latitude blocking events, where there may not necessarily be westerly winds on the poleward side of the block. Such a modification was implemented for the high latitudes only by Tyrlis et al. (2021), where the poleward threshold was adapted such that only non-easterly winds were present, rather than strong westerlies, i.e. $GHG_p < 0$.

2.4.3 θ Gradient Reversals

Another variable commonly used to identify blocking is potential temperature (θ) on a PV surface. As with Z500, potential temperature on a PV surface decreases from the equator to the pole, and blocks can be identified by reversals in

the meridional potential temperature gradient (Fig. 2.5b). In their work, Pelly and Hoskins (2003a) and Tyrlis and Hoskins (2008) defined blocking using potential temperature on the PV = 2 pvu surface (hereafter θ_{PV2}), also known as the dynamical tropopause. This overturning of potential temperature contours is indicative of RWB, a key mechanism behind blocking dynamics (see Sect. 2.5.3). According to the Pelly-Hoskins blocking index (B), local instantaneous blocking at longitude λ_0 is said to occur when:

$$B = \frac{2}{\Delta\phi} \int_{\phi_{cen}}^{\phi_{cen}+\Delta\phi/2} \theta_{PV2} \, \mathrm{d}\phi - \int_{\phi_{cen}-\Delta\phi/2}^{\phi_{cen}} \theta_{PV2} \, \mathrm{d}\phi > 0 \tag{2.6}$$

where $\Delta\phi$ is a typical meridional scale for blocking (taken to be 30°), ϕ_{cen} is the annual mean central blocking latitude (CBL) $\pm$4 degrees. The CBL is defined as the climatological maximum in eddy kinetic energy, varying from 60°N around Scandinavia, to 45°N around the dateline (see Figure 4 in Pelly and Hoskins (2003a)). If $B > 0$ for at least 15 adjacent degrees of longitude for four or more consecutive days, then this is defined as a "blocking episode".

Most of the problems encountered with the traditional AGP index are not encountered when considering the Pelly-Hoskins index instead (Barriopedro et al., 2010), due to the finer detail that a PV-θ-based index is able to provide (Pelly and Hoskins, 2003a). As such, it has also become a popular choice for blocking identification in many other studies (e.g. Berrisford et al., 2007; Tyrlis and Hoskins, 2008; Masato et al., 2009, 2013a; Wachowicz et al., 2021). However, this form of the Pelly-Hoskins blocking index requires the calculation of the CBL, which requires another dataset and is thus computationally more complex. Additionally, θ_{PV2} is not as readily available as other atmospheric variables in some datasets. Therefore, some studies altered the original Pelly-Hoskins index such that it searches for reversals in Z500 (by substituting Z for θ_{PV2} in Eq. 2.6) instead (e.g. Masato et al., 2013b; Zappa et al., 2014).

2.4.4 Z500 Anomalies

A different approach to identifying blocks is to consider them as a region of anomalously anticyclonic circulation, rather than a reversal of a meridional gra-

dient. One such way to do this is to think of blocks as local maximum in Z500, or regions of large positive Z500 anomalies. The simplest and earliest methods of this type rely on a Z500 anomaly from some climatology, either from a fixed global climatological value (Charney et al., 1981; Knox and Hay, 1984), a threshold that varies according to location (Hartmann and Ghan, 1980), or a threshold that varies according to time of year (Shukla and Mo, 1983).

A more recent and more sophisticated block detection algorithm that utilises Z500 anomalies is known simply as the Anomaly (ANOM) index (Woollings et al., 2018; Schiemann et al., 2020). The calculation of this index is as follows:

1. At each grid point, the daily Z500 data are used to calculate a day-of-year (DOY) climatology. For smoothing, a 31-day running mean is also applied.
2. Daily Z500 anomalies from this DOY climatology for each grid point are calculated.
3. The DOY anomalies are grouped by month, and the 90th percentile anomaly value for latitudes between 50-80°N is found. After further smoothing (a three-month rolling mean), these Z500 anomalies become the blocking threshold for the entire hemisphere for that month. In other words, the same threshold (say, γ_{Jan}) applies for the Pacific, Atlantic, Urals, Greenland, etc. for the month of January, a different threshold (γ_{Feb}) applies everywhere in the NH for February, and so on.
4. Blocking events are subsequently identified as contiguous areas that exceed the blocking threshold if:
    - The total area of grid points exceeding the threshold is at least 2 million square kilometres,
    - The day-to-day overlap of blocked grid points exceeds 50%, and
    - The previous two conditions are met for at least 5 consecutive days.

Though the calculation process is quite complex, the ANOM index does have some favourable characteristics. Firstly, it performs well for blocks of all shapes in all locations since it does not search for a reversal in Z500 as the AGP index does. Therefore, it is far better at detecting stationary ridges and weaker blocks than the AGP index, provided the block's anomaly exceeds the strength threshold.

Furthermore, minimum size and persistence thresholds are built in to the index calculations to ensure that the features detected as blocks by the ANOM index are most likely actual blocking anticyclones, reducing the amount of spurious detections.

Liu et al. (2018) followed another method for defining persistent maxima in anomalous Z500. They sought anomalies in both space and time and ultimately show that blocks can be thought of as regions where the Z500 anomaly from the zonal mean is large. Mathematically, this is expressed as:

$$Z_* = Z_{500} - [Z] \tag{2.7}$$

where Z_* is the Z500 anomaly from the zonal mean and $[Z]$ is the zonal mean Z500. Blocks are then defined as "cores" of contiguous grid points where this anomaly exceeds 100 m. While this blocking detection method identifies the main blocking regions of the Northeast Pacific and Northeast Atlantic, the blocking frequencies are larger than those found in most other climatological blocking studies (see Fig. 9 in Liu et al. (2018)). The frequencies are largest where there is a climatological ridging due to the extension of subtropical highs, and as such this method also has the issue of the false identification of subtropical highs as blocks. For this reason, Suitters et al. (2023) adapted the calculation in Liu et al. (2018) to account for the climatological wave pattern, and identified more realistic blocking frequencies in these areas. More details on this calculation are given in Sect. 4.2.

2.4.5 PV Anomalies

It is also possible to define blocks as a local negative PV anomaly. The most common index doing this was devised by Schwierz et al. (2004). In their study, the vertically-averaged PV deviation between 500 and 150 hPa from the 15-year climatological mean (denoted differently here to Schwierz et al. (2004), as APV', to avoid confusion with notation used throughout the rest of the thesis), are identified. A two-day running mean smoothing is applied to the APV' field, and cores of APV' that satisfy certain criteria are retained as blocks. The four criteria are

an amplitude of at least -1.2 pvu, an overlap of at least 70% between each 6-hour period, a size of 1.8 million square kilometers, for a duration of at least 5 days.

The APV' blocking index is able to reproduce the blocking climatologies obtained in other studies, but like all blocking indices, has some subtle differences in the location and magnitude of the exact position of blocks (Schwierz et al., 2004). For example, the blocking frequency magnitudes are slightly less than calculated in the Pelly-Hoskins index (Schwierz et al., 2004; Pelly and Hoskins, 2003a). However, this index has also proved popular for blocking studies (e.g. Croci-Maspoli et al., 2007; Altenhoff et al., 2008; Sillmann and Croci-Maspoli, 2009; Pfahl et al., 2015; Steinfeld and Pfahl, 2019).

2.5 Blocking Dynamics

There are many processes that can contribute to blocking (Woollings et al., 2018), which makes the dynamics of each blocking event very complex. Adding to the complexity is the fact that the importance of certain dynamical processes differs both regionally (Drouard and Woollings, 2018) and globally (Miller and Wang, 2022). The two main dynamical mechanisms responsible for blocking that are most relevant for the results in the thesis are block-eddy interactions and diabatic processes. These are discussed in Sects. 2.5.1 and 2.5.2 respectively, and some of the other processes are summarised in Sect. 2.5.3.

2.5.1 Block-Eddy Interactions

For all of the mechanisms described in this subsection, a critical assumption is made between the characteristics of transient eddies and blocks. The two features can be distinguished by their different spatiotemporal scales. Eddies are assumed to be on the synoptic scale in both space and time, i.e. have a lifespan on the order of a few days and a size on the order of 1000 km. Blocks, on the other hand, have a longer time scale (days–weeks) and a larger spatial scale (several thousand km). These separations are crucial because it implies that the vorticity field is stronger, further-reaching, and longer-lasting for blocks than for eddies. This means that the eddies do not induce any motion on the block, but the

block does induce motion on the eddies which goes on to cause both eddy deformation and attraction/repulsion towards/away from the block. These processes are described below.

The Eddy Straining Mechanism (ESM)

The eddy straining mechanism (ESM) was one of the first theories that explained how synoptic-scale transient eddies act to maintain a block (Shutts, 1983). The central argument in the ESM is that the straining of eddies upstream of a blocking region balances the vorticity budget by counteracting against dissipation. As an equation, this can be expressed as:

$$\overline{\zeta' \mathbf{u}'} \cdot \nabla(\overline{\zeta} + \beta y) = -\alpha \overline{\zeta'^2} \tag{2.8}$$

where ζ is the vertical component of absolute vorticity, $\mathbf{u}$ is the 3D wind vector, β is the beta-parameter (how the Coriolis parameter, f, varies meridionally), α is a dissipation constant, an overbar indicates a time average, and a prime denotes a deviation from the time mean. The term on the right hand side is an expression for eddy enstrophy, which is balanced by the eddy vorticity flux on the left hand side.

Immediately upstream of dipole-like blocks, there is a region of high eddy enstrophy where the eddies become strained around the blocking flow (Fig. 2.6). This coincides with a region of net dissipation when eddies divert around the block. Through analysis of Eq. 2.8, Shutts (1983) argued that in this dissipative region of high eddy enstrophy, the eddy vorticity flux must be downgradient, i.e. equatorward, towards lower background PV values in the subtropics. In turn, this means that eddy vorticity is taken away from the poleward branch of the split jet and brought towards the equatorward branch by the eddy vorticity flux. As a result, anticyclonic forcing is provided just upstream of the blocking high (clockwise arrow in Fig. 2.6), and cyclonic forcing just upstream of the cut-off low in the dipole block (anticlockwise arrow), which helps maintain the blocking pattern.

Another consequence of Eq. 2.8 is that eddies of both polarities induce the

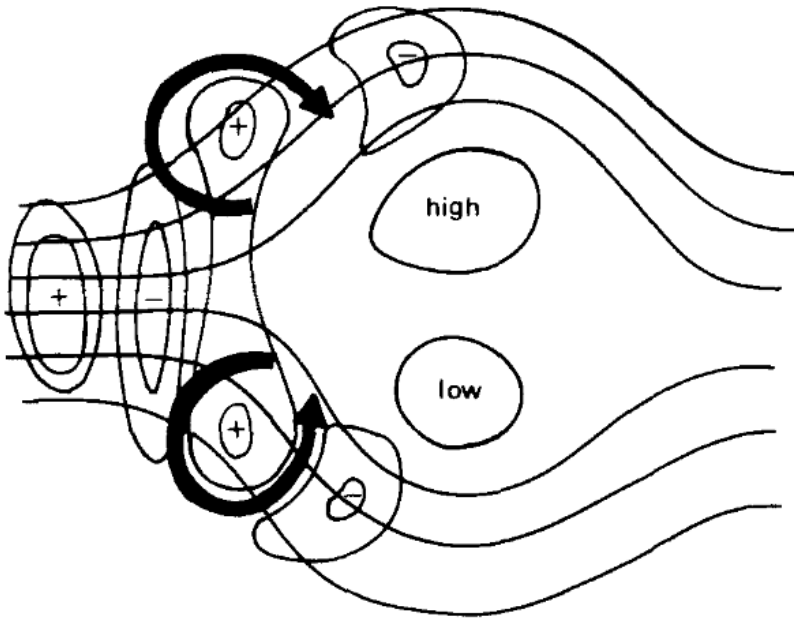

Figure 2.6: Schematic of the eddy straining mechanism around a dipole block (Fig. 1 in Shutts (1983)). Anticyclonic (cyclonic) eddies are depicted by plus (minus) symbols. The black lines around the dipole show the jet stream. The arrows show the direction of vorticity forcing induced by the eddies on the block.

same forcing pattern on the block due to the straining around the block. Downstream of blocks, where eddies are strained in a different direction as the upper-level flow converges, eddy enstrophy would be low and thus the PV flux would instead act in the upgradient direction (polewards). The result of this is to provide a dipole of eddy vorticity forcing opposite to that of the blocking pattern. Therefore, the ESM can explain why blocks do not move downstream and instead can retrogress upstream, since the forcing applied from the eddies encourages upstream maintenance and simultaneously discourages it downstream.

However, there are some inconsistencies with the ESM theory for block maintenance. The main problem with the ESM is that it assumes that the block takes a dipolar configuration as it requires the splitting of the jet stream around the block. However, as demonstrated in Sect. 2.2.1, this is not always the case. A lot of blocks do take on the appearance of a dipole once they are mature, but all blocks do not necessarily go through this lifecycle (Sousa et al., 2021). When a block is younger, it might appear as a ridge or an omega block, which might not split the jet stream into two branches. Therefore, the ESM may be able to explain how a block is maintained once it is already mature, but cannot explain the on-

set nor decay of a blocking event. As previously mentioned, the ESM also treats both polarities of synoptic eddies in the same way, whereas other later studies considered that they could interact with blocks in opposing ways.

The Selective Absorption Mechanism (SAM)

The SAM, developed by Yamazaki and Itoh (2009) and refined by Yamazaki and Itoh (2013a), differs from the ESM in that it describes the eddy feedback on blocks as a vortex-vortex interaction and considers the polarities of the synoptic eddies differently. For a block to persist for longer than a week, to counter against dissipation Yamazaki and Itoh (2013a) argue that low PV must be taken up by the blocking anticyclone, and this is achieved by absorption of smaller synoptic scale eddies by the block. A schematic of this situation is shown in Fig. 2.7.

First, the case of a synoptic anticyclone approaching a block is described:

1. The vorticity is more anticyclonic (i.e. lower) to the east of the eddy, and less anticyclonic (i.e. higher) to the west of the eddy. This is because the ambient

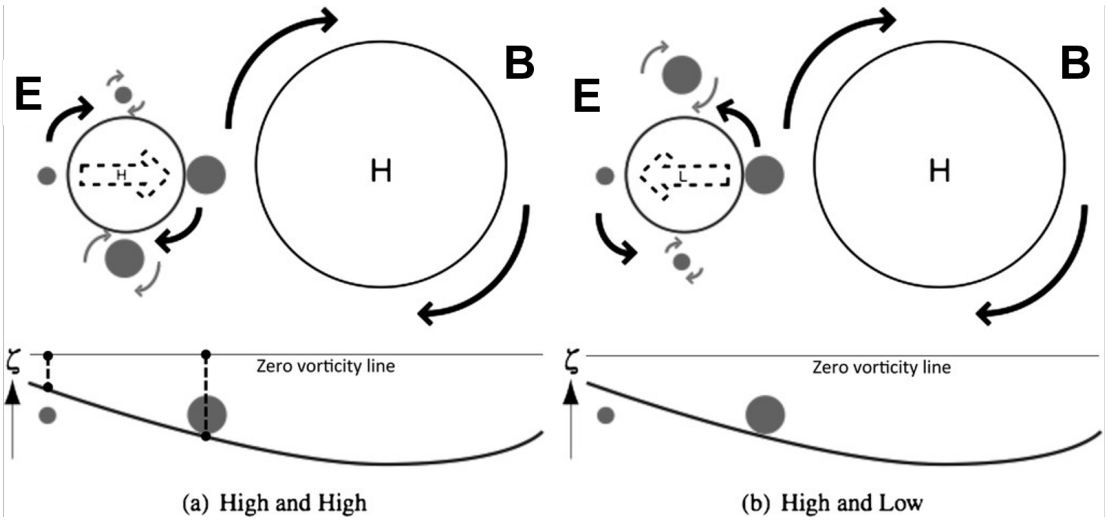

Figure 2.7: Schematic of the selective absorption mechanism, in the case of (a) a blocking anticyclone and a transient anticyclone, and (b) a blocking anticyclone and a transient cyclone. The blocking high is denoted by the vortex labelled "B", and the eddy by "E". Grey circles qualitatively signify the magnitude of vorticity: the larger the vorticity magnitude, the larger the grey circle. The size of these grey circles is marked on the bottom half of the diagram, in relation to the size of the total ambient vorticity field, induced by B. Black arrows denote the large-scale circulation around each vortex, grey arrows show the circulation induced by the advected vorticity around E, and the dashed black arrow inside vortex E shows the direction of movement of the eddy. In this diagram, north is upwards. Adapted from Fig. 1 in Yamazaki and Itoh (2013a).

vorticity induced by the block becomes less anticyclonic as radial distance from the block increases, and the eastern side of the eddy is closest to the block. This is depicted by the grey circles to the right and left respectively of vortex E in Fig. 2.7a.

2. The anticyclonic circulation around the eddy (black lines around vortex E) advects this ambient vorticity clockwise around it.
3. This means that the vorticity on the southern side of the eddy is more anticyclonic than the vorticity on its northern side (grey circles above and below vortex E).
4. This vorticity pattern induces strong anticyclonic flow on the south side of the eddy, and a weaker anticyclonic flow on the northern side (grey arrows).
5. As a result, differential vorticity advection is generated that means that the eddy moves towards the block (dashed black line inside vortex E).

The reverse arguments can be made in the case of a synoptic cyclone approaching a blocking high (Fig. 2.7b). In this situation, the strongest anticyclonic flow is induced on the northern side of the eddy rather than the southern side, due to the cyclonic circulation of vortex E, which results in differential vorticity advection that moves the eddy further away from the block.

This difference in behaviour between blocks and eddies of different polarities is central to the SAM theory. According to the SAM, blocking anticyclones attract and absorb synoptic anticyclones (Fig. 2.7a), and repel synoptic cyclones (Fig. 2.7b). Yamazaki and Itoh (2013a) also argue that unlike the ESM, the SAM provides an explanation for how blocks can become self-sustaining and very persistent. The larger or more intense a blocking anticyclone is, the further its vorticity field extends, meaning that it can attract anticyclones from further away and absorb them, which further strengthens the block and extends its vorticity further.

Another key implication from the theory of the SAM is that it can apply to blocks of any configuration, and is not just restricted to dipolar blocks as in the ESM (Yamazaki and Itoh, 2013a). The SAM approximates the blocking anticyclone as an anticyclonic vortex, without the need for a cyclonic vortex to be

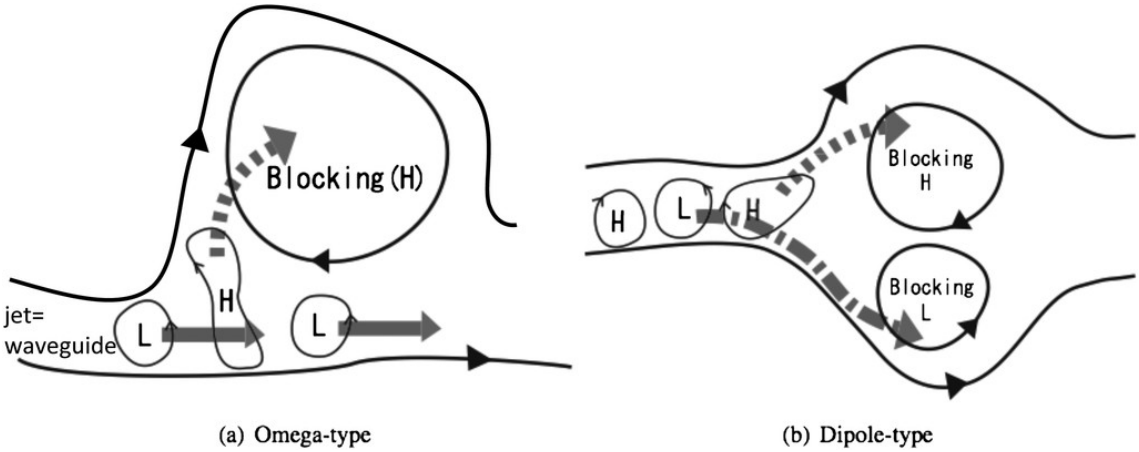

Figure 2.8: Illustration of how (a) omega blocks and (b) dipole blocks attract or repel eddies of different polarities, according to the SAM. Taken from Fig. 2 of Yamazaki and Itoh (2013a).

present, and thus the same arguments can be applied for ridge- or omega-like blocks (Fig. 2.8a). Furthermore, if the block *does* have a dipolar shape, the SAM can also explain how the stationary cut-off low is maintained. Just like blocking anticyclones attract eddies of the same polarity, the cyclonic part of the block also attracts cyclonic vortices and repels anticyclonic ones (Fig. 2.8b). However, the SAM does not explain the onset and decay phases of the blocking lifecycle as well, since it assumes that the blocking vortex is much larger than the eddy vortex, which is not true when the block is first developing or decaying.

In a subsequent study, Yamazaki and Itoh (2013b) were able to verify that the SAM was acting to maintain blocks by using numerical experiments that changed block shape and amplitude, as well as the location of storm tracks. It was concluded that the SAM could explain the maintenance of blocks irrespective of these initial conditions supplied to the model, meaning that the SAM theory is robust and reproducible, and in Sect. 4.5.2 some evidence of blocking anticyclones attracting synoptic-scale eddies is also found.

The Eddy-Block Matching Mechanism (EBMM)

Finally in this section, Luo et al. (2014) combined the ESM and SAM to devise a blocking mechanism that can explain not just the maintenance of the block, but also its onset and decay. It is based on the nonlinear multi-scale interaction (NMI) model of Luo and Cha (2012), and is called the eddy-block matching mechanism

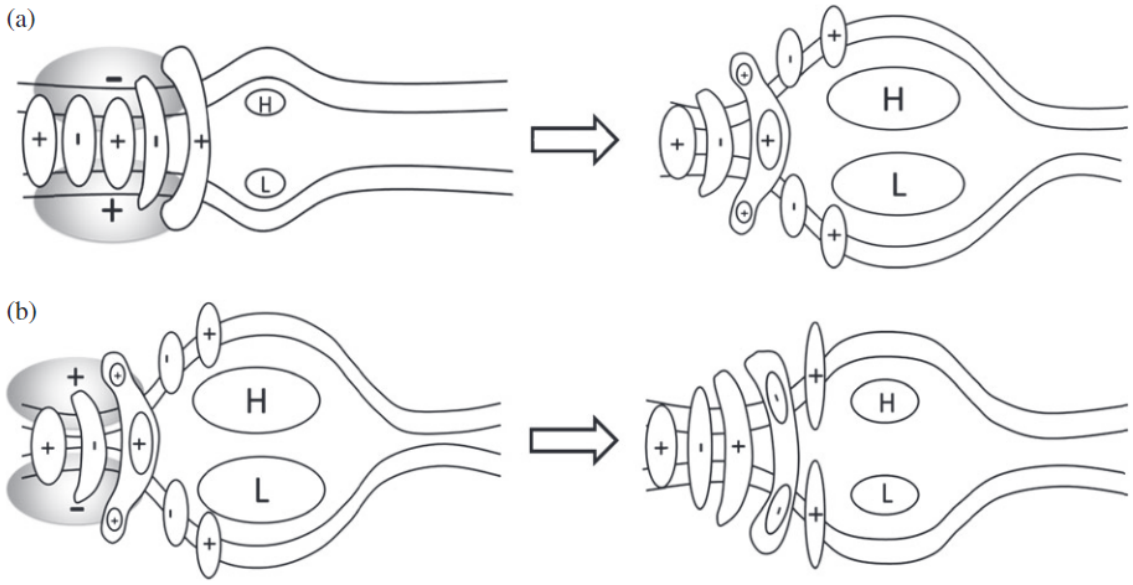

Figure 2.9: Schematic of the eddy-block matching mechanism during the (a) onset and (b) decay phase of a dipole block. Synoptic eddies are marked by the plus and minus symbols, and the polarity of the eddy vorticity forcing is shown by the grey shading and signs. Taken from Fig. 11 of Luo et al. (2014).

(EBMM, Fig. 2.9), which is fully detailed in Luo et al. (2014). In summary, the EBMM states that given even a weak pre-existing anticyclonic region (i.e. a ridge) that is able to deform and strain approaching upstream eddies, then a downgradient eddy vorticity flux is applied to the region, just like in the ESM. The resulting dipole in eddy vorticity forcing then reinforces the pre-existing anticyclonic region by providing suitable background conditions for block formation (Fig. 2.9a). Then, once the eddies have been strained, anticyclonic/cyclonic eddies can be attracted and absorbed by the blocking high/cut-off low, providing a more direct source of low/high vorticity for block maintenance, as in the SAM. When eddy vorticity forcing is opposite to the block's dipole shape (i.e. the eddies induce an upgradient PV flux), then the block decays (Fig. 2.9b).

2.5.2 Diabatic Processes

The dynamical processes so far discussed in this section all fail to take the effect of moisture, specifically diabatic heating, into account. Moist dynamics were only recently discovered to be influential in blocking dynamics, alongside those from dry processes. One of the very first studies that examined the role of diabatic heating in blocking was performed by Pfahl et al. (2015). In that study,

the trajectories of air parcels that enter a blocking region (determined via the LAGRANTO trajectory analysis; Sprenger and Wernli (2015)) were calculated over a 21-year NH blocking climatology, determined by the PV-anomaly based method from Schwierz et al. (2004). It was found that up to 45% of trajectories underwent over 2 K of diabatically-induced heating in the three days prior to entering the blocking region, and in the preceding seven days, this percentage increased to up to 70%. Diabatic heating appears to be more important for the dynamics of blocking anticyclones compared to non-blocking anticyclones, with fewer transient anticyclones containing trajectories that underwent diabatic heating than blocks. Finally, Pfahl et al. (2015) showed that the importance of diabatic heating changes as a block event evolves, with diabatically-heated trajectories being more common at the start of a block than at its latter stages.

The work by Steinfeld and Pfahl (2019) expanded on the earlier study by Pfahl et al. (2015), by working with a longer climatology (36 years), examining the spatial and seasonal importance of diabatic heating, and by discussing how latent heating changes the structure of blocks. The authors were able to identify two different trajectory regimes:

- A "diabatic cooling" regime, which comprised 54% of the blocking air mass trajectories three days prior to entering the block (and 33% seven days prior). These air parcels underwent a mean diabatic potential temperature change of -3.7 K, consistent with longwave radiative cooling, and represent air that has been incorporated into the block via processes such as the SAM (Steinfeld and Pfahl, 2019). One in five of these trajectories originated in the block itself, and indicate the recirculation of air within the blocking anticyclone.
- A "diabatic heating" regime, 46% of the trajectories three days prior to blocking. The median heating along these trajectories was 8.5 K, and was caused by cloud formation (deduced by the reduced specific humidity and increased altitude of the trajectories).

Interestingly, half of the trajectories in the cooling regime undergo diabatic heating between 3 and 7 days before entering the block, implying that diabatically-warmed air can also be advected into the block by the large-scale flow (Steinfeld and Pfahl, 2019). Additionally, of the diabatically-heated trajectories, one in ten

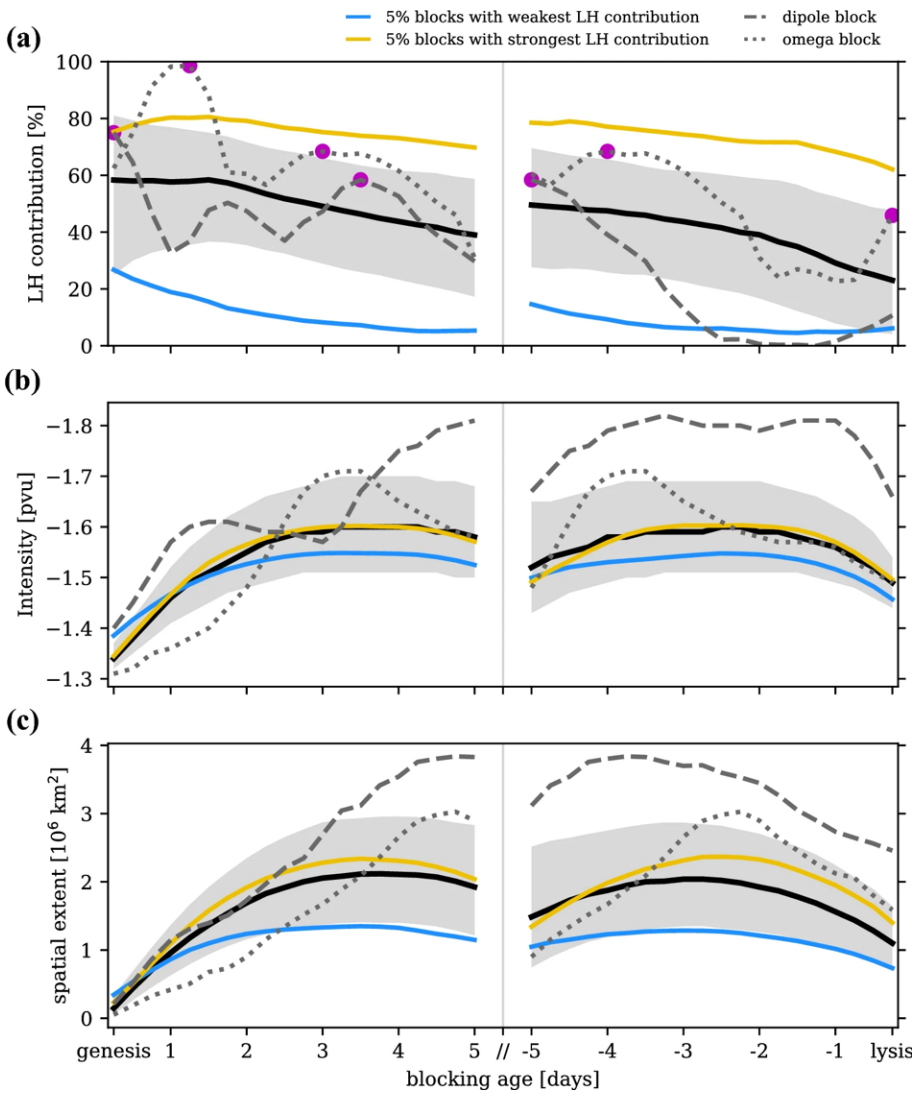

Figure 2.10: Median characteristics (black lines) for all blocks in Steinfeld and Pfahl (2019), as a function of blocking age, showing the contribution of trajectories that undergo diabatic heating (a), the intensity of the block in terms of its PV anomaly (b), and its area (c). The interquartile range is shown by grey shading, and the yellow and blue lines show the means for blocks with the strongest and weakest contribution from diabatic heating, respectively. An example lifecycle for a dipole block (dashed) and an omega block (dotted) are shown, and "latent heat bursts" (see text for details) are shown by the purple dots. Taken from Fig. 6 of Steinfeld and Pfahl (2019).

meet the ascent rate threshold indicative of a WCB (defined by an ascent of 600 hPa in a 48 hour period by Madonna et al. (2014)), and these air parcels undergo considerably more heating than those that are non-WCB trajectories (median of 25 K).

Steinfeld and Pfahl (2019) also studied the lifecycle of blocks in relation to where the latent heating occurs both spatially and temporally. Agreeing with the results from Pfahl et al. (2015), diabatic heating was most prevalent for air parcels

that enter the block close to its onset, and reduced to a minimum near the decay of the block. This is shown in Fig. 2.10a. Another key result shown in this figure is that certain blocks can undergo "latent heat bursts" (LHBs), which are times where there is a maximum in trajectories containing diabatic heating, and that these periods are associated with the greatest intensification and spatial expansion of blocks (Fig. 2.10b, c). On average, a block has 2.3 LHBs in its lifetime (Steinfeld and Pfahl, 2019). Furthermore, Steinfeld and Pfahl (2019) demonstrate that diabatic heating results in larger and stronger blocks than blocks with no diabatic heating, showing that the structure of blocks is also modified by the presence of diabatic processes. Finally, it was also shown that blocks often form over regions of intense diabatic heating (the oceanic storm tracks), and travel to areas with less latent heating as they mature, until they decay in regions with very little latent heating (continents) in winter (Steinfeld and Pfahl, 2019).

This result led to the idea that atmospheric blocking characteristics may be sensitive to the amount of latent heating that occurs upstream (Steinfeld et al., 2020). By comparing experiments with the Integrated Forecast System (IFS) from the ECMWF, where the latent heating was switched either switched off or kept on over WCB regions upstream of five blocking cases, it was found that the shape, size, and persistence of a block changes depending on the state of the upstream diabatic heating. In some cases, it was even found that the occurrence of a block depended on whether or not latent heating was switched on or off. This is because latent heating modifies the structure and propagation speed of the upper-level wave pattern (Steinfeld et al., 2020). However, whether or not latent heating affects block development also depends on the state of the background flow, for example a block was shown to still occur when the flow was already highly amplified.

2.5.3 Other Mechanisms

Planetary Wave Dynamics

Blocking patterns can simply be the result of planetary-scale wave dynamics (Legras and Ghil, 1985) as an unstable but stationary feature. Austin (1980) found

that the regions of blocking maxima coincide with the places where Rossby waves of different wavelengths constructively interfere with each other. This suggests that the ridge amplification associated with blocks simply comes from the constructive interference of multiple planetary-scale waves. Similarly, it has been found that blocking events can have a certain signature in the upstream wave pattern before onset (Altenhoff et al., 2008). For example, blocks that form in the Atlantic sector often have a precursor wavetrain signal, 110° upstream up to five days before block onset (Altenhoff et al., 2008).

Rapid Cyclogenesis

Rapid cyclogenesis has also been linked to the formation of blocking events. Colucci (1985) examined two cases where bomb cyclogenesis led to block development both up- and downstream, where the cyclone that produced the cut-off low became part of the dipole block in both cases. The rapid development of a cyclone produces a large warm sector, which allows the northward advection of subtropical air (with low PV) into the mid-latitudes. As described in Sect. 2.5.2, extratropical cyclones are also important during the maintenance stage of a block, in that they also provide the block with diabatically-generated low PV via its WCB.

Traffic Jam in the Jet Stream

A mechanism to explain block onset has been suggested, where it was likened to a build-up of traffic on a highway (Nakamura and Huang, 2018). Many analogies between the jet stream and a highway were made, which are summarised here. From this way of thinking, one can view the jet stream as a highway with a fixed capacity for wave activity. Once this capacity for wave activity is exceeded, congestion occurs and a blocking event results. The jet stream's capacity for local wave activity is modulated by the stationary wave pattern, just as a highway's capacity is governed by the speed limit. More stationary wave activity (or a higher speed limit on a highway) decreases the capacity of the jet stream/highway, making blocking/congestion more likely. Likewise, if wave activity/traffic density is locally increased (through latent heating for example in the jet stream, or traffic

joining the highway), congestion happens and a blocking event occurs as a result.

Rossby Wave Breaking

Overturning within the large-scale planetary circulation (known as Rossby wave breaking, RWB) is also an important process by which low-PV air can be brought up to mid-latitudes and cut off from the rest of the flow, causing a blocking event (Masato et al., 2012; Altenhoff et al., 2008; Sousa et al., 2021). RWB can occur in either a cyclonic or an anticyclonic direction, with cyclonic RWB favoured over oceanic basins and anticyclonic over continents (Masato et al., 2012). As a result, Greenland blocking is often associated with cyclonic RWB over the North Atlantic, whereas European blocking is more frequently connected to anticyclonic breaking. In the NH, wave breaking that causes a blocking event is more likely to be cyclonic than anticyclonic (Drouard et al., 2021), though RWB direction also has a relationship with block duration. Blocks that last longer than 10 days preferentially break cyclonically, and blocks that last around 5 days long break anticyclonically most often (Drouard et al., 2021).

2.6 Objective Feature Tracking of Anticyclones

The other important aspect of this thesis is transient synoptic-scale anticyclonic eddies. These anticyclones are distinct from blocks in that they lack the persistence and quasi-stationarity of blocks, and are also typically smaller in size. In this section, the climatological characteristics of non-blocking anticyclones are examined and compared to those of blocking anticyclones. Additionally, the concept of objective feature tracking is introduced, with a particular focus on how anticyclones (both blocking and non-blocking) move in space and time.

2.6.1 Anticyclone Climatologies

There has been a lot of focus on the detection and tracking of extratropical cyclones (Hodges et al., 2011), while the use of tracking algorithms for exploring the characteristics of anticyclones has been much rarer. A thorough study by Ioannidou and Yau (2008) examined the climatologies of three types of anticyclone

(continental, subtropical and blocking) in the NH DJF period, utilising an objective feature tracking algorithm (hereafter referred to as TRACK, (Hodges, 1994, 1995, 1999)). Many variables associated with ACs were tracked (namely MSLP, geopotential height at various levels, relative vorticity, and PV), with tracking thresholds set according to the standard deviations of the spatial mean fields. For example, this meant that when a feature has a MSLP of 15 hPa or more, or a Z500 of 120 m or more above the spatial mean, then it was considered to be an anticyclone. The quasi-stationary background field (i.e. stationary waves) was filtered out before tracking through the removal of wavenumbers below 3 and above 21.

Their study looked into the genesis regions of all anticyclones in North America and Eurasia, finding that in general they move from northwest to southeast, with two or three maxima of anticyclone genesis in each region. These are found in the far northwest of Canada, the west coast of the USA around 40°N, and Texas in North America. Meanwhile, Eurasian anticyclone genesis hotspots are found in Kazakhstan, eastern China, and eastern Russia. By looking at the Z500 feature tracking, they found that anticyclones that enter the known blocking regions in the northwest Pacific and Atlantic basins tend to last only 5 or 6 days, suggesting that a block event is a result of a sequence of smaller anticyclones that move into the block (see also McWilliams (1980); Lupo (1997); Hauser et al. (2022); Suitters et al. (2023)). These features also move around 30° east during this 5-6 day period, and similar conclusions were drawn from tracking PV at 250 hPa instead.

In a different study by Pepler et al. (2019), anticyclone climatologies for both hemispheres, in all times of year, were generated using another tracking algorithm developed by the University of Melbourne (Murray and Simmonds (1991); Simmonds et al. (1999)). In this study, anticyclones are identified as areas of sufficiently low Laplacian of the MSLP field, which are then tracked in 6-hourly intervals. While their study was focused on all anticyclones, not just the ones that cause blocking, some important results are still relevant for blocks. Firstly, they found that all anticyclones are strongest and most frequent in the NH cool season (November-April), which is also true of blocking anticyclones, and in the NH, they are at their strongest (i.e. maximum MSLP) at around 61°N. Another result is the fact that more than 40% of all anticyclones in the NH move at a speed

slower than 20 km/h, which is perhaps indicative of blocking in the northeast Pacific and Atlantic basins.

While tracking anticyclones, care needs to be taken as to how to filter the background state in either space or time, or both - which was addressed in work by Donohoe and Battisti (2009). In their study, TRACK was used to follow anticyclonic regions of sea level pressure with an amplitude of above 3 hPa once the background field was removed. This background field was removed in one of two ways: (1) a spatial filter that removes planetary wavenumbers smaller than or equal to 5, with the resulting anomaly field transformed to T42 resolution; or (2) a temporal filter that removes features that vary on a timescale of less than 20 days via a sixth-order double-pass Butterworth filter. Their results found that the use of the spatial filter does not eliminate non-synoptic features, such as the semi-permanent subtropical ridges, leading to confusion between the mean state and the eddy statistics. The spatial filter also leads to a much larger magnitude asymmetry between tracks of anticyclones and cyclones - with a 130% difference, compared to only a 20% difference in the temporally-filtered data.

2.6.2 Tracking Blocking Anticyclones

While there are some studies that have tracked all anticyclones (see above), there have been very few that have focused solely on blocking anticyclones, presumably because of their assumed quasi-stationarity. This assumption was tested in a recent study by van Mourik et al. (2024), where blocks (defined using the adapted AGP index as in Sousa et al. (2021)) were followed using a 2D cell-tracking algorithm (Lochbihler et al., 2017), and the zonal propagation velocity of the blocks determined. It was found that blocks can propagate either up- or downstream by up to 1500 km per day, implying that the assumption of quasi-stationarity in blocks is not always valid. Furthermore, blocks have different characteristics depending on their direction of propagation, for example, westward-moving blocks tend to be larger than eastward-moving blocks.

2.6.3 Combining Anticyclone Tracking with Block Detection

Recently, some studies have demonstrated the importance of combining the tracking of anticyclones to blocking. In other words, a Eulerian perspective on blocking (identifying blocks using methods such as those described in Sect. 2.4) is combined with a Lagrangian technique (similar to those described in the previous section). This marries the quasi-stationary blocking events to the more transient weather systems that might interact with the block.

A study by Hauser et al. (2022) examines a March 2016 European blocking event from three different perspectives and allows for a complete dynamical overview of the event. Their work took the isentropic PV tendency equation:

$$\frac{\partial q}{\partial t} \mid_{\theta} = -\mathbf{u_{\theta}} \cdot \nabla_{\theta} q + S_q \tag{2.9}$$

where q is Ertel PV (Ertel, 1942) (hereafter "PV"), $\mathbf{u_{\theta}}$ is the isentropic horizontal wind vector, ∇_{θ} is the gradient taken along an isentropic surface, and S_q are the non-conservative sources and sinks of PV; and showed that Eq. 2.9 can be used to derive an equation showing how temporal anomalies in PV (q') change in time according to different processes (Hauser et al., 2022):

$$\frac{\partial q'}{\partial t} = \frac{\partial q'}{\partial t} \mid_{qb} + \frac{\partial q'}{\partial t} \mid_{bc} + \frac{\partial q'}{\partial t} \mid_{div} + \frac{\partial q'}{\partial t} \mid_{eddy} + \frac{\partial q'}{\partial t} \mid_{noncons} + \frac{\partial q'}{\partial t} \mid_{res} \tag{2.10}$$

The first term on the right hand side (subscript "qb") is the quasi-barotropic PV tendency, i.e. the contribution towards a change in PV anomaly according to barotropic upper-tropospheric Rossby waves due to the phase and group propagation of the waves, as well as due to the advection of the waves by the background flow (the deformation of the anomalies). The baroclinic PV tendency ("bc") describes the interactions between PV anomalies in the upper and lower troposphere (the baroclinic growth of the PV anomalies). Divergent flow ("div") also generates a PV tendency and is assumed to be primarily due to latent heat release near the tropopause. The fourth term, "$eddy$", is the contribution from convergence of PV anomaly flux (hereafter "eddy flux convergence"). The final two terms describe changes to PV due to non-conservative processes ("$noncons$") and small residual changes ("res") due to a changing background state.

With these tendencies mathematically defined (see Hauser et al. (2022) for more details), the blocking period is then examined from three different perspectives:

- *A Eulerian perspective.* The PV anomaly field is projected on to the seven weather regimes as defined by Grams et al. (2017), with the aim of determining how a regime's dynamics is driven by PV anomalies. In this case, EuBL in particular is then defined as the mean of the low-frequency PV anomalies, averaged between 500–150 hPa. Each of the terms in Eq. 2.10 are also projected on to the EuBL pattern such that the main drivers from a PV perspective towards producing this weather regime can be found.
- *A "Quasi-Lagrangian" perspective.* This processes requires the tracking in space and time of vertically-averaged 500–150 hPa PV anomalies, identified using a less-strict version of the Schwierz et al. (2004) criteria (for example, not requiring any spatial overlap between time steps and identifying weaker anomalies). Splitting and merging of PV anomalies are also accounted for (see Appendix in Hauser et al. (2022)). Quasi-Lagrangian PV anomalies (QLPVAs) that overlap at least 10% with the Eulerian PV anomaly (EPVA) associated with the EuBL weather regime are said to be contributing to the dynamics of the block. The importance of quasi-barotropic, baroclinic, divergence and non-conservative PV tendencies in each QLPVA that contributes to the EPVA is then quantified (Teubler and Riemer, 2016).
- *A Lagrangian Perspective*. Individual air parcels that form part of the QLPVAs are also identified and the amount to which they undergo diabatic heating and changes to PV are examined using LAGRANTO (Sprenger and Wernli, 2015), particularly around WCB outflow regions (Hauser et al., 2022).

The main results from this study are now briefly discussed. The EPVA in the March 2016 block event was mainly driven by barotropic advection of anomalous PV into it by the upper-tropospheric flow, followed by divergent PV tendencies. The relatively large importance of the divergent PV tendency term suggests that diabatic processes could also be important for the dynamics of this block. Further evidence for this comes from the pulse-like amplification in the divergent

and barotropic PV tendencies of the QLPVA before and during the block, which is potentially indicative of LHBs (Steinfeld and Pfahl, 2019). Ultimately, the role of diabatic processes in this block's dynamics was confirmed by the Lagrangian perspective, which showed large-amplitude diabatic heating of air parcels (from WCB outflow) that coincided with the pulses in QLPVA amplitude. Another conclusion from Hauser et al. (2022) is that while each of the three above perspectives is useful on their own, when all three are analysed together a lot more information about the block's dynamics can be deduced. This results in a possible framework that is able to be re-used for thorough investigations of other case study events, however the large amount of computing required means that this method is not suitable for a climatological study of all blocks.

In a subsequent study (Hauser et al., 2023), only the Eulerian and Quasi-Lagrangian perspectives were pursued to analyse the year-round climatological life cycle dynamics of Greenland blocking (defined by the GL regime, again from Grams et al. (2017)). They found that there were two pathways towards the GL regime from a PV perspective. The so-called "upstream pathway" consists of QLPVAs that lead to Greenland blocking that originate from upstream of Greenland over North America. A second pathway, the "retrogression pathway", which is more frequent than the former, contains QLPVAs that emerge again from North America, but travel past Greenland into Northern Europe, before turning and retrogressing back towards Greenland a few days before blocking. A schematic of these two routes to blocking is shown in Fig. 4 in Hauser et al. (2023). Both pathways were found to have large divergent PV tendencies, which again suggests that diabatic processes are important in governing how QLPVAs amplify for Greenland blocking.

The studies of Hauser et al. (2022) and Hauser et al. (2023) cover similar themes to those in this thesis. Table 2.2 summarises the main similarities and differences between those studies and the results presented in this thesis. Further details and comparisons to these studies are provided later in the thesis, where appropriate.

The findings from Yamazaki and Itoh (2013a), van Mourik et al. (2024), Hauser et al. (2022) and Hauser et al. (2023) strongly suggest that atmospheric blocking

Similarities	Differences
Both authors are seeking to ascertain the principal sources of PV modification within blocking anticyclones	The contribution of diabatic PV modification towards blocking is identified in different ways
Blocking is considered from both a Eulerian and Lagrangian perspective (in Hauser et al. (2023) and this thesis)	Blocks and eddies are identified using different (but complimentary) variables for the main climatological relationships obtained in the studies
As a result, both authors conclude that blocking cannot be considered as a static entity - the Lagrangian behaviour of blocking can be crucial towards its dynamics	This thesis compares and contrasts three case study blocks, but in Hauser et al. (2022), only one block is examined in detail
It is concluded that synoptic-scale eddies are influential towards the blocking lifecycle	The importance of diabatic PV modification in blocking appears greater in the work of Hauser et al. (2022) than for the blocks examined in this thesis

Table 2.2: A summary of the main similarities and differences between the work in this thesis, and the work of Hauser et al. (2022) and Hauser et al. (2023).

cannot be considered from a wholly quasi-stationary, Eulerian perspective. In reality, blocks are fluid and transient, and can also interact with transient anticyclonic features from upstream. Therefore there is the need to further examine the link between the two in the rest of this thesis.

2.7 Blocking in Numerical Weather Prediction

2.7.1 Block Representation

There has long been a problem in how well blocking is forecast in weather and climate models (Davini et al., 2021). In a study by Rodwell et al. (2013), it was found that the pattern that leads to 6-day ECMWF forecast busts (defined by high Z500 root mean square error, and small anomaly correlation coefficient) over Europe has a verifying analysis of a dipole block, with the high over northwestern Europe and low over the southeast Mediterranean. Furthermore, a consistent signal in medium-range numerical weather prediction (NWP) models is that blocking

frequency is underestimated, compared to the observations. This result emerges when a block is defined using a Z500 reversal method (Tibaldi and Molteni, 1990; Matsueda, 2009), potential temperature gradient reversals (Pelly and Hoskins, 2003b), or weather regimes (Ferranti et al., 2015).

There are particular problems when it comes to the timing of onset of blocking in NWP. Tibaldi and Molteni (1990) showed that the onset of a blocking event is often poorly represented if it happens a few days into the forecast, but if the forecast is initialised during blocked conditions (i.e. is forecasting the maintenance period of the block), skill is much better. This finding is backed up by Pelly and Hoskins (2003b), who found that for a year of ensemble forecasts from the ECMWF, onsets were the most unpredictable stage of the blocking lifecycle, but predictability by the probabilistic ensemble was greater than the single deterministic forecast.

When examined from a weather regimes perspective, it has been found that the missed onset of a BL regime is responsible for the least accurate medium-range forecasts initialised in an NAO+ regime (Ferranti et al., 2015). This is particularly problematic because Vautard (1990) showed that a transition from NAO+ to BL is one of the most favoured changes in the Euro-Atlantic sector. Furthermore, medium-range weather forecasts initialised in a BL regime are the least skillful from day 9 onwards, when compared to those initialised in an AR, NAO+ and NAO- regime (Ferranti et al., 2015), and this is a result of the mistiming of the decay of the blocking event. BL persistence is underestimated, which is in contrast to the overestimation of the longevity of more zonal flows (Ferranti et al., 2015).

There are also suggestions that block prediction in NWP is more skillful in certain locations compared to others. Ferranti et al. (2015) also found that the NAO- weather regime, associated with Greenland blocking, had the largest inherent predictability. However, when the blocking occurred further east over the East Atlantic (AR regime) or over Europe (BL), the flow becomes less predictable. Furthermore, medium-range prediction of blocking is perhaps more skillful over the Pacific than the Atlantic sector (Matsueda, 2009), potentially due to the differing blocking mechanisms in these locations (Miller and Wang, 2022).

2.7.2 Improving Block Representation: Meteorology

The rest of this section will discuss some ways in which the representation of blocking depends on certain features of the model. While the models most relevant to this thesis are those used for medium-range NWP, most of the literature discusses changes to general circulation models (GCMs) that improve blocking instead. Therefore, both sets of models will be described here.

Role of Upstream Features

The first aspect to be discussed is the representation of upstream features and how they influence how a block is then forecast. Maddison et al. (2019) examined uncertain block onsets in 6-day ECMWF ensemble forecasts, and concluded that the intensity and position of the upstream cyclone prior to block onset changes the evolution of the Rossby wave pattern and therefore affects the evolution of a blocking event. In particular, the onsets of blocks show sensitivity towards the upstream geopotential height and upper-tropospheric PV pattern. The sensitivity to the geopotential height pattern shows an upstream surface cyclone, normally over the North Atlantic, and PV sensitivity is largest around the edges of the blocking ridge. PV sensitivity is also linked to the surface cyclone through the WCB, where diabatic processes are known to decrease upper-tropospheric PV and therefore encourage blocking (Maddison et al., 2019), and it is found that there is a correlation between the strength of the WCB in the ensembles and how sensitive the block onsets are to the representation of PV in the model. Features even further upstream also need to be represented correctly in order to get an accurate downstream block forecast. On some occasions, Maddison et al. (2019) found that the upstream Rossby wave pattern was also poorly forecasted prior to block onset, which led to errors in timing and location of block onsets. Furthermore, a Rossby wave feature well-known to be important for European blocking forecasts is the presence of a trough over the Rocky Mountains (Rodwell et al., 2013). A composite of all 6-day European ERA-Interim bust events shows this Rockies trough in the initial conditions, along with anomalously high convective available potential energy (CAPE) over the Great Plains of the USA. These two features often lead to outbreaks of mesoscale convective systems (MCSs) over the

eastern half of the USA, and it is shown that the inaccurate forecasting of these MCSs is what leads to the errors in downstream European weather patterns (Rodwell et al., 2013).

Model Biases

Though in the medium-range initial condition error is a larger contributor to forecast error than model error (Rabier et al., 1996), it is still important to know that errors and biases within a model can influence the representation of blocking, particularly at longer lead times. For example, the mean state of the model, in particular the mean location and intensity of the mid-latitude jet stream, influences where blocking is found climatologically within said model (Kaas and Branstator, 1993). If this mean state of the model contains a bias, then it could also be expected to have a bias in the location and frequency of blocking. Scaife et al. (2010) found that since blocking is often diagnosed using Z500-based indices, the climatological meridional gradient of Z500 within a model influences blocking frequency in that model. In particular, where this gradient is too strong (implying a speed bias in the jet), block frequency is underestimated, but correcting this Z500 bias also improves the representation of blocking frequency (Scaife et al., 2010). Similar findings arise when models have a bias in the storm track location and density (Zappa et al., 2014).

Synoptic Eddy Representation

Despite the fact that it is known that synoptic scale eddies are important for blocking dynamics (Sect. 2.5.1), to this author's knowledge the only existing literature that addresses this focuses on synoptic cyclones (e.g. Colucci, 1985; Maddison et al., 2019). There is a literature gap in the role of how the forecasts of *anticyclonic* eddies go on to influence the forecasts of blocking. This open question will be considered in Sect. 6.

2.7.3 Improving Block Representation: Model Configuration

Model Resolution

Another way that block representation can be improved in both NWP and GCMs is to increase the resolution of the simulations (e.g. Anstey et al., 2013; Dawson and Palmer, 2015; Davini and D'Andrea, 2016; Schiemann et al., 2017). In a study that examined the representation of European weather regimes in IFS NWP simulations at three different horizontal resolutions, Dawson and Palmer (2015) found that when simulated at a resolution of T1279 (approximate grid spacing of 16 km), the analysed weather regime persistence and spatial patterns were reproduced very well. However the lower resolutions (with 40 km and 125 km approximate grid spacing) performed much worse, and the lowest resolution (typical of GCMs) demonstrated the known underprediction biases in European blocking (Davini and D'Andrea, 2016).

The improvement in blocking representation in GCMs at higher resolutions is well known, but the effectiveness of increasing both horizontal and vertical resolutions differs according to location (Davini and D'Andrea, 2016). For example, increasing horizontal resolution in CMIP5 models reduces the negative blocking bias for Atlantic blocking, but has negligible effect on the representation of Greenland or Pacific blocking (Anstey et al., 2013; Schiemann et al., 2017). Conversely, increasing the vertical resolution of the GCMs improves block representation almost everywhere (Anstey et al., 2013). Schiemann et al. (2017) found that the bias reduction in GCMs with higher resolution was also dependent on season, with fewest improvements with summer blocking representation at high resolution.

Model Parameterisations

The aforementioned study by Dawson and Palmer (2015) also examined the importance of parameterised stochastic physics on the representation of blocking in the IFS, as well as resolution changes. It was found that the implementation of stochastic physics to the low- and medium-resolution forecasts improved the forecasts of blocking, with the medium-resolution forecast with stochastic physics becoming comparable with the high-resolution run with no stochastic

physics (Dawson and Palmer, 2015). Another model parameterisation that improves the onward representation of blocking is that for convection (Maddison et al., 2020). A convection scheme that has memory of recent convective activity in the MetUM leads to more accurate simulation of diabatic heating within a WCB, and thus more accurate representation of a downstream blocking ridge. However, as highlighted by one of the case studies in Maddison et al. (2020), some blocks are just inherently unpredictable, and even with a more sophisticated paramaterisation of convection, the onset of blocking can still be missed by medium-range forecasts.

Chapter 3

Data and Methods

3.1 Data

3.1.1 ERA5

The ERA5 reanalysis from the ECMWF is a dataset containing hourly values of many atmospheric variables from 1950 to the near-present day (Hersbach et al., 2020). It is based on an operational version of the IFS from 2016 at its full resolution of 0.25° latitude and longitude, over 137 vertical levels. In this thesis, the ERA5 data have been regridded to a coarser resolution to improve computation speed (Sect. 4.2). Since blocks are large-scale phenomena, this does not appreciably alter the quantitative results in this work.

Whenever a climatology is required, data are taken from ERA5, using a period from 1 Jan 1979–31 December 2021. Note, the whole ERA5 period from 1940 onwards was not considered for determining a climatology; it was decided to only use data from the more reliable satellite observation era (1979 onwards).

3.1.2 Met Office Unified Model

Some of the results in this thesis are obtained by analysing output from the MetUM. In this section, the main features of this model are summarised. More details on the specific configurations, parameterisation schemes, and forecasts run using the MetUM are provided later in Sect. 5.2.6.

The MetUM is an NWP model that solves the following governing Navier-Stokes equations in the atmosphere (Wood et al., 2014):

- The momentum equation:

$$\frac{\mathrm{D}\mathbf{u}}{\mathrm{D}t} + 2\boldsymbol{\Omega} \times \mathbf{u} = -c_p\theta\nabla\Pi + \mathbf{g} + \mathbf{S_u} \tag{3.1}$$

- Potential temperature equation:

$$\frac{\mathrm{D}\theta}{\mathrm{D}t} = S_\theta \tag{3.2}$$

- Continuity equation:

$$\frac{\partial\rho}{\partial t} + \nabla \cdot (\rho\mathbf{u}) = 0 \tag{3.3}$$

- Equation of state:

$$\Pi^{(1-\kappa)/\kappa} = \left(\frac{R}{p_0}\right)\rho\theta \tag{3.4}$$

where $\boldsymbol{\Omega}$ is the rotation rate of the Earth, c_p is the specific heat of dry air at constant pressure, $\Pi = (p/p_0)^\kappa$ is the Exner pressure, p is pressure, p_0 is a reference pressure of 1000 hPa, $\kappa = R/c_p$, R is the specific gas constant of dry air, g is the apparent gravitational vector, ρ is the density of air, and $\mathbf{S_u}$ and S_θ are the sources of momentum and heat respectively.

The model uses the ENDGame (Even Newer Dynamics for General atmospheric modelling of the environment) dynamical core (Thuburn, 2016) to solve Eqs. 3.1–3.4 using a semi-implicit, semi-Lagrangian framework and obtain the prognostic variables $\mathbf{u}$, Π, ρ, and virtual dry potential temperature, θ_{vd}, for each model grid point at each time step. Each prognostic variable is output on a regular longitude-latitude grid, with a hybrid-height vertical coordinate that follows the underlying terrain (with 70 vertical levels up to a height of 80 km). Horizontal discretisation of the fundamental equations is performed using an Arakawa C-grid staggering (Arakawa and Lamb, 1977), and Charney-Phillips staggering is used in the vertical (Charney and Phillips, 1953). The MetUM configuration used in this thesis is the Global Atmosphere 7.2 (GA7.2), which is an updated version of GA7 described in Walters et al. (2019)[1]. Full details about the version of the MetUM used in this thesis (version 12.1) can be found in the documentation pages (Met Office, 2022).

[1]There is no updated publication for GA7.2.

3.1.3 MOGREPS-G

RQ3 is investigated through the analysis of ensemble forecasts. Ensemble forecasts from the Met Office's MOGREPS-G (Met Office Global and Regional Ensemble Prediction System - Global) suite are used in this thesis. Specific details about the forecasts analysed are provided in Sect. 6.2.1, while this section gives a brief background description of MOGREPS-G. Full information about MOGREPS-G can be found in Bowler et al. (2008).

MOGREPS-G is a global ensemble weather prediction model which is run four times every day. The ensemble consists of one control member and 17 perturbed members (18 total), and a larger ensemble is generated by time-lagging the current cycle with the preceding one. The model contains full atmosphere-ocean coupling, and the atmospheric horizontal resolution is N640, i.e. approximately 0.3° grid spacing, equivalent to approximately 20 km in the mid-latitudes (Met Office, 2024c).

Each ensemble member is perturbed in two ways. The initial conditions of each member are perturbed from the control member via an ensemble transform Kalman filter (Bishop et al., 2001). Additionally, the evolution of each member's forecast is perturbed using stochastic perturbations to the model parameterisations (Bowler et al., 2008). Since it was first implemented operationally in September 2008, many upgrades have been made to the MOGREPS-G system, which have aided both its computational cost and forecast performance (Inverarity et al., 2023).

3.2 Methods

The methods used in a recently published study (Suitters et al., 2023) that forms Sect. 4 of this thesis are largely applicable to the thesis as a whole. Therefore, these methods are described here in Sects 3.2.1–3.2.5. In Suitters et al. (2023), I performed all of the data analysis all writing as part of the article, as well as the corrections after the peer-review stage. The Methods section concludes with Sect. 3.2.6, a previously unpublished comparison of two pre-existing blocking indices with the new blocking detection method described below.

3.2.1 Z'_* Definition

Despite the large array of existing block detection methods (discussed in Sect. 2.4), the majority have some drawbacks that would make a climatological study of the AC eddies that contribute to blocking difficult. For example, some methods require a certain aspect of subjectivity, produce unrealistically small blocks, or even fail to detect blocks of a certain shape (Barriopedro et al., 2010). These issues are particularly prominent for Z500 reversal-based techniques. It is also desirable to identify the AC eddies and blocks at the same time, and mobile synoptic-scale AC eddies are unlikely to produce a marked reversal in the meridional Z500 gradient. Thus, a Z500 anomaly-based detection method was pursued.

In this study, blocks and AC eddies are defined as regions with a large positive Z500 anomaly from the zonal mean. The algorithm from Liu et al. (2018) is adapted in this study, to also consider the climatological wave patterns. The instantaneous Z500 anomalies used to define the transients and the blocks (Z'_*) are calculated at each grid point (with longitude λ and latitude ϕ), at each time step t, and are given by:

$$Z'_*(\lambda, \phi, t) = Z_*(\lambda, \phi, t) - \overline{Z_*}(\lambda, \phi, t) \tag{3.5}$$

where $Z_*(\lambda, \phi, t)$ is the instantaneous Z500 anomaly from the instantaneous zonal mean, and $\overline{Z_*}(\lambda, \phi, t)$ is the climatological (1979-2021) monthly deviation from the zonal mean Z500, where three-month smoothing has been applied.

3.2.2 $\overline{Z_*}$ Background State Climatology

At this stage, the importance of accounting for the climatological wave pattern ($\overline{Z_*}$) is noted. Figure 3.1 shows the monthly climatological $\overline{Z_*}$ pattern for all 12 months of the year. A stationary wave train is evident for much of the autumn, winter, and spring months, with the largest anomalies in winter. These anomalies are also consistent with the shape of the climatological North Atlantic and North Pacific storm tracks (Hoskins and Hodges, 2019). Climatological ridging occurs over a large band from the central North Atlantic to central Eurasia, with a deep trough to the east of this centred over northern Japan. Over the eastern

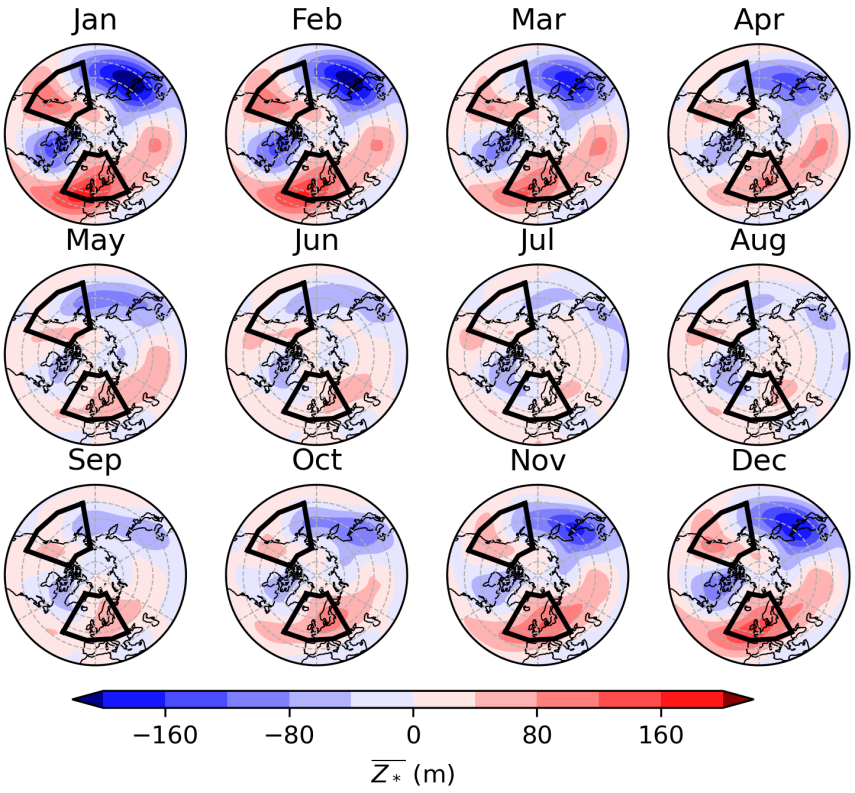

Figure 3.1: Monthly climatological $\overline{Z_*}$ from 1979–2021 (in metres) for January–December (shading). Also shown are the ATL and PAC regions (black boxes) used in this study.

North Pacific and western North America, a smaller and less intense region of ridging is present, followed by another trough downstream over the northeast of the continent. In summer, the same pattern manifests but is much weaker. Without considering $\overline{Z_*}$ when calculating the blocking index, regions of climatological ridging would show a large positive blocking frequency bias due to the high Z_*. Similarly, block frequency bias would be largely negative over regions of climatological troughing. In the work that follows, blocks are therefore considered to be anomalous circulation patterns within the climatological ridges and troughs, rather than simple anomalies in the zonal flow pattern.

3.2.3 Tracking AC Eddies

The 6-hourly positive Z'_* centres are followed using an objective feature-based tracking algorithm (TRACK; Hodges (1994, 1995, 1999)). Tracking begins when $Z'_* \geq 60$ m and stops when the strength of an eddy goes below this value. This

low threshold allows for the path of the eddy to be tracked both before and after it is part of a block, providing insights into the life cycle of AC transient eddies that contribute towards blocks. The tracks of the eddies are then filtered according to whether they are considered to contribute to a blocking event or not (Sect. 3.2.5).

In this work, TRACK is used to identify anticyclones corresponding to positive Z500 anomalies with respect to the instantaneous zonal mean component, once the climatological zonal mean anomaly is subtracted. Small scales are removed by spectral filtering, lowering the original resolution of the data to T42 resolution. Once the maxima in Z500 anomaly field are identified, tracks are constructed by finding nearest neighbours in consecutive time steps rather than the more sophisticated optimization method (Hodges, 1994, 1999) as there are typically only a small number of systems in any time step and blocks are often stationary features.

3.2.4 Block Events

The Z'_* field is also used to calculate a Eulerian blocking index at each grid point every six hours. For a grid point to be blocked, Z'_* must exceed 100 m for five or more consecutive days. This results in a 43-year time series at each grid point determining the periods in which the Z'_* magnitude and persistence threshold are met for blocking. Finally, sector blocking events (hereafter "blocks") are defined to occur when the area of blocked grid points inside a domain exceeds 1.0×10^6 km^2 (around 10% of either domain). This is only half the minimum size criterion imposed in Schiemann et al. (2020) for the ANOM index, but sensitivity tests showed that the results presented in this study are not dependent on the minimum size threshold (not shown). It should be noted that while a 5-day persistence criterion is imposed on the grid point-level Z'_* index, a persistence threshold is not applied to the definition of sector blocking.

There is an important distinction to be made between the persistence of the grid point Z'_* blocking index, and the persistence of a sector blocking event. This is illustrated in the schematic shown in Fig 3.2. Each red box denotes a grid point that meets the “blocked” anomaly magnitude and persistence conditions via the Z'_* index. In Days 1 and 2, a small group of grid points is blocked (area

of 0.8×10^6 km^2), but not enough to exceed the sector blocking definition of 1.0×10^6 km^2. From Days 3–5, two additional grid points meet the 5-day persistence criterion, resulting in a group of grid points large enough such that sector blocking occurs. This sector block event only lasts for three days, as from Day 6 onwards the area of blocked grid points decreases to below the threshold again. This example shows how a slightly more mobile, or smaller, block may only meet the sector block threshold for a few days, despite the grid point level 5-day persistence criterion. A similar situation can arise when a larger block occurs outside of either the ATL or PAC domains, but the edge of the block is inside one of the domains. However in all of these scenarios, it is still possible that severe surface conditions can be brought about by these "edge cases", and indeed AC eddies can still help to form or maintain these blocks. Therefore, these "edge cases" are retained in the analysis.

Sector blocking events are determined for two regions: the Euro-Atlantic (hereafter "ATL", 30° W–30° E, 45° N–75° N) and the North Pacific/northwest North America (hereafter "PAC", 170° W–110° W, 40° N–70° N). The domains are shown by black boxes in Fig. 3.1. These domains are both 60 degrees longitude wide, which is similar to the domain width used in Pelly and Hoskins (2003a) but 15 degrees larger than in Tyrlis and Hoskins (2008). However, the ATL and PAC

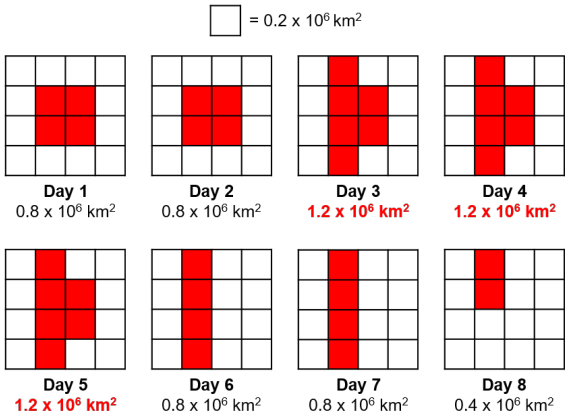

Figure 3.2: Schematic showing the difference between the persistence of the Z'_* index at grid point level, and the persistence of a sector blocking event. For simplicity, each box represents an area of 0.2×10^6 km^2. Red boxes represent grid points that exceed the minimum Z'_* threshold for blocking for a minimum of 5 days. The numbers below each day show the daily total blocked area in this scenario, with numbers in red showing days where the sector block area threshold (1.0×10^6 km^2) is exceeded.

domains were defined to be this wide in this study to account for the moving position of the climatological blocking maxima in these regions in different seasons. This was done while also minimising the chance that more than one blocking event is captured in the domain at the same time. The regions were also designed to align with large population centres with relatively large climatological blocking frequencies, such that the blocks analysed in this study have the potential to cause widespread impacts. For example, the PAC domain as defined in this study is able to capture the dynamics from the severe North American heatwave in June 2021, which would not be the case if the domain was positioned closer towards the climatological summer blocking frequency maximum.

3.2.5 Attributing Tracks to Events

A final step is required to associate Z'_* tracks with blocking as defined by the blocking index for further analysis. Three scenarios where the tracks and blocks overlap are considered to be contributing eddies (Fig. 3.3):

- "Through" eddies (Track A in Fig. 3.3), where a Z'_* track starts and finishes outside a block, but travels through a group of blocked grid points somewhere in its lifetime.
- "Absorbed" eddies (Track B) where a Z'_* track starts outside and finishes inside a collection of blocked grid points.
- "Edge" eddies (Track C) that fluctuate between coinciding with blocked grid points, and outside a block. These tend to occur on the edge of a group of blocked grid points, or in the onset/decay phase of a block.

Anomaly tracks can also coincide in space and time with blocking events in two other ways, which will briefly be mentioned here. First, "internal" tracks are Z'_* tracks that predominantly (over 80% of the time) remain inside a block throughout their lifetime. These are normally very slow-moving features, which are representative of the movement of the blocking anticyclone centre. These tracks are therefore not considered to be AC eddies that contribute to blocking. Secondly, blocks can also occasionally produce "spawned" eddies, which are Z'_*

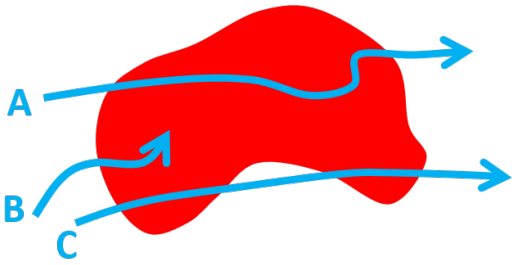

Figure 3.3: The three scenarios where AC tracks are considered to be contributing to blocking. Track A shows an eddy that passes through the block, Track B shows an eddy absorbed by the block, and Track C shows an eddy that fluctuates between coinciding with a block and not with a block. Tracks A, B and C are all considered to be AC eddies contributing to blocking.

tracks that start inside a blocked region and leave at some stage later in their lifetime. These cases are also not considered to be eddies that contribute to the block they spawn from, however they may go on to become an AC eddy associated with a different blocking event outside of their genesis region.

3.2.6 Comparison of AGP, ANOM, and Z'_* Indices

This section shows a comparison of the Z'_* index to the AGP and ANOM indices (Sect. 2.4) to highlight how difficult it is to design a blocking index that captures all types of blocking, and to illustrate the performance of the new Z'_* index. An example for a blocking ridge, omega block, AWB, CWB, and a dipole block is shown in Fig. 3.4.

The blocking ridge (Fig. 3.4a-c), in this example, is the shape that is captured least well by the three indices. There are no blocked grid points according to the AGP or ANOM indices, because the core of the block is too weak and too small, respectively. Only the Z'_* index recognises that blocking is occurring at this time. Some of the common problems with the AGP index (Barriopedro et al., 2010) are also displayed in Fig. 3.4a in that it picks out the subtropical highs (in the southwest) and also identifies small clusters of grid points as blocks in the other three corners that are not real blocks.

The omega block (Fig. 3.4d-f) is captured better in all three of the indices than the ridge. The AGP index only detects a small region around the centre and east of the omega block, whereas the ANOM index extends the block the furthest

northwest. In the AWB case (Fig. 3.4g-i) once again the AGP detection method covers the least of the block while the ANOM index captures the most block area. Conversely in the CWB example (Fig. 3.4j-l), the ANOM index does not detect any blocking at all, again because this incipient block is too small. Meanwhile, the AGP index only covers a small portion of the block on the eastern flank which is north of the cut-off low. The Z'_* index captures the largest block area in this case, but still fails to detect the cyclonic curvature of the ridge towards Iceland and Greenland. Finally, the dipole block is represented fairly well by all three methods (Fig. 3.4m-o), with AGP producing the smallest and ANOM the largest

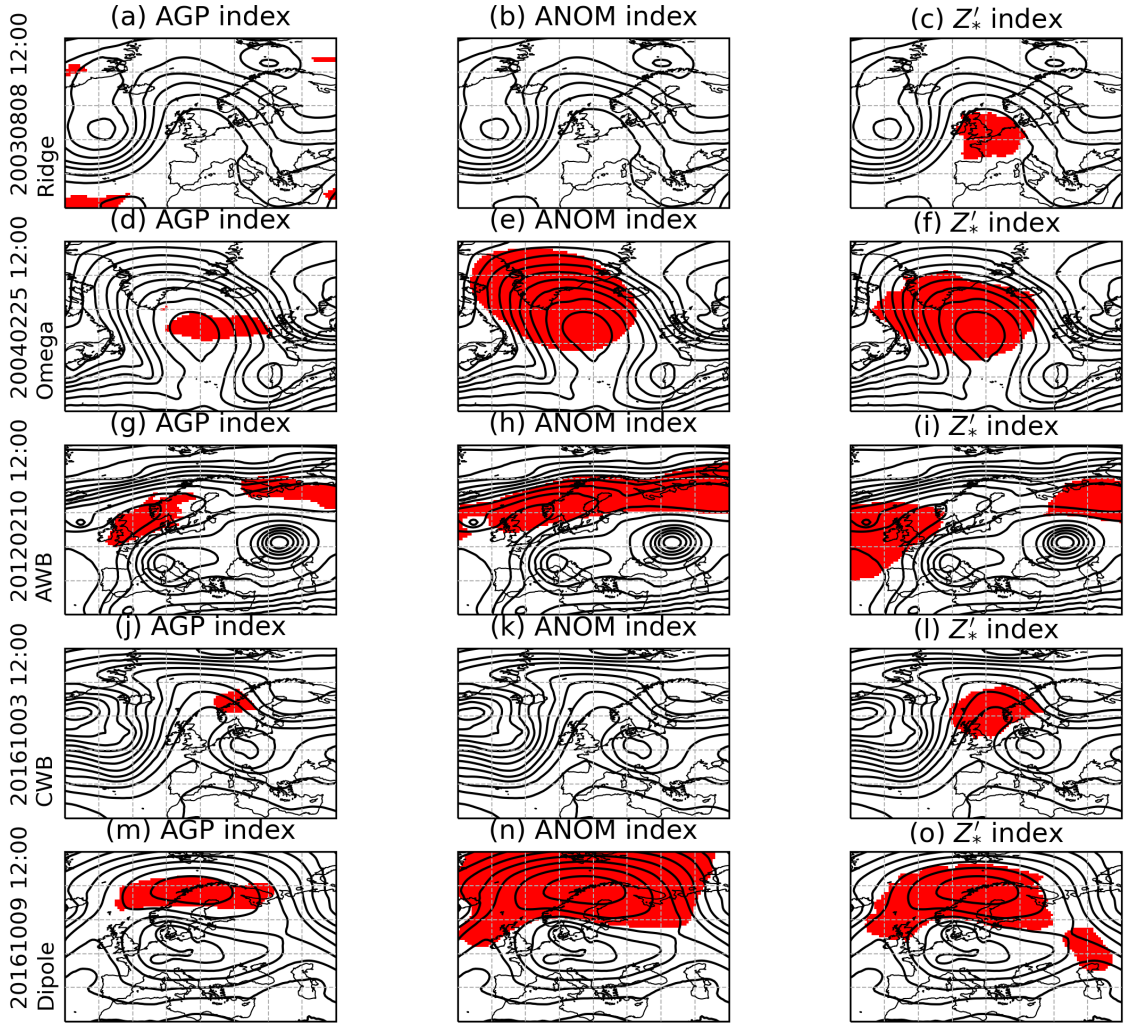

Figure 3.4: Comparison of the AGP (left column), ANOM (middle) and Z'_* blocking indices (right) for the five example blocking shapes shown in Fig. 2.1: ridge (a-c), omega block (d-f), anticyclonic wave breaking (g-i), cyclonic wave breaking (j-l), and dipole/Rex block (m-o). Blocked grid points according to each index (see text for details) with 5-day persistence are shown in red, and Z500 at 60m intervals is shown in black. Data is from ERA5, on an F128 Gaussian grid.

block once again. In this example however, the Z'_* index is detecting a spurious block in the southeast.

The examples shown in Fig. 3.4 demonstrate that each blocking index has its own strengths and weaknesses (as in Barriopedro et al. (2010)), and highlights the difficulty in designing a block detection algorithm that performs well in all scenarios. This is perhaps the most significant reason that there exists such a wide variety of blocking detection methods, and it is important to recognise which method is most suitable for the purpose of each study. Out of the the AGP, ANOM and Z'_* indices, it could be said that the AGP index is only suitable for analysing blocks where there is also a cut-off low nearby (AWB, CWB, and dipole blocks). On the other hand, the ANOM index may be more useful because it captures a larger proportion of the block, but would be unsuitable for use when analysing the onset or decay stages of the block due to its large minimum area threshold. Meanwhile, the Z'_* index would be suitable for studying blocks of all shapes and sizes.

Chapter 4

Transient Anticyclonic Eddies and Their Relationship to Atmospheric Block Persistence

4.1 Motivation

This section investigates the first research question of the thesis, and seeks to determine whether there is a relationship between the persistence of a block and the AC eddies it interacts with. It has been known for a long time that synoptic-scale transient features influence blocking dynamics (Sect. 2.5.1), but a study as to how this manifests climatologically has so far been lacking. Therefore in this chapter, the links between block persistence and both the number and strength of its contributing AC eddies are examined.

The rest of this chapter consists of Sects. 2.1, 3–7, and A2–A6 from Suitters et al. (2023) (Sect. 1 from this paper is redundant given the more comprehensive literature review in Sect. 2 of the thesis, and the rest of Sect. 2 from Suitters et al. (2023) can be found in Sect. 3.2 in this thesis). As previously mentioned, I performed all of the data analysis and writing in this article.

4.2 ERA5 Details

The data used in this study are taken from the ECMWF 5th generation reanalysis (ERA5) (Hersbach et al., 2020). The blocking index and feature-tracking are

based on analysis of 6-hourly Z500 data from 1 March 1979 – November 2021 with an F128 grid resolution. This is a regular Gaussian grid, with a grid size of approximately 0.7°, and is coarser than the full ERA5 resolution of 0.25°. Experiments were performed at different resolutions and the conclusions made did not change appreciably. Thus, the F128 resolution was chosen in the interest of computational speed. Data are additionally separated into the traditional meteorological seasons for further analysis in this work: winter (December, January, February; DJF), spring (March, April, May; MAM), summer (June, July, August; JJA), and autumn (September, October, November; SON).

4.3 Case Study of a Block and its Transient Eddies

In this section, a case study is discussed to illustrate how transient eddies can contribute to both establishing and maintaining a blocking event. This event meets the sector blocking definition in the ATL region for 11.25 days, from 25 February–8 March 2011, and has a total of two AC eddies (with an additional two internal tracks and one spawned track). Figure 4.1 shows the Z'_* field and blocked points at 12 UTC for every day of the event. Additionally, all AC eddy, internal, and spawned tracks for this event are shown.

On 25 February, a ridge breaking in the far east of the domain gives rise to grid-point level blocking (Fig. 4.1a). At this stage, there is no Z'_* track in the domain, though one is present over the Scandinavian block just outside the ATL domain (not shown). By 26 February (Fig. 4.1b), a small AC eddy (dark blue line) originating from the mid-Atlantic can be seen approaching from the west as a low-amplitude ridge in the Z'_* field. This eddy enters the domain on 27 February (Fig. 4.1c) and this associated ridge amplifies, while the block situated in the east of the sector over Scandinavia remains in place. On 28 February (Fig. 4.1d), the western ridge breaks and connects to the Scandinavian block, resulting in many more blocked grid points in the domain, even in the west by this stage. Also on 28 February, the ATL block spawns an eddy (light blue line in Fig. 4.1) that travels towards the Ural Mountains until 3 March. A small internal track is also present on the far eastern part of the domain, associated with a slight movement

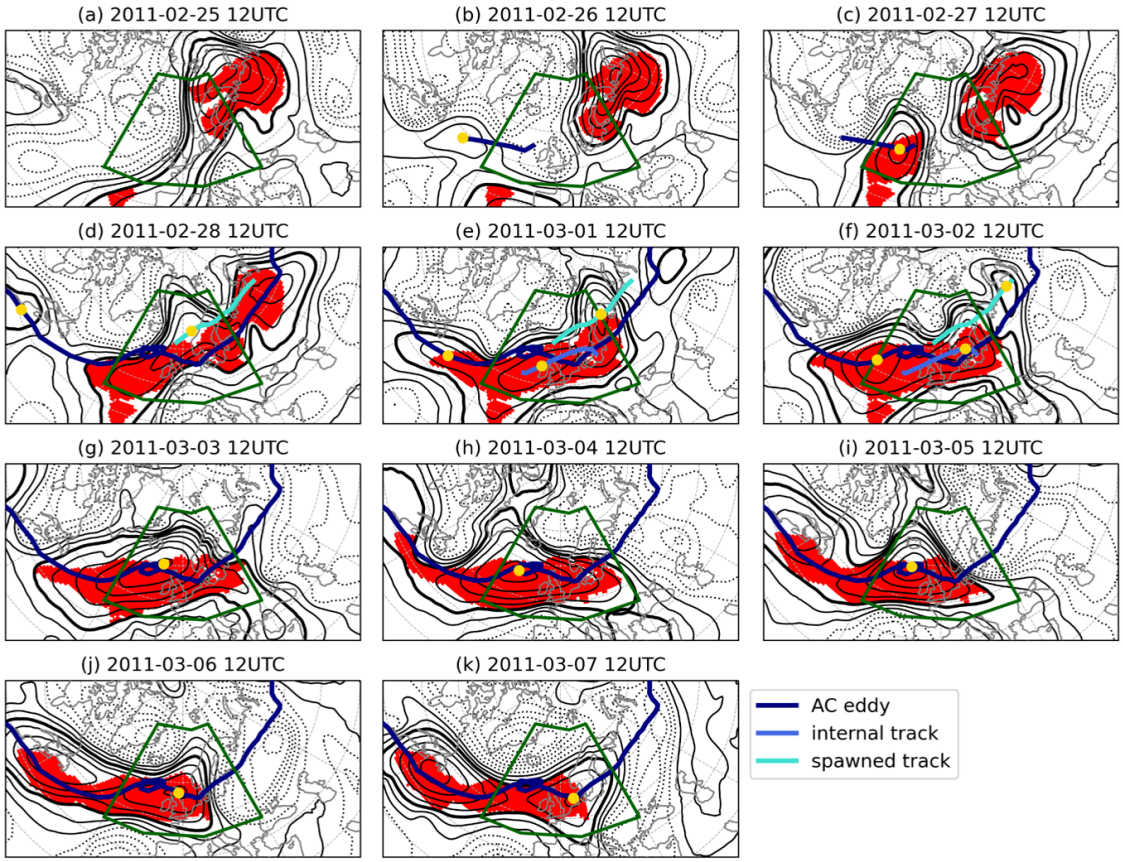

Figure 4.1: Blocked grid points (red shading) and Z'_* anomaly field (black contours at 50 m intervals; negative values dashed, 100 m line bold) at 12 UTC for each day of an ATL blocking event (the ATL region is depicted by the green box). AC eddy tracks (dark blue), internal tracks (medium blue) and spawned tracks (light blue) that coincide with this blocking event are also shown, with each track's position at the valid time shown by the yellow dot.

in the central anticyclone between 28 February 12 UTC and 1 March 12 UTC (so no yellow dot is shown). Meanwhile, another AC eddy has already begun travelling towards the block. This eddy originated from the United States, and will eventually travel all the way to Japan, via the ATL block, travelling around 240 degrees longitude from start to end. At this early stage (28 February), this eddy is still fairly small, but over the next few days it grows in both size and amplitude as it connects to the ATL block (Fig. 4.1d-f). Another, more prominent internal track develops inside the block from 1–2 March. Once inside the block, the Atlantic AC eddy slows down (as shown by the loop in its track from 3–5 March, Fig. 4.1g-i). On 6 and 7 March, the AC eddy begins to speed up again as it travels east towards Japan, and the ATL block slowly decays (Fig. 4.1j-k). Once the track

leaves the ATL domain, very few grid points remain blocked and the block event finishes.

A short discussion on how AC eddies contribute to blocking dynamics is now introduced. Figure 4.2 shows how the area and intensity of the ATL sector block introduced here varies throughout its lifetime, and also shows the timings of the AC eddy interactions with it. The ATL block area (black line) quickly increases in the first 3–4 days, remains relatively constant at $5.0\times$ 10^6 km^2 for 2–3 days, and then decreases again in the final 4–5 days. The ATL block intensity (grey line) starts off high, associated with the intense Scandinavian block to the east of the ATL domain. After a brief decrease, the intensity increases to over 350 m just after the area reaches its maximum. After 3 March, the intensity steadily

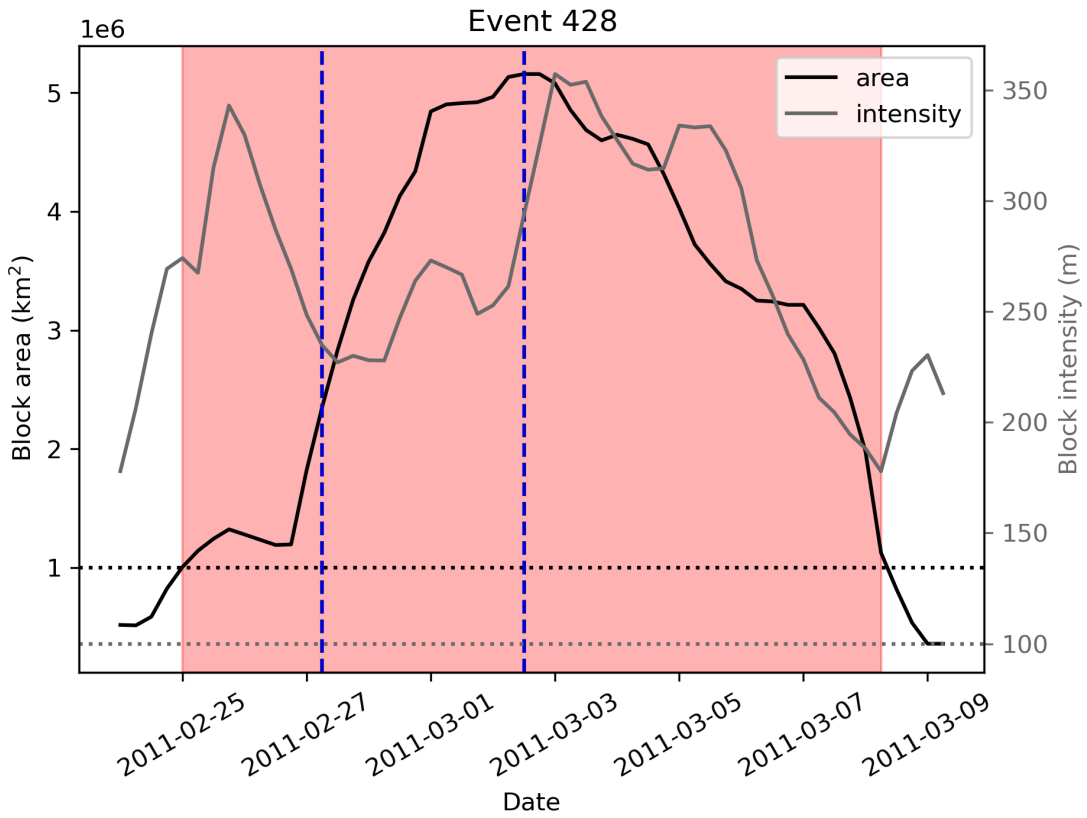

Figure 4.2: Time series of the blocking example introduced in Sect. 4.3, showing the block area (black, left axis) and intensity (grey, right axis; measured as the maximum Z'_* in the ATL domain at each time). Red shading indicates the times at which sector blocking was occurring in the ATL domain, with horizontal dotted lines showing the minimum area and intensity thresholds for sector blocking. Vertical blue dashed lines denote the times at which AC eddy centres (yellow dots in Fig. 4.1) first coincide with a blocked grid point in the ATL domain.

decreases along with the block area in the ATL region.

The arrival of the first AC eddy into the block is associated with the sharp increase in sector block area, and the second AC eddy coincides with the rise in intensity of the block. The increase in block area (intensity) occurs 12–18 hours before the first (second) AC eddy centre enters the block, implying that the eddies have a field of influence that extends beyond their tracked centres. Increases in block intensity and/or area that coincide with the arrival of an AC eddy are also detected for many other blocks in this study (not shown). These findings are very important in determining the longevity of a block. Larger, more intense blocks require more time to advect them downstream or dissipate (e.g., Yamazaki and Itoh, 2013b), and thus AC eddies that strengthen or broaden blocks can also be expected to increase their persistence.

4.4 Northern Hemisphere Z'_* Index Blocking Climatology

Before examining the transients that maintain blocks in the ATL and PAC domains, a climatology of NH blocking using the Z'_* index (from Eq. 3.5) is presented to motivate the selection of these two regions. Figure 4.3 shows the percentage of blocked days in winter, spring, summer, and autumn for the Northern Hemisphere. The spatial distribution of blocking frequency is consistent with many previous studies that utilise Z500 anomalies for block detection (e.g., Barriopedro et al., 2010; Schiemann et al., 2017; Woollings et al., 2018). Blocking occurs most frequently in three regions: the Northeast Pacific/Northwest North America, Northeast Atlantic/Western Europe, and Scandianvia/Ural Mountains. The effect of considering the climatological stationary wave features ($\overline{Z_*}$) is noticeable here by comparing Fig. 4.3 with that of Liu et al. (2018) where $\overline{Z_*}$ is not considered (their Fig. 9). Climatological blocking frequencies as measured using the Z'_* index are half as frequent in the Pacific and Atlantic maxima than in Liu et al. (2018) (climatological frequency of 16% vs 30%). The seasonal variation in blocking frequency found in many previous studies (e.g. Dole and Gordon, 1983; Barriopedro et al., 2010; Schiemann et al., 2017; Woollings et al., 2018) is also re-

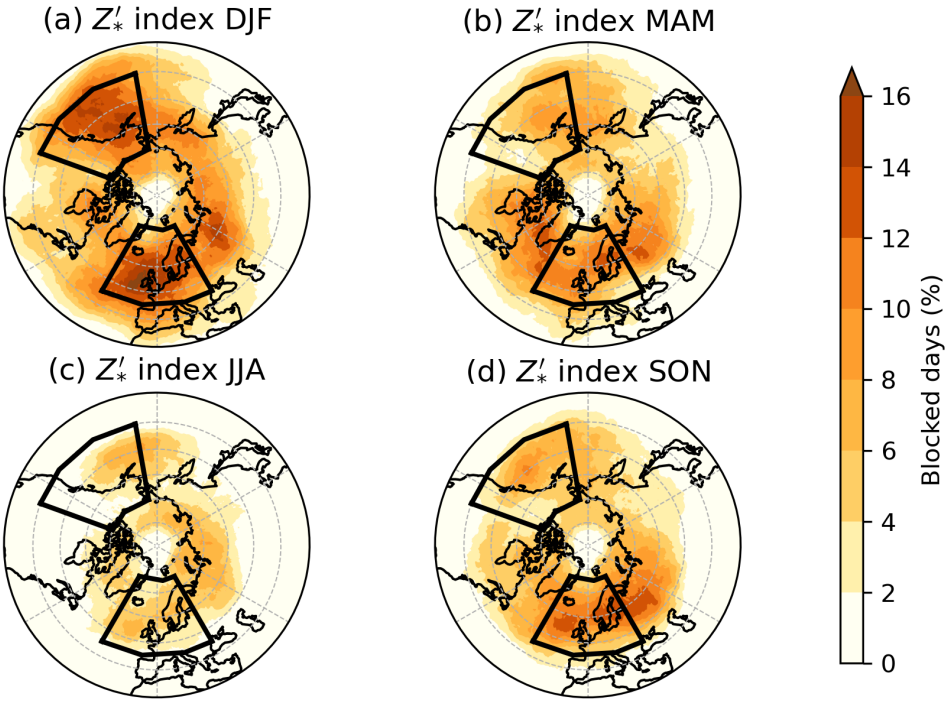

Figure 4.3: Blocked day frequency according to the Z'_* index, showing the percentage of days in a season that are blocked in (a) winter, DJF; (b) spring, MAM; (c) summer, JJA; and (d) autumn, SON. Black boxes indicate the ATL and PAC regions.

produced here, with blocking being most common in winter and least common in summer.

While Fig. 4.3 implicitly shows how many days in each season are blocked on average, the length of each individual block can vary greatly around its average length. The distribution of sector block persistence for the ATL and PAC regions is shown in Fig. 4.4, along with the first (Q1), second (Q2), and third (Q3) quartiles. Results for winter and summer are discussed in detail here since these are the seasons where blocking has the potential to bring the most severe hazards, with spring and autumn distributions shown for completeness in Sect. 4.8.1. Sector block events with a persistence of fewer than 5 days are generally uncommon in DJF, but the JJA Q1 values are less than five days. This indicates that a sizeable proportion of JJA blocks are small in size and only marginally exceed the minimum area threshold for sector blocking.

The shape of the persistence distributions shown in Fig. 4.4 is qualitatively

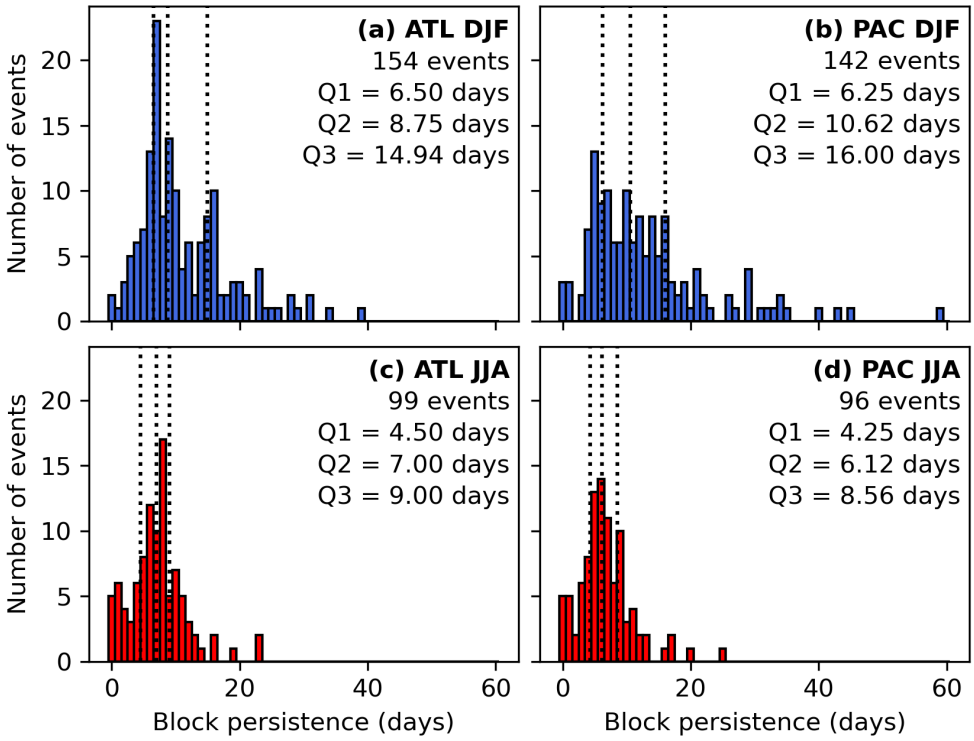

Figure 4.4: Histograms showing sector blocking event persistence frequency in winter (a, b) and summer (c, d) for the ATL (a, c) and PAC (b, d) sectors. The first (Q1), second (Q2), and third (Q3) quartiles of block persistence are indicated by the dotted lines.

similar to the distributions found in other studies that use different blocking indices (e.g., Wiedenmann et al., 2002; Diao et al., 2006; Drouard and Woollings, 2018; Detring et al., 2020) in that shorter blocks are far more common than long events. The high climatological blocking frequency in winter shown in Fig. 4.3 is due to both a larger number of blocking events, and a longer duration of these blocks. In both sectors, the quartiles of block persistence are much larger in DJF than JJA, with DJF blocks having a median length comparable to the third quartile in JJA. The distribution of block persistence is remarkably similar in the ATL domain for DJF, MAM and SON (MAM and SON shown in Fig. 4.8), with the longest blocks lasting 39.25 (DJF) and 39.75 (SON) days, while the longest JJA ATL block persisted for 23 days. Slightly more seasonal variation with block persistence is found in the PAC region (c.f. Fig. 4.8), and with the exception of DJF (where the longest block is 59 days long), PAC block lifetimes are slightly shorter than those found in the ATL domain.

4.4.1 59-Day PAC Block

The following subsection was not part of the journal article as printed in Suitters et al. (2023), but is included here as a supplementary discussion of the block in the PAC sector that had a persistence of 59 days (Fig. 4.4b). This remarkably long sector blocking event according to the Z'_* index could be considered to be two distinct blocks separated by only one day; however the Z500 anomaly inside the domain still exceeded the blocking threshold. Despite this, blocked conditions were present in the sector throughout the detected event, and are described below.

The event began on 13 December 1984 and ended on 11 February 1985. At the start of the event, a blocking ridge is positioned to the west of the domain and persists here for approximately 16 days. Three days after this, the ridge translates eastwards, weakening as it does so (the end of the first "potential event"). However another ridge re-intensifies in the eastern portion of the domain straight after this, and the whole system re-intensifies and persists here for another 24 days. Hereafter until the end of the event in mid-February, the block retrogresses westwards again and generally weakens.

An event of this length suggests that the conditions in the PAC domain during this time were very distinct from the climatological pattern in this location. Indeed, measurements of the Northern Oscillation Index (NOI), which measures the pressure difference between the northeast Pacific and Darwin, Australia, was particularly high during this period, and was classified as a "strong" positive NOI (Schwing et al., 2002).

4.5 Relationship between Block Persistence AC Transient Eddies

4.5.1 Number of AC Eddies

The persistence, mean area, and number of associated transient AC eddy tracks of each blocking event for both regions in winter and summer are shown in Fig. 4.5. Correlations between these three measures are also shown on each panel, and

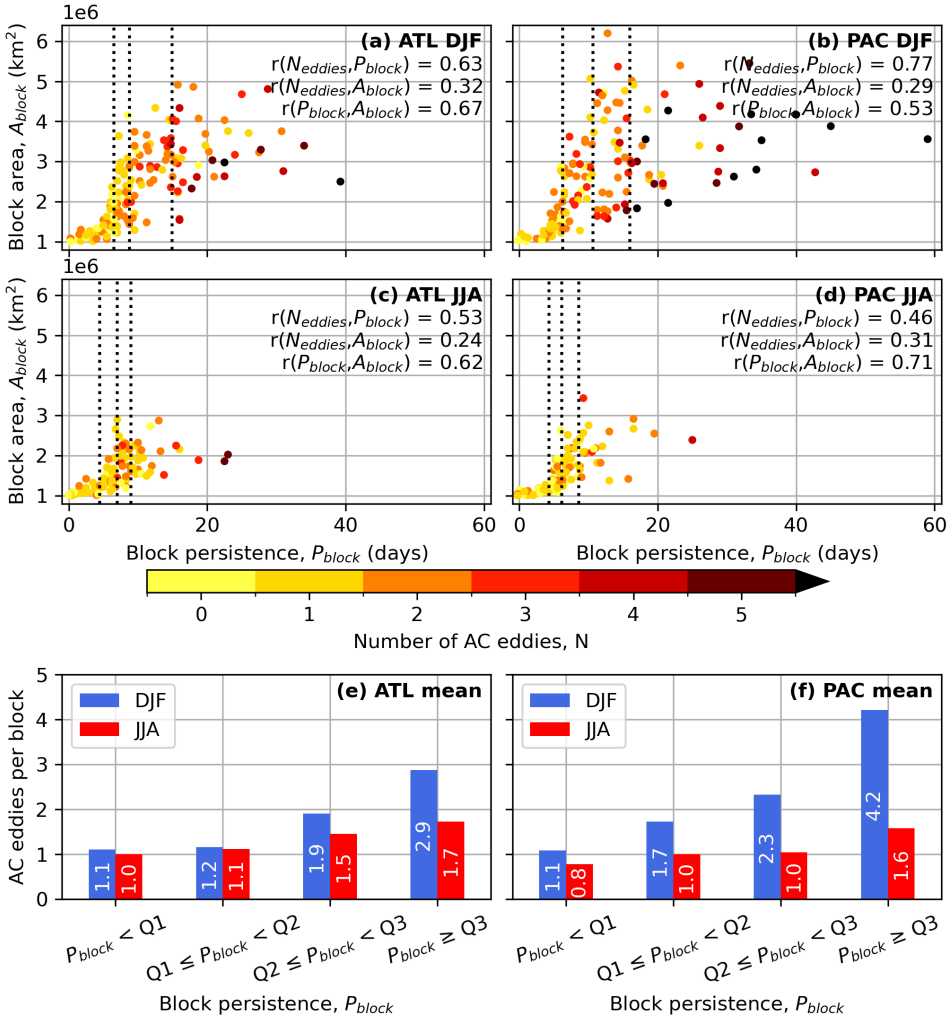

Figure 4.5: (a-d) Number of anticyclonic transient eddies (N_{block}) that contribute to blocking events in winter (a, b) and summer (c, d) for the ATL (a, c) and PAC (b, d) regions. Blocking events are characterised by their persistence (P_{block}) and mean block area (A_{block}). Pearson's correlation coefficients between N, P, and A are indicated for each sector and season (all are significant to the 95% confidence interval). Q1, Q2, and Q3 (as in Fig. 4.4) are indicated by the dotted lines. (e-f) Mean number of AC eddies per block of a particular persistence, defined in terms of the quartiles for a season, for the ATL (e) and PAC (f) regions in DJF (blue) and JJA (red).

all are statistically significant ($p < 0.05$). As with the histograms in Fig. 4.4, MAM and SON blocks behave similarly to DJF blocks in terms of AC eddy number, thus only winter and summer blocks are discussed here, with results from MAM and SON included in Sect. 4.8.2.

Longer blocks are generally larger, and this relationship is strongest in summer in the PAC region (correlation of 0.71). Larger blocks take longer to naturally

dissipate (Yamazaki and Itoh, 2013a), so this result is not surprising. Additionally, more persistent blocks generally have more transient AC eddies contributing to them, and this is a combination of a larger number of these eddies either ending in or passing through the block. The correlation between block persistence and block area is comparable to the correlation between persistence and number of AC eddy interactions in DJF for both sectors. The JJA correlations between persistence and number of AC eddies are weaker but still reasonably strong, suggesting that the number of AC eddy interactions with a block is somewhat less important in summer. The relationship between the area of a block and the number of AC eddies it interacts with is comfortably the smallest of the three correlations shown, as for a given area, there is large variability in the number of AC eddies a block interacts with.

Despite the general observation where more persistent blocks interact with more AC eddies, there is also substantial variability in the number of AC eddies for a block of given persistence, where between 2 and 6 eddies can be seen to be contributing the most persistent 25% of blocks (Fig. 4.5a-d). However despite this large variability, the number of AC eddies a block interacts with increases as its persistence increases at all times of year (Fig. 4.5e-f). The shortest 25% ($P < Q1$) of winter ATL blocks have an average of 1.1 AC eddies contributing to them, but the longest 25% ($P \geq Q3$) have nearly three times as many eddies (2.9). The relationship is even stronger in the PAC sector, where the longest 25% of blocks interact with nearly four times as many AC eddies as the shortest 25% of blocks (4.2 and 1.1 eddies, respectively). The aforementioned 59-day DJF PAC block event interacted with eight upstream AC eddies. In summer in both sectors, the longest 25% of blocks only have up to twice as many AC eddies contributing than the shortest 25%, confirming that the relationship between AC eddy number and persistence is weaker. While corr(N,P) in JJA is smaller than in DJF for both sectors (0.53 vs 0.63 in ATL, 0.46 vs 0.77 in PAC), JJA blocks are also less persistent. Therefore, it is perhaps not surprising that the average number of AC eddies per block for longer blocks is smaller in JJA than DJF. Correlations between N, A, and P in both sectors in MAM and SON are generally comparable to those in DJF, with an average number of AC eddies per block larger than JJA but smaller than

DJF (Fig. 4.9).

4.5.2 AC Eddy Strength and Speed

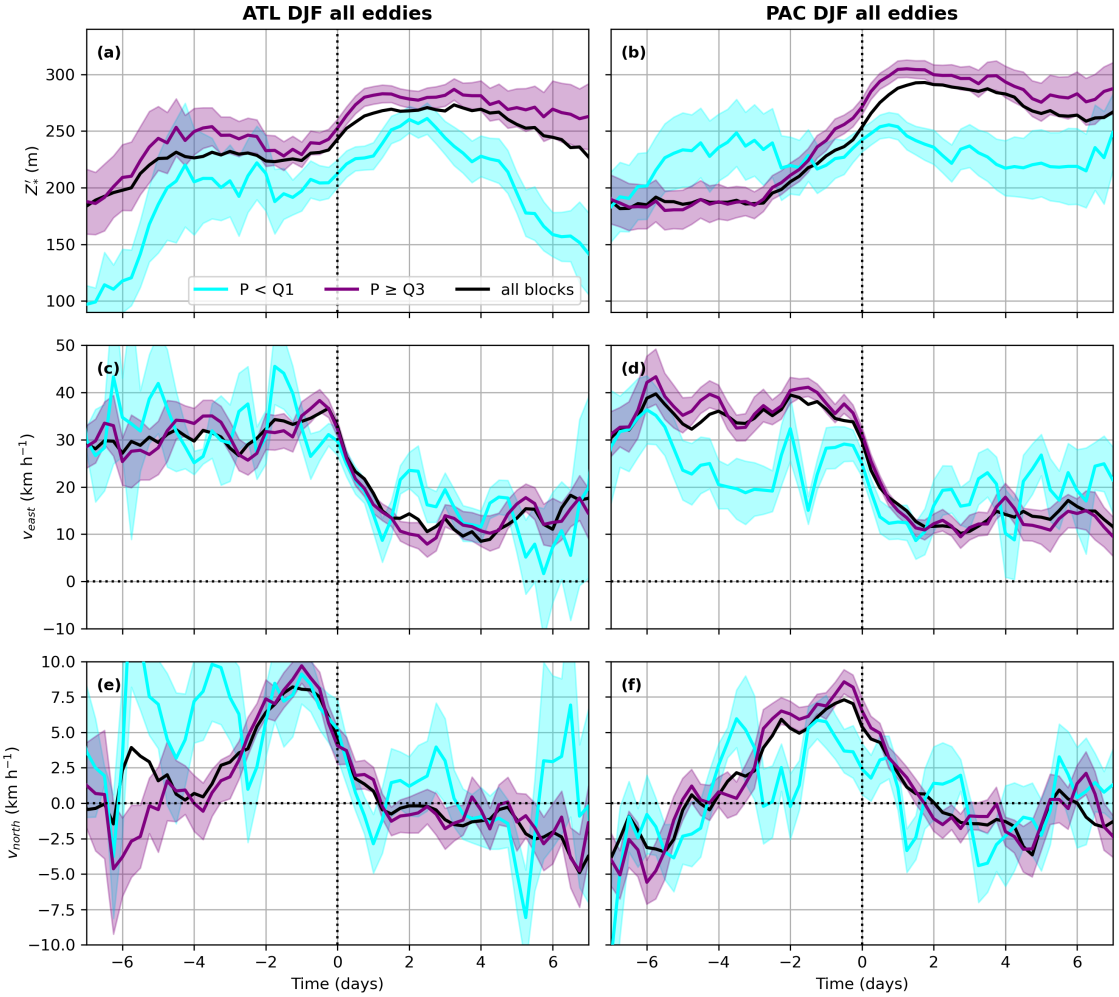

Figure 4.6: Characteristics of transient AC eddies that contribute to blocking in DJF. The mean strength, measured by the maximum Z'_* (a, b), zonal velocity v_{east} (c, d), and meridional velocity v_{north} (e, f) of AC eddies that contribute to blocks of all lengths in the ATL (left) and PAC (right) domains are shown in black. The same mean quantities are also shown for only the AC eddies that contribute to the shortest (cyan) and longest (purple) 25% of blocks, with shading indicating the standard error from the mean at each time step. Negative times indicate the period before the eddy enters a block in the domain, and positive times indicate times after entering a block.

It is possible that the characteristics, in addition to the amount, of AC eddies interacting with a block can influence its persistence. First, the mean strength (as measured by the magnitude of Z'_* at the AC eddy centre), and zonal and meridional speeds of all AC eddies are discussed, for blocks of all persistences. Black

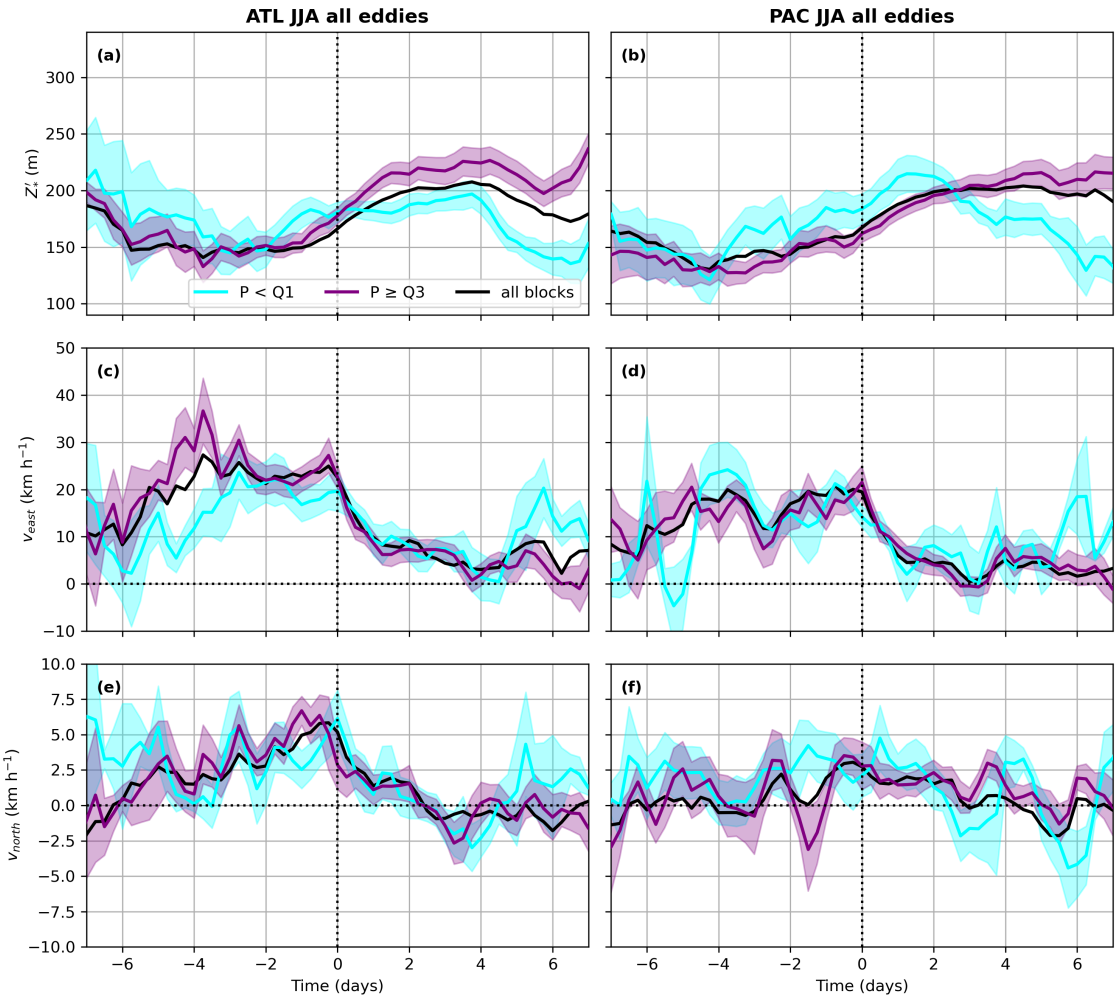

Figure 4.7: As Fig. 4.6, but for AC eddies that contribute to JJA blocks.

lines in Figs. 4.6, 4.7 show the strength, zonal speed and meridional speed of all AC eddies in the 7 days before and after entering blocks in DJF or JJA respectively, in both the ATL and PAC domains. The general behaviour of the eddies is similar in both the ATL and PAC regions, and the charactersitics of "absorbed" and "through" eddies are qualitatively similar to those of all AC eddies (not shown). In the days before the eddies enter a block, their strength remains fairly constant in JJA, and in DJF for ATL sector blocks (Figs. 4.6a, 4.7a-b). AC eddies contributing to DJF ATL blocking are stronger than their PAC counterparts before entering the block. JJA eddies are of a similar strength in both domains, but weaker than those in DJF. In the ATL domain, AC eddies in both DJF and JJA begin to strengthen by day -1, and then strengthen further by around 50 m in the first two days after entering a block (time = 0 line in Figs. 4.6, 4.7). In the PAC region, the intensification is stronger for DJF eddies (nearly 100 m) and begins at around day

-3. It is possible that this could be a sign that the block is acting to strengthen the upstream AC eddies, consistent with the EBM mechanism (Luo, 2005). However, it could also potentially because the PAC region is slightly to the east of the North Pacific climatological blocking maximum (Fig. 4.3), meaning AC eddies intensify upon entering a block just outside the domain. However, further intensification does occur once the eddies are inside a block in the PAC domain between days 0 and +1. After this, in both regions, there is a steady decay of the eddy strength (though they are still as intense or stronger than they were before blocking). However, the strength of a block can be maintained by the absorption of additional AC eddies later in its lifetime (not shown), if it persists for long enough.

The AC eddy zonal speed contributing to all blocks (black lines in Figs. 4.6c-d, 4.7c-d) is also fairly constant in the days before the eddy enters a block. Winter eddies move eastwards faster than those in summer, and the difference between seasons is largest in PAC. The slower eastward progression of AC eddies in JJA is consistent with the slower and weaker jet streams during summer months. Despite the speed differential of the eddies between DJF and JJA, it is found that the distance travelled by each AC eddy does not change considerably between the two seasons (not shown). Upon entering the block, the eddies rapidly decelerate such that their zonal speed halves compared to days -7 to 0. Unlike with eddy strength, the zonal speed of the eddies remains constant through to day +7 and beyond.

The evolution of the meridional speed of the AC eddies that contribute to all blocks in both domains is more complex (black lines in Figs. 4.6e-f; 4.7e-f). In the seven days before entering a block, AC eddies gradually accelerate northwards in both domains during winter, and in summer in the ATL, though their meridional speeds are around four times smaller than their zonal speeds. This northward acceleration is potentially indicative of two things. Firstly, it signifies the building of a ridge through the northward advection of higher geopotential heights, which is a characteristic of blocking. However, it can also be the result of eddies being attracted by the block via the SAM. AC eddies then rapidly decelerate meridionally once inside a block, reaching small southward speeds. The rapid deceleration of

the eddies, both zonally and meridionally, is typical of blocking dynamics, since blocking systems are quasi-stationary. Meridional speed for PAC summer blocking AC eddies is fairly constant before and during blocking. In MAM and SON (Sect. 4.10), AC eddies behave in largely the same way as outlined here, with intermediate speeds and strengths between those in DJF and JJA.

A similar analysis can be performed for AC eddies that interact with the shortest and longest 25% of blocks in both sectors (cyan and purple lines respectively in Figs. 4.6, 4.7), to determine whether there is a relationship between the strength or speed of the eddies and the persistence of the blocks they contribute to. If there is no overlap of the standard errors from the mean between AC eddy characteristics of different block persistences, then the results are said to be statistically significant.

The longest 25% of DJF ATL blocks interact with stronger AC eddies than the least persistent 25% of blocks (Fig. 4.6a), with the mean eddy strength for longest blocks being about 40 m larger at the time that the eddies enter the block. The same is true in the PAC domain in winter (Fig. 4.6b). The longest 25% of blocks in both sectors in SON also absorb stronger AC eddies than the shortest 25% of blocks (Fig. 4.11a-b). In both domains during JJA, the longest blocks are not the result of interacting with stronger AC eddies (Fig. 4.7a-b), and in fact stronger AC eddies result in less persistent blocks in the PAC in JJA. Additionally, the AC eddies contributing to both the longest and shortest 25% of blocks at t = 0 in the ATL region in JJA are stronger than the mean eddy strength, perhaps suggesting two contrasting pathways for block maintenance. The persistence of MAM blocks in the ATL domain also does not appear to depend on the strength of the absorbed AC eddies, but in the PAC similar behaviour to that in DJF and SON is shown (Fig 4.10).

It may appear from Figs. 4.6a-b, 4.7a-b that AC eddies that interact with the least persistent blocks become weaker and fast-moving again from day +4 onwards. To some extent, the same is true at times over +7 days for AC eddies that contribute to more persistent blocks (not shown). While it is true that such AC eddies do weaken and speed up at these times, the block is no longer present at these time steps, so these eddies are no longer interacting with blocks.

AC eddies contributing to the longest PAC blocks intensify by about 120 m from days -3 to +1, which is double the amount seen in the ATL domain in DJF. Associated with this marked increase in intensity, these AC eddies also move significantly faster than eddies contributing to shorter blocks (Fig. 4.6d, f). This speed discrepancy at the point of absorption is only also demonstrated in MAM (Fig. 4.10), which suggests that AC eddy speed is not usually a reliable indicator of how long a block may persist for. In both domains in JJA (and MAM, Fig. 4.10), AC eddies that contribute to the shortest 25% of blocks do not markedly intensify upon entering a block like those entering longer blocks do, underlying the more transient nature of these shorter-lived block events. It is therefore possible that the lack of intensification of AC eddies upon entering a block could be a signal that the block will not persist.

4.6 Discussion

Yamazaki and Itoh (2013a) explain that blocks require a source of low-PV in order to counteract the effects of dissipation, and AC eddies can be thought of as a way to replenish the low-PV inside the block. Although the AC eddies in this study are defined using Z500, the invertibility principle of PV (Hoskins et al., 1985) means that ridges of low-PV correspond to ridges of high Z500, and therefore similar arguments can be made here. Thus, eddies that bring an AC Z500 anomaly towards a block can also be expected to provide an AC anomaly of PV, so we can therefore approximate both blocks and AC eddies to be vortices of low-PV. Following the SAM, blocking vortices induce a stronger AC forcing than the eddies, which results in the eddies being attracted towards the block. When AC eddies enter a block, vortex merging occurs, where the two vorticity centres combine into a larger, stronger vortex. This new blocking vortex then exerts a stronger AC vorticity on its surroundings than before, which allows AC eddies to be attracted towards the block from further away, until they themselves merge with the block. This positive feedback loop potentially allows blocks to become self-sustaining (Yamazaki and Itoh, 2013a), and therefore leads to some very long blocking events with many contributing AC eddies (like those seen in DJF in the

PAC region in Fig. 4.5).

As shown in Sect. 4.5.2, block persistence in the ATL domain is less sensitive to AC eddy strength than in the PAC region, particularly in MAM and JJA. The correlation between the number of AC eddies and block persistence is also weaker (though still relatively strong) in the ATL than PAC (Sect. 4.5.1). It is possible that in the ATL region, competing blocking dynamics are being detected for the Atlantic and continental European portions of the domain. Miller and Wang (2022) showed that synoptic-scale fluctuations in Z500 are important factors in European blocking dynamics, whereas Atlantic block dynamics are instead determined more by planetary-scale, longer timescale anomaly patterns such as the North Atlantic Oscillation (NAO). These differing factors may account for the weaker dependence of ATL block persistence on the number and strength of AC eddies.

The finding that longer JJA PAC blocks result from the absorption of weaker AC eddies results from the positioning of the PAC domain. In JJA, the PAC domain only partially covers the climatological blocking frequency maximum in this area (Fig. 4.3), with a large portion to the west not being considered in this study. When the PAC domain is shifted 30°W to cover the entire climatological blocking maximum (not shown), no statistical significance exists between eddy strength for the shortest and longest 25% of blocks, akin to the ATL in JJA (Fig. 4.7a). Therefore, it can also be deduced that counteracting blocking dynamics are being detected in the original PAC domain. The strongest AC eddies lead to more blocking to the west of the PAC domain, resulting in only small persistences in the PAC due to it only capturing the eastern flank of such block events. Weaker AC eddies lead to more blocks inside the PAC domain itself, leading to higher persistences since the blocks are wholly within the sector. This explains why, for the PAC domain in JJA, it appears that longer blocks interact with weaker AC eddies. Clearer relationships between AC eddy strength and block persistence could be produced when the PAC (and to a lesser extent, the ATL domain) are aligned more with the seasonal climatological block frequency maxima, however the results presented here are still important since the blocks analysed have the potential to cause more impacts than those e.g. over the Pacific Ocean. The

methodology presented here can be applied robustly anywhere, provided that climatological block frequency is relatively high.

4.7 Conclusions

This study has used objective feature-tracking of synoptic-scale AC eddies that help contribute to atmospheric blocking events to analyse the climatological relationship between transient AC eddy number, intensity, and block persistence in the North Pacific (PAC) and Euro-Atlantic (ATL) regions. It is found that in both sectors, more persistent blocks are associated with more transient AC eddies, and this relationship is weaker in summer compared to other times of the year. The PAC region exhibits a larger variability in the number of eddy interactions for blocks of different lengths than the ATL region, though both regions show that the most persistent blocks interact with the most AC eddies. These results suggest that blocks can be maintained through repeated absorption of AC eddies, potentially supporting the SAM theory (Yamazaki and Itoh, 2013a). In general, the number of AC eddies a block interacts with is important for determining its persistence in all locations at all times of year. However, not all persistent blocks are the result of a large number of AC eddy interactions, which indicates that other dynamical processes are also important for block maintenance in these cases (e.g., interactions with waves originating from the tropics (Austin, 1980); and moist dynamics (e.g. Pfahl et al., 2015; Steinfeld and Pfahl, 2019)).

Conversely, the relationship between the persistence of blocks and the strength of the AC eddies it absorbs is more complex. At all times of year, block length in the PAC region is also dependent on AC eddy strength. In all seasons apart from summer, the most persistent 25% of blocks have absorbed statistically significant stronger AC eddies than the least persistent 25% of blocks. In summer the reverse is true in that longer blocks result from the absorption of weaker AC eddies, though this is perhaps an artefact of the choice of domain. For the ATL domain, stronger AC eddies only increase the length of the block in autumn and winter, whereas ATL block length appears to be unaffected by eddy strength in spring and summer. Therefore, the relationship between block persistence and

AC eddy strength appears to be more variable than that with the number of AC eddies, due to the dependence on location and time of year.

AC eddies increase the persistence of blocks through increasing their area and/or intensity. This means that blocks require a longer period of time to either advect them downstream, or naturally decay through dissipation. A larger number of, or more intense, AC eddies result in larger block area or intensity increases, thus leading to longer-lasting blocks.

Analysis of AC transient eddies associated with blocks of all lengths in both sectors leads us to conclude that winter eddies are stronger and faster than their summer counterparts. Most AC eddies intensify and accelerate northwards towards the block just before entering, which could potentially signal an attraction via the SAM, (Yamazaki and Itoh, 2013a). Nonetheless, more evidence on the vortex-vortex interactions between AC eddies and blocks are required to ascertain whether this mechanism is actually taking place. However, generally AC eddies that enter the least persistent 25% of blocks do not undergo this intensification once inside the block, thus meaning that this behaviour could be used as a potential indicator for how long a block may persist for. All AC eddies rapidly decelerate once inside a block, consistent with the slow-moving nature of block events.

Though the results presented in this study clearly present a positive correlation between AC eddy numbers and block persistence, there remains the question of whether the amount of AC eddies is what is *causing* the longer block lifetimes. It could be expected that a more persistent block absorbs more eddies simply because it has more time to absorb these AC eddies than shorter ones. Additional tests are required to ascertain whether this is the case. For example, idealised model experiments could be performed that analyse the rate of AC eddies passing through a particular region changes according to whether a block is present or not. Similarly, experiments should be performed that determine whether a particular block persists for different lengths of time whether or not it has AC eddies passing through it. However, two pieces of evidence support the hypothesis that higher AC eddy numbers do cause longer blocks because (i) around the times that AC eddies enter blocks, they become stronger and/or larger (Fig. 4.2)

which means they would take longer to decay through dissipation; and (ii) there is the suggestion that AC eddies are attracted towards blocks as they approach which seems to confirm the SAM (Figs. 4.6, 4.7).

This study only considers dry dynamical processes, namely multi-scale interaction between the large-scale blocks and smaller-scale AC eddies. While the results presented here suggest there is a strong, significant relationship between block persistence and the amount of AC eddies a block interacts with, this process is certainly not the only dynamical process occurring during the maintenance phase of a block. The most important missing piece of this study is the extent to which moist dynamics, for example diabatically-heated outflow from warm conveyer belts (e.g. Pfahl et al., 2015; Steinfeld and Pfahl, 2019), also affect block persistence. We hypothesise that in persistent blocks with very few AC eddy interactions, other maintenance processes such as diabatically-generated negative PV anomalies are instead dominant. Similarly, in short blocks with many AC eddy interactions, there may be other processes (e.g. diabatic cooling) that causes the block to decay quickly despite the continued AC eddy forcing. Further work is required to compare these dynamical differences between blocks with many contributing AC eddies to those with few AC eddy contributions. Furthermore, our results have also highlighted the existence of two further types of AC eddies, namely those that pass through the block, and those that are spawned by the block and propagate downstream. These types of AC eddies require further investigation, particularly as it is possible that they can go on to interact with another block event downstream. Finally, this work has only considered the AC eddies that contribute to blocking anticyclones, whereas some blocks (omega or dipole blocks) also have quasi-stationary cyclones as part of the blocking system. Further analysis is required to examine whether more (or more intense) cyclonic eddies increase the persistence of blocking cyclones, in a similar way that AC eddies increase the persistence of the anticyclonic part of blocks.

4.8 Supplementary Material

4.8.1 Block Persistence Distribution for MAM and SON

Histograms showing the block persistence distribution for MAM and SON in both the ATL and PAC regions is shown in Fig. 4.8. The distributions are broadly similar to those found in DJF for the respective regions, with similar Q1, Q2, and Q3 values.

4.8.2 Number of AC Eddies Contributing to MAM and SON Blocks

The relationship between block area, persistence, and number of contributing AC eddies for MAM and SON for both the ATL and PAC domains is shown in Fig. 4.9. In both domains in both seasons here, the general patterns between the three variables is the same as those found in DJF. Pearson correlation coefficients are as

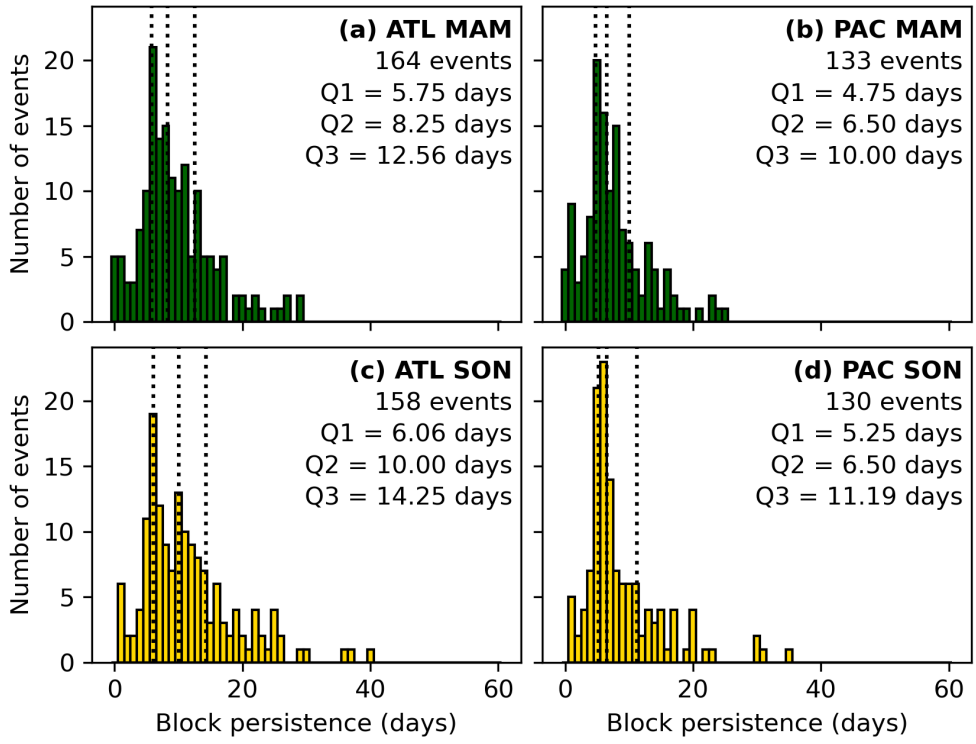

Figure 4.8: As in Fig. 4.4, but for MAM (a, c) and SON (b, d).

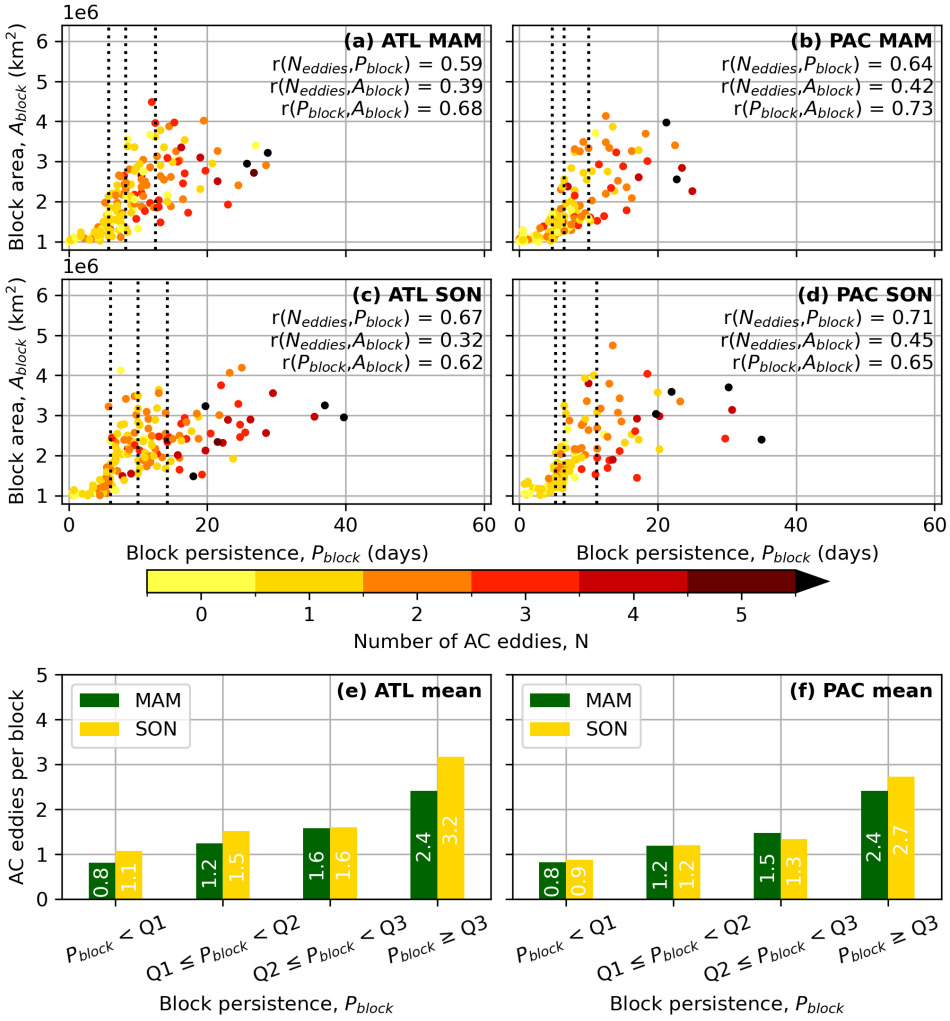

Figure 4.9: As Fig. 4.5, but for MAM (a, c), SON (b, d), and ATL and PAC means (e, f).

high they are in DJF for these seasons between block persistence and the number of AC eddies (0.59–0.71), block persistence and area (0.62–0.73), and number of AC eddies and block area (0.32–0.45).

4.8.3 AC Eddy Strength and Speed for Blocks in MAM and SON

The mean AC eddy intensity, zonal and meridional speeds for MAM and SON for blocks of all lengths are shown by the black lines in Figs. 4.10, 4.11. The eddies exhibit the same qualitative characteristics as those in DJF and JJA, but

with intermediate values. Both speed and intensity for MAM and SON are also very similar to each other.

4.8.4 AC Eddy Strength and Speed for Blocks of Different Lengths in MAM and SON

AC eddy speed and strength for blocks of different lengths for MAM and SON is shown in Figs. 4.10 and 4.11. Generally, like in JJA and DJF, the strength and speed of the eddy is independent of the persistence of the block it contributes to. However, MAM PAC eddies appear to also show some variation in their strength according to how long the block is, but the standard errors are large and sometimes overlapping.

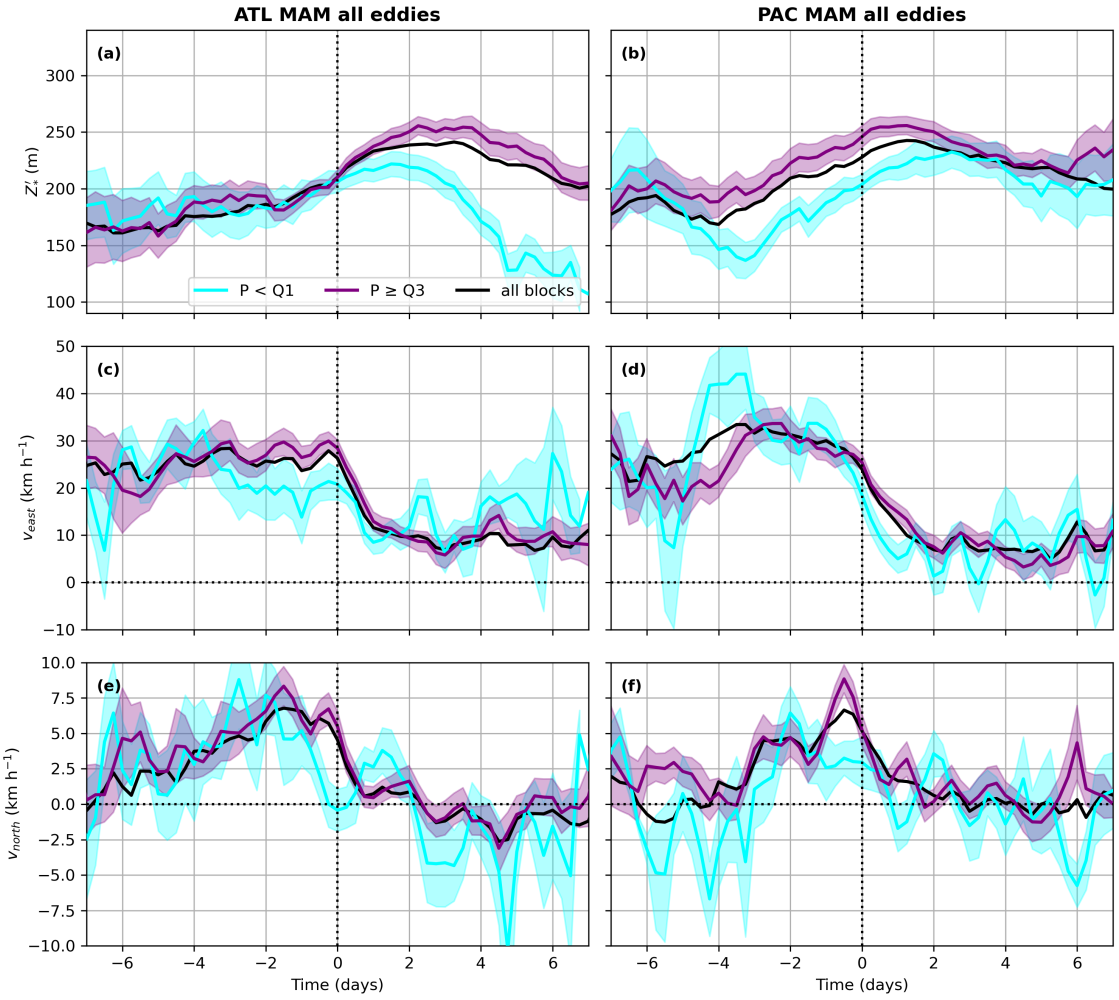

Figure 4.10: As in Fig. 4.6, but for MAM.

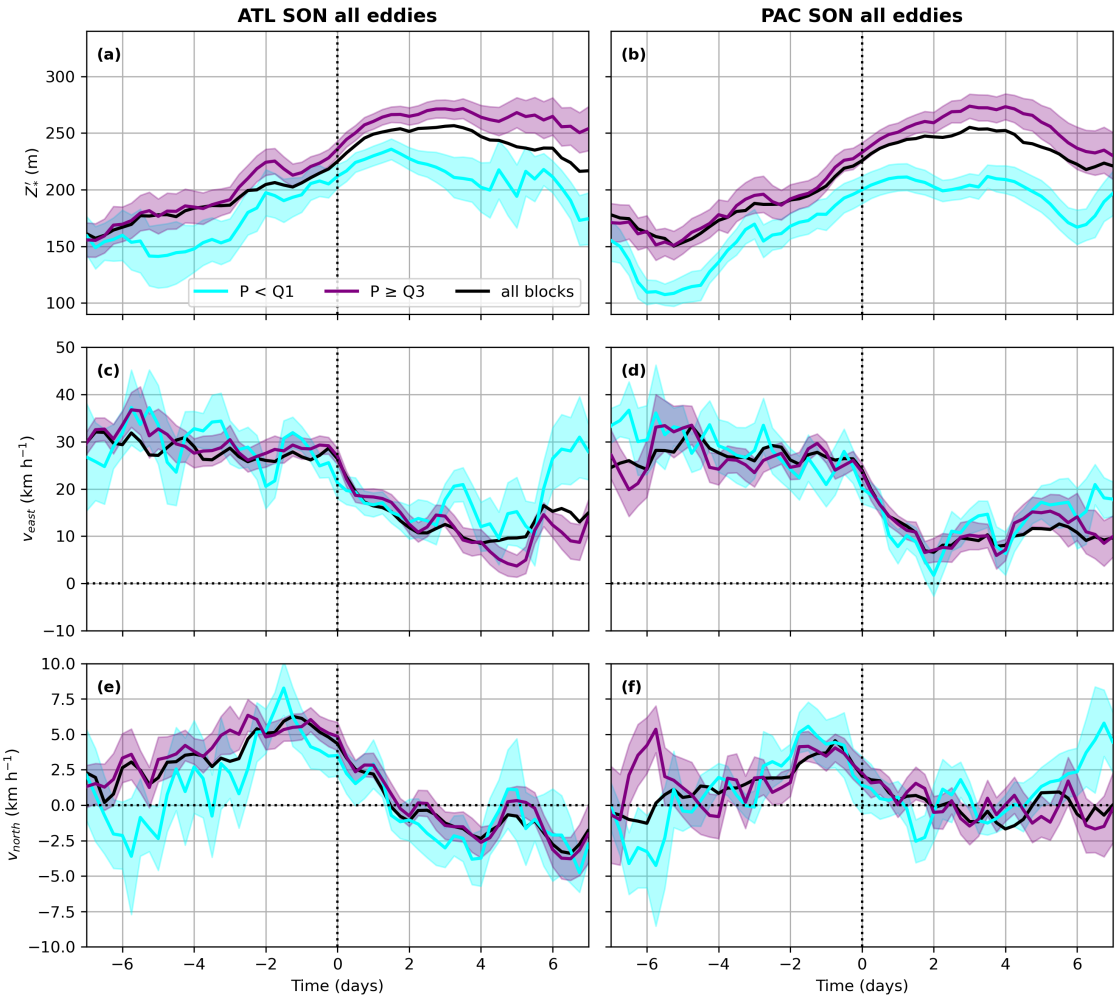

Figure 4.11: As in Fig. 4.6, but for SON.

Chapter 5

Dynamics of Blocks with Different Numbers of AC Eddies

5.1 Introduction

In the previous chapter, it was shown that AC eddies have a strong relationship with the persistence of the blocks they interact with (see also Suitters et al. (2023)). The number of AC eddies is an important factor which correlates well with the persistence of a block, but there is considerable case-to-case variation in the number of AC eddies and block persistence (i.e. other processes contribute towards the persistence of a block). The analysis in Sect. 4 did not consider the effect of diabatic processes on the dynamics of blocks, but many recent studies have highlighted the importance of moist dynamics for blocking, particularly (but not exclusively) during the onset phase (e.g. Pfahl et al., 2015; Steinfeld and Pfahl, 2019). Therefore, it is hypothesised that for blocks of similar persistence, but with differing amounts of contributing AC eddies, the relative importance of dry and moist dynamics is also different. In particular, it is suggested that in blocks with fewer eddies, diabatic processes would be more influential in affecting the PV in the block than in cases with more eddies, in order for the block to last for a similar amount of time. On the other hand, for a block with many AC eddy interactions, it might not be necessary for diabatic dynamics to be as strong for the block to persist.

The above hypothesis is tested in this chapter, through the analysis of three case studies in the ATL sector. Therefore, it is required that cases with a similar

persistence but a different number of AC eddies are examined, compared and contrasted. The case studies chosen for analysis are summarised in Table 5.1: they each have a persistence of 8.5–11.75 days, but vary in the number of AC eddy interactions (0, 1, or 2). The February 2019 block coincided with unseasonably warm weather in the UK and other parts of Western Europe (Sect. 5.3.1), and therefore it is interesting to analyse the dynamics of this event. The other two cases were therefore chosen to have a similar duration, but a different number of AC eddy interactions. Due to the limitations of computing time, and model versions (see Sect. 5.2.6), the choice of blocks to examine was severely limited, which led to the choice of the March 2021 and August 2021 cases. Analysis of the case studies will focus on two aspects:

1. How, and when, PV fluxes converge or diverge in the block, and how AC eddies contribute towards this, and
2. Which diabatic processes promote or discourage blocking, and when these occur.

Then, these findings will be put into the context of the PV budget of each block to examine the relative importance of each process at different blocking stages and how they alter the PV within the block. Item (1) above will be achieved by calculating the PV flux convergence in the block using ERA5 data and a region around the tracked AC eddy centres, and attributing PV flux convergences within the block to either eddy or non-eddy sources. Item (2) will be studied through the analysis of diabatic tracers from forecasts simulated by the MetUM, with a focus on how different processes modify the mid- and upper-tropospheric PV within a block. More detail on the methods is given in Sect. 5.2. For the purposes of this analysis, the assumption is made that the contribution to blocks via AC eddies and diabatic processes are independent and separate from each other. The validity of this assumption is discussed in further detail in Sect. 5.7.

Case Study	Onset	Decay	P_{block} (days)	N_{eddies}	$N_{internal}$	$N_{spawned}$
Feb 2019	20/02/19 06 UTC	01/03/19 18 UTC	9.50	2	1	0
Mar 2021	14/03/21 12 UTC	23/03/21 00 UTC	8.50	1	1	1
Aug 2021	22/08/21 18 UTC	03/09/21 12 UTC	11.75	0	0	3

Table 5.1: Summary of the three case studies that are analysed in this chapter, including their persistence (P_{block}), number of "through" or "absorbed" AC eddies (N_{eddies}), number of "internal" tracks ($N_{internal}$), and number of "spawned" AC eddies ($N_{spawned}$).

5.2 Methods

5.2.1 Block Definitions

To be able to analyse the various dynamical processes occurring inside the blocks in this chapter, they must be suitably defined. To do this, the same $Z*'$ blocking index is used as in the previous Chapter, with a 100 m threshold and a 5-day persistence criterion. This provides the blocked grid points every 6 hours in each of the three blocking case studies, and thus the processes that modify PV are only calculated within this blocked area at every time step.

5.2.2 q'_* Definition

A variable that responds more readily than the Z500 used in the previous chapter is sought for identifying the dynamical processes acting throughout the three case studies. PV is a quantity that is often used when examining blocking dynamics, and blocks can be considered to be regions of anomalously low (anticyclonic) PV in the midlatitudes (e.g. Woollings et al., 2018). Frictional and diabatic processes can locally modify the PV structure of a block (either encouraging or discouraging blocking), and attributions from different dynamical processes can be obtained, such as quasi-barotropic and baroclinic interactions, divergence, and advection (e.g. Hauser et al., 2022). Therefore, PV is a more appropriate measure to use when studying the dynamics of blocking events, and thus the PV anomaly

variable q'_* is defined here, which is analogous to Z'_* used in the previous chapter:

$$q'_*(\lambda, \phi, \theta, t) = q_*(\lambda, \phi, \theta, t) - \overline{q_*}(\lambda, \phi, \theta, t) \tag{5.1}$$

PV (q) on an appropriate isentropic surface (θ) is used in place of Z500. Here, q_* is the PV anomaly from the zonal mean, and $\overline{q_*}$ is the climatological monthly anomaly from the zonal mean. PV on an isentropic surface has been chosen for analysis because the only cross-isentropic vertical motion in isentropic coordinates results from diabatic processes, which are examined in further detail in this chapter. If PV were to be analysed between pressure surfaces (e.g. 500 – 150 hPa like in Hauser et al. (2022)), vertical fluxes of PV would need to be considered, which are not explicitly calculated in the work that follows. Since the PV signature of blocking is most apparent in the upper troposphere, isentropic surfaces close to the tropopause are chosen to calculate q'_* on. For the February 2019 and March 2021 case studies, the $\theta = 320$ K surface is suitable, but the higher temperatures, and therefore deeper troposphere, in summer mean that 330 K is chosen for the August 2021 block.

The suitability of preferring PV over Z500 for the analysis in this chapter is briefly discussed here. One would expect regions of high geopotential height to align with areas of low PV, through the principle of invertibility of PV (Hoskins et al., 1985). By extension, it would therefore be expected that anticyclonic (i.e. positive) Z500 anomalies, Z'_*, would also coincide with anticyclonic (i.e. negative) anomalies in PV, q'_*. Since the PV field is less smooth than the Z500 field with much more smaller-scale detail, a comparison of the time-mean components in Eq. 5.1 is sought to assess the need of an alternative blocking detection method using PV. Thus, the monthly climatological deviations from the zonal means, $\overline{Z_*}$ and $\overline{q_*}$, are shown in Fig. 5.1 for February, March, August and September (the four months of the case studies). The climatological $\overline{Z_*}$ pattern has already been analysed in Sect. 3.2.2, so the discussion here will focus on the $\overline{q_*}$ field and comparisons between it and $\overline{Z_*}$. Similar to $\overline{Z_*}$, the $\overline{q_*}$ pattern is higher in magnitude in February and March (FM) than in August and September (AS). In FM, the strongest anticyclonic regions in both fields are located over the eastern North Atlantic to Western Europe (-1.5 to -1.8 pvu), with a less strong anticyclonic area

over the eastern North Pacific to western North America. The deepest climatological trough (about +1.8 pvu in February) in FM is located over east Asia and the western North Pacific, and a weaker cyclonic region is located over eastern North America. The climatological PV anomaly maxima/minima are shifted slightly to the west of the Z500 anomaly minima/maxima throughout the hemisphere. Assuming a perfect correlation between Z500 and PV through invertibility (though this relationship is examined more later), this slight offset can be explained through the typical westward tilt of mid-latitude weather systems with height, and the fact that the 500 hPa surface is typically lower than the 320 K surface. The small $\overline{Z_*}$ maximum over central Eurasia at 80°E is the only feature that does not appear as a minimum in $\overline{q_*}$.

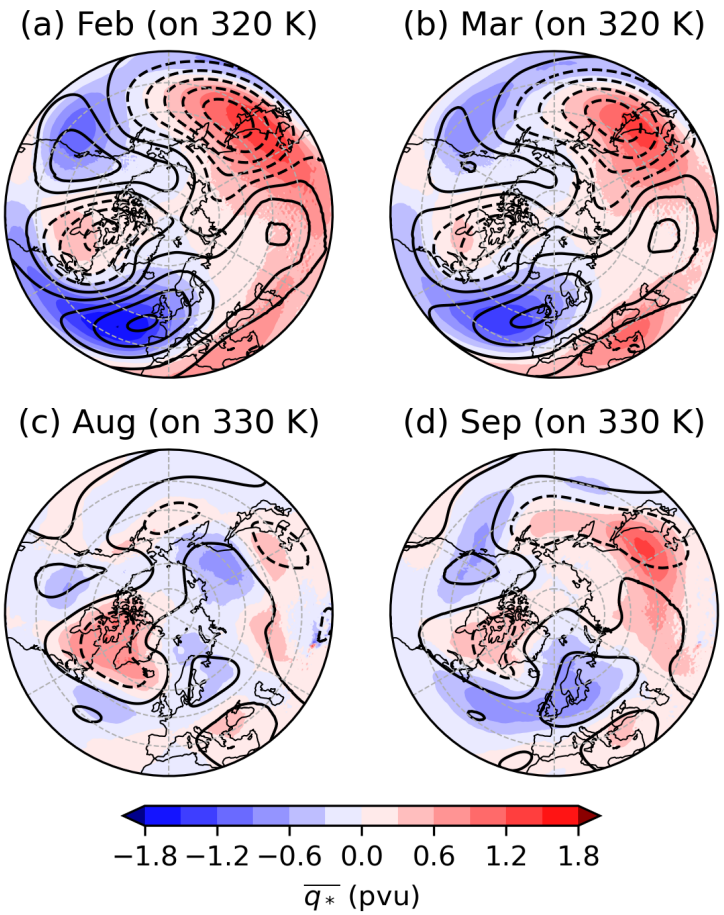

Figure 5.1: $\overline{q_*}$ on the 320 K surface (a, b), and 330 K surface (c, d) for the four months where data are needed for the three blocking case studies (shading). The corresponding $\overline{Z_*}$ contours for the same months are also shown (black, interval of 50 m, negatives dashed).

In AS the PV pattern is also comparable to the Z500 pattern. There is a weak (minimum of -0.9 pvu) anticyclonic $\overline{q_*}$ signature over much of North America, the North Atlantic, and mid-high latitude Eurasia in August. A similarly weak (+0.9 pvu) cyclonic region exists over Greenland and at around 40-50°N over eastern China. By September, the broad Eurasian anticyclonic region recedes westwards as the Chinese cyclonic area expands west in its place, and the magnitudes of all fields becomes a little larger (much more widely $\pm$0.9 pvu).

The overlap between the $\overline{q_*}$ and $\overline{Z_*}$ fields shown in Fig. 5.1 suggests that anticyclonic regions of q'_* could align with anticyclonic regions of Z'_*. Therefore, it is possible to consider the blocks (as defined using the Z500-derived method) from a PV perspective without introducing a blocking detection method based on PV. This PV thinking aligns with many other studies that examined blocking dynamics (e.g Yamazaki and Itoh, 2013a; Drouard et al., 2021; Hauser et al., 2022) and therefore the results obtained by using this q'_* metric will be more comparable with existing work.

5.2.3 Defining q'_* AC and Spawned Eddies

Since it is assumed that negative q'_* regions are aligned with positive Z'_* areas, it is also assumed that the Z500 AC and spawned eddies are also eddies in PV. However, in the previous chapter, only the track centres were considered to be the eddies, but for this analysis a more two-dimensional approach is required to examine the effect of AC eddies on the blocking dynamics, since their field of influence extends much further than just at their tracked centre.

Therefore, the q'_* AC and spawned eddies are defined to be the area within a certain contour around the tracked Z'_* centre. A threshold was chosen such that any grid point where the Z'_* field is over 70% of the strength at the tracked centre is defined as the AC or spawned eddy. This leads to the eddies being generally slightly smaller than the blocks they contribute to, however this number was chosen arbitrarily. Varying the threshold to a higher percentage does not change the conclusions drawn in this study, so 70% was kept as the threshold.

5.2.4 PV Equation

An equation describing the evolution of PV is sought which includes a contribution from the anomalies identified in Sect. 4. PV can only be created or destroyed by sources or sinks of PV (S_q), which are diabatic or frictional processes:

$$\frac{\mathrm{D}q}{\mathrm{D}t} = S_q \tag{5.2}$$

The Lagrangian rate of change can be decomposed into a contribution from a local (Eulerian) rate of change, and the advection of PV into/out of the area, so Eq. 5.2 becomes:

$$\frac{\mathrm{D}q}{\mathrm{D}t} = \frac{\partial q}{\partial t} + \mathbf{u} \cdot \nabla q = S_q \tag{5.3}$$

where $\nabla = (\frac{\partial}{\partial x}, \frac{\partial}{\partial y}, \frac{\partial}{\partial z})$ is the 3D gradient operator.

It is also known that the atmosphere must satisfy the continuity equation:

$$\frac{\partial \rho}{\partial t} + \nabla \cdot (\rho \mathbf{u}) = 0 \tag{5.4}$$

Multiplying all terms in Eq. 5.3 by ρ we achieve the following:

$$\rho \frac{Dq}{Dt} = \rho \frac{\partial q}{\partial t} + \rho \mathbf{u} \cdot \nabla q = \rho S_q \tag{5.5}$$

Using the product rule for differentiation, the middle equality in Eq. 5.5 can be expressed as:

$$\rho \frac{\partial q}{\partial t} + \rho \mathbf{u} \cdot \nabla q = \frac{\partial (\rho q)}{\partial t} - q \frac{\partial \rho}{\partial t} + \rho \mathbf{u} \cdot \nabla q \tag{5.6}$$

and therefore Eqs. 5.4 and 5.6 can be used to derive the following from Eq. 5.5:

$$\frac{\partial (\rho q)}{\partial t} + q \nabla \cdot (\rho \mathbf{u}) + \rho \mathbf{u} \cdot \nabla q = \rho S_q \tag{5.7}$$

Finally, another use of the product rule for differentiation leads to the ability to write Eq. 5.7 in terms of the divergence of a PV flux:

$$\frac{\partial (\rho q)}{\partial t} + \nabla \cdot (\rho q \mathbf{u}) = \rho S_q \tag{5.8}$$

At this stage, the Cartesian coordinates in Eq. 5.8 are replaced by an isen-

tropic coordinate system, following Haynes and McIntyre (1987). Defining the isentropic gradient operator as $\nabla_\theta = (\frac{\partial}{\partial x_\theta}, \frac{\partial}{\partial y_\theta}, \frac{\partial}{\partial \theta})$, the wind vector along an isentropic surface as $\mathbf{u}_\theta = (u_\theta, v_\theta, \dot{\theta})$, and replacing ρ with an equivalent "pseudo-density" for the isentropic coordinate system ($\sigma = -\frac{1}{g}\frac{\partial p}{\partial \theta}$), the isentropic form of Eq. 5.8 is:

$$\frac{\partial(\sigma q)}{\partial t} = -\nabla_\theta \cdot (\sigma q \mathbf{u}_\theta) + \sigma S_q \tag{5.9}$$

Decomposing the PV on the right hand side into a zonal mean $[q]$, and anomaly component, q_*, and using the definition of q'_* from Eq. 5.1, an equation explaining the rate of change of PV, in terms of deviations from the zonal mean is therefore:

$$\frac{\partial(\sigma q)}{\partial t} = -\nabla_\theta \cdot (\sigma [q] \mathbf{u}_\theta) - \nabla_\theta \cdot (\sigma q'_* \mathbf{u}_\theta) - \nabla_\theta \cdot (\sigma \overline{q_*} \mathbf{u}_\theta) + \sigma S_q \tag{5.10}$$

Finally, the approximation of an incompressible atmosphere (constant σ) is applied. Experiments showed that this step did not qualitatively change the results presented in this work, and is therefore pursued in the interests of computing speed. Therefore, the equation that is evaluated in the work that follows is:

$$\frac{\partial q}{\partial t} = \underbrace{-\nabla_\theta \cdot ([q] \mathbf{u}_\theta) - \nabla_\theta \cdot (q'_* \mathbf{u}_\theta) - \nabla_\theta \cdot (\overline{q_*} \mathbf{u}_\theta)}_{\text{(A)}} + \underbrace{S_q}_{\text{(B)}} \tag{5.11}$$

A quantitative examination of Eq. 5.11 for each of the three case studies is undertaken to establish the PV budget in each block, and how the various terms contribute to the onset, maintenance and decay of the blocks. The effect of the flux convergence terms (A) is determined by analysing the cumulative effect of PV flux convergences within the block, and how AC or spawned eddies also impact this measure. The three terms analysed are therefore the flux convergence of zonal mean PV flux ($[q]\mathbf{u}_\theta$), the convergence of anomalous PV flux ($q'_*\mathbf{u}_\theta$), and the convergence of "background" PV flux ($\overline{q_*}\mathbf{u}_\theta$) by the full wind field. These three terms are only assessing the adiabatic changes to PV within the block. Secondly, the source term (B), whose contribution comes from diabatic and frictional processes, will be studied through the use of diabatic tracers in the MetUM (explained in Sect. 5.2.6).

5.2.5 Dry Dynamics Data Source

The adiabatic terms (A) are determined from ERA5 reanalysis data. PV and horizontal winds from ERA5 on the appropriate upper-tropospheric isentropic surface (as discussed in Sect. 5.2.2) are used in the calculations of the PV flux divergences. For consistency with the methodology from the previous chapter, data are on an F128 grid with a temporal resolution of 6 hours for the duration of each block. The "block" in each case study, in terms of its boundary and its duration, and the associated Z'_* tracks, are defined using the method from Sect. 3.

5.2.6 Model Setup

Diabatic Tracers

Quantifying diabatic heating and the corresponding changes to PV in studies such as this is often achieved through trajectory analysis. This is most commonly done using a tool called LAGRANTO (Sprenger and Wernli, 2015), which is an offline piece of software that uses modelled winds to calculate air parcel trajectories and determine their PV and potential temperature modifications along their paths. LAGRANTO was used to ascertain the prominence and source regions of diabatically-heated air in blocking (Pfahl et al., 2015; Steinfeld and Pfahl, 2019; Hauser et al., 2022), however trajectory-based analysis tools such as this are not used in this work because they unable to directly determine the reason for diabatic PV modification (e.g. friction, convection, etc.). Since this is one of the subquestions in the examination of RQ2, another method must be used to attribute the diabatic PV modification for these case study blocks.

The MetUM has a set of inline tools called diabatic tracers which can be used to diagnose and account for changes to PV or potential temperature due to various parameterisations in the model. They were developed at the University of Reading, and were implemented into the MetUM through collaboration with Claudio Sanchez at the UK Met Office. This section describes their derivation, which parameterisation schemes modify PV or potential temperature, and how these are useful to better understand the processes resulting in blocking.

In the following, the derivation from Stoelinga (1996), Gray (2006), and Saf-

fin et al. (2016) is summarised to introduce the origin of diabatic tracers for PV, while an equivalent process can be followed for potential temperature (Martínez-Alvarado and Plant, 2014).

PV can be expressed as a combination of relative ($\nabla \times \mathbf{u}$) and planetary ($2\mathbf{\Omega}$) vorticity, and the static stability of the atmosphere ($\nabla\theta$):

$$q = \frac{1}{\rho}(\nabla \times \mathbf{u} + 2\mathbf{\Omega}) \cdot \nabla\theta \tag{5.12}$$

Its Lagrangian rate of change has been shown by Ertel (1942) to be:

$$\frac{\mathrm{D}q}{\mathrm{D}t} = \frac{1}{\rho}((\nabla \times \mathbf{u} + 2\mathbf{\Omega}) \cdot \nabla\dot{\theta} + \nabla\theta \cdot \nabla \times \mathbf{F}) \tag{5.13}$$

where $\mathbf{F}$ is friction. We seek the evolution of PV through a forecast of length T, and to see where PV is diabatically generated or destroyed in space and time throughout this forecast. Therefore, Eq. 5.13 is integrated along forecasted air parcel trajectories, i.e.:

$$\int_{t=0}^{t=T} \frac{\mathrm{D}q}{\mathrm{D}t}\,\mathrm{d}t \; = q - q_0 = \int_{t=0}^{t=T} S_q\,\mathrm{d}t \tag{5.14}$$

where $q_0 = q(0)$ is the conserved PV and S is the right hand side of Eq. 5.13. The term containing S_q can be discretised by considering the contribution to S_q by each physical process i, such that $S_q = \sum S_{q,i}$. When this sum is integrated, a collection of PV tracers is obtained, $\sum q_i$, which each result in a change to the PV, Δq_i (defined below), such that Eq. 5.14 becomes:

$$q = q_0 + \sum q_i = q_0 + \Delta q_i + \varepsilon_q \tag{5.15}$$

The error term, ε_q, arises due to the missing PV that is unresolved in the model after the advection process. In the MetUM, each q_i is the result of various parameterisations, or numerical corrections, within the model. The PV tracers considered to be important in this study are highlighted in Table 5.2. Each tracer is advected by the forecasted flow, and with the exception of q_0, accumulate incrementally as the forecast progresses. Each of the PV tracers highlighted in Table 5.2 has an equivalent potential temperature tracer, θ_i.

Symbol	Name	Description
q_0	Conserved PV tracer	PV component that is not modified by parameterisations in the model. It is only advected by the flow.
Δq_{cloud}	PV tracers due to cloud processes	A combination of changes to PV due to: • Large-scale precipitation parameterisation (cloud microphysics) (Wilson and Ballard, 1999). • Cloud pressure rebalancing: The PC2 cloud scheme in the MetUM (Wilson et al., 2008) can attribute changes to the temperature or condensate of an air parcel due to pressure changes from large-scale diabatic ascent. This will also result in modifications to the PV of the air parcel. • PC2 checks: The PC2 scheme (Wilson et al., 2008) also checks that moist variables are consistent with each other and have a realistic value after every time step. If there are inconsistencies, the moisture is reset, which also produces changes to temperature and therefore PV.
Δq_{conv}	Convection PV tracer	Changes to PV in the model due to parameterisation of convection (Gregory and Rowntree, 1990). This is a sum of two components of PV generation/destruction output by the MetUM, from diabatic heating ($\Delta q_{conv,heat}$) and frictional ($\Delta q_{conv,fric}$) processes. The equivalent θ-tracer ($\Delta\theta_{conv}$) is not partitioned by these constituent parts.
Δq_{BL}	Boundary layer PV tracer	Changes to PV according to the boundary layer scheme (Lock et al., 2000). Again, this is the sum of diabatic heating ($\Delta q_{BL,heat}$) and frictional ($\Delta q_{BL,fric}$) parts.
Δq_{rad}	Radiation PV tracer	Modifications to PV due to the parameterisation of longwave (LW) and shortwave (SW) radiation (Edwards and Slingo, 1996). LW radiation is usually the dominant process.
Δq_{GWD}	Gravity wave drag PV tracer	PV modifications due to parameterisation of gravity wave drag (Van Niekerk and Vosper, 2021).
Δq	Total PV change	Sum of all non-conserved PV tracers, i.e. $\Delta q = \Delta q_{cloud} + \Delta q_{conv} + \Delta q_{BL} + \Delta q_{rad} + \Delta q_{GWD}$
Δq_I	PV inconsistency tracer	The non-conservation of PV due to the dynamical core of the MetUM. Specifically, it is the difference between the advected PV and the calculated PV, once advection has been completed in the model (numerical diffusion). Here, it is considered to be the dominant measure of the error of the PV tracers (Saffin et al., 2016).

Table 5.2: Description of the PV tracers considered in this work.

In this setup of the MetUM, diabatic tracer accumulations are output every six hours, with each value at a particular lead time $t = T$ showing how PV or θ has been modified from the start of the forecast ($t = 0$) until the valid time $t = T$. Therefore, if a physical process i were to have a constant effect on the evolution of Δq_i, the value of this tracer would increase steadily as lead time increases. However, this also implies that the PV inconsistency (approximately equal to the PV tracer error, as noted in Table 5.2) also increases with lead time. Indeed, Saffin et al. (2017) found that the magnitude of the PV inconsistency increases with lead time in the 2 km below the tropopause within ridges (their Fig. 5a). Therefore, analysis of the PV tracers at longer lead times becomes less reliable as the model dynamical core is less able to close the PV budget, compared to at shorter lead times.

PC2 Cloud Scheme Changes

The PC2 cloud scheme resolves the large-scale clouds in the MetUM (Wilson et al., 2008). As shown in Table 5.2, changes to PV can occur according to the PC2 scheme (Δq_{cloud}), and sometimes corrections need to be applied in order to balance the PV budget in the model (Δq_{PC2}). After the simulations for the case studies in this Chapter were run, the author was alerted to a change in the MetUM that changes the way in which Δq_{PC2} is calculated, which also has an effect on the parameterisation of SW radiation, Δq_{SW}. A single forecast was re-run with the updated PC2 setting, and changes to Δq_{PC2} and Δq_{SW} were observed, compared to the original simulations. For completeness, this comparison is shown in Sect. A.1. However, the majority of these changes occurred within the boundary layer, with a somewhat smaller change found in the mid-upper troposphere. Thus, since blocks are identified in this study only by their mid-upper tropospheric characteristics, it was decided that all simulations did not require re-running with the updated PC2 scheme correction in the interests of computing time.

Forecast Runs

For this work, the MetUM is run in atmosphere-only mode at N640 resolution. This corresponds to a horizontal grid-spacing of 0.28125° longitude and 0.1875°

latitude, which is approximately 20 km in the mid-latitudes. Sensitivity tests were carried out testing additional model resolutions of N320 and N1280, and it was found that N640 produced the best compromise between spatial detail in the diabatic tracer fields, and computing time. A forecast of 8 days is initialised every 24 hours at 00 UTC for days before, during, and after each blocking case study.

5.2.7 PV Budget

In a perfect forecast, accounting for slight differences between the two models, the PV in the ERA5 reanalysis (q_{ERA}) should be approximately equal to the PV in the MetUM (q_{UM}):

$$q_{ERA} \approx q_{UM} \tag{5.16}$$

So, using the definition of q'_* (Eq. 5.1), the total PV can be written as:

$$q = q'_* + [q] + \overline{q_*} \tag{5.17}$$

And also using the right hand side of Eq. 5.15, we can deduce that:

$$q'_* + [q] + \overline{q_*} \approx q_0 + \Delta q + \varepsilon_q \tag{5.18}$$

Therefore, it is possible to quantitatively compare the contribution of each term towards the PV budget of each block. In particular, Eq. 5.18 can be used to determine the relative importance of diabatic effects compared to those of anomalous PV, for example, in each block. Note that a background PV climatology, $\overline{q_*}$, was unobtainable from the MetUM, so the ERA5 background PV was used in the calculation of q'_* for the MetUM.

5.3 February 2019 (2 AC Eddies)

5.3.1 Event Synopsis

The evolution of the February 2019 blocking event, in terms of both Z'_* and q'_*, along with the tracked Z'_* centres, at various stages throughout the event, is

shown in Fig. 5.2. At block onset (20 February 06 UTC, Fig. 5.2a), there is no AC eddy present, and instead the event starts as a ridge that builds to the east of a deep cyclone, with a small internal track highlighting slight eastward movement of the nascent blocking anticyclone. This ridge is evident as both a region of positive Z'_* and negative q'_*. The first AC eddy centre enters the block 18 hours later (Fig. 5.2b), which appears as a high-amplitude q'_* anomaly in excess of -4 pvu just downstream of the cyclone to the west. There is remarkable overlap between the tracked AC eddy centre (and therefore Z'_* maximum) with the q'_* minimum here, which reinforces the concept that the AC eddy centres followed with TRACK can also be used to approximate centres of negative PV anomalies. As these anomalies break anticyclonically, the block grows in size until reaching a steady state (Fig. 5.2c, d). A second, slightly weaker q'_* minimum (and cyclonically-tilted Z'_*

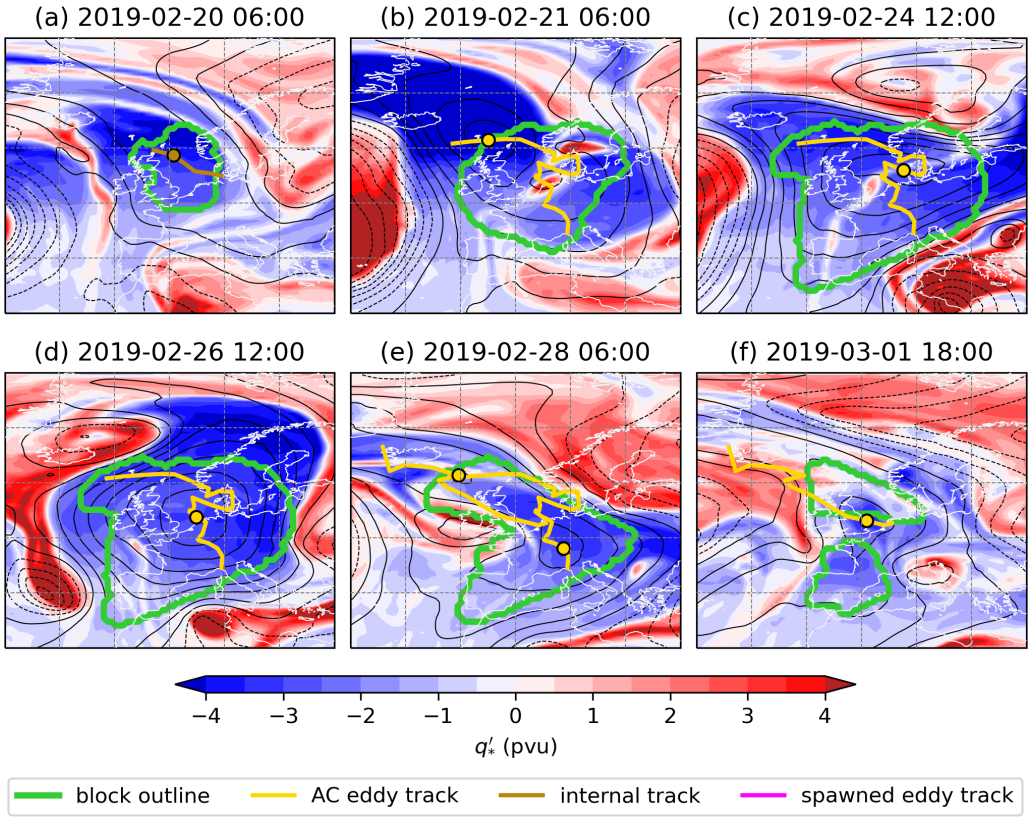

Figure 5.2: Z'_* at 500 hPa (black contours at 50 m intervals, negative dashed), q'_* on 320 K (filled contours), block outline according to the Z'_* blocking index, and Z'_* tracks (AC eddies in yellow, internal tracks in brown, spawned eddies in pink) with dots signifying the centre of this track at the valid time, for various stages in the block: (a) block onset, (b) when the first AC eddy centre enters the block, (c, d) mature block, (e) when the second AC eddy enters the block, and (f) decay.

ridge) circulates anticyclonically around the block from the southwest at these times, and this PV anomaly remains within the block until its decay. By the time the second AC eddy enters the block from the northwest (Fig. 5.2e), the block has already begun its decay phase as it shrinks in size and a small cyclone moves eastwards through the centre of the block. The second AC eddy is much weaker than the first, and is not associated with a distinct q'_* minimum, and as such does not act to lengthen the persistence of the block much further. For the final 6-hour period where ATL sector blocking is met (Fig. 5.2f), the block is in two halves due to being split by the cyclone now centred over Italy, and despite the presence of the second AC eddy, the block event finishes.

Time series summarising how the area (contrary to Sect. 4, this is the area of *instantaneous* blocking, i.e. $Z'_* \geq 100$ m with no persistence applied) and strength of the block, in terms of both mean Z'_* and mean q'_*, are shown in Fig. 5.3. The block area (Fig. 5.3a) and strength as measured using Z'_* (Fig. 5.3b; black line) follow a similar pattern. From 20-23 February, both of these metrics gradually increase as the block grows. After the first AC eddy centre enters the block on 21 February, the block increases in size more rapidly for about 24 h, but there

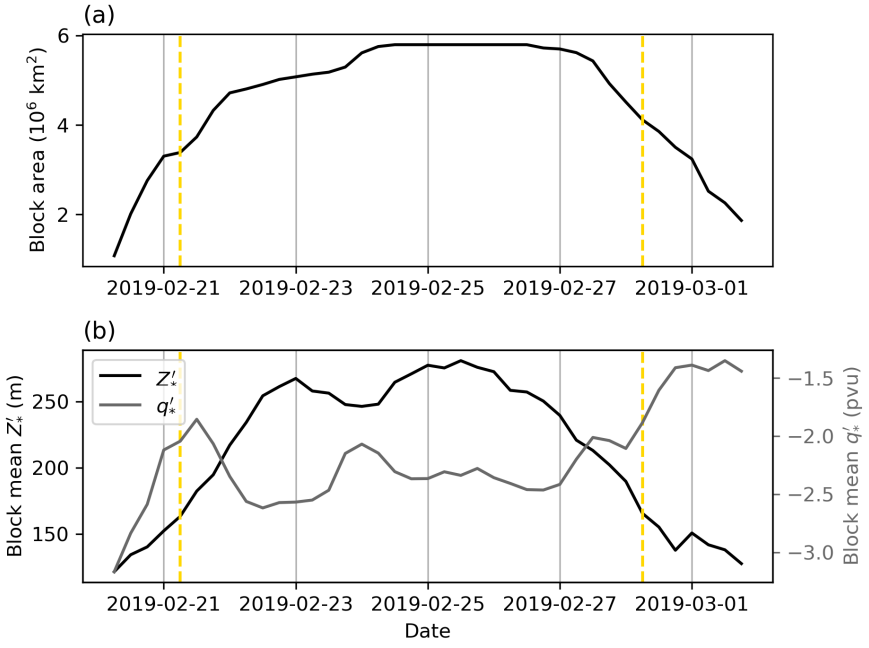

Figure 5.3: Temporal evolution of the block in terms of (a) its area, and (b) its strength, measured in terms of its mean Z'_* (black) and q'_*. Times where AC eddy centres first cross the block boundary are marked as vertical yellow dashed lines.

is no associated increase in mean Z'_*. Then, block area is fairly constant from 23 February, and its mean Z'_* strength remains approximately constant until 26 February. The mean Z'_* begins steadily declining after this time, but the area of the block remains steady until a day later, after which the area of the block also steadily declines. The arrival of the second AC eddy to the block on 28 February does not reverse the shrinking of the block, and only causes a very brief uptick in the Z'_* of the block.

Aside from the early stages of the block, the mean strength of q'_* in the block (Fig. 5.3b; grey line) is as expected, given the behaviour of Z'_* (positive Z500 anomalies coincide with negative PV anomalies). However, on 20-21 February as the block is growing, the mean q'_* increases, contrary to what would be expected of a developing block. This can be explained by the two small, but strongly positive, regions of q'_* within the block contour that separate the two q'_* minima (Fig. 5.2b). The brief increase in mean q'_* on 24 February is also associated with another PV streamer entering the block (Fig. 5.2c).

This block was notable for the exceptional prolonged mild weather it brought to the UK and much of northwestern Europe. In the UK, 20°C was exceeded for the first time in a winter month, with this threshold being breached in stations in the London area and parts of Wales and northwest England. The maximum temperature reached 21.2°C in Kew Gardens on 26 February, which remains the UK's record-highest winter daily maximum temperature, and similar records were also broken in the Channel Islands, France, and the Netherlands (Young and Galvin, 2020).

5.3.2 Dry Dynamics

PV Flux Convergence

The PV flux convergences from all components in (A) in Eq. 5.11, and the total PV flux convergence ($-\nabla_\theta \cdot (q\mathbf{u}_\theta)$) associated with the February 2019 block are presented in Fig. 5.4. Examples showing the anomalous and zonal mean PV fields, and their convergences, for selected periods of the block, are shown in Fig. 5.5. Through Eq. 5.11, a negative PV flux convergence (divergence of PV flux)

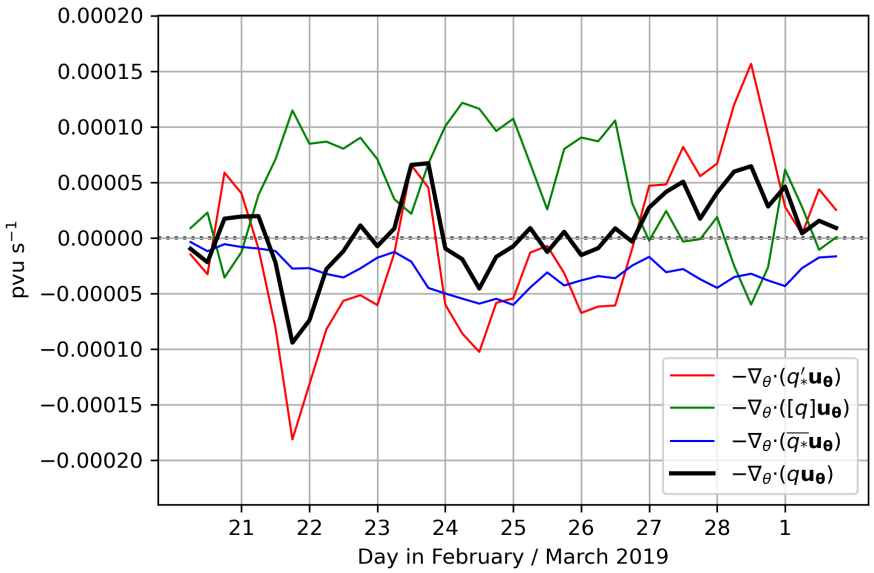

Figure 5.4: Cumulative PV flux convergences within the February 2019 block by the total winds, on the 320 K surface, by the anomalous PV (red), zonal mean PV (green), background PV (blue), and total PV (black).

implies loss of PV and therefore encourages blocking. Though the time series is noisy, important statements can be made from the results. The behaviour of the total PV flux can be split into three parts: (1) predominantly negative PV flux convergence from 20–24 February, aside from two brief maxima; (2) approximately zero net convergence from 24–27 February; and (3) positive PV flux convergence from 27 February until block decay. Therefore, PV flux convergence within the block predominantly acts to promote and maintain the block in Stage 1, there is net-zero effect in Stage 2, and PV flux convergence encourages the decay of the block in Stage 3.

At onset (20 February 06 UTC, Figs. 5.4, 5.5a-d), total PV flux convergence is approximately zero, suggesting that the block did not form as a result of strong PV fluxes. However soon after this on 21 February, total and anomalous PV flux convergence rapidly decrease to its lowest level throughout the entire block (Figs. 5.4, 5.5i-j) and is the result of strong northerly winds in the northeastern corner of the block decelerating within the block's negative q'_* region (this could be seen as a convergence of anomalously negative PV flux). The two brief maxima in total PV flux convergence on 20 and 23 February during the period of general negative PV flux convergence are both caused by the same phenomenon. At these times, a small-scale PV streamer (identified by a local positive q'_* maximum, seen to the

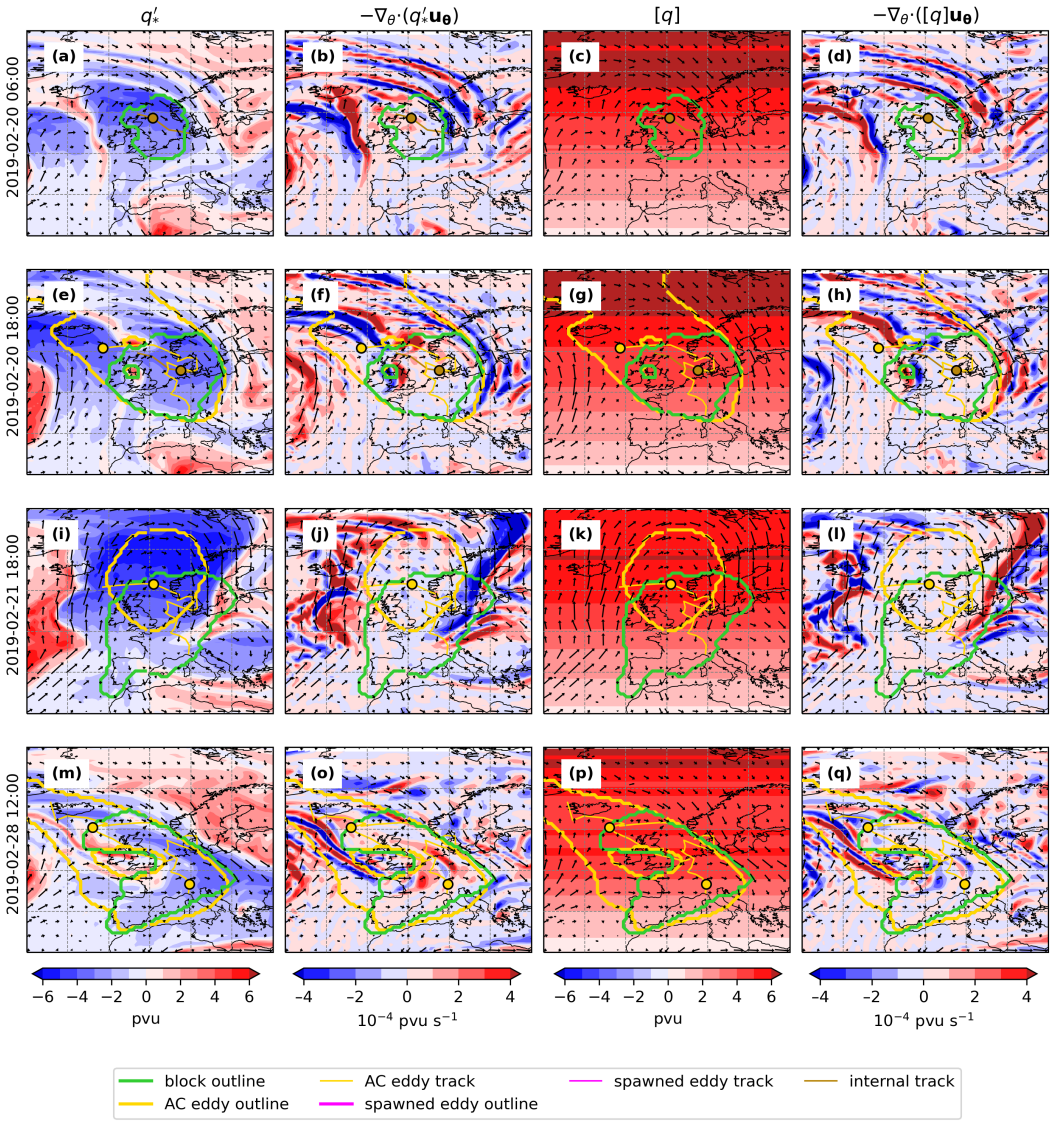

Figure 5.5: Shading: (a, e, j, m) Anomalous PV (q'_*), (b, f, j, o) convergence of anomalous PV, (c, g, k, p) zonal mean PV ($[q]$), and (d, h, l, q) convergence of zonal mean PV, on selected dates in the block: 20-02-2019 06 UTC (a-d), 20-02-2019 18 UTC (e-h), 21-02-2019 18 UTC (i-l), and 28-02-2019 12 UTC (m-q). All values are on the 320 K surface. Also shown are winds on the 320 K surface (black), block outline (green), internal tracks (brown), and AC eddy tracks and contours (yellow).

west of the block in Fig. 5.5a, and inside the block on Fig. 5.5e) enters and mixes with the main negative q'_* anomaly within the block. The momentary increases in PV within the block (seen in Fig. 5.3b) align well with these maxima in PV flux convergence (Figs. 5.4, 5.5f) and so can be seen as the mechanism for which the block momentarily weakens.

In the period from 27 February 00 UTC until the end of the block event, there is net positive PV flux convergence within the block. At this time, the only com-

ponent acting to consistently maintain the block is negative convergence of background PV flux. However, this is not enough to counteract the decay of the block through convergence of anomalous PV flux (Figs. 5.4, 5.5o). This convergence of q'_* is due to the approach of the cyclone that acts to break the block into two halves (see also Fig. 5.2e, f).

Interestingly, the anomalous and zonal mean PV flux convergences are in antiphase with each other throughout. In general, $[q]$ increases as latitude increases, resulting in a positive meridional gradient of zonal mean PV (Fig. 5.5c, g, k, p). Meanwhile, often the block is situated just to the south of the q'_* minimum (Fig. 5.5a, e, f, m), resulting in a negative meridional gradient of anomalous PV. Therefore, the opposing directions of the gradients of these two components mean that their effect on the maintenance of the block are opposite. In general, when the magnitude of anomalous negative PV convergence is larger than zonal mean positive PV flux convergence, blocking is encouraged (Stage 1), when the two are of similar magnitude block growth reduces (Stage 2), and when the magnitude of anomalous PV convergence is larger than that of zonal mean PV, the block decays (Stage 3). Throughout the block, the effect of the background PV flux is to slightly reduce the PV within the block, but to a lesser extent than the other two components (except at decay).

Influence of AC Eddies on PV Flux Convergence

In this section the role of the AC eddies in causing PV to increase or decrease in the block is examined from the perspective of how much of the PV flux convergence overlaps with the position of such eddies. Figure 5.6 shows the relative contribution towards the all-block PV flux convergences from AC eddies, and also highlights the amount of overlap between the block and eddy contours. The first AC eddy contour does not encroach on the block until 18 UTC on 20 February, so for the first 12 hours of the block there is no contribution towards the all-block PV flux divergence from AC eddies. For a brief period, at 18 UTC on 20 February (Fig. 5.5e-h), while the block is still in its infancy and growing in size, 100% of the block is within the AC eddy. After this however, only around 30% of the block is also covered by the AC eddy. This percentage slowly grows

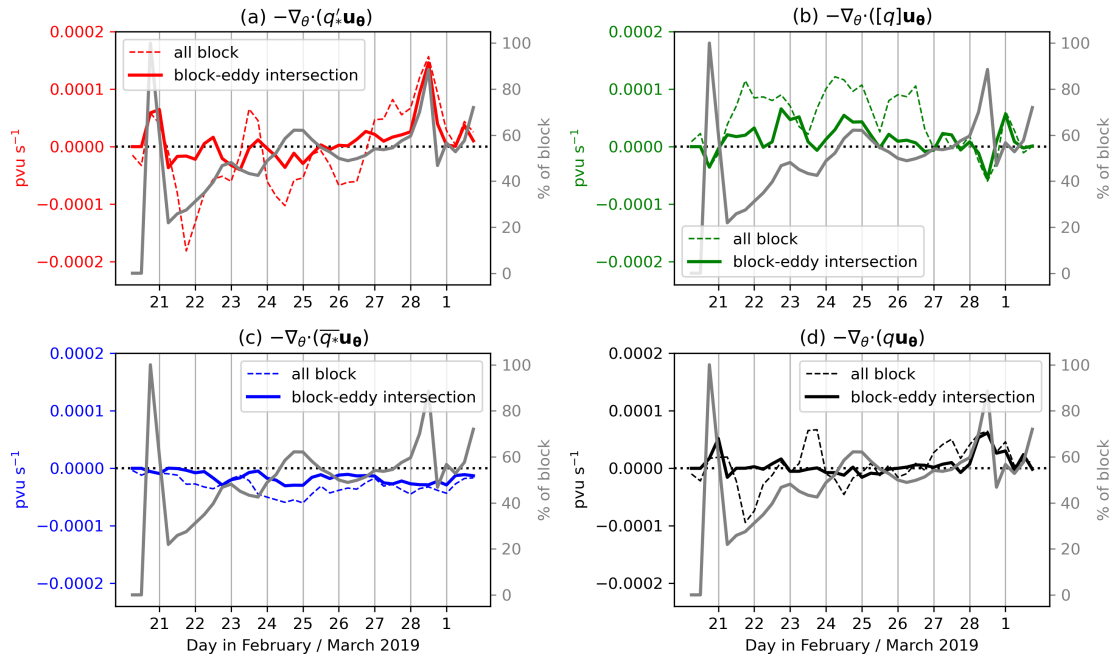

Figure 5.6: Contributions to the area-normalised (a) anomalous, (b) zonal mean, (c) background, and (d) total PV flux convergences, by the portion of the block that intersects with at least one AC eddy contour (solid coloured lines, left axis). Also shown are the curves for the appropriate component for the block as a whole (as in Fig. 5.4; dashed lines, left axis) and the percentage of the total block area that intersects with an eddy (grey lines, right axis).

as the block matures and the AC eddy meanders within the block itself, reaching around 60% by 28 February 00 UTC. Hereafter, a larger proportion of the block is encapsulated by AC eddy contours, due to the arrival of the second AC eddy and the weakening and shrinking of the block.

Since AC eddies can be approximated as regions of large-magnitude negative q'_*, it might be expected that AC eddies are responsible for a large amount of the convergence of anomalous PV inside the block. However, as demonstrated in Fig. 5.6a, for most of the time the AC eddy is in fact only contributing a small proportion of the net q'_* convergence analysed in the block. This is despite the first AC eddy being well within the block interior for a lot of its lifetime. There are two main reasons behind the weak contribution of the first AC eddy towards maintaining this block. Firstly, due to the position of the AC eddy as it enters the block (from the northwest/north), it is often the case that while the circulation within the eddy is weak, it acts to advect negative q'_* out of the block on the western side of the eddy, and advect it back in again on its eastern side. This results in a very

small net loss or gain of PV in the block due to the circulation of the eddy. Secondly, once the eddy is within the interior of the block, the winds within the eddy contour are even weaker which leads to even less convergence of anomalous PV flux. PV flux divergences/convergences are much stronger around the periphery of the block where both winds and PV gradients are stronger, and therefore contribute far more to the net loss or gain of PV in the block. Figures 5.5i-l demonstrate both of these situations clearly.

The same two arguments listed above can also explain the weak contribution towards the all-block convergences of zonal mean, background, and total PV flux (Fig. 5.6b-d). Only when the second AC eddy enters the block, and most of the block is captured by one (or both) AC eddies, are AC eddies influential in driving the gain of PV within the block.

5.3.3 Diabatic Dynamics

PV Inconsistency Analysis

Before analysing the diabatic dynamics in this case study, an appropriate forecast lead time must be chosen, over which the diabatic tracers are allowed to accumulate. Sufficient lead time must be given to allow the tracers to accumulate and be representative of the physical processes that modify them. WCBs are known to be influential in blocking dynamics (e.g. Steinfeld and Pfahl, 2019), which have an ascent rate in the order of 600 hPa over 24–48 hours (Madonna et al., 2014). Therefore, the minimum time over which tracers must be accumulated for the purpose of this study is one day. However, the reliability of the diabatic tracer accumulations generally decreases with lead time (Saffin et al., 2016), so it is important to analyse sufficiently short lead times such that the findings are more likely to be representative of the real atmosphere. The following discussion explains the choice of lead time used to analyse the February 2019 block.

The magnitude of the upper-tropospheric (500-200 hPa) block-mean PV inconsistency and total diabatic PV tracers are shown in Fig. 5.7. In general, $|\Delta q_I|$ increases with forecast lead time. In other words, the difference between the advected and calculated PV in the model within the block is greater at larger lead

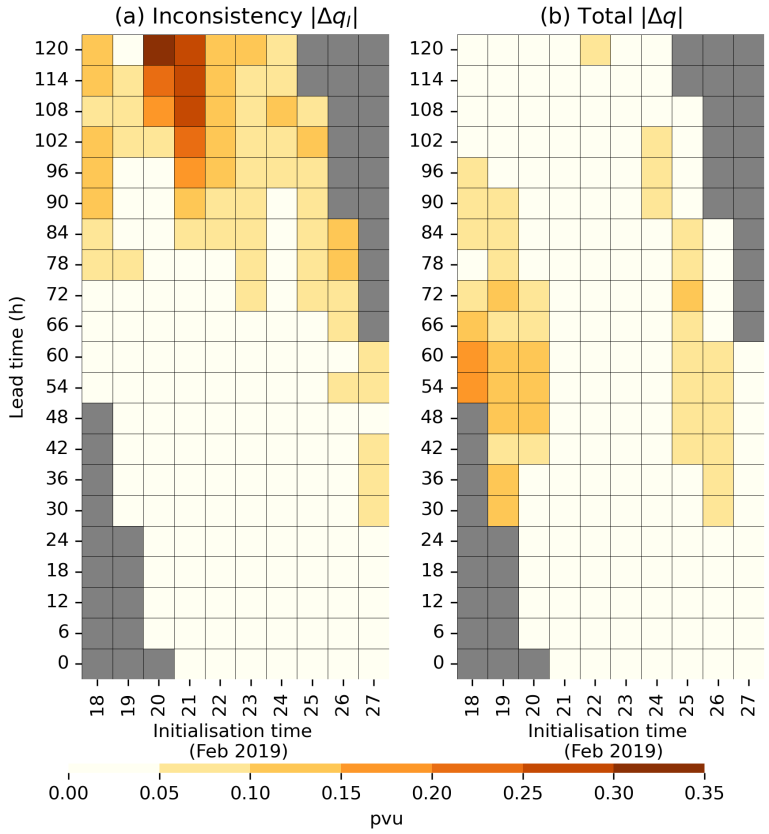

Figure 5.7: Magnitude of the (a) PV inconsistency tracer, Δq_I, and (b) total PV diabatic tracer, Δq, as a function of forecast initialisation and lead times. Each cell is coloured according to the mean value of the appropriate variable between 500-200 hPa inside the block. Forecasts were initialised at 00 UTC on the dates shown on the x-axis. Grey squares indicate times where the forecast valid time is outside of the blocking times.

times. At lead times exceeding approximately 96 hours, the block-mean $|\Delta q_I|$ is greater than the block-mean Δq in all forecasts, but this pattern begins to appear at earlier lead times in certain forecasts (e.g. T+72 h for forecasts initialised on 25, 26 February). This means that the error in the magnitude of diabatically-generated PV is larger than the diabatically-generated PV itself. Therefore, results at longer lead times should be ignored and analysis should be restricted to shorter lead times that still allow for sufficient tracer accumulation. For this reason, all diabatic tracer analysis for the February 2019 block has been done with a lead time of 60 hours. This allows for as much accumulation time as possible before the PV inconsistency becomes similar in size to the total change in PV.

Another secondary result, that will be discussed in more detail in Sect. 5.3.3, is that the total change to PV is more prevalent at the beginning of the block, and its importance diminishes as the block matures and decays (Fig. 5.7b). This

pattern presents itself at all lead times, not just at T+60 h. On the other hand, the magnitude of the PV inconsistency appears to have no relationship to the age of the block.

Total Δq and $\Delta\theta$

First, an overview into the total diabatic tracers are given, in terms of Δq and $\Delta\theta$ at selected times during the block. 60-h accumulations of diabatic tracer are analysed, such that the results presented at the stated valid time originate from forecasts initialised 60 h earlier. Thus, consecutive simulations are used to analyse the diabatic effects, rather than the results from one single initialisation time. Maps of Δq and $\Delta\theta$ at a height of approximately 10 km are shown in Fig. 5.8, and vertical cross-sections at 55°N through the block are presented in Fig. 5.9.

At the time of block onset (Figs. 5.8a, b, 5.9a, b), both diabatic PV loss and latent heating are near their maximum intensities of the blocking period. Though spatially irregular (particularly for Δq), local diabatic loss of PV in the block approaches -1.0 pvu while heating exceeds 20 K (Fig. 5.8a, b). This level of heating within a 60 h period is consistent with air that has entered the block from the outflow of a WCB of an extratropical cyclone (Pfahl et al., 2015), like that to the west of the block. The majority of the air that is inside the mid-upper troposphere of the block at onset undergoes diabatic heating, resulting in loss of PV (Fig. 5.9a, b) and helping to induce an upper-level negative PV anomaly which promotes block development.

Three days later on 23 February (Figs. 5.8c, d, 5.9c, d), diabatic loss of PV and diabatic heating of air parcels arriving in the block have strongly reduced. Much of the mid-upper tropospheric air within the block has had negligible PV modification by diabatic processes in the MetUM. Some parts of the block even contain air that has had its PV increased in the 60 h leading up to this time, except from perhaps in the far east, where diabatic heating is also at its strongest. This behaviour is perhaps not surprising, and agrees with the findings of Steinfeld and Pfahl (2019) that generally, the importance of diabatic heating for blocking dynamics reduces as block lifetime increases. However, these authors also suggest that in some cases, "bursts" of latent heating can occur that further intensify

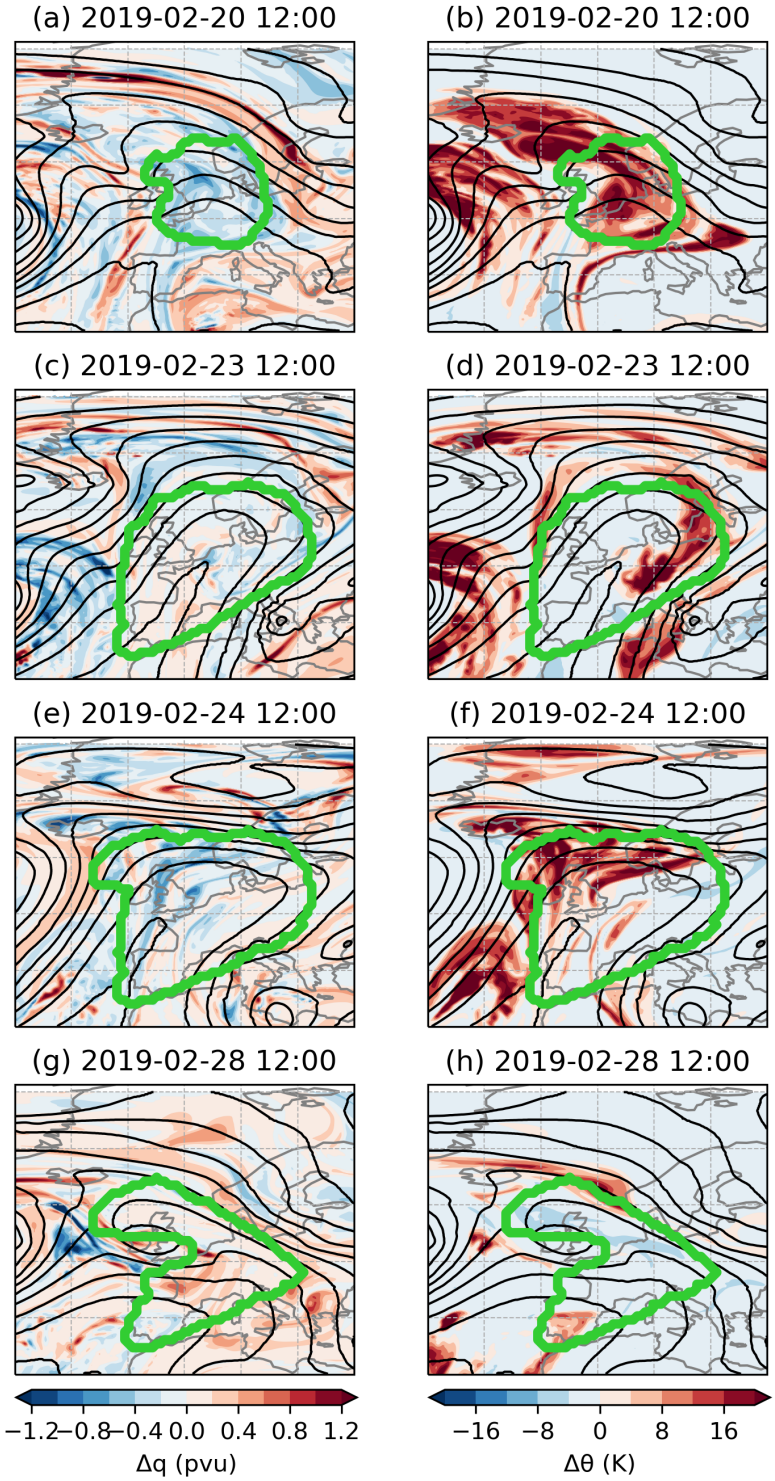

Figure 5.8: Δq (a, c, e, g) and $\Delta\theta$ (b, d, f, h) tracers on a model level height of 9120.904 m, with 60 h accumulations, valid at 12 UTC on various stages in the February 2019 block. For example, this means that the 60 h accumulations shown for 20 February 12 UTC come from forecasts initialised on 18 February at 00 UTC. Also shown is the block contour in green, and forecasted Z500 (interval 80 m) in black.

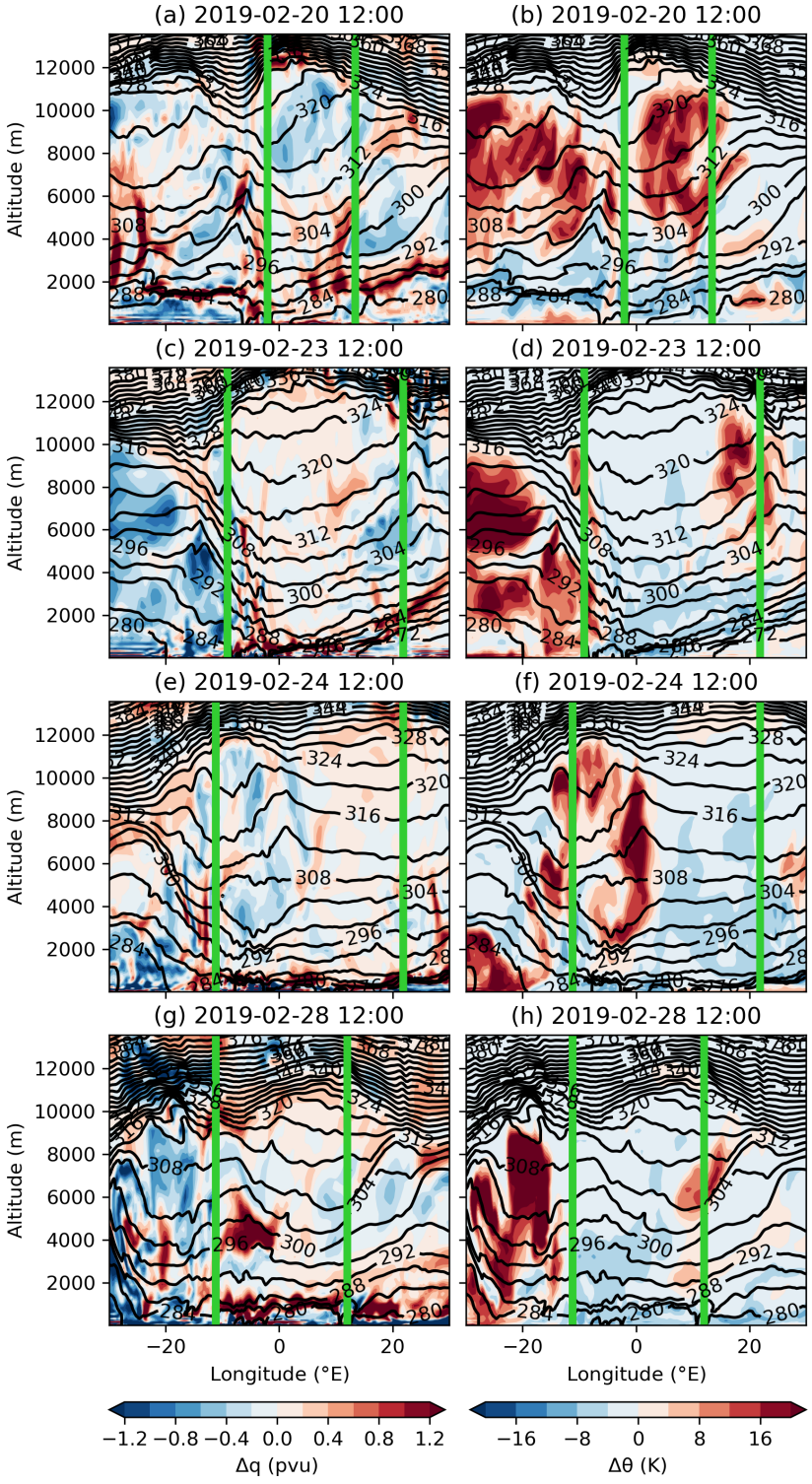

Figure 5.9: Vertical cross-sections of Δq (a, c, e, g) and $\Delta\theta$ (b, d, f, h) tracers at 55°N, with 60 h accumulations, valid at 12 UTC on various stages in the February 2019 block (as in Fig. 5.8). Also shown are forecasted isentropes (black lines). The block, according to Suitters et al. (2023), is found between the two vertical green lines.

the block, and it is possible that this also occurs in the February 2019 block. The diabatically-driven reduction of PV and diabatic heating intensifies again (4 days after block onset), with enhanced PV loss and heating in the west of the block (Figs. 5.8e, f, 5.9e, f). A more localised, but stronger, area of diabatic PV loss is also present in a filament extending east from the Greenwich Meridian, associated with the tropopause fold and PV streamer (see also Fig. 5.2c).

On the day before the block decays (Figs. 5.8g, h, 5.9g, h), diabatic processes modify the PV of the air within the block much less than in the previous days. PV is now increasing due to diabatic processes in the northwestern corner of the decaying block, which further helps to reduce the block area by reducing the magnitude of the negative PV anomaly associated with the block at this time. In the southern half of the block, the effect of parameterised processes on PV is much weaker and more mixed. Diabatic heating in air parcels in the mid-upper troposphere of the block has also drastically reduced by this time, with most regions demonstrating weak diabatic cooling instead.

Diabatic Tracer Components

Whilst the net effect of all parameterised processes in the MetUM can be seen in Figs. 5.8 and 5.9, it is also useful to attribute the contributions of individual processes. Here, the modification to q and θ due to the following parameterisations are discussed: cloud processes ($cloud$, containing a contribution from microphysics, cloud pressure rebalancing, and PC2 checks), convection ($conv$, due to frictional and diabatic heating), and radiation (rad, from shortwave and longwave). These processes produce the largest changes to q and θ for this case study. Analysis similar to that in the previous section will be presented at block onset for the three aforementioned components, before a time series of their mean effect in the block as a whole is analysed.

Maps and cross-sections at the time of block onset at the same altitude and latitude respectively as those in Figs. 5.8 and 5.9 are presented for the three processes of interest in Figs. 5.10 and 5.11. The cloud parameterisations are responsible for large and widespread diabatic heating in air that is situated in the mid-upper troposphere of the block, with the convection parameterisation producing a smaller

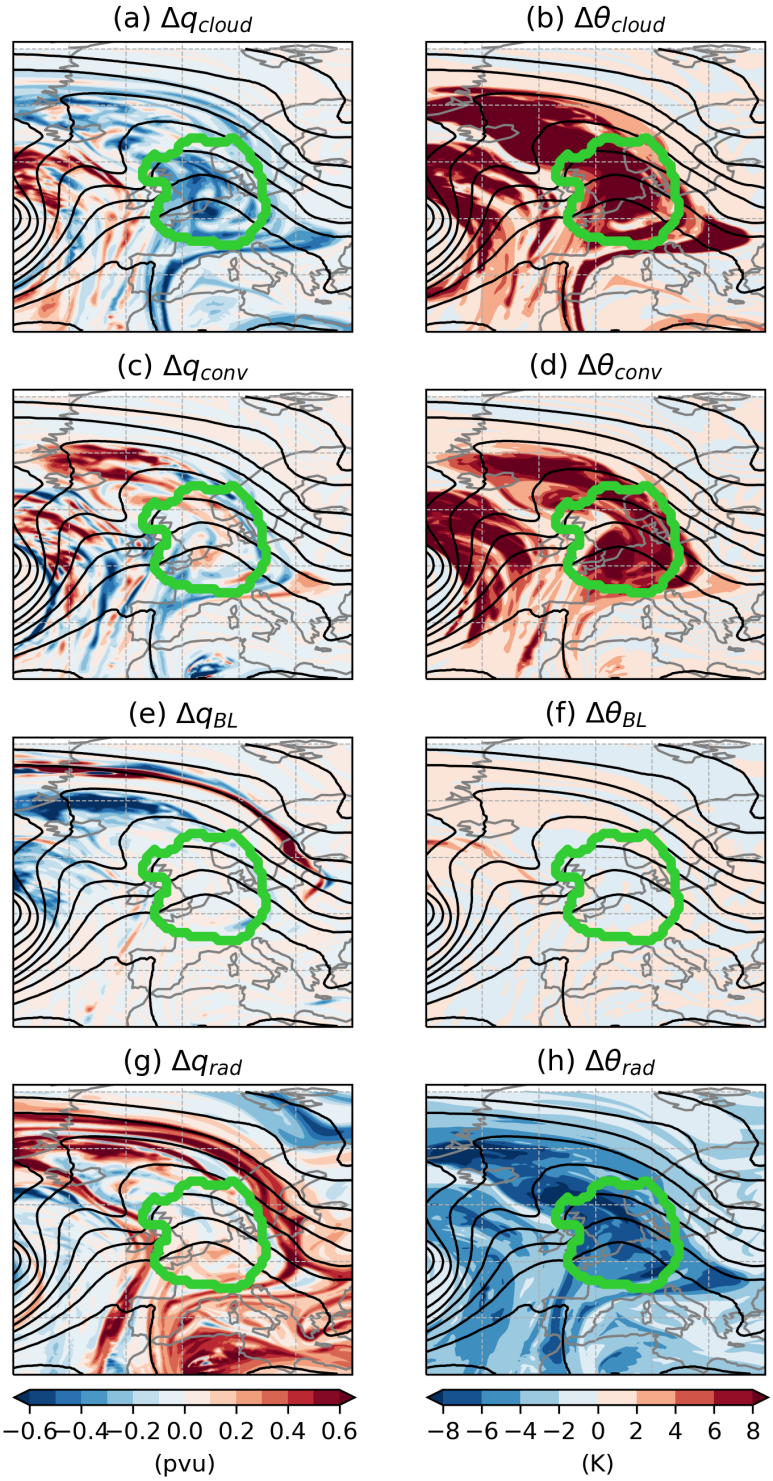

Figure 5.10: Diabatic tracer components, from a 60 h accumulation (valid time 20 February 2019 12 UTC), at a model height of 9120.904 m. The left hand column shows Δq components, and right column shows $\Delta\theta$ components from: (a, b) cloud processes, (c, d) convection, (e, f) boundary layer, and (g, h) radiation. Also shown is the block contour from Suitters et al. (2023) in green, and forecasted Z500 (interval 80 m) and mean sea level pressure (interval 4 hPa) in black and purple.

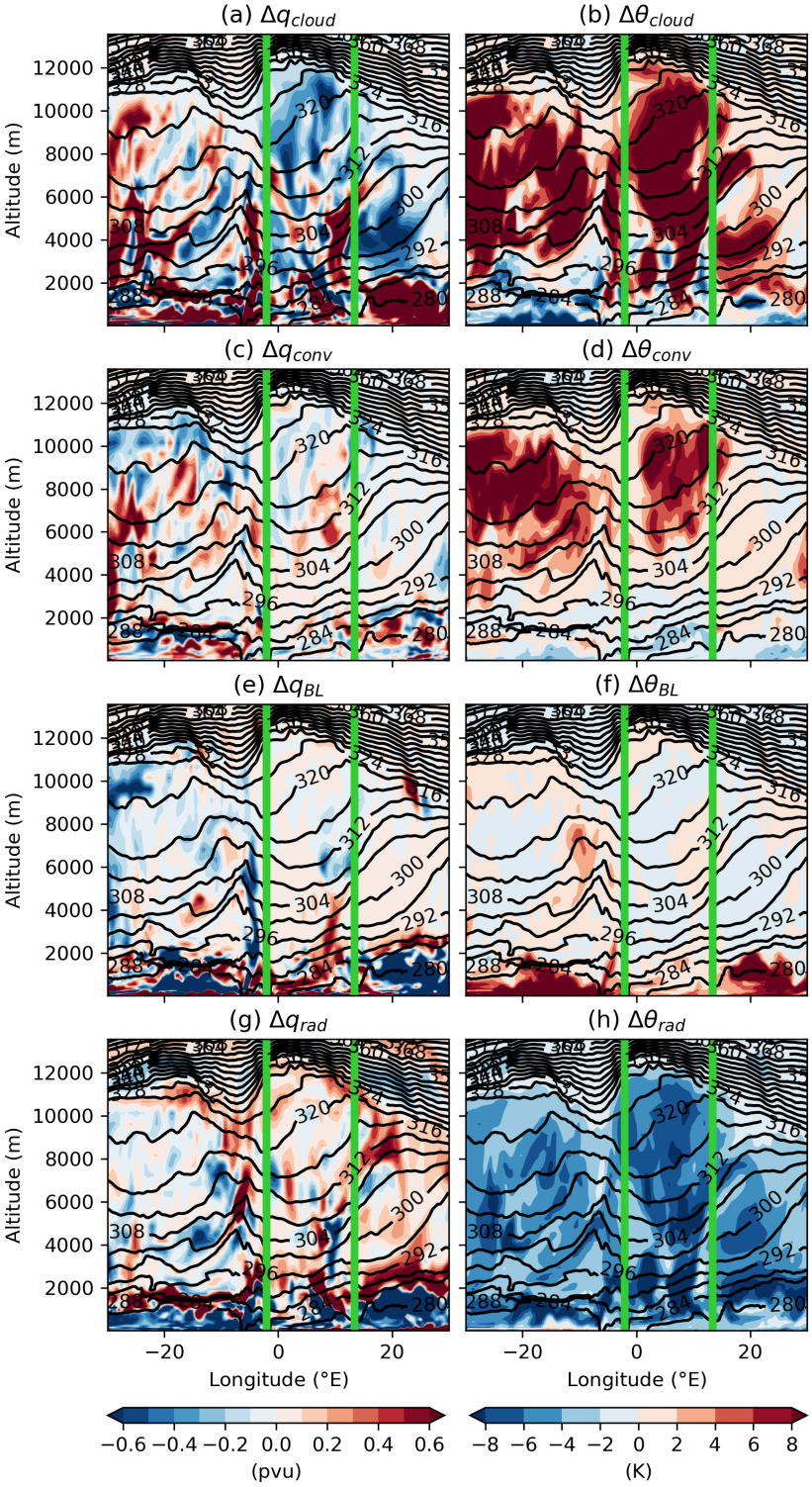

Figure 5.11: Vertical cross-sections of Δq (left) and $\Delta\theta$ (right) components, from a 60 h accumulation (valid time 20 February 2019 12 UTC), at a latitude of 55°N. Components shown are (a, b) cloud processes, (c, d) convection, (e, f) boundary layer, and (g, h) radiation. Also shown are forecasted isentropes (black lines). The block, according to Suitters et al. (2023), is found between the two vertical green lines.

magnitude, but still negative, diabatic PV trend (Figs. 5.10b, d and 5.11b, d). This air has also mostly had its PV reduced by the same processes (Figs. 5.10a, c and 5.11a, c) at the time of block onset. The contribution to cloud processes in this case is dominated by microphysics parameterisation (not shown). The fact that these large-scale cloud and convective processes are producing the most heating and reduction in PV provides further evidence that the source of this air is from a WCB (Maddison et al., 2020). Parameterisation of boundary layer processes is, at this location, not responsible for much modification to q or θ within the block (Figs. 5.10e, f and 5.11e, f). Finally, longwave radiation produces widespread cooling throughout the depth of the troposphere and throughout the area of the block (Figs. 5.10h, 5.11h), and is by far the dominant radiative process occurring in the block. Its effect on PV modification is more variable and somewhat weaker than other components, but in general results in PV gain (Figs. 5.10g, 5.11g).

The results presented in Figs. 5.8-5.11 provide a snapshot of the diabatic processes in the block at selected times, heights or latitudes. However, it is more useful at this stage to present the diabatic processes that modify PV within the entire block. Figure 5.12 shows an overview of the diabatic processes occurring at different stages of the February 2019 event. Each line shows the contribution from 60 hour accumulations of each diabatic tracer, in grid points inside the ERA5 block between 500-200 hPa.

The total diabatic change to PV, Δq, has largest magnitude at the start of the block, and the net result of diabatic processes is to decrease the PV inside the block (Fig. 5.12). As suggested in Figs. 5.10 and 5.11, the largest contributor to PV reduction in the block in the early stages is the parameterisation of cloud processes (Δq_{cloud}). The boundary layer (Δq_{BL}) and convection (Δq_{conv}) schemes are also responsible for PV reduction in air that enters the block in the early stages, though are many times weaker than the role of cloud processes. Gravity wave drag (Δq_{GWD}) parameterisation has a negligible effect on PV modification inside the block throughout the event, whereas radiation (Δq_{rad}), dominated by longwave cooling, acts to increase the PV inside the block throughout.

The magnitude of Δq gradually decreases in the first four days of the block, until reaching a minimum magnitude on 23 February. This decrease occurs de-

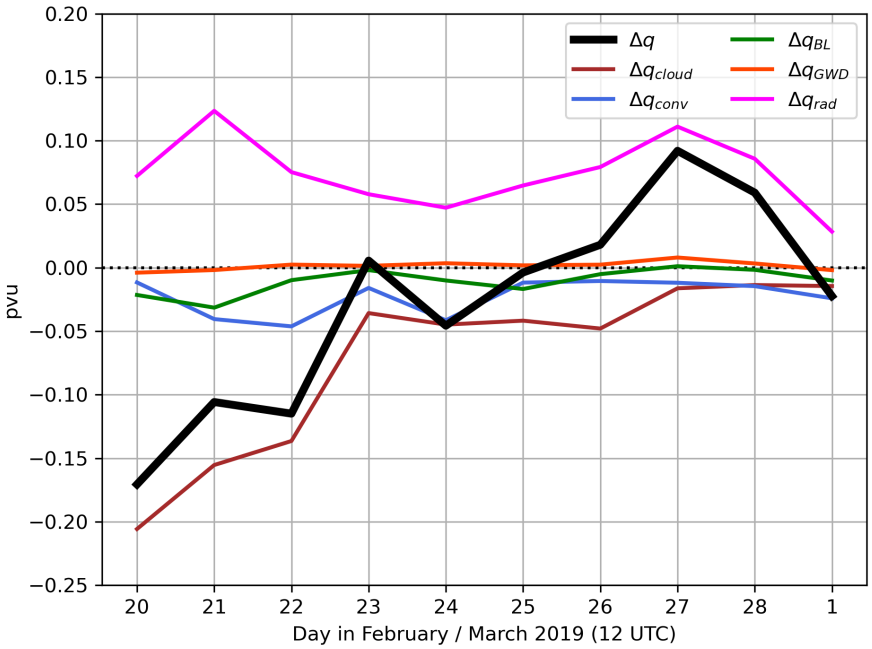

Figure 5.12: Mean 60-h diabatic tracer accumulations, for grid points only within the block, as defined in ERA5, at the valid time, between 500-200 hPa. Components shown are total diabatic change to PV (black), and changes due to parameterisation of: cloud processes (brown), convection (blue), boundary layer (green), gravity wave drag (orange) and radiation (magenta).

spite a reduction in Δq_{rad} and is mainly driven by the decrease in PV loss from cloud processes, along with a slight decrease in loss from Δq_{BL} (Fig. 5.12). 24 hours later however, there is a second reduction of PV again, coinciding with the minimum in Δq_{rad}, with only slight increases in Δq_{conv} and Δq_{cloud} PV loss. Therefore, rather than there being a sudden injection of diabatically-induced low-PV air from WCB activity in an LHB, as described in Steinfeld and Pfahl (2019), the local minimum in Δq here is the result of a temporary relaxation of PV gain through longwave radiative cooling.

From 25-27 February, Δq again increases, which is mainly due to an increase in PV by radiation (Fig. 5.12). Δq_{conv} remains fairly constant from 25 February onwards until block decay, and Δq_{cloud} only becomes comparatively small from 27 February onward. When net Δq is positive (i.e. diabatic processes have a net effect of increasing the PV inside the block), Δq_{rad} dominates, with cloud processes, boundary layer, and convection parameterisations becoming almost negligible.

5.4 March 2021 (1 AC Eddy)

5.4.1 Event Synopsis

The March 2021 event lasted 8.5 days between 12 UTC on 14 March and 00 UTC on 23 March. Selected time steps of its Z'_* field, Z'_* blocking index, Z'_* tracks and q'_* field are shown in Fig. 5.13. The block begins as the result of the deceleration of an AC eddy that originated from the western Atlantic, and the block grows primarily to the east of the AC eddy centre (Fig. 5.13a). Initially the AC eddy and resulting block, are relatively weak, but by 06 UTC on 15 March, its Z'_* exceeds 200 m, and q'_* is below -3 pvu. At this time, the Z'_* maxima and q'_* minima are also reasonably well co-located with each other. However, once the AC eddy leaves the block, for a time there is a mismatch between the Z500 and PV anomaly fields (Fig. 5.13b). Despite having a broad Z'_* maximum (by definition) inside the block at this time, the q'_* signature is characterised by negative q'_* in the southwest and positive q'_* in the northeast. The positive q'_* has been shorn from the cyclone

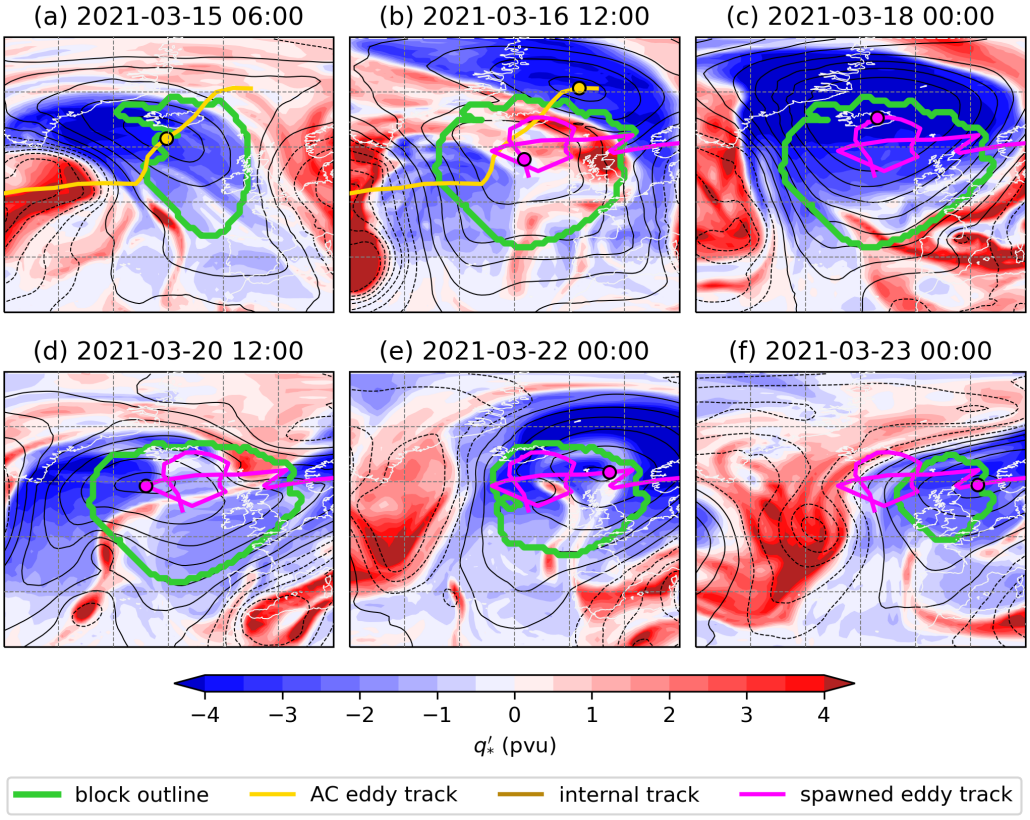

Figure 5.13: As in Fig. 5.2, but for various stages in the March 2021 block. For reference, the block onset was at 2021-03-14 12:00, and decay at 2021-03-23 00:00.

to the west of the block and has circulated around the north of the block as the AC eddy exits the block. The weak q'_* minimum in the block's southwest forms in situ, increases in magnitude, and then becomes coincident with the spawned eddy after about one day (Fig. 5.13c). The q'_* field is replaced again later in the block (Fig. 5.13d), but this minimum does not form in the block itself, and instead arrives from upstream. However, this is not associated with a distinct Z'_* maximum (rather a deformation of the Z'_* field), and therefore is not considered an AC eddy in the earlier methodology. By 22 March (Fig. 5.13e), the Z'_* maximum and q'_* minimum have been advected towards the eastern portion of the block, along with the spawned eddy, and the western extent of the block has reduced as a result. Ultimately, the block decays when the spawned eddy becomes even more mobile, advecting the anomalies with it, allowing for a cyclone to take the place of the block in the mid North Atlantic (Fig. 5.13f).

The same features highlighted above are reflected in the timeseries of area and intensity of the block (Fig. 5.14). The area of the block follows a relatively smooth pattern: rapid constant rate of growth for around 2 days, followed by 5 days of little change in area when the block is mature, and finally a 2-day decay where area decreases at a constant rate. There are no spikes in block area growth

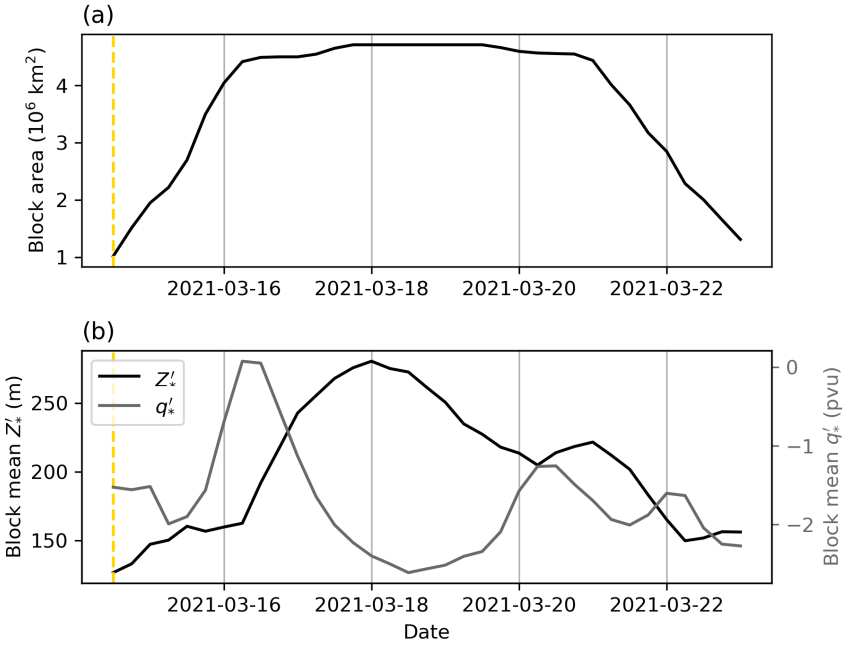

Figure 5.14: As in Fig. 5.3, but for the March 2021 case study.

associated with AC eddy interactions (like those seen for the February 2019 block) since the AC eddy interaction occurs at block onset.

Mean Z'_* inside the block follows a similar pattern, with a few notable exceptions. Firstly, the growth of mean Z'_* is slow for the first two days of the block, before growing rapidly by over 100 m in the 36 hours preceding 00 UTC on 18 March. Unlike the February 2019 block, there is no prolonged period of constant mean Z'_*, and instead the mean Z'_* gradually decays as soon as the peak is reached. There is a secondary peak in mean Z'_* on 21 March, which is related to the stretching of the Z'_* field (Fig. 5.13d).

The more complicated relationship between the spatial overlap of Z'_* and q'_* seen in Fig. 5.13b is also reflected in the disparity in the mean Z'_* and q'_* inside the block in the first 2 days (Fig. 5.14b). The small-scale filament of positive q'_* in the block on 16 March does not result in a decrease in Z'_*, but the block-mean q'_* is about 0 pvu at this time. Once this positive q'_* streamer leaves the block however, the mean q'_* decreases as the mean Z'_* increases as expected (and vice versa). This highlights that smaller-scale features might be represented in the q'_* field but not the Z'_* field.

5.4.2 Dry Dynamics

PV Flux Convergences

Figure 5.15 shows the convergences of total, anomalous, background and zonal mean PV fluxes in the March 2021 block, and the spatial distribution of anomalous and zonal mean PV fluxes on selected dates is shown in Fig. 5.16. Like with the February 2019 block, the PV flux convergence curves are noisy (Fig. 5.15), but the behaviour of the total PV flux convergence from 14–17 March is broadly similar to that in the first period of the February 2019 block. At the time of onset, there is weak net negative PV flux convergence within the block, mostly from negative convergence of anomalous PV flux (larger in magnitude than February 2019 at onset). This is only partially cancelled out by the positive convergence of zonal mean PV flux (Fig. 5.16a-d). Then much like the February 2019 case, shortly after onset, a smaller-scale region of positive q'_* associated with a PV streamer, enters

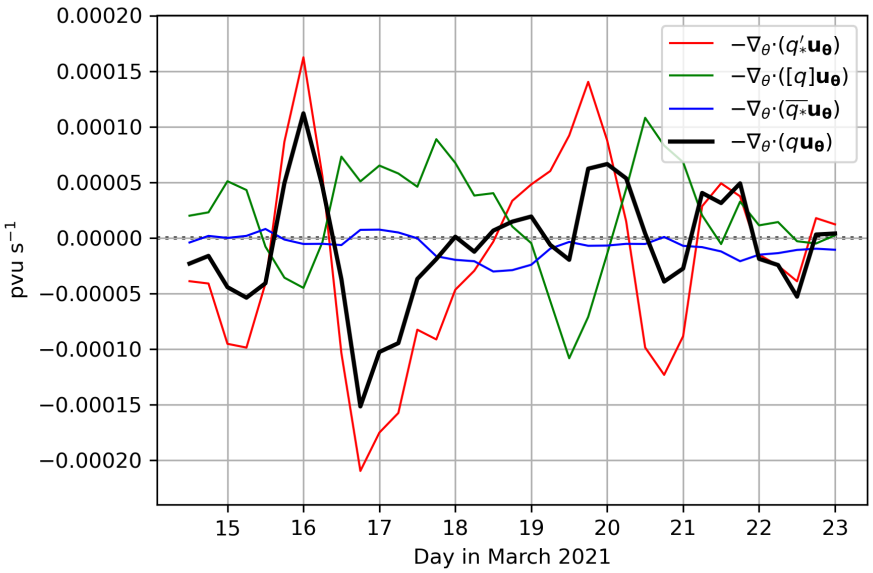

Figure 5.15: As in Fig. 5.4, but for the March 2021 block

the block, causing brief but large anomalous and total positive PV flux convergences (Fig. 5.16f). However this is again followed by an even sharper reversal back to negative PV flux convergence once the PV filament has been advected out of the block at 18 UTC on 16 March. This reversal is also associated with the "replacement" of the first q'_* minimum by a second minimum from the west.

After this point until 00 UTC on 18 March, the convergence of anomalous PV flux rapidly increases. Combined with the near-zero convergence of background PV flux, and fairly constant convergence of zonal mean PV, this means that the total negative convergence of PV also reduces rapidly in magnitude. Two further, more longer-lived PV streamers interact with the block from 19 and 21 March which, like the first streamer, lead to weak negative convergence of zonal mean PV and stronger convergence of anomalous PV. These streamers again mean that the net effect of PV flux convergence in the block is to increase the PV inside the block (see also Fig. 5.14). In between these streamers, the q'_* minimum is once again replaced by a different one from the west, which briefly results in weak negative PV flux convergence in the block. After 22 March, there is mostly weak net negative convergence of PV in the block again, seemingly opposing the decay of the block. However, this occurs at a stage where the anticyclonic region associated with the block becomes much more mobile (seen by the track in e.g. Fig. 5.16m), meaning that while the block event is over, the now transient

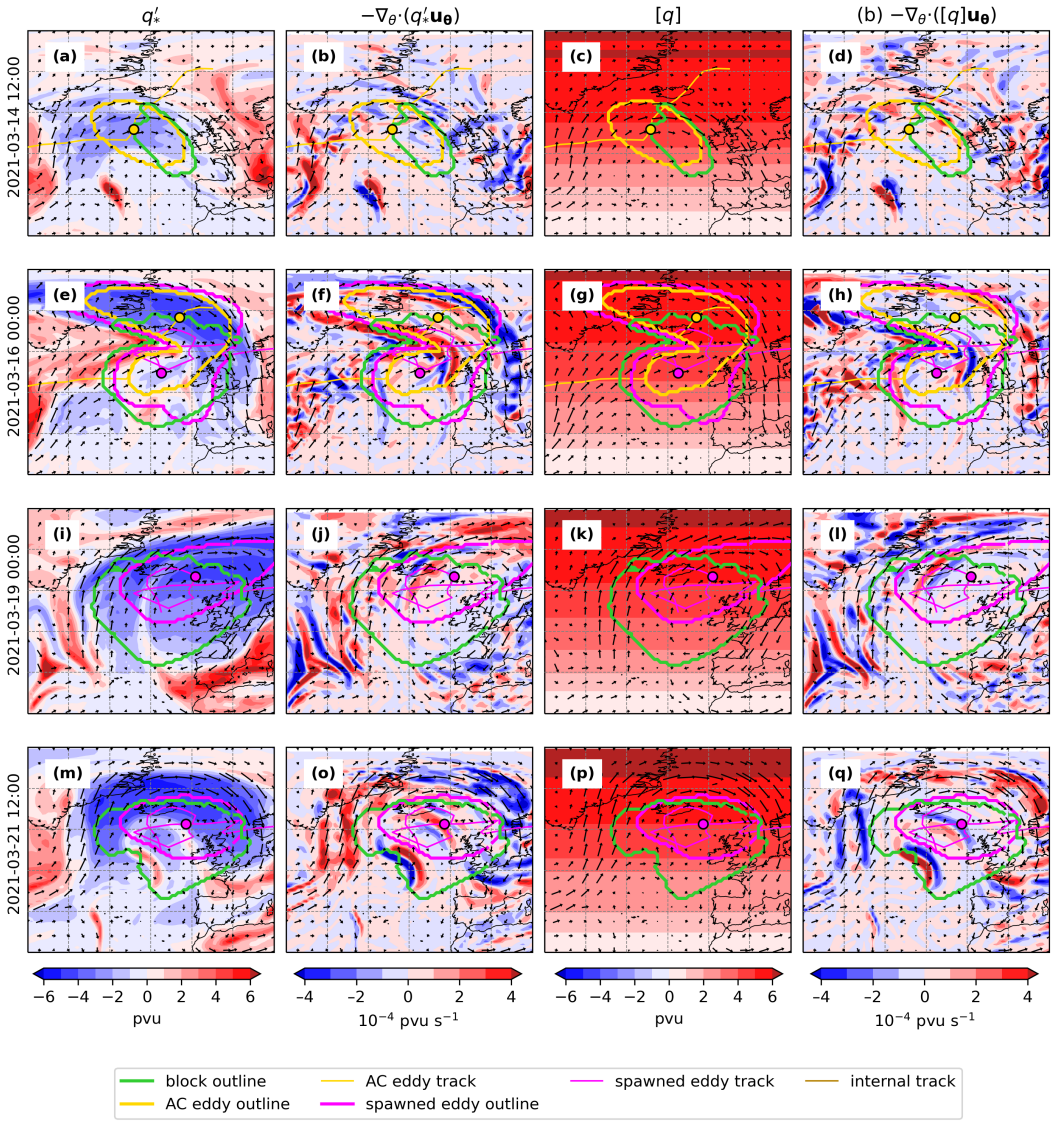

Figure 5.16: As in Fig. 5.5, but for (a-d) 14-03-2021 12 UTC, (e-h) 16-03-2021 00 UTC, (i-l) 19-03-2021 00 UTC, and (m-q) 21-03-2021 12 UTC during the March 2021 block. In addition, spawned eddies are shown in magenta.

anticyclone continues to be maintained by the negative convergence of PV.

AC and Spawned Eddy Contributions

The contribution of tracked Z'_* centres to the PV flux convergences in the March 2021 block is shown in Fig. 5.17. It should be noted that, unlike the February 2019 block, for most of the time it is a spawned eddy emerging from the block itself, not AC eddies from upstream, that interact with the blocking anticyclone in this case. The only upstream AC eddy interactions take place at the very start of the block, from 14 March 12 UTC – 16 March 12 UTC. The spawned eddy forms at 00

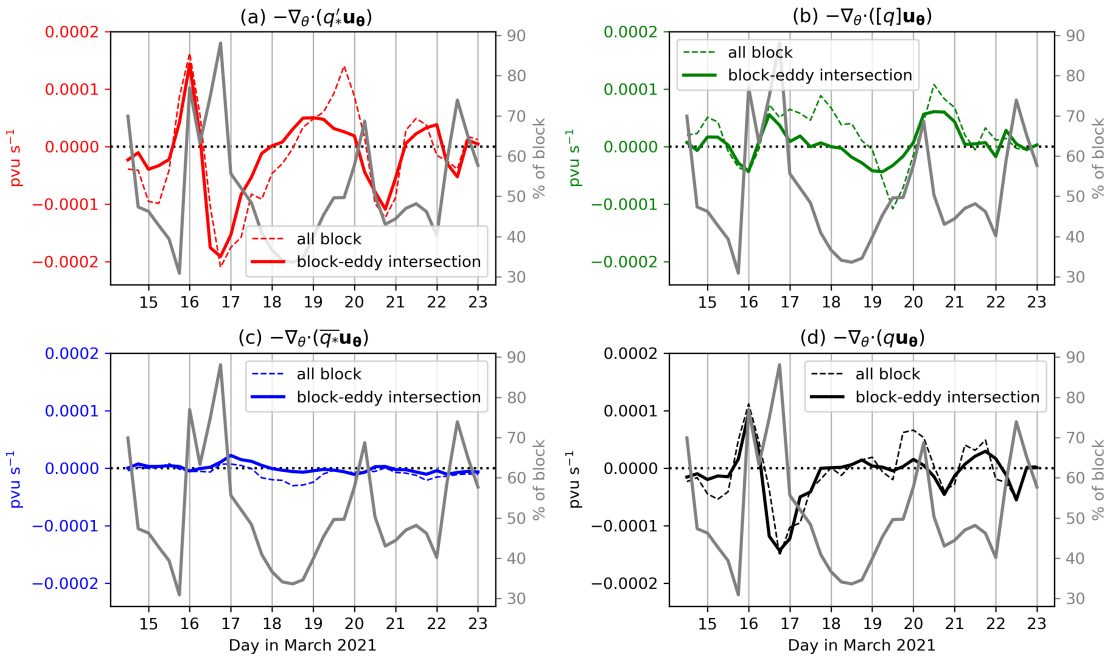

Figure 5.17: As in Fig. 5.6, but for the March 2021 case study. In this case, the grey line shows the percentage of the block area that constitutes of an AC and/or a spawned eddy.

UTC on 16 March, and remains interacting with the block until it decays.

In the early stages of the block on 14–15 March (during the upstream AC eddy interaction), the AC eddy generally makes up 30–50% of the area of the growing block. Simultaneously, the AC eddy contributes to 30–50% of the convergence of anomalous, zonal mean and total PV (Fig. 5.17a, b, d). The remaining PV flux convergence field is situated in the southwest of the block away from the eddy. Upon genesis of the spawned eddy on 16 March in the centre of the block, the majority of the block is now part of this spawned eddy contour and as a result most of the PV flux convergences are due to this spawned eddy. This is at odds with the February 2019 case - here when a tracked Z'_* centre was in the core of the block, it did not contribute much towards the PV flux convergence of the whole block. This can perhaps be explained by the stronger, more anticyclonically-curved winds in the March 2021 block which leads to more negative convergence within the block at this stage.

When the spawned eddy moves to the northern portion of the block from 17–20 March, the majority of the block becomes outside of its influence again. During this time, there is approximate net-zero convergence of background (as there is

throughout the block event) and zonal mean PV due to the spawned eddy (Fig. 5.17b, c), meaning that the convergence of zonal mean PV comes from non-eddy sources, mostly to the block's west (Fig. 5.16i-l). Meanwhile the convergence of anomalous PV is much smaller in magnitude than for the block as a whole. In this sense, at this stage the March block is similar to the February 2019 block in that the majority of the PV flux convergence takes place away from the Z'_* centre.

From 20 March onwards, the spawned eddy once again is in the centre of the block. This Z'_* centre appears to be the dominant source of convergence of anomalous PV despite only being 40% of the block area (Fig. 5.17a). However, in the rest of the block, mostly in the southwest, a dipole of positive and negative convergence (outside of the eddy contour) produces approximately zero net PV convergence (Fig. 5.16m-q). The other components of PV flux convergence are contributed to much less by the spawned eddy.

5.4.3 Diabatic Dynamics

PV Inconsistency Analysis

Like was done for the February 2019 case study, before analysing the moist dynamics of the March 2021 case, an analysis of the PV inconsistency is required such that an appropriate tracer accumulation time is selected. Block-mean upper tropospheric (500-200 hPa) $|\Delta q_I|$ and $|\Delta q|$ are shown in Fig. 5.18 for the March 2021 case. Like in the February 2019 block, $|\Delta q_I|$ generally increases with forecast lead time in each forecast, however its behaviour at shorter lead times is more complex. There are occasions where, even at very short lead times, the PV inconsistency is comparable to the total change in PV. This behaviour is undesirable and makes it difficult to choose a lead time that is to be used for every forecast for consistent analysis of the diabatic tracers. Therefore, to be consistent with the results presented for the February 2019 block, a lead time of 60 hours is also used to analyse the diabatic processes in the March 2021 block. However, it should be noted that the size of $|\Delta q_I|$ in comparison to $|\Delta q|$ throughout this block make the results in the following section less reliable.

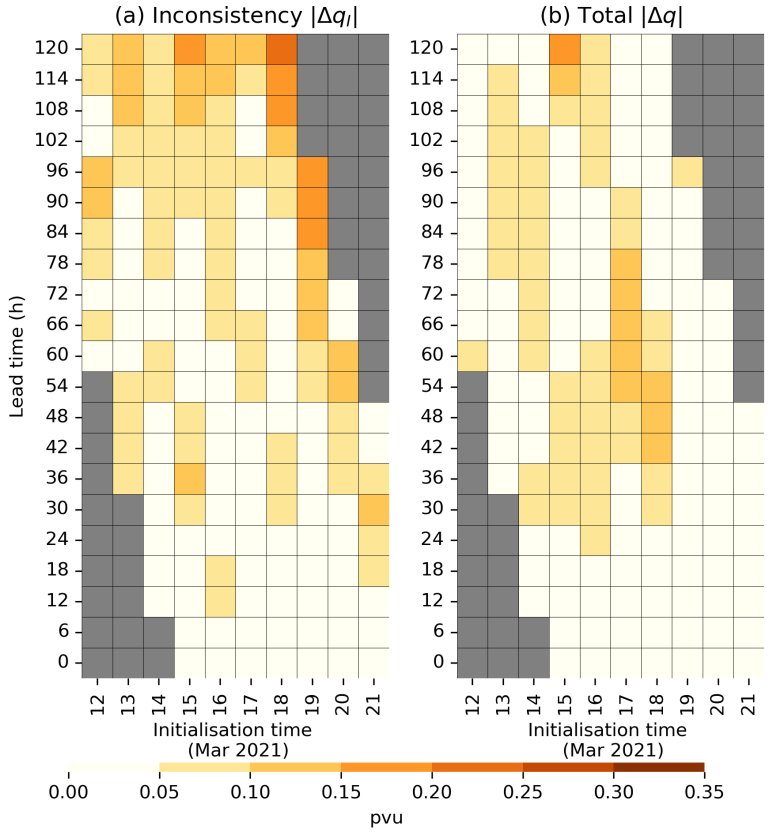

Figure 5.18: As in Fig. 5.7, but for the March 2021 block.

Diabatic Modification to PV

The modifications to PV within the March 2021 block by diabatic processes are now analysed through investigation of diabatic tracers. Like the February 2019 block, block-mean diabatic tracer accumulations between 500 and 200 hPa are taken from forecasts with a 60 hour lead time. The spatial pattern of the PV tracers are broadly similar to those seen in the February 2019 case, so analysis focuses on the time series of tracer accumulation rather than instantaneous cross-sections or maps of tracer. These time series are presented in Fig. 5.19.

Diabatic reduction of PV at block onset is modest and fairly constant from 14–18 March, and is 3 times smaller in magnitude than at the onset of the February 2019 block. The negative region of upper-tropospheric Δq and diabatic heating appears to be shallower here than in the February case (Fig. 5.20). The largest diabatic contributor to PV reduction in the block at onset is Δq_{conv}. Δq_{cloud} is slightly smaller than Δq_{conv} at onset, and is four times smaller than during the February case study. Also unlike the February block, where microphysics dom-

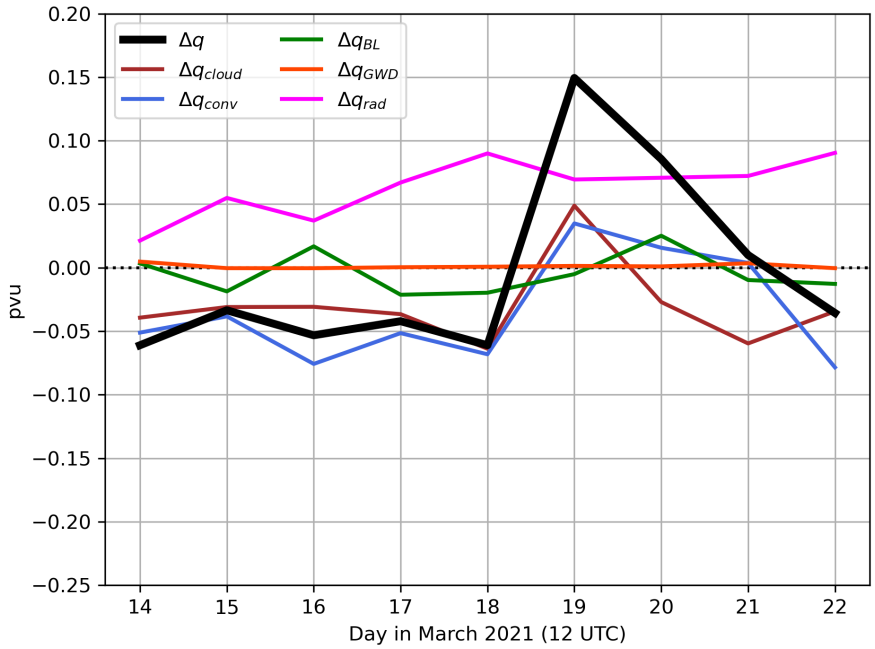

Figure 5.19: As in Fig. 5.12, but for the March 2021 block.

inates the cloud term, the three individual components of Δq_{cloud} in the March 2021 case (microphysics, PC2 checks and pressure rebalancing; refer back to Table 5.2) contribute almost equally (not shown). At onset, Δq_{BL} and Δq_{GWD} are once again small. The effect of GWD on PV modification inside the block is once again negligible throughout the block, and the boundary layer parameterisation again produces a generally small change to PV. The effect of Δq_{rad} is subtly different in this March 2021 block than the February 2019 case. While in both cases longwave cooling dominates and results in a gain of PV inside the block, its magnitude typically increases as the March 2021 block ages, compared to the double-peak structure in the February 2019 block.

From 19–21 March, diabatic processes promote block decay, much more strongly than they were encouraging block development earlier. This is driven by the changing of signs of Δq_{conv}, Δq_{cloud}, and Δq_{BL}. At its peak on 19 March, diabatically-driven PV gain is 0.15 pvu, three times as large as the PV loss earlier in the block. Cloud and convective processes briefly promote block decay on 19 and 20 March as their effect is to increase the PV in the block. However, on the last day of the block (22 March), Δq becomes slightly negative again, mostly driven by a negative Δq_{conv} and Δq_{cloud}. This implies that in the absence of any other effects,

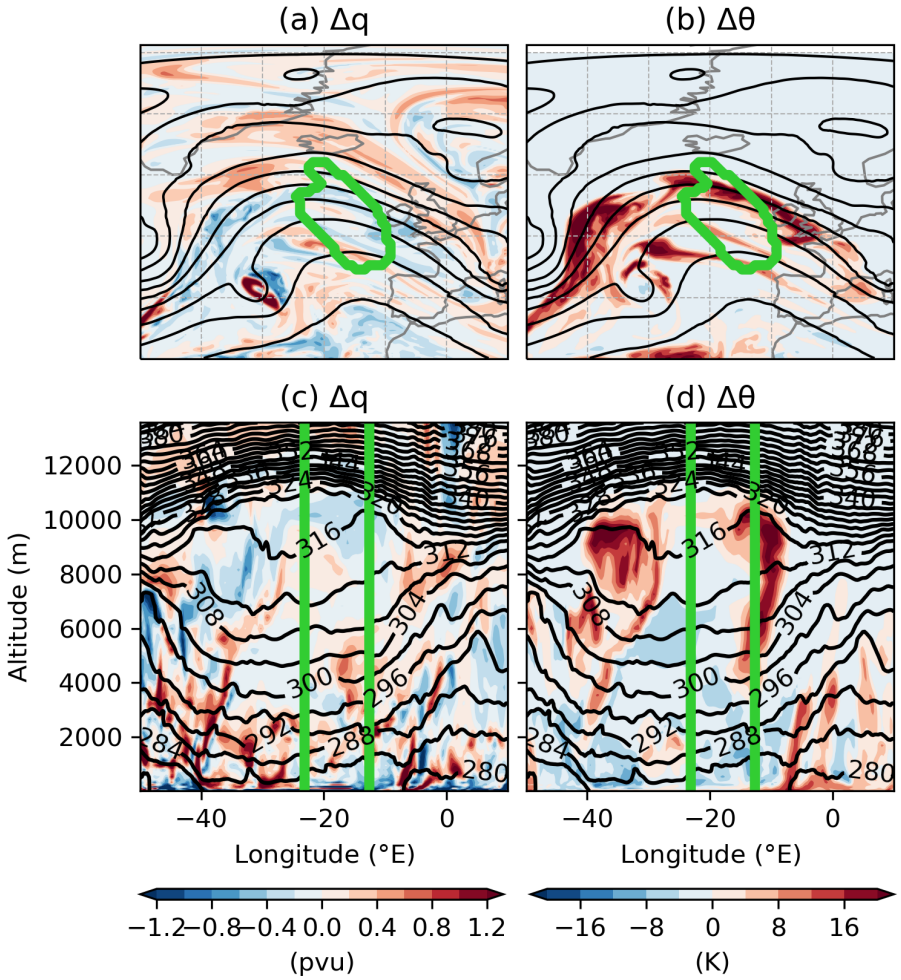

Figure 5.20: Total change to PV (a, c) and potential temperature (b, d) at time the onset of the March 2021 block. The top row shows maps at a height of 9120.904 m and the bottom row shows vertical cross sections at 55°N. Black lines in (a, b) show Z500, and in (c, d) show potential temperature, while green contours indicate the block.

the block may re-intensify. However, the block is already shrinking at this stage, which is driven by the incursion of an upper-level trough to the western portion of the block. In addition, what remains of the block has become far more mobile, as previously discussed, implying that the anticyclonic centre is reinforced by diabatic processes, but its lack of stationarity means it no longer classifies as a block in the Euro-Atlantic.

5.5 August 2021 (0 AC Eddies)

5.5.1 Event Synopsis

A synopsis of the August 2021 case study is now given here. The Z'_* field and tracks, q'_* field and block contours on selected days in this event are shown in Fig. 5.21. For this case study, q'_* is shown on the 330 K surface, rather than the 320 K surface used for the other two case studies, due to the higher tropopause in summer.

The event starts (Fig. 5.21a) as a weak maximum in Z'_* (less than 150 m). Most of the block also contains a region of large-magnitude negative q'_* (broadly below -2.0 pvu) concentrated in the southwestern two-thirds of the block. A streamer of positive q'_* is present in the block at onset too that connects the large cyclone to the west with the smaller cut-off low to the southeast. The negative q'_* region increases in magnitude and size over the next few days and aligns with the (also in-

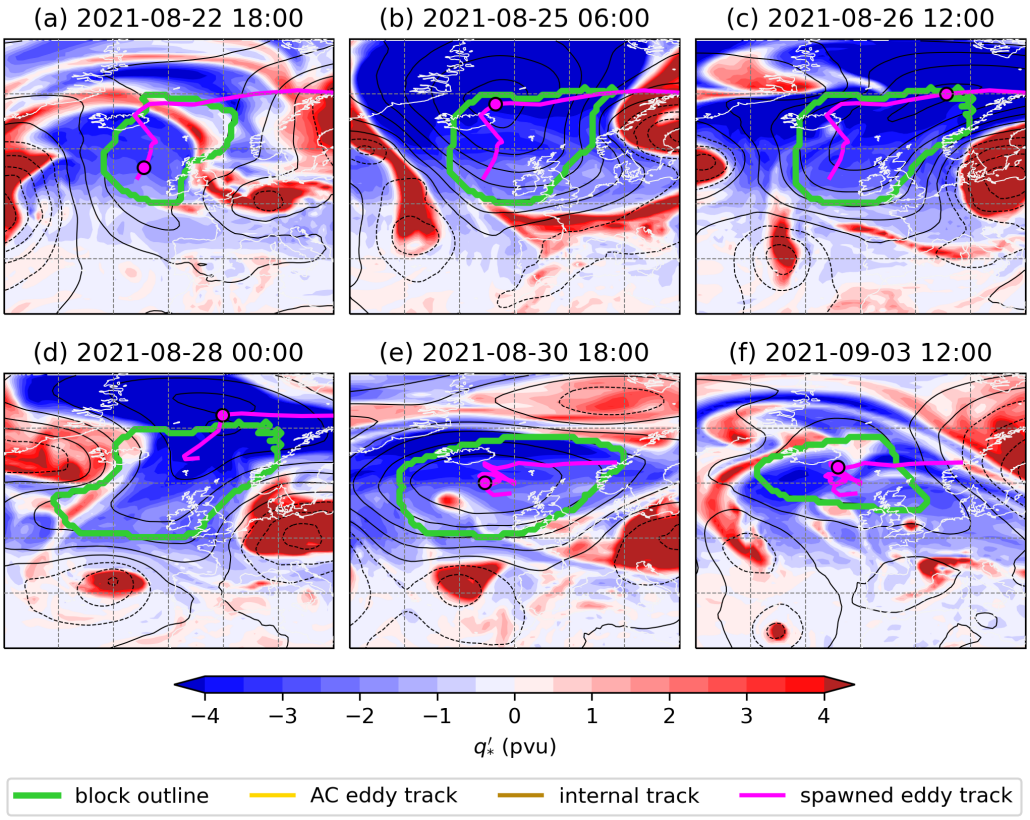

Figure 5.21: As in Fig. 5.13, but for selected times in the August 2021 case study. Note in this case study, q'_* is given on the 330 K surface, not 320 K as in the other two examples.

tensified) Z'_* maximum and first tracked spawned eddy (Fig. 5.21b), which allow the block to expand to the east. The first spawned eddy leaves the block on 26 August (Fig. 5.21c) but still leaves large-magnitude Z'_* and q'_* within the block. These large-magnitude anomalies coincide with a second spawned eddy which exits the block on 28 August (Fig. 5.21d). Over the next few days, the block realigns and the Z500 anomaly changes shape, with its long axis becoming more zonal in direction (Fig. 5.21e). By 30 August, the third and final spawned eddy has formed and has begun to meander around the block interior. The q'_* field is still predominantly large-magnitude and negative within the block, although there is another small-scale region of positive q'_* inside the block at this time, south of Iceland. This small positive q'_* region gradually circulates around the block and loses its identity as it mixes with the main negative q'_* area (not shown). The block decays (Fig. 5.21f) from the south as both the q'_* and Z'_* strength decrease and cyclonic features approach from the south and west.

Timeseries of the area and intensity of the August 2021 block are shown in Fig. 5.22. The area of the block follows a subtly different evolution to that in the other two analysed blocks. The August 2021 block has a prolonged growth stage: quickly growing for the 12 hours after onset, then more gradually expand-

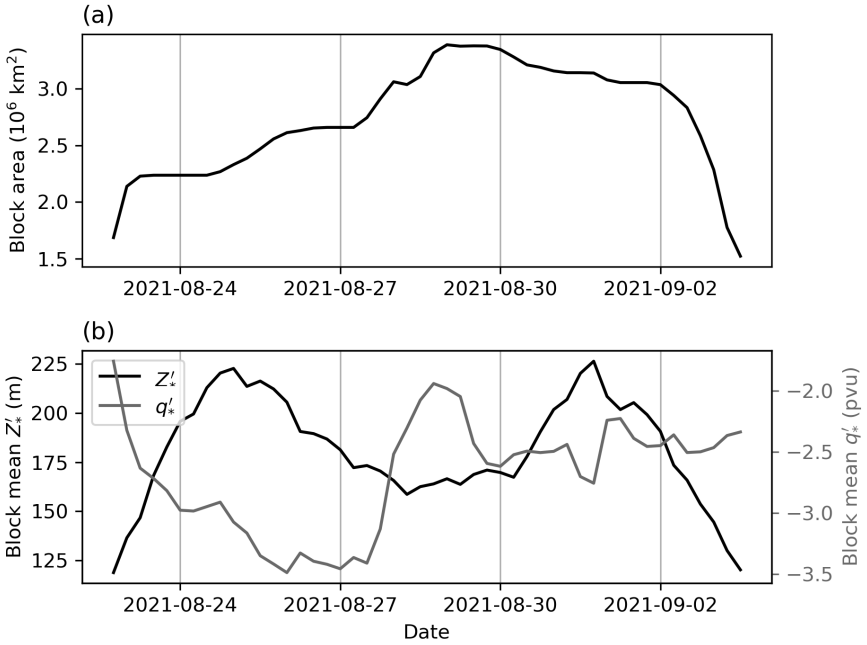

Figure 5.22: As in Fig. 5.3, but for the August 2021 block.

ing for the next 2-3 days, before one final more rapid period of growth until 29 August. In total, the block increases its area for around 6-7 days. Unlike the other blocks, there is no period of approximately equal area. Instead, as soon as the block reaches its maximum size on 29 August, the block slowly decays until 2 September, when the decay is much more severe.

The progression of the August block's strength is not as straightforward as the February 2019 or March 2021 blocks. There are two peaks in Z'_* intensity, on 25 August during the slow growth phase, and on 31 August while the block is slightly shrinking in size. Both Z'_* peaks are similar in magnitude, around 225 m. In between, there is a minimum in block mean Z'_* of 160 m that occurs when the block is at its largest. This minimum can be attributed to the two spawned eddies leaving the block, momentarily reducing the magnitude of the Z'_* inside the block itself. The timeseries of q'_* is even more complex. The minimum q'_* of -3.5 pvu occurs close to the first maximum in Z'_*, however the second peak in Z'_* coincides with a far smaller and less well-defined minimum in q'_* of -2.8 pvu. The departure of the first spawned eddy has little effect on the strength of the q'_* inside the block, however there is a marked increase in block-mean q'_*, to -2.0 pvu, when the second spawned eddy departs. After a brief recovery in q'_* over the next 24 hours, the magnitude of this PV anomaly remains fairly constant at about -2.6 pvu until the block decays.

5.5.2 Dry Dynamics

PV Flux Convergence

PV flux convergences from each component for the August 2021 block are shown in Fig. 5.23. Examples of the spatial distributions of the convergences are shown in Fig. 5.24. Like with the other two blocks, there is strongly negative total PV flux convergence in the early stages of the block (which reduces PV), as a result of marked negative convergence of anomalous PV flux. The PV flux convergence is of similar magnitude to the other two cases. The northeastern portion of the block contains a positive PV streamer at onset (Fig. 5.24a), but negative q'_* is advected into the block in this region, resulting in strong negative convergence

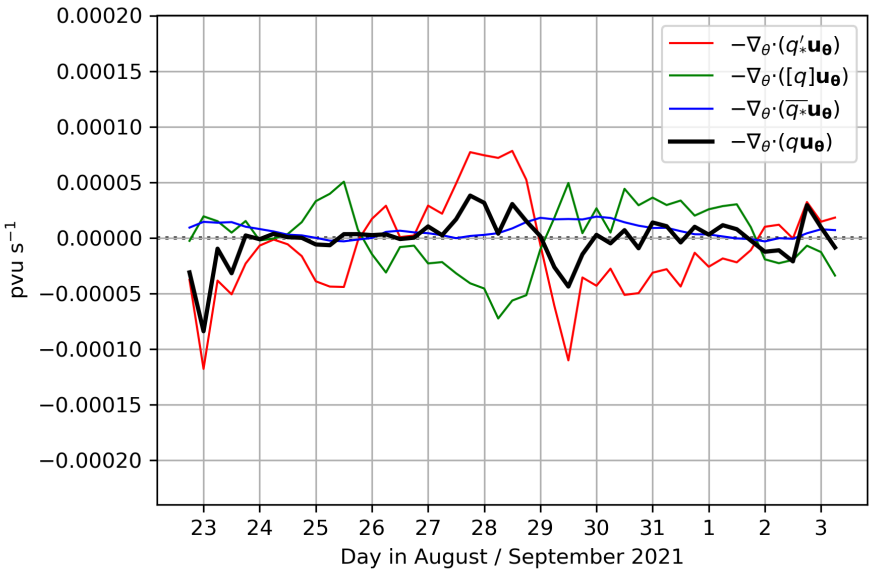

Figure 5.23: As in Fig. 5.4, but for the August 2021 block, and flux divergences are calculated on the 330 K surface.

of anomalous PV flux (Fig. 5.24a-b). This period of high-magnitude total PV flux convergence is brief, lasting until 00 UTC on 24 August.

Then, until 27 August, convergence/divergence of zonal mean PV almost entirely balances divergence/convergence of anomalous PV, resulting in a net-zero PV flux convergence. As the first two spawned eddies leave the block on 26 and 28 August, and the associated q'_* minimum is advected northeastwards (Fig. 5.24e), and a negative eastward q'_* gradient is established in the western half of the block. This results in convergence of q'_* within the block as a whole, and a period of modest total PV flux convergence, despite net negative convergence of zonal mean PV (Fig. 5.24e-h) from 27–29 August. This period coincides with the decrease in block strength seen in Fig. 5.22b. As the negative q'_* recovers inside the block, aided by an upstream impulse of negative q'_* which briefly leads to net negative PV convergence on 29 August, anomalous PV once again diverges from the block. However this time, the coincidental convergence of zonal mean and background PV nearly cancels this out, leading to noisy, but approximately zero total PV flux convergence in the block as a whole from 30 August until the end of the block (Fig. 5.24m-q).

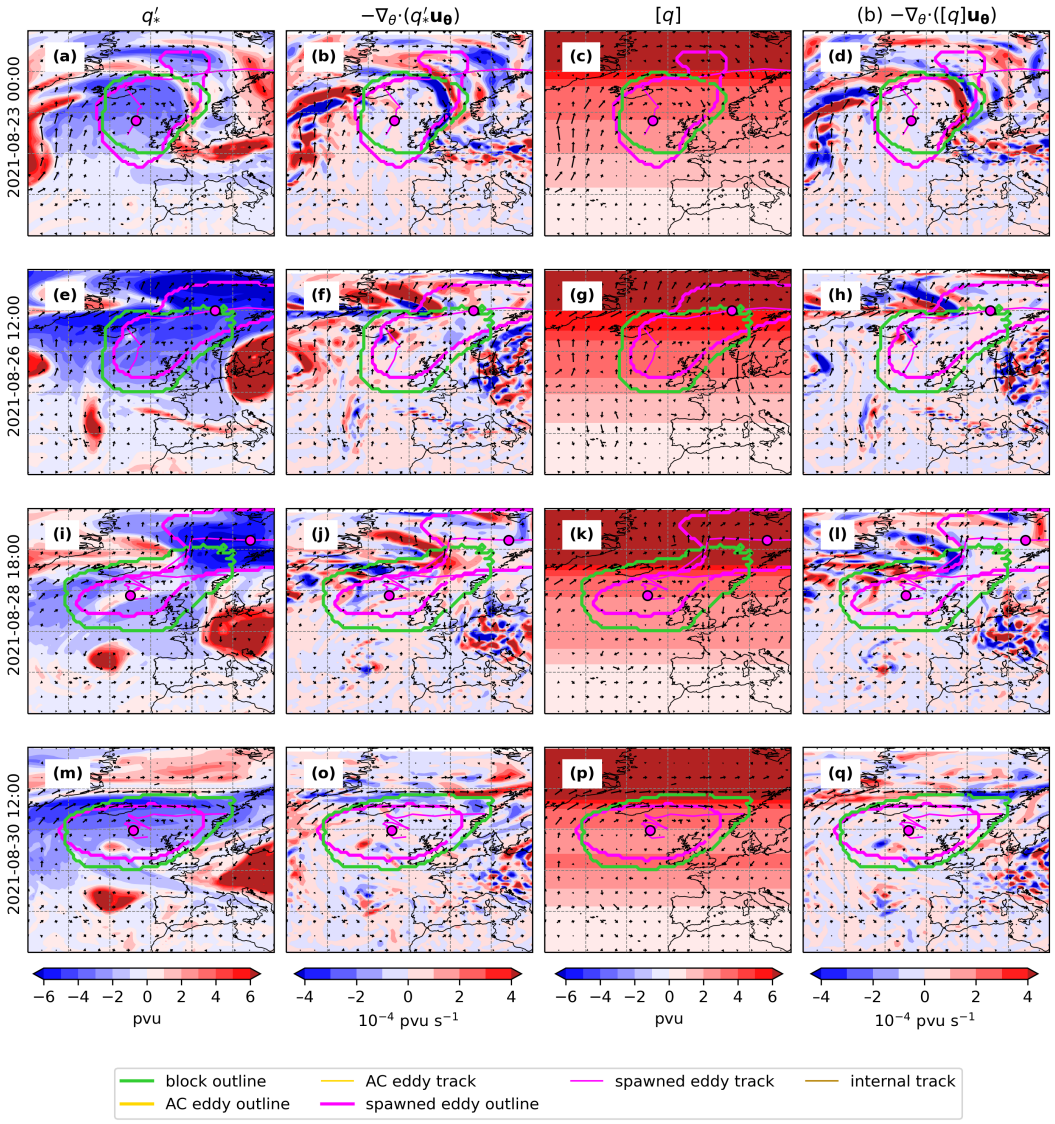

Figure 5.24: As in Fig. 5.5, but showing fields on the 330 K surface during the August 2021 block on (a-d) 23-08-2021 00 UTC, (e-h) 26-08-2021 12 UTC, (i-l) 28-08-2021 18 UTC, and (m-q) 30-08-2021 12 UTC.

Contribution of Spawned Eddies

The influence of the spawned eddies on the blocking dynamics is now examined (Fig. 5.25). The majority (over 60%) of the block area is associated with an eddy at most times. As a result, most of the time, spawned eddies also contribute to the majority of the PV flux divergences/convergences in the block as a whole. Despite this, some interesting examinations can be made, which are discussed here.

As the block's first spawned eddy approaches the northern boundary of the block on 25–26 August, there is a peak in the amount of total PV flux convergence,

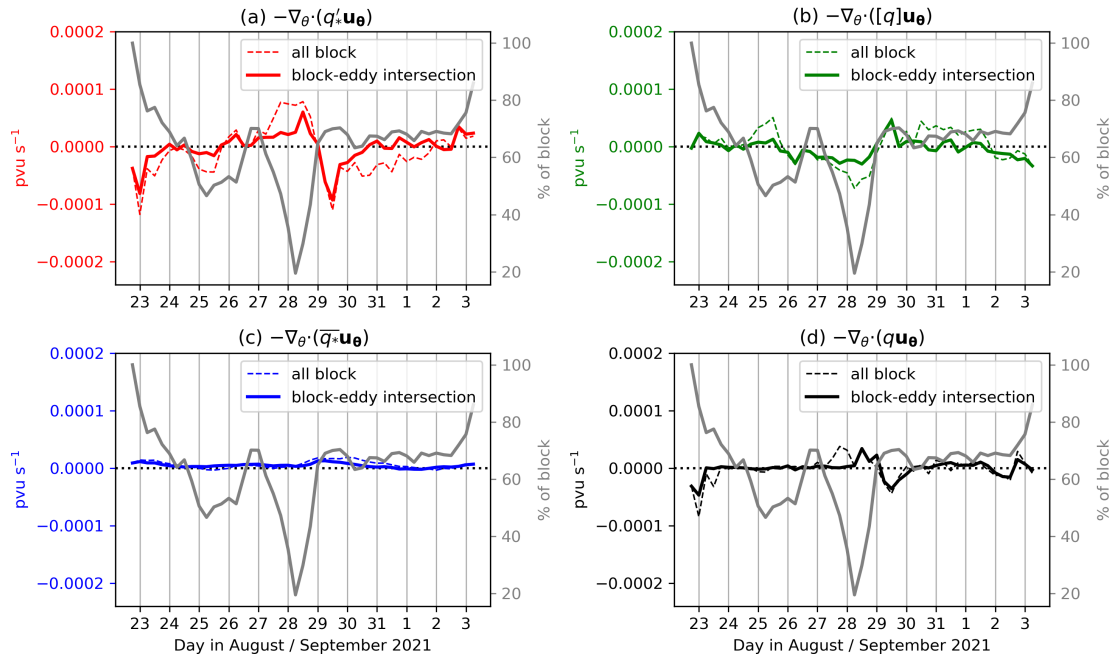

Figure 5.25: As in Fig. 5.6, but for components of PV flux divergence on the 330 K surface for the August 2021.

driven by a peak in the convergence of anomalous PV, as previously discussed. At this time, the spawned eddy is taking up less than half of the area of the block, and the amount of q'_* flux convergence associated with the eddy is only about 25% that in the total block. As discussed in other case studies, this is perhaps surprising given that tracked q'_* centres can also be approximated as minima in q'_*. But similarly to the first AC eddy in the February 2019 case study, the circulation of the eddy leads to q'_* flux divergence in the west of the block/eddy and convergence in the east, leading to a small net q'_* flux (e.g. Fig. 5.24a,e).

On 28 August 06–12 UTC, the first spawned eddy is leaving the block and the second one begins in the centre of the block. Despite there being two spawned eddies interacting with the block at the same time, their combined area results in only a small proportion intersecting the block (20–40%). However, the spawned eddies appear to be contributing to the majority of the convergence of anomalous PV flux at this time, which counteracts the cancellation of positive and negative anomalous PV flux convergence on the northern edge of the block (Fig. 5.24i-l). This is less apparent when zonal mean PV flux convergence is taken into account. A further cancellation problem presents itself towards the end of the block, where the remaining spawned eddy has an approximate zero effect on the whole-block

anomalous PV flux convergence, and convergence of zonal mean PV flux (which themselves lead to an approximate zero flux in the block itself).

5.5.3 Diabatic Dynamics

PV Inconsistency Analysis

This section uses the PV inconsistency tracer, Δq_I, to determine a suitable forecast lead time to use for analysing the diabatic processes occurring in the block. The magnitude of the PV inconsistency and total change in PV tracers, as a function of lead time and initialisation time, for the August 2021 block are shown in Fig. 5.26. As before, the values presented in the figure are an average from grid points within the ERA5 block in the mid-upper troposphere. However, due to the higher tropopause in summer, the higher boundary is 150 hPa instead of the 200 hPa used in the other two case studies.

In general, there is an increase in $|\Delta q_I|$ as forecast lead time increases, though this pattern is not as consistent as in the February 2019 block. Forecasts initialised

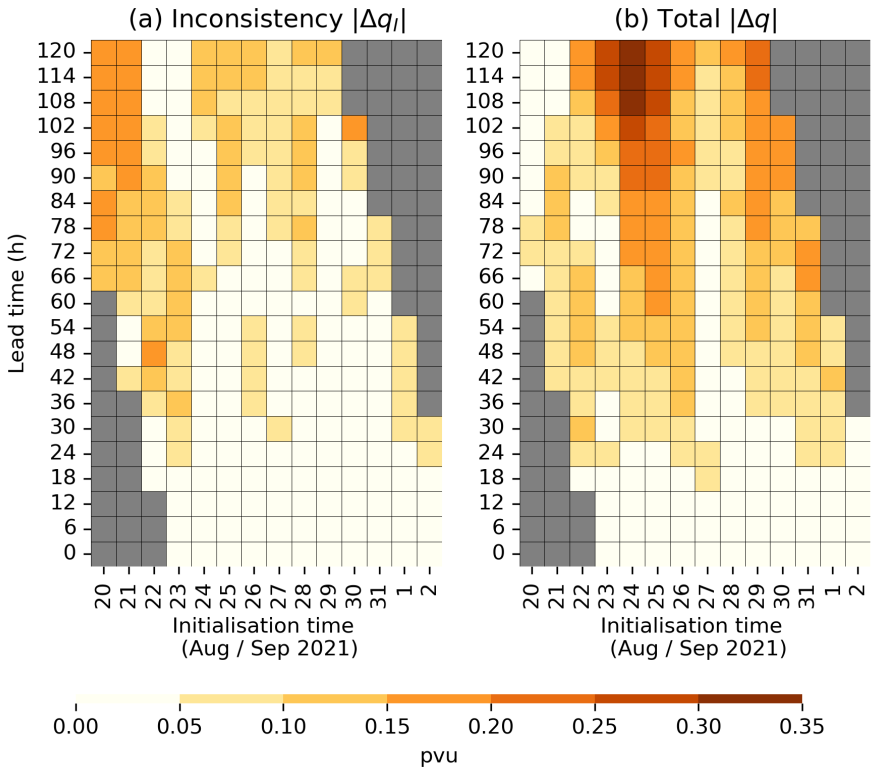

Figure 5.26: As in Fig. 5.7, but for the August 2021 case study. Instead of using a vertical average from 500-200 hPa, here an average from 500-150 hPa is used.

earlier on also tend to have larger $|\Delta q_I|$ at a particular lead time than forecasts initialised later on in the block. There is a distinct difference in the pattern of total $|\Delta q|$ compared to the other two blocks analysed. In forecasts initialised from 20-24 August, the magnitude of PV generated/destroyed increases markedly with lead time (and is much larger than the $|\Delta q_I|$ tracer mean at these times too). However, there is a marked lull in diabatically-driven PV modification in the middle of the block. Towards the end of the block, diabatic activity increases again, though to a lesser extent than earlier in the block.

The fact that, particularly early in the block, $|\Delta q|$ is much larger than $|\Delta q_I|$, for lead times below approximately 60 h, any lead time less than this could be used for analysis of diabatic processes. However, for consistency with the previous two case studies, and such that the results can be more directly compared, an accumulation time of 60 h is also pursued here.

Diabatic Modification to PV

Fig. 5.27 shows the contribution of each diabatic tracer component to the total modification of PV in the block as a whole, every 24 hours. Unlike for the February and March case studies, the vertical averages shown in Fig. 5.27 have an upper limit of 150 hPa to reflect the higher tropopause in late summer. Once again,

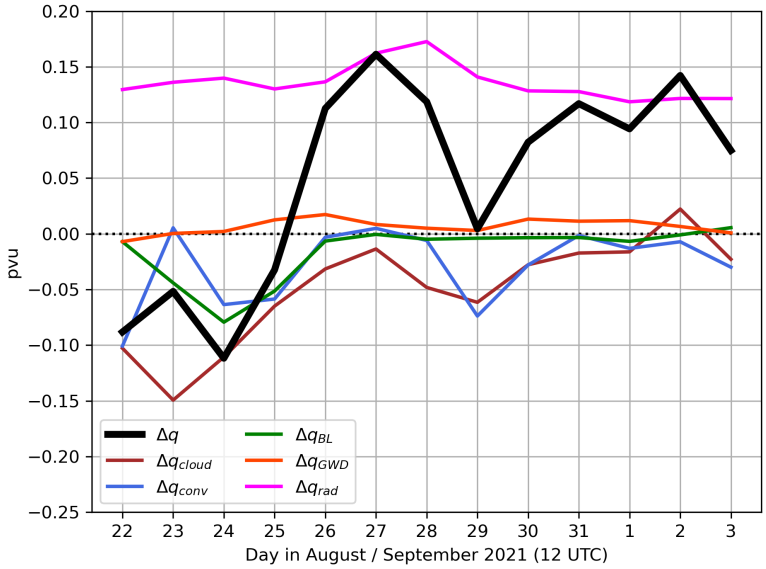

Figure 5.27: As in Fig. 5.12, but for the August 2021 block, with means taken between 500-150 hPa.

diabatic modification analysis is focused on the time series due to the broadly similar spatial pattern of diabatic tracer between the three case studies.

Total diabatic loss of PV peaks early in the block, with a similar magnitude to the February 2019 case. Like with the February 2019 case, the onset of the August 2021 block is associated with widespread loss of PV in a large portion of the block, and coincides with a larger region of diabatic heating in excess of 20 K (Fig. 5.28). In the first few days of the block, the most important contributor to PV decreases is Δq_{cloud}. Unlike the two case studies discussed earlier, Δq_{BL} is more significant than Δq_{conv} for most of the early stages of the block.

The diabatic reduction of PV does not last long however, and from 26 August onwards until the block decays, diabatic processes are acting to increase the PV

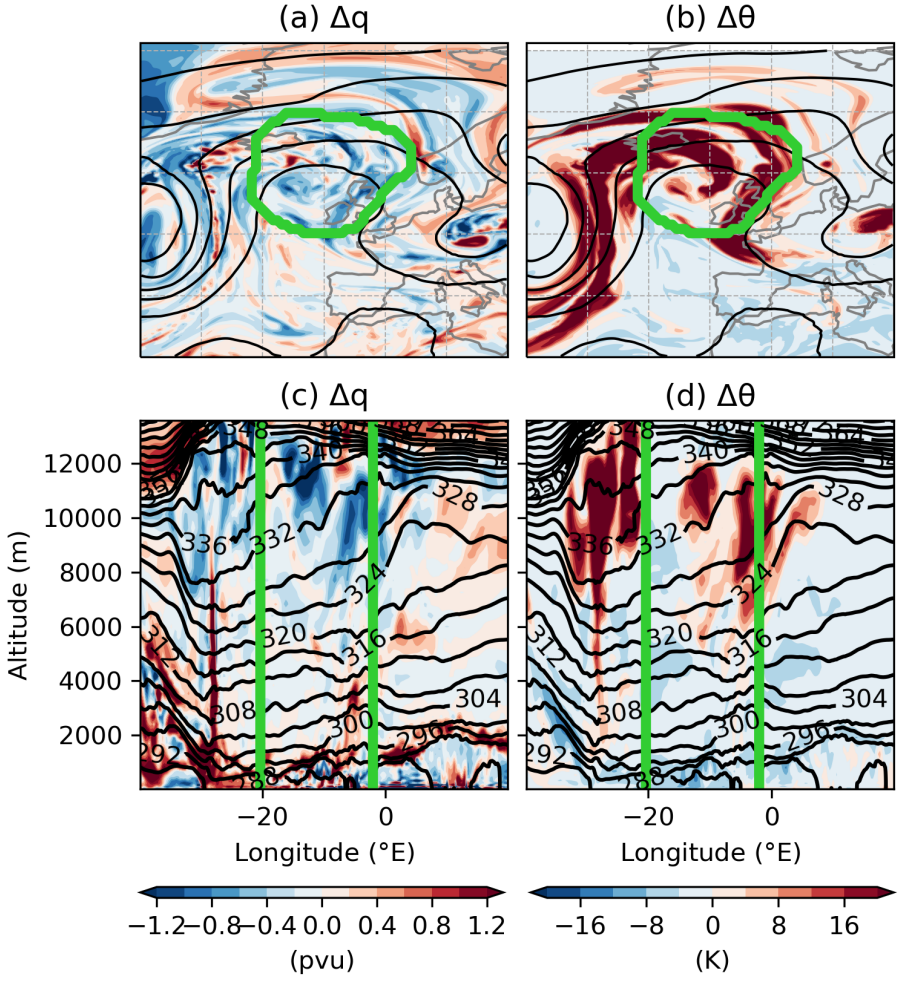

Figure 5.28: As in Fig. 5.20, but for 23-08-2021 12 UTC, in the early stages of the August 2021 block. Maps are shown here at a height of 10137.232 m and cross-sections at 60°N.

in the block instead, discouraging block development. As with the other blocks, Δq_{rad} is positive throughout and is almost entirely responsible for the gain of PV in the block. Δq_{GWD} is positive throughout, but similarly to the other blocks, has a very small contribution to the dynamics of the block. Once the magnitudes of PV loss from Δq_{conv}, Δq_{cloud} and Δq_{BL} decrease after 26 August, there is not enough PV loss to counteract the effect of longwave radiation, which results in the net positive Δq seen for the remainder of the block.

5.6 PV Budget Analysis for All Cases

A summary of all three case studies is presented in Fig. 5.29. The appropriateness of the MetUM to approximating the conditions inside the block is shown, by comparing terms from Eq. (5.17) in both the MetUM and ERA5 (Fig. 5.29a-c). Additionally, the decomposition of PV in the MetUM is shown in terms of the conserved, diabatic, and error PV terms (Fig. 5.29d-f). Finally, the time series from earlier in the text are repeated for the total PV flux convergence and upper-tropospheric diabatic PV change to examine the importance of each process at each stage of the blocks (Fig. 5.29g-i), and compare how they change the PV budget. Comparisons are also made between the three different blocks.

5.6.1 Comparison of PV Budgets

First, this section describes the evolution of the PV budget in each case study, and draws a comparison between the ERA5 and MetUM PV budgets shown in Fig. 5.29a-c. The PV budgets from the two models are remarkably consistent with each other in the February 2019 and August 2021 cases, especially given the 60-hour lead time of the MetUM results. However, while q_{ERA} and q_{UM} follow the same general pattern as each other for the March 2021 block, there are large differences (up to 2 pvu) between the two PV budgets, from 14–17 and 20–21 March. This disparity is just as apparent at shorter lead times (not shown), which suggests that the two models are simulating the PV signature of this block differently. A consistent signal throughout the three case studies is that $[q]$ is slightly larger in the MetUM than in ERA5. In the February 2019 and August 2021 cases,

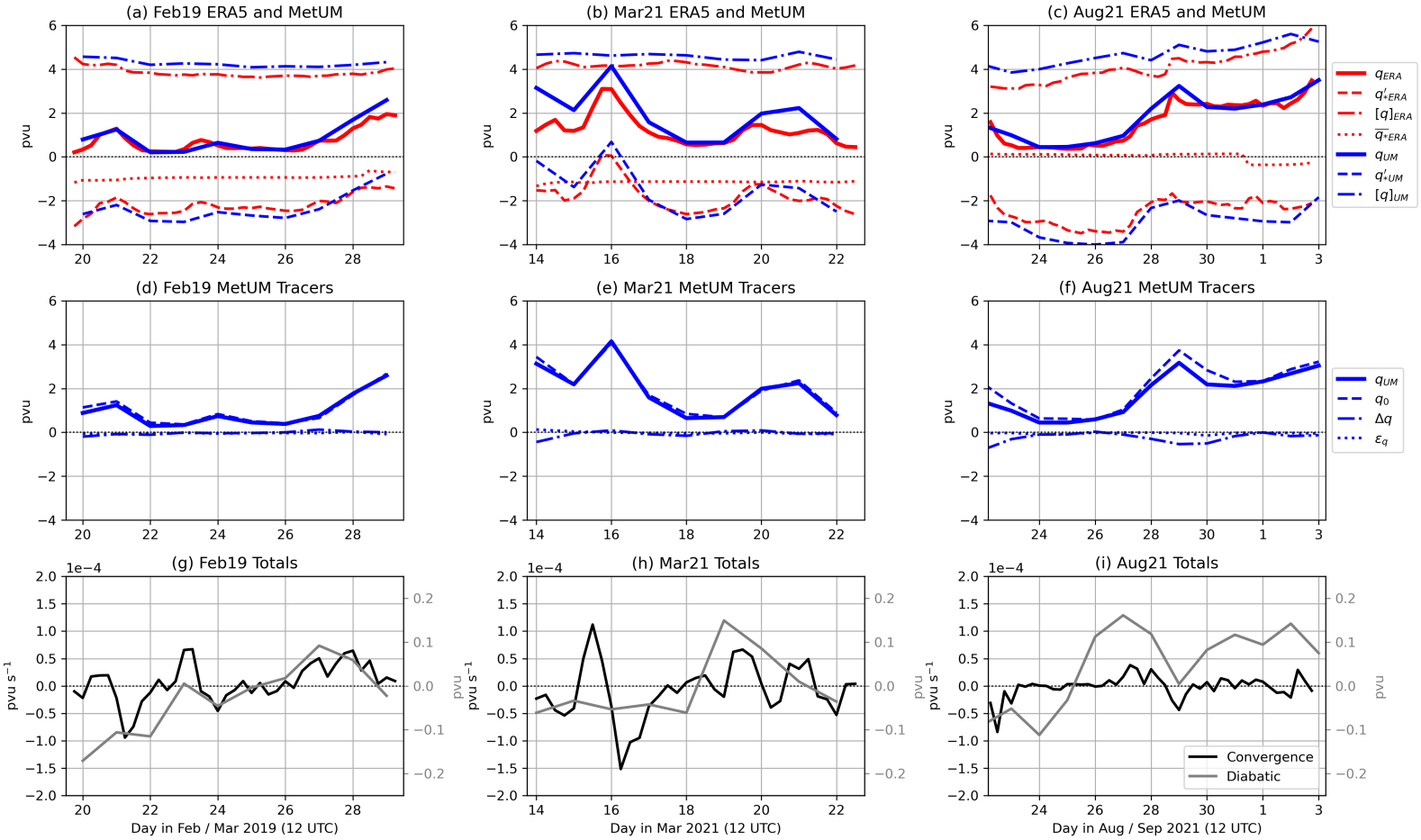

Figure 5.29: Quantities for the entire block for each case study. (a-c) Comparison of terms from Eq. (5.17) on the appropriate isentropic surface as calculated using ERA5 (red) and 60 hour forecasts from the MetUM (blue). Solid lines show the total PV, dashed lines show the anomalous PV, dash-dotted lines show zonal mean PV, and the dotted line shows background PV from ERA5 only. (d-f) Decomposition of the MetUM PV budget (solid) on the isentropic surface in terms of conserved PV (dashed), diabatic change to PV (dash-dotted), and error term (dotted), from 60 hour forecasts. (g-i) Total PV flux convergence on the isentropic surface (black) and 60-hour upper-tropospheric diabatic tracer accumulations (grey). Results are shown for each case study: February 2019 (left) on the 320 K surface, with diabatic tracer accumulations from 500-200 hPa; March 2021 (centre), as the February 2019 case study; and August 2021 (right), on the 330 K surface, with diabatic tracer accumulations from 500-150 hPa.

the MetUM also has a slightly larger magnitude q'_* term than ERA5, whereas the relationship is more varied in the March 2021 block. The majority of the disparities between the total q between the MetUM and ERA5 in the March 2021 block comes from differences in how q'_* is evaluated in the two models.

At the beginning of the February 2019 block, its q'_* is negative and large-magnitude. Until 28 February, the block's q'_* fluctuates around -3 to -2 pvu. Meanwhile, $[q]$ in the block is very stable at just under +4 pvu throughout the block event, and the $\overline{q_*}$ is constant at -1 pvu apart from a slight increase when the calendar month changes. These three components mean that q_{ERA} fluctuates between 0 and +1.5 pvu as the q'_* also fluctuates, apart from 27 February onwards where q gradually increases to +2 pvu at decay.

In a similar way to the February 2019 block, the dominant factor in determining the variation in q_{ERA5} in the March 2021 block is the q'_* term, which fluctuates from 0 to -3 pvu. Most of this fluctuation arises from PV streamers and the replenishment of negative q'_* following these incursions of high-q'_* air. Both $[q]$ and $\overline{q_*}$ are steady throughout the block, at +4 and -1 pvu respectively.

The PV budget in the August 2021 block appears to have two stages to it. In the first, from 22-27 August, q'_* is fairly constant at -3 to -4 pvu, and $[q]$ is also constant at +3 to +4 pvu. Along with a negligible $\overline{q_*}$, this means that in this stage of the block, the total PV, q, is about +0.5 pvu. However after this period, from 28 August onwards, there is a reduction in magnitude of q'_* by about 1 pvu, and a similar magnitude increase in $[q]$. As a result, the block's mean PV exceeds 2 pvu during this time. This reduction in block strength coincides with the loss of three spawned eddies (and as a result, the loss of distinct q'_* minima) from the block interior, along with a stretching of the block in the zonal direction and PV streamers entering the blocking region.

5.6.2 Comparison of MetUM Components

Here, the contribution of the conserved and diabatically-modified PV tracers to q_{UM}, with a 60-h accumulation, on a single isentropic surface, is discussed for each block event. These are shown in Fig. 5.29d-f. For all three blocks, the vast majority of the MetUM PV budget consists of conserved PV, q_0, with diabatic

change to PV on this surface, Δq and the error term, ε_q very small in comparison. The only exceptions to this occur at block onset, where Δq is slightly larger in magnitude and negative, especially for the onset of the August 2021 block where it approaches -1 pvu. A secondary maximum in PV loss via diabatic processes also occurs in the August 2021 block, again nearing -1 pvu, around 29 August.

5.6.3 Comparison of Blocking Dynamics

Finally, the importance of two processes in the block - PV flux convergence on an isentropic surface, and upper-tropospheric PV modification - will be compared for the three blocks. The reasons for the shapes of the curves shown in Fig. 5.29g-i have already been discussed in earlier sections; therefore this section will examine the similarities and differences in these dynamical processes between the three blocks, and link them to changes in each block's PV budget (Fig. 5.29a-c).

The magnitudes of total PV flux convergence are weakest in the August 2021 block and largest in the March 2021 case. The *magnitude* of the diabatic PV modification for all three blocks is similar; however diabatic *reduction* in PV is largest in February 2019 and smallest in March 2021. On the other hand, diabatically-driven PV *increases* are largest, and more consistent, in the August 2021 case and smallest in the February 2019 block.

Peaks and troughs in PV modification by diabatic processes and convergence align fairly well with peaks and troughs in each block's PV budgets in the February 2019 block. The reduction in block-mean q from 21–22 February coincides with a marked maximum in PV flux divergence, along with sustained diabatically-induced PV loss. Similarly, the maximum in PV flux convergence and reduction in diabatic PV loss on 23 February is accompanied by a small increase in block-mean PV. Likewise as the block decays, there is modest PV flux convergence and PV gain from diabatic processes, and as a result q increases.

The dynamics behind the March 2021 block's PV budget are more complicated. Block onset is marked by slight PV flux divergence and diabatic PV loss, which results in the slight decline in block-mean PV from 14–15 March. On 16–17 March, the mean PV in the block sharply increases and then rapidly decreases again, which is the result of strong PV flux convergence and divergence

in quick succession. Two smaller-amplitude peaks in block-mean PV coincide with smaller peaks in PV flux convergence on 19 and 21 March. The PV of the block is at its smallest as the block decays, during the time of noisy and variable PV flux convergence and small-magnitude diabatic PV modification.

Onset of the August 2021 block is characterised by a slight reduction in block-mean q, associated with very weak PV flux divergence but relatively strong diabatic PV loss. However, the PV signature in the block quickly stabilises as PV flux divergence becomes negligible and the potency of diabatic PV reduction rapidly reduces. The previously-mentioned increase in PV in the second half of the block coincides with a prolonged period of negligible PV flux divergence and diabatic PV gain.

5.7 Summary and Conclusions

This chapter investigates the hypothesis that blocks with a similar persistence, but with differing numbers of contributing AC eddies, have varying contributions towards their dynamics from adiabatic and diabatic processes. Three cases studies with a block persistence of 9–12 days are analysed to test this hypothesis: February 2019 (2 AC eddies), March 2021 (1 AC eddy) and August 2021 (0 AC eddies). Their PV budgets are calculated and processes contributing to this are determined. Firstly, isentropic PV flux convergences from ERA5 (assumed to be the adiabatic component) are found for each block, and the contribution of AC eddies to these convergences also analysed. Secondly, the diabatic contribution to upper-tropospheric PV modification is found by utilising the diabatic tracer tools in the MetUM. The main findings are discussed here.

The early stages of each block are characterised by both PV flux convergence and diabatic reduction of PV. These both have the effect of reducing PV within the block at onset, consistent with block formation. Despite coinciding with regions of high-magnitude negative anomalous PV, the AC eddies in these case studies are not responsible for a large amount of the total PV flux convergence/divergence inside the blocks. This is because for most of their lifetime, the AC eddies are situated within the interior of the block where PV gradients and winds are light. As

such, PV flux convergence is often maximised around the periphery of the block where gradients and winds are greater. However, when AC eddies first enter (or leave) a block, they are responsible for bringing their associated PV characteristics towards the block and therefore in these cases will contribute more to the PV flux convergence/divergence within the block. Another factor that was not considered in determining block persistence in the previous Chapter was how many spawned eddies a block produces. These spawned eddies can also be expected to induce PV gradients around the edges of the block as they exit the block interior, and are also shown to be somewhat important in some of the cases studied here.

PV flux convergence magnitudes were found to be smallest in the block with 0 AC eddies (August 2021), and largest in the block with one AC eddy (March 2021). On the other hand, the size of diabatic modification to PV did not appear to depend on the number of AC eddies a block interacted with, and in fact, the block with 0 AC eddies also had the strongest and most prolonged PV increases from diabatic processes. This means that the block with the weakest PV reduction from negative PV flux convergence also had the strongest PV gain from diabatic effects. It is therefore unclear as to how this block was able to be as persistent as it was, given very weak forcing from both adiabatic and diabatic processes. Further questions are raised towards the maintenance of blocks when spawned eddies are also considered, of which both the March 2021 and August 2021 cases show. It could be expected that these eddies act to take away anomalously low PV from the block and increase block PV. This might be the case in blocks where spawned eddies leave the block from its eastern boundary (as seen in the March 2021 block), however in the August 2021 block all spawned eddies exit the block from the north. This has the effect of providing a dipole of PV flux convergence and divergence on each flank of the spawned eddy, leading towards a net-zero effect on the block's PV on the whole. Therefore, further investigation is required into blocking cases where spawned eddies leave the block towards the east to study whether they do in fact cause a decrease in block intensity. Similarly, more cases are required for studying when AC eddies enter a block from the west to determine whether or not they increase block intensity, as was the case in March 2021.

The hypothesis that blocks with more AC eddies have a smaller contribution towards blocking dynamics from diabatic effects is also challenged by the February 2019 case. It was the block with the most AC eddies, so it might have been expected that it was going to be the block with the largest contribution towards its dynamics from PV flux divergence, and the least from diabatic effects. However, it was the second-highest in both of these categories. This also strongly suggests that a much larger sample size is required to be able to make robust conclusions either confirming or denying this hypothesis entirely. Unfortunately, this was not possible in this work due to the time and computing constraints involved in running the MetUM. Another important aspect that was not considered in previous work, but appears to be important in determining fluctuations in a block's PV budget is the impact of regions of positive PV anomalies. In all three case studies examined here, PV streamers of positive q'_* enter the block at different times, temporarily leading to positive PV flux convergence and thus increasing the block's PV. The number and/or intensity of these small-scale PV streamers could therefore also be important in determining how long a block is able to persist for.

Another important point that also challenges the hypothesis is that in each of the three blocks, the magnitude of diabatic loss of PV was considerably smaller than that from PV flux convergence. Diabatic effects can therefore be thought of as providing an additional "push" towards block formation/decay, on top of the dominant effect of PV that is advected into or out of the block. This is somewhat different to the findings in Hauser et al. (2022), where although diabatic processes were also not the most important processes towards block maintenance, they seemed to have a larger role than the results presented in this Chapter suggests. Though a larger sample size than four blocks is needed (one in Hauser et al. (2022) and three here), this provides further evidence that the role of diabatic PV modification is highly variable. Indeed, the results in this thesis also show that the main source of diabatic PV loss in blocks can also be different. In the February 2019 and August 2021 cases, parameterisation of cloud processes was the most influential process that reduced PV at block onset, whereas in March 2021, convection parameterisation was largest. Both of these sources however confirm that WCB activity plays a role in blocking dynamics, agreeing with previous work

(e.g. Steinfeld and Pfahl, 2019).

Throughout this Chapter, it has been assumed that the effects of AC eddies and diabatic processes on the block are independent of each other. The aim of this was to determine whether PV flux advection (via the eddies) or diabatic PV modification is most important for the three blocks examined here. However, it is highly likely that their effects on blocking cannot be considered entirely separately in this way and further study is required in order to unite these two processes. Since mid-level diabatic heating leads to the generation of an upper-level negative PV anomaly, it is possible that the q'_* AC eddies that interact with blocks are themselves caused, or at least enhanced, by diabatic processes. Thus, the role of diabatically-modified PV for the dynamics of these three blocks is likely to be greater than that determined in this study, potentially closer to the values found in Hauser et al. (2022).

Finally, the results presented here demonstrate that despite the stationarity of blocking events, their dynamics are a lot more variable and non-stationary. While the Z500 signature of blocks might remain fairly constant throughout the event, upper-level PV within blocks is far more mobile, and sources of anomalously low PV are constantly advected out of the block and replaced by another one from upstream. Had AC eddy tracking been performed on anomalies in PV rather than Z500, one would expect the three blocks examined here to have even more PV AC eddies than Z500 ones, and therefore the results could have been different. Further work could therefore instead track q'_* centres and analyse the relationship between block persistence and the amount of PV eddies a block interacts with.

Chapter 6

Forecasts of Anticyclonic Eddies and their Impacts on Block Forecasts

6.1 Introduction

In Chapter 4, it was shown that there is a statistical relationship between the persistence of a block and the AC eddies those blocks interact with. Furthermore, it was demonstrated that AC eddies act to increase the size and/or the intensity of the block that they enter, and the results in Chapter 5 show that AC eddies act to promote block development when they first enter a block. Additionally, it was shown in Chapter 5 that diabatic dynamics can also influence block development, but are of a lesser importance than dry dynamics. Thus far in the thesis, the action of AC eddies and diabatic processes towards forecasts of blocking have not been discussed. It is important to consider these because blocked weather patterns have been shown to lead to forecast busts (Rodwell et al., 2013) and are the least predictable weather regime (Ferranti et al., 2015).

This chapter focuses on the importance of accurate AC eddy forecasting to accurate forecasting of blocks. Recent work has shown that the representation of cyclonic eddies has an impact on the skill to which blocking is forecast (Maddison et al., 2019), where more accurate cyclonic eddies in forecasts result in better blocking forecasts. However, it is unknown whether a similar relationship is found in forecasts of AC eddies and blocks.

The choice to test the effect of AC eddies on blocking forecasts, rather than that of diabatic dynamics, is motivated by the study of Selz et al. (2022). In their work,

it is concluded that while mid-latitude planetary-scale predictability is limited by the upscale interaction of diabatic heating within clouds, the initial condition uncertainty is more important in the medium-range. Therefore, this chapter tests the hypothesis that the representation of AC eddies in forecasts also affects the forecasts of the blocks that they interact with, through the use of an ensemble forecast. The use of an ensemble means that a greater range of initial condition uncertainty is sampled and simulated (Leutbecher and Palmer, 2008). In particular, the size, strength, location, and timing of AC eddies interacting with the example blocks investigated in the previous chapter is explored to examine whether these factors affect the persistence, size, location, and intensity of the blocks.

6.2 Methods and Data

6.2.1 Data Source

The data used in this chapter are obtained from daily MOGREPS-G (Sect. 3.1.3) forecasts, initialised at 00 UTC. The forecasts analysed run for 8 days, and are all focused around two of the three case studies analysed in the previous chapter (initialised 10–28 February 2019, and 8–22 March 2021). Since the August 2021 block has no AC eddy interactions, it is not analysed in this chapter. Forecast Z500 and isentropic PV (on the 320 K surface) are used to derive instantaneous Z'_* and q'_* fields for the control forecast (referred to as "member 0" in what follows) and all 17 perturbed members ("members 1–17"). The MOGREPS-G anomaly calculations require the background climatology, $\overline{Z_*}$ or $\overline{q_*}$ (Sect. 3.2.1). Ideally, this background state would be derived from the MOGREPS-G climatological analyses of Z500 and PV fields. However, there is no long-term record of such variables from MOGREPS-G, since the model is continuously updated and therefore a meaningful climatology cannot be obtained. Therefore, the background state from ERA5 is used in these calculations. It is assumed that the differences between the MOGREPS-G analysis and ERA5 reanalysis are negligible for this work. Finally, for comparison with the instantaneous ERA5 Z'_* and q'_* fields, which are assumed to be the "truth", the MOGREPS-G data are regridded from their native resolution (N640, equivalent to a grid-spacing of approximately 20 km in the

mid-latitudes) to the F128 resolution used with the ERA5 data.

6.2.2 Forecast Skill: The ZAL Metric

The performance of each blocking forecast is evaluated using a methodology based on the SAL (Structure, Amplitude, Location) calculation for determining the accuracy of precipitation forecasts (Wernli et al., 2008), and the PAL (PV anomaly, Amplitude, Location) metric used for verification of PV in WCB outflow (Madonna et al., 2015). In this work, it is termed as the "ZAL" metric, which evaluates the performance of a forecast in predicting the (i) strength, Z, (ii) area, A, and (iii) location, L, of a block, compared to ERA5 reanalysis. ZAL is calculated over a particular domain that is large enough to capture the majority of the block in both reanalysis and forecasts throughout the verification period.

Z is a comparison between the normalised domain-mean, block only ($\langle ... \rangle$) strength of the instantaneous anomalous Z500 field, Z'_*, in the forecast ("f") and reanalysis ("r"), and takes a value between -1 and 1, i.e.:

$$Z = \frac{\langle Z'_{*f} \rangle - \langle Z'_{*r} \rangle}{\langle Z'_{*f} \rangle + \langle Z'_{*r} \rangle} \tag{6.1}$$

A positive Z indicates that the forecast is overpredicting the instantaneous block strength compared to ERA5, and vice-versa. The term A compares the normalised instantaneous block area, A_{inst}, between the forecast and reanalysis, and is again between -1 and 1:

$$A = \frac{A_{inst,f} - A_{inst,r}}{A_{inst,f} + A_{inst,r}} \tag{6.2}$$

When A is positive, the forecast overpredicts the instantaneous block area. Finally, L compares the locations of the centres of the block, $\mathbf{x}$, in the forecast and reanalysis, and is always between 0 and 1:

$$L = \frac{\mid \mathbf{x_f} - \mathbf{x_r} \mid}{d} \tag{6.3}$$

where d is the distance of the longest great circle line drawn in the domain. A higher L indicates a worse forecast in the position of the block.

The ZAL metric can also be used to identify forecasts that replicate the char-

acteristics of the block well. Since Z, A, and L are all normalised values between -1 and 1 (0 and 1 for L), the Cartesian distance (D) of a forecast's point in ZAL space from the perfect forecast (at the origin, $Z = A = L = 0$) shows how well the forecast performs. Therefore, where the result of:

$$D = \sqrt{Z^2 + A^2 + L^2} \tag{6.4}$$

is small, a particular forecast is said to be a "good" forecast.

6.2.3 Predictability Barriers

Uncertain periods in a forecast can be visualised by plotting a certain measure of forecast error on a graph of forecast lead time (h) against initialisation time (t_{in}), such that the forecast validity times ($t_{val} = t_{in} + h$) are seen as diagonal-sloping lines. This is shown in Fig. 6.1, where $t_{val,1}$ is earlier than $t_{val,2}$. Normally, one would expect the forecast error to increase as h increases, because ensembles tend to diverge at longer lead times. On a graph of h against t_{in}, this would lead to hor-

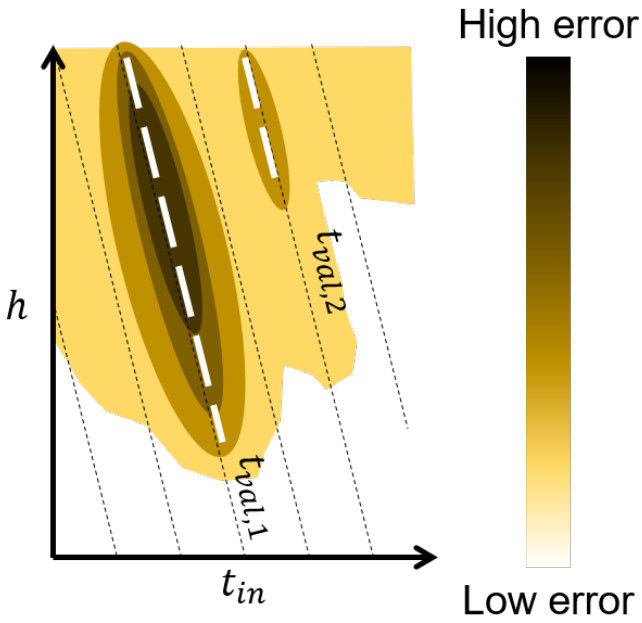

Figure 6.1: Schematic of the error of the ensemble in a given metric (see text for details), as a function of forecast initialisation time, t_{in}, and forecast lead time, h. Constant validity times, t_{val}, are depicted by the diagonal dashed black lines. White dashed lines at $t_{val,1}$ and $t_{val,2}$ indicate examples of predictability barriers (PBs, see text for definition).

izontal stripes of gradually increasing error from bottom to top. However, sometimes periods of enhanced unpredictability emerge as regions of increased error that follow a line of constant t_{val}. Shown in Fig. 6.1 by the dashed white lines, these events are sometimes referred to as "predictability barriers" (PBs, similar to those defined in Sánchez et al. (2020)). PBs are synoptic events at a particular validity time that exhibit poor predictability for a range of forecast initialisation and lead times. Such barriers are often only overcome at later initialisation times, with shorter lead times. For example, the PB at $t_{val,1}$ in Fig. 6.1 is only overcome by the ensembles with later initialisation times (at very short lead times), whereas the PB at $t_{val,2}$ is able to be resolved more quickly.

In this work, PBs are identified by validity times that have a large Z_{mean} and/or A_{mean} and/or L_{mean} at many initialisation times, where Z_{mean}, A_{mean}, and L_{mean} are the mean Z, A, and L values from each ensemble member. Mathematically, this is expressed for $Z_{mean}(t_{in}, h)$ as:

$$Z_{mean}(t_{in}, h) = \frac{1}{N_{mem}} \sum_{n}^{N_{mem}} Z_n(t_{in}, h) \tag{6.5}$$

where N_{mem} is the total number of ensemble members and Z_n is the Z value that ensemble member n has, for example. $A_{mean}(t_{in}, h)$ and $L_{mean}(t_{in}, h)$ are determined in an equivalent fashion to Eq. 6.5. If an ensemble member has no instantaneous blocking at that t_{val}, it is excluded from the above calculations. These steps are then repeated for each h from each t_{in}, such that the mean ZAL statistics are derived for each t_{val} from a combination of different initialisation and lead times. These mean quantities are then plotted like in Fig. 6.1 to identify the more unpredictable periods of blocking.

PBs, if present, are identified for the February 2019 and March 2021 blocks examined in the previous chapter. If any of the validity times of the PBs are close to the timings of any AC eddy interactions with the block, they are chosen to be studied in more detail to examine whether the poor forecast performance depends on how AC eddies are represented in the ensemble.

Once a PB has been identified, the individual forecasts are examined in more detail. In the work that follows, forecasts from a single t_{in} are chosen for further

analysis. The t_{in} is chosen such that its members at the PB validity time have a large spread in their Z, A, and L values, which indicates increased uncertainty in the forecast. These members are then plotted on a "ZAL diagram", which shows the degree to which each member deviates from ERA5 in block area, intensity, and location. An example is given in Fig. 6.2. In this case, the ensemble member denoted by the circle symbol is closest to ERA5, since it has the smallest Z, A, and L.

The ZAL diagram is used to subjectively select ensemble members with the aim of producing a smaller ensemble. Each small group consists of members from the same initialisation time that represent the block in a similar way such that a mean of this smaller group is representative of all members within it. Two additional checks are required to ensure that the members being grouped together are similar realisations of the block event. Firstly, their distance from the ZAL origin is calculated, and members are only considered to be similar to each other if this distance is similar. Secondly a manual check is required to examine maps of Z'_* for each member in each ensemble to ensure they look similar to each other. To aid with this second manual check, a group of webpages was created in associa-

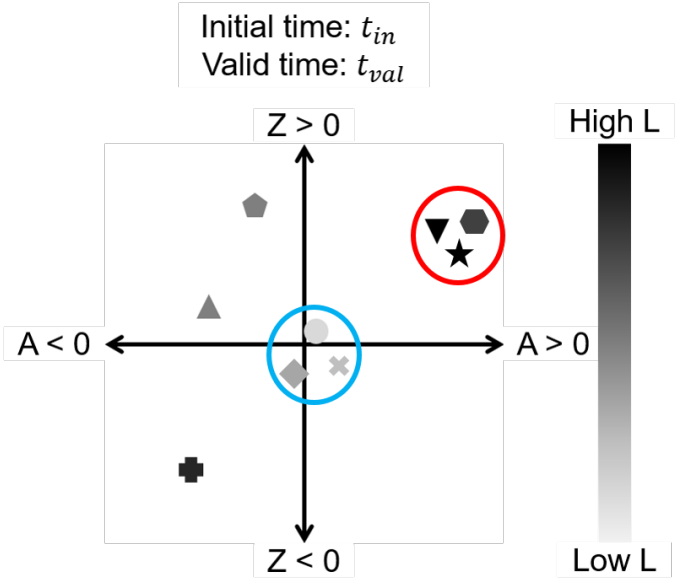

Figure 6.2: Schematic showing a ZAL diagram for a particular valid time, t_{val}. Each shape represents a different ensemble member, initialised at the same initialisation time, t_{in}. Z, A, and L are calculated in a specific domain only. The red and blue rings indicate groups of ensemble members with similar ZAL characteristics, and are used to highlight the members to be used as part of their own smaller ensemble.

tion with Duncan Ackerley and Dan Suri at the Met Office, which shows postage stamps of the Z'_* pattern for all members, along with other useful output. More detail on this MOGREPS-G blocking identification tool is given in Sect. A.2.

Examples of two groups of members are shown by the blue and red rings in Fig. 6.2. Creation of these smaller groups is preferred over analysis of individual ensemble members to reduce the impact of the individual initial conditions on the evolution of the forecasts. This subjective method is also simpler than a more sophisticated method of grouping together ensemble members, using for example k-means clustering, but along with the manual check of the Z'_* fields, it is still able to group together members that represent the block in a similar way because of the small number of cases that are studied here.

Group-mean Z'_* and q'_* are computed for every group for each t_{val}, and these fields are compared to ERA5. In particular, the Z'_* field in the small ensembles around the location of the ERA5 tracked AC/spawned eddies is scrutinised, to determine the characteristics of the eddy in the forecast and examine the consequences in terms of forecasted block evolution.

6.2.4 Summary of Methods

A brief summary of the steps required for analysing the representation of AC eddies and their effects on block forecasting is given below.

1. Compare the forecasted block strength, size, and location in MOGREPS-G to ERA5. This is done for each ensemble member, at each appropriate t_{in} and h, using the ZAL metric.

2. Calculate Z_{mean}, A_{mean}, and L_{mean}, using the ZAL values from each ensemble member, at each appropriate t_{in} and h.

3. Identify PBs at a given t_{val} from Z_{mean}, A_{mean}, and L_{mean}, derived from a combination of different t_{in} and h.

4. Choose PBs that coincide with block-AC eddy interactions. For a forecast from a single t_{in} at this t_{val} with a large spread in the ensemble, create a ZAL diagram.

5. Use the ZAL diagram to assign some members to smaller groups that simulate the block similarly. Members in these groups will:
   - Appear in a similar position on the ZAL diagram,
   - Have a similar distance from the origin, D, and
   - Have a similar Z'_* pattern around the block at t_{val}, determined by manual inspection.
6. Examine the group-mean Z'_* fields before, during, and after the PB, determining whether any forecast errors or uncertainty is caused by misrepresentation of AC eddies.

6.3 February 2019

6.3.1 Mean ZAL

The ensemble mean ZAL metrics, initialised from each t_{in} as a function of h, for forecasts around the February 2019 block, are shown in Fig. 6.3. ZAL results are shown for the sector between 30°W – 30°E, 30–75°N since the block is predominantly situated inside this area throughout. The magnitudes of the errors are largest in A and smallest in Z. In general, the magnitudes of mean Z, A, and L increase as lead time increases, for most initialisation times. However, two PBs are evident, particularly in A, where the magnitude of forecast error is largest at shorter lead times. The first PB, valid around 20–21 February, is associated with overestimation of block strength (Fig. 6.3a) and area (Fig. 6.3b), and also has a slight positional error. This PB coincides with block onset (20 February). The later, broader PB, from 28 February – 3 March, shows that the ensemble somewhat overpredicts block strength (Fig. 6.3a) whilst simultaneously underpredicting the instantaneous blocking area (Fig. 6.3b), with more of a positional error than the onset PB (Fig. 6.3c). The block event finishes in early March so this PB is associated with the mistiming, and the extent to which, the instantaneously blocked points decay in this domain.

Since the PBs are most evident when comparing instantaneous block area, the ensemble mean RMSE and ensemble spread in instantaneous block area are also

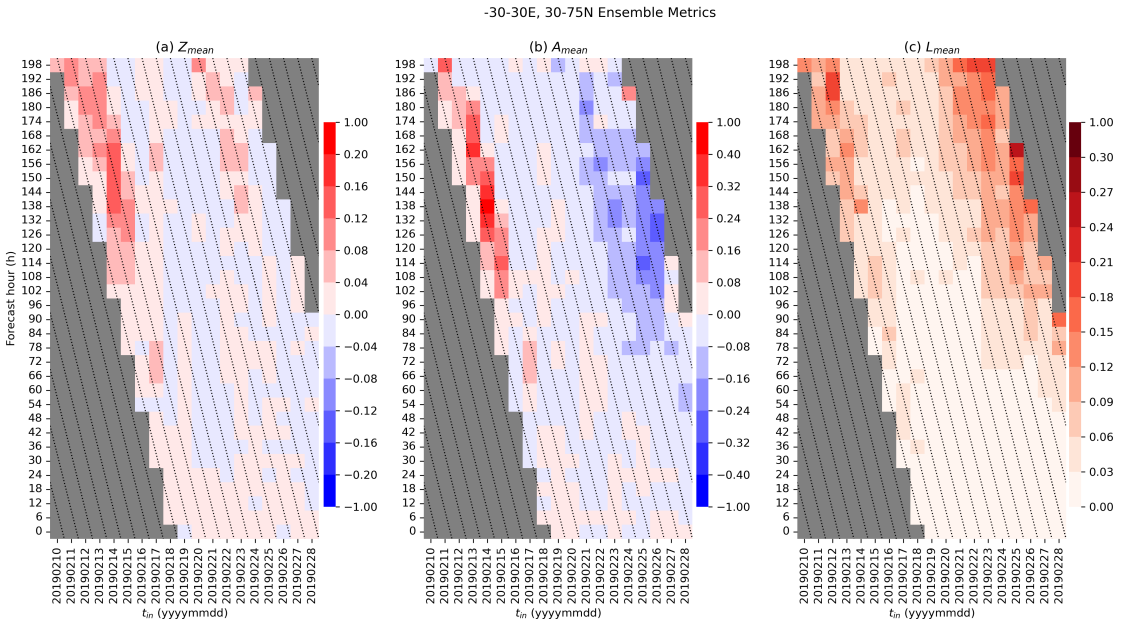

Figure 6.3: Ensemble mean ZAL metrics during the February 2019 block: mean strength error, Z_{mean} (a), mean area error, A_{mean}, and mean location error, L_{mean} (c), between 30°W–30°E, 30–75°N, as a function of forecast initial time (t_{in}) and forecast lead time (h). Grey squares indicate periods where instantaneous blocking was not present in either dataset, or times outside of ± 2 days of the ERA5 block event).

analysed for the February 2019 block. These are shown in Fig. 6.4. Again, RMSE and spread mostly increase for all initialisation times as lead time increases. However, the same PBs visible in Fig. 6.3 are also seen in the RMSE and ensemble spread. Furthermore, the magnitude of the ensemble mean RMSE is larger than the ensemble spread during these PBs, so it can be concluded that during PBs, the ensemble is underdispersive.

6.3.2 Block Onset Predictability Barrier

First, the PB associated with the onset of the block and the first AC eddy (validity time of 20 February 2019 06 UTC; PB1) is analysed in more detail. The ZAL for each ensemble member at this t_{val} from forecasts initialised from 13–20 February, and the ensemble means, are shown in Fig. 6.5. As shown in Fig. 6.3, the mean Z and A remain relatively high and relatively constant for a t_{in} of 13, 14, and 15 February. Thereafter, mean Z and A magnitudes decrease, and the spread eventually reduces, indicating that the PB has been overcome by the ensembles. Excluding the forecast initialised on 18 February, the ensemble overpredicts block

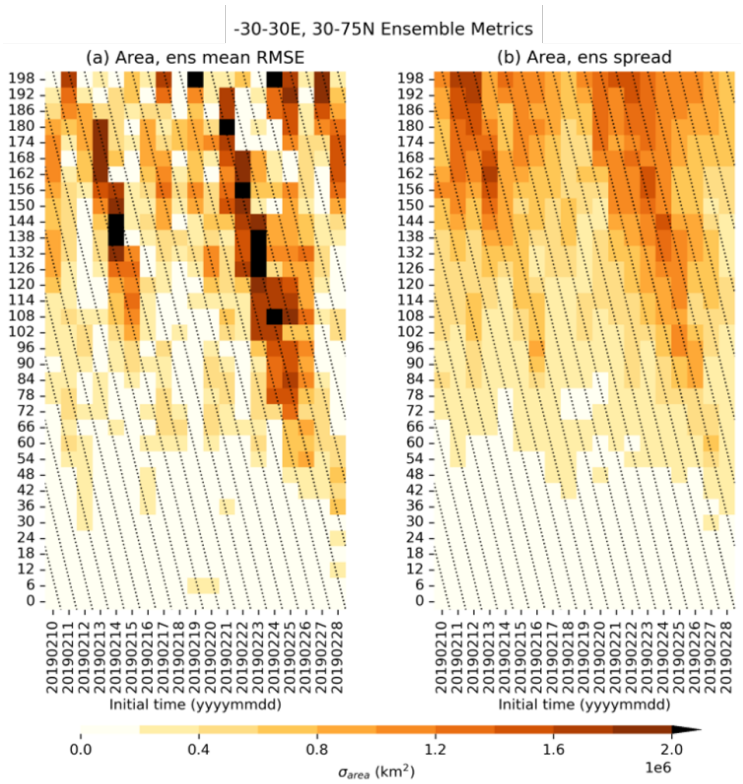

Figure 6.4: Ensemble mean RMSE (a) and spread (b) in instantaneous block area, in the same domain as in Fig. 6.3, for the February 2019 block, as a function of forecast initial time (t_{in}) and forecast lead time (h).

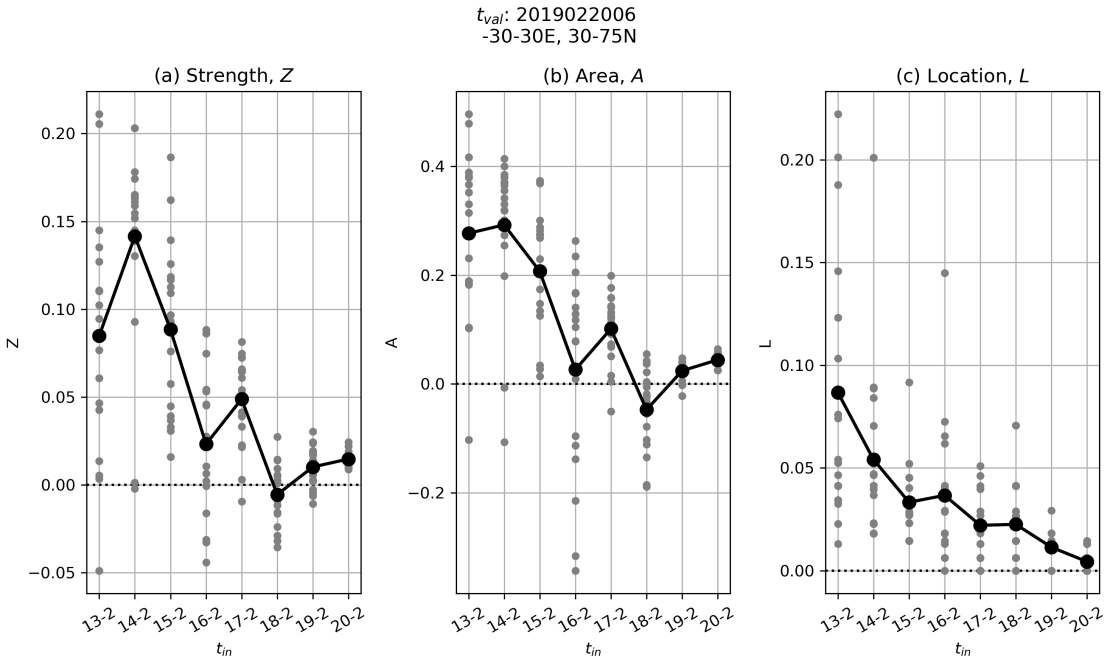

Figure 6.5: ZAL statistics, valid at the predictability barrier on 20 February 06 UTC, for each ensemble member (grey) for initialisation times from 13–20 February. Z_{mean} (a), A_{mean} (b), and L_{mean} (c) are shown as a time series in black.

area and strength in the mean. As lead time reduces, the location of the block's centre is predicted better.

During this PB for forecasts initialised on 13–15 February, the majority of members overpredict the intensity and area of the block by up to 20% and 50% respectively. Only two (three) members in forecasts initialised on these three days underestimate the instantaneous block intensity (block area). Even though the ensemble spread reduces in forecasts initialised closer to the PB, the forecast initialised on 16 February ($h = 78$ hr) is particularly interesting. Z_{mean} and A_{mean} are around zero but with considerable spread around this from the individual members. While two-thirds of the members overpredict block strength and intensity, the remaining third strongly underestimate these block metrics. Therefore, forecasts from this valid time warrant further investigation.

A ZAL diagram for the forecast initialised on 16 February, and distance of each ensemble member from the origin, valid for this PB, is shown in Fig. 6.6. It reiterates the fairly large spread between the ensemble members despite the mean being close to the origin. The members that underpredict block strength also underpredict block area, and vice versa. However, there is less spread in the location of the centre of mass of the forecasted block than there is of the area and intensity. For this reason, after manual inspection of the Z'_* field for each ensemble member individually to check that the forecasts in the following groups appear similar (not shown - see Sect. A.2 for an example from another case study), it was decided that three groups could be created. The three groups consist of means of members that underestimate the block area and intensity (Group A),

Name	**Members**	**Description**
MOGREPS-G	0–18	All-member ensemble mean
Group A	3, 8, 15, 16	Members that underpredict block area and intensity
Group B	0, 1, 5, 7, 10, 11, 13	Members that are closest to the origin in Fig. 6.6, i.e. that resemble the ERA5 block the closest at t_{val}
Group C	12, 14, 17	Members that overpredict block area and intensity the most

Table 6.1: Description of the groups analysed for the onset PB of the February 2019 block.

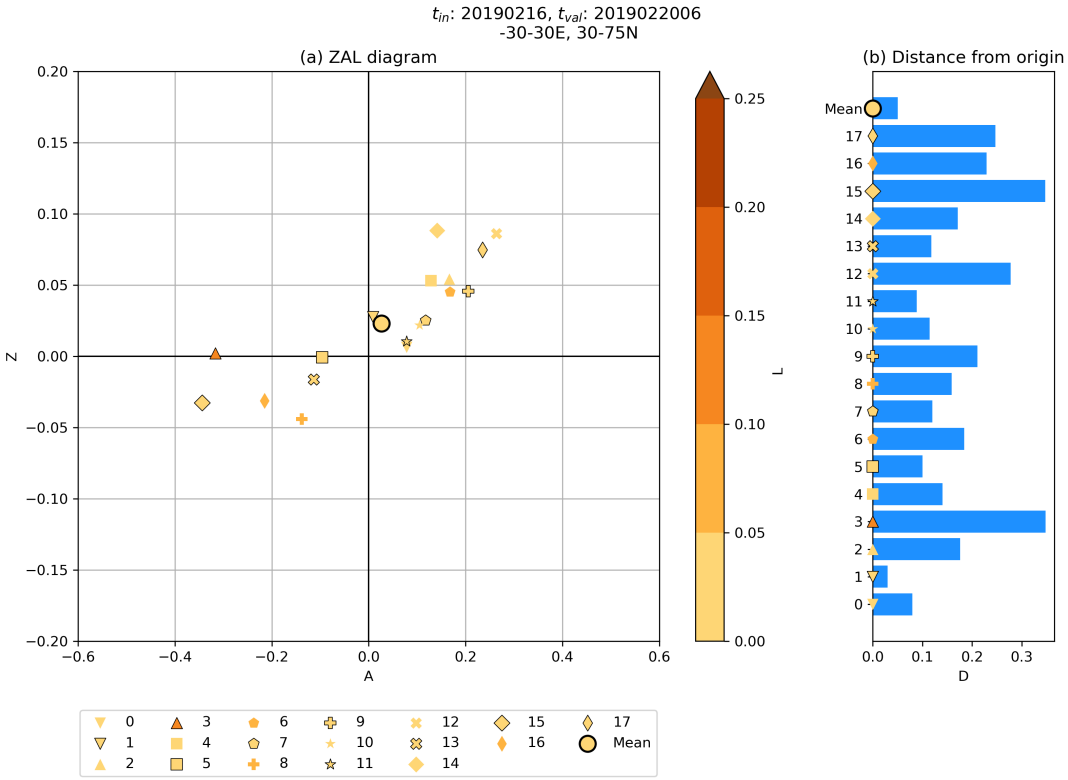

Figure 6.6: (a) ZAL diagram for the ensemble forecast initialised on 16 February 2019, 00 UTC, and valid at 06 UTC on 20 February 2019. Each shape corresponds to a different (labeled) ensemble member, and the mean is shown by the large circle with a thick black outline. (b) Distance of each ensemble member from the origin ($Z = A = L = 0$).

one that performs well in terms of area and strength (Group B), and one that overpredicts the block area and intensity (Group C). These groups will also be compared to the entire MOGREPS-G ensemble mean. Groups A, B, and C are summarised in Table 6.1.

Now, the representation of AC eddies in the entire MOGREPS-G mean, and Groups A-C are studied. Three t_{val} are examined - 18 hours before the PB (19 February 12 UTC, Fig. 6.7), the PB itself (20 February 06 UTC, Fig. 6.8), and once the PB has been overcome (23 February 00 UTC, Fig. 6.9). On 19 February, a pre-existing AC eddy moves eastwards to the eastern edge of the domain, which is captured well in all four group means. The small group of instantaneous blocking over Iceland in ERA5 (Fig. 6.7a) becomes the AC eddy that enters the yet-to-form block[1]. The MOGREPS-G ensemble mean represents the size, position, and

[1]This feature is recognised by TRACK as an AC eddy at this point, but later merges with a wave-breaking event in this region. The resulting anticyclonic Z'_* centre becomes the tracked AC eddy that merges with the block.

intensity of this AC eddy fairly well (Fig. 6.7b, g). Groups A and B have the AC eddy slightly too far to the northwest, which leads to slight negative Z'_* errors to the north of Scotland, though the q'_* field still compares well to ERA5. However, the northwestern extent of the AC eddy in Group B is greater. Conversely, the AC eddy in Group C is too large and slightly too intense, resulting in positive Z'_* errors in the North Sea which is also reflected in the q'_* pattern (Fig. 6.7e, j).

These slight discrepancies between the groups and ERA5 are more prominent at the time of the PB (Fig. 6.8). By this time, the ERA5 block has just formed and a small internal track begins to move eastwards, while the main AC eddy merges with a wave breaking event in the northwest. While the Z'_* pattern of the block, and the resulting shape, size and intensity of the block, are represented well in the MOGREPS-G ensemble mean and Group B (Fig. 6.8b, d), the magnitude of q'_* to the north of Scotland is represented far better in Group B (Fig. 6.8i). On the other hand, the PV anomalies in Group C match better with those in ERA5, despite the overprediction of Z'_* and block area in this group (Fig. 6.8e, j). The magnitude of both the geopotential height and PV anomalies at this time are underestimated in Group A (Fig. 6.8e-f). These results suggest that the representation of the AC eddy 18 hours before this PB was important for the subsequent development of the block. Group A underestimated the size and speed of approach of the AC eddy, which resulted in a slower onset of the block. While the eddy in Group B was slightly misplaced 18 hours previously, it still captured the behaviour of the AC eddy well enough to model the block onset at the PB accurately, and the larger and more intense AC eddy in Group C led to a larger and more intense block at onset.

Seven-day forecasts for the ensemble mean and each group are shown in Fig. 6.9, with a t_{val} of 00 UTC on 23 February. It is interesting to note that this is after the PB has been overcome, and this is reflected in the way in which each group models the block at this time. For the most part, the majority of the block structure is consistent between groups and ERA5 (for example, note the location of the AC eddy track centre is within the highest Z'_* contour in each ensemble, which is remarkable for this lead time). The smaller-scale PV anomaly structure is less consistent between the groups and ERA5, however. Despite this, this result

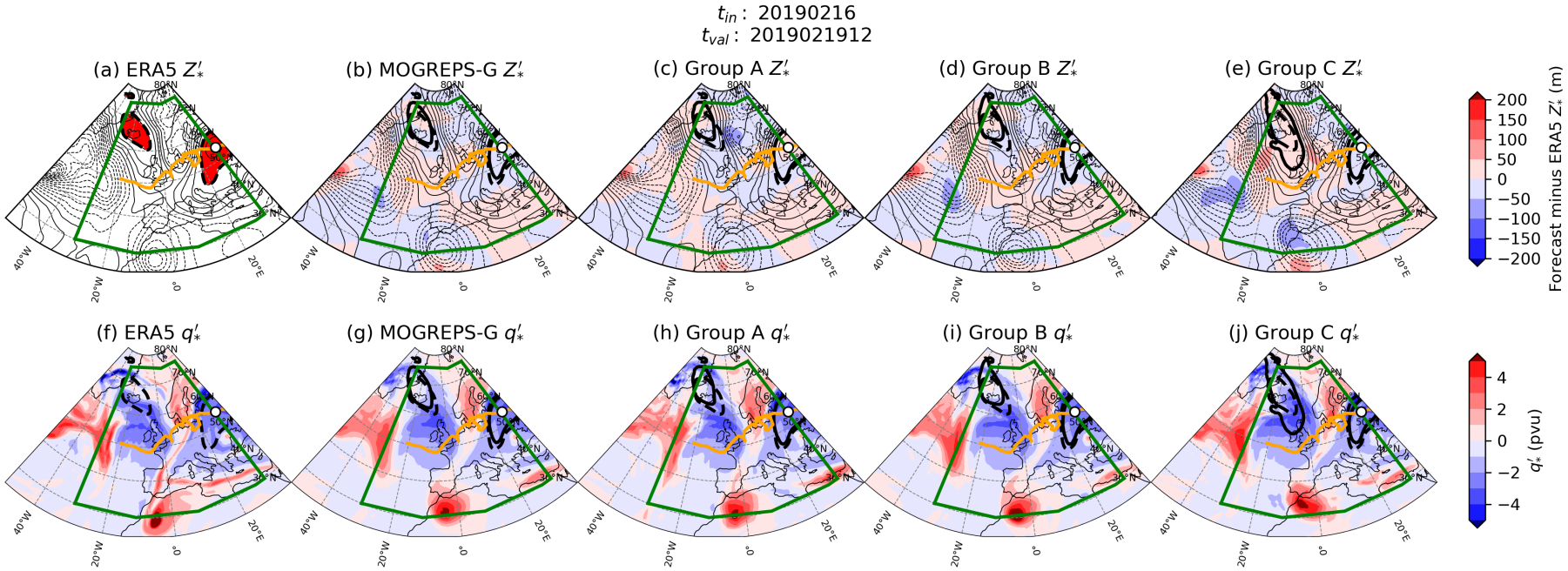

Figure 6.7: Z'_* (black, negatives dashed, every 25 m; top row) and q'_* (shading; bottom row) at 19 February 2019, 12 UTC, for (a, f) ERA5, and (b-e, g-j) forecasts initialised on 16 February 2019. Red shading in panel (a) shows the ERA5 instantaneous blocked points (where $Z'_{*inst} \geq 100$ m), and this contour is replicated in panels (b-j) by the thick dashed line. Results are also shown for ensemble means from (b, g) the entire MOGREPS-G ensemble, (c, h) Group A, (d, i) Group B, and (e, j) Group C. The solid thick black lines in (b-e, g-j) show the outline of instantaneously blocked points in that particular ensemble. Filled contours in (b-e) show the difference between the forecasted and ERA5 Z'_*. The orange line(s) in each panel show the path of any Z'_* tracks (from ERA5 only), with its position at the valid time shown by the white circle, and the green box shows the domain in which ZAL statistics are computed in.

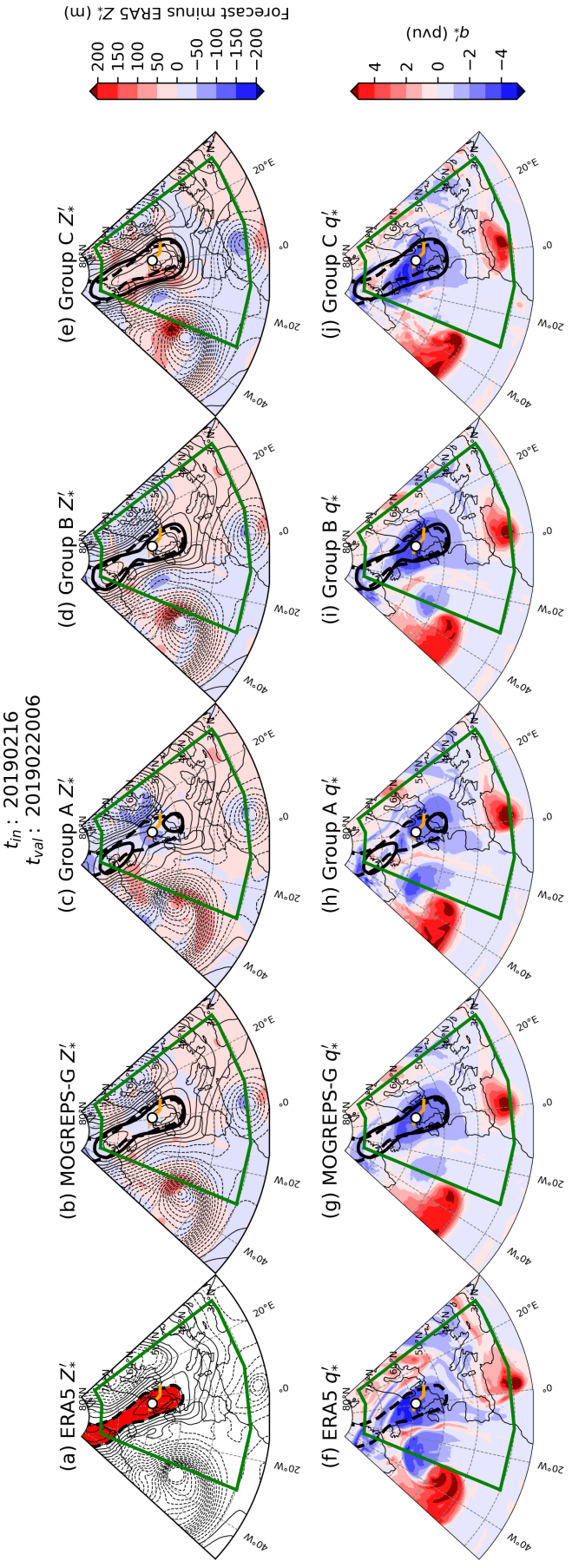

Figure 6.8: As in Fig. 6.7, but for a validity time of 20 February 2019, 06 UTC.

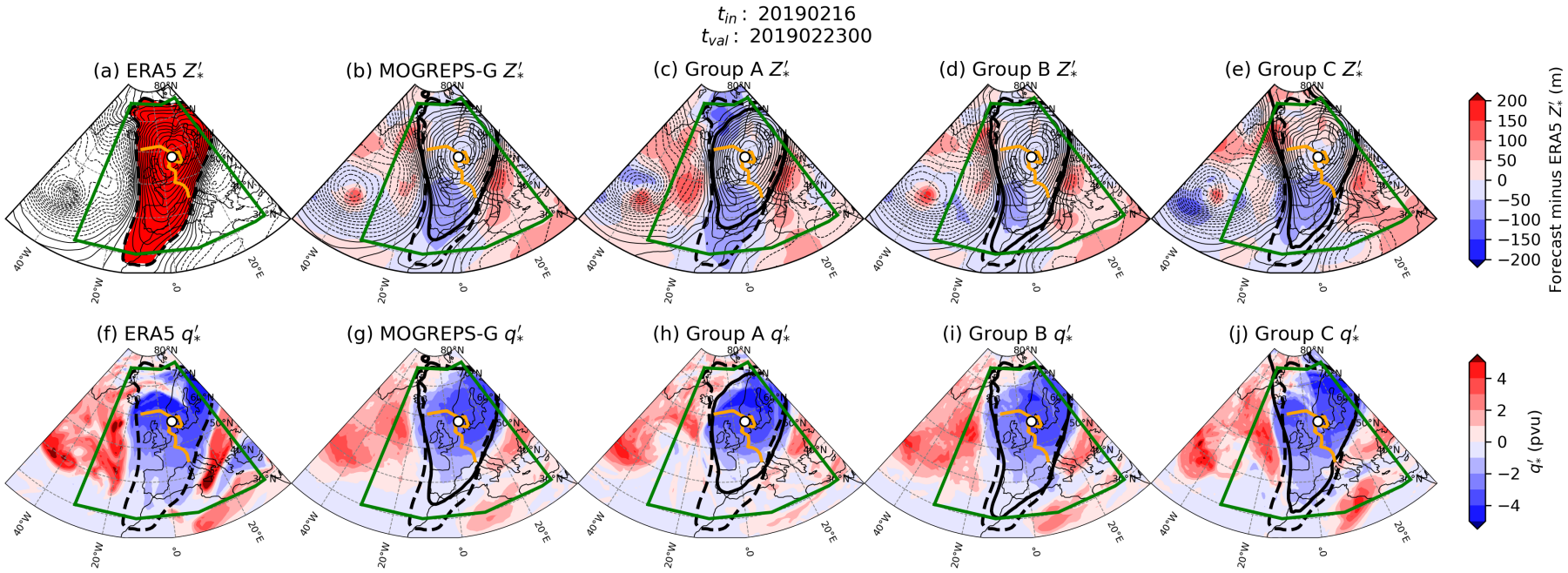

Figure 6.9: As in Fig. 6.7, but for a validity time of 23 February 2019, 00 UTC.

shows that the representation of the AC eddies in this case was only important for the correct modelling of the block at onset, and did not lead to subsequent forecast errors once the block had been established in all groups.

6.3.3 Block Decay Predictability Barrier

The same analysis is performed for the PB around the decay of the block (PB2). As demonstrated in Fig. 6.3, this PB is broader than the one at onset, implying that consecutive forecasts did not accurately model the decay of the block. To match with the definition of the decay of the block event from earlier chapters, analysis of this PB will be performed at a t_{val} of 18 UTC on 1 March 2019.

ZAL statistics for ensemble members and the mean, initialised on 22–28 February and valid at 18 UTC on 1 March 2019, are shown in Fig. 6.10. As with the onset PB, the spread in the error tends to decrease as forecasts are initialised closer to the PB, however this reduction takes longer with this PB, with spread only drastically reducing on forecasts initialised on 26 or 27 February onwards. The ensemble predominantly overpredicts block strength slightly when initialised on 22–25 February, but thereafter strength is primarily underestimated. Block area is underestimated throughout by the majority of the ensemble, and shows con-

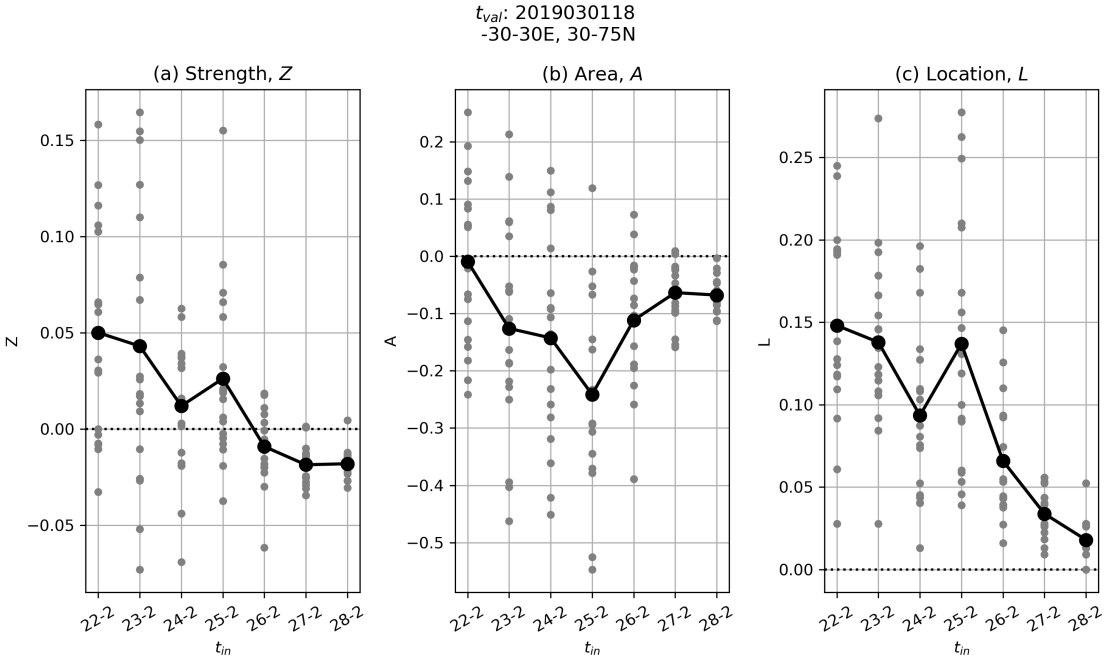

Figure 6.10: As in Fig. 6.5, but for a t_{val} of 18 UTC on 1 March 2019.

siderable spread (e.g. ranging from a near 50% underestimation to more than a 20% overestimation in members initialised on 23 February). The largest ensemble mean underestimation in block area occurs in the 4.75 day forecast, initialised on 25 February. Spread in the location of the block's centre is also fairly large for this decay PB (nearly 30% of the total domain size in some cases), and except on 25 February, decreases as lead time decreases.

Examination of forecasts from a t_{in} of 23 February will be performed for this particular PB, due to the considerable spread and therefore uncertainty in the blocking forecast. Once again, focus will be given to whether the representation of the AC eddy is important for determining how the forecasted block evolves.

The ZAL diagram for this PB, from the ensemble initialised on 23 February, is shown in Fig. 6.11. The large spread within the ensemble is re-emphasised here, with the majority of members underpredicting block area while also making the block too intense. Only five of the 18 members underestimate block strength, and a different five overpredict block area. There is also considerable spread in

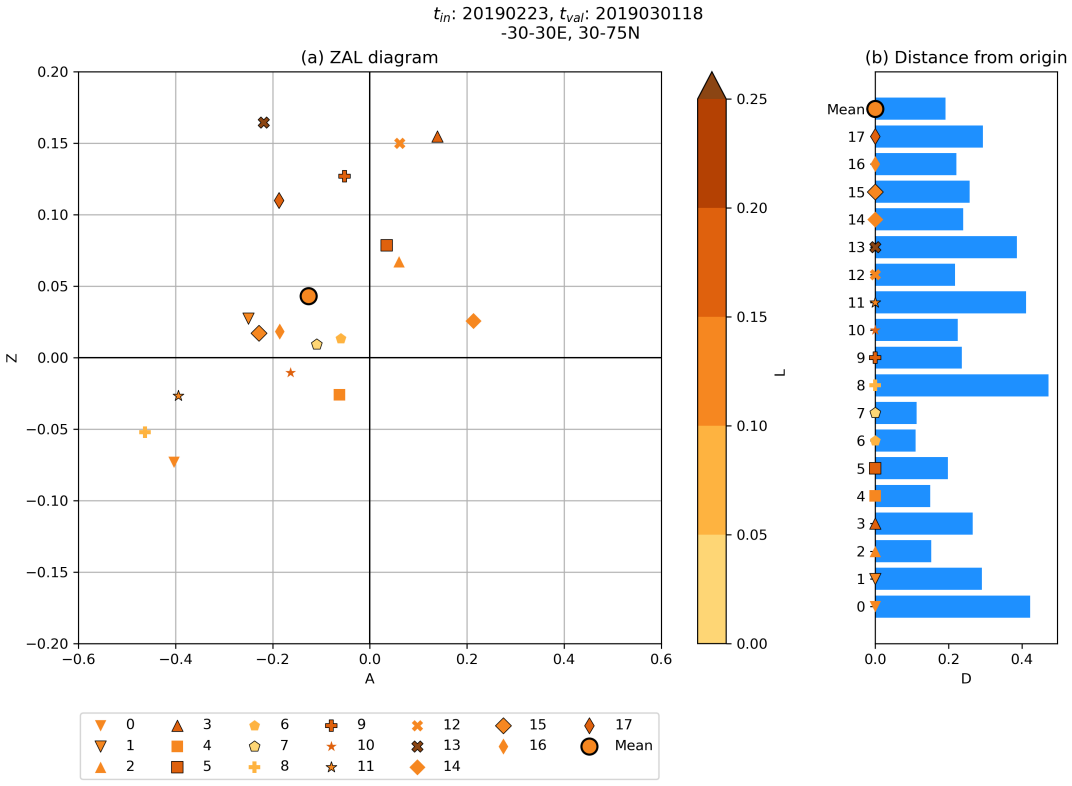

Figure 6.11: As in Fig. 6.6, but for a t_{in} of 23 February and a t_{val} of 1 March 18 UTC.

the error in location of the block, where generally those members that have the largest errors in block area and intensity also having the largest errors in position. The mean has small Z and A, when compared to the other members, but has a large L.

Plotting the members in this way once again allows for the creation of smaller groups of members that simulate the block behaviour similarly. Four scenarios are considered: (i) the entire MOGREPS-G ensemble mean, (ii) the largest underprediction of block area, (iii) good forecasts with the smallest D, and (iv) the largest overprediction of block strength while also underpredicting block area. The members in each of these groups are outlined in Table 6.2.

For the groups initialised on 23 February, three validity times are investigated: 54 hours before the PB (28 February 00 UTC, Fig. 6.12), the PB itself (Fig. 6.13), and 12 hours after the PB (the end of the forecast, Fig. 6.14). On 28 February, there are two AC eddies interacting with the instantaneous blocking field (6.12a). The easternmost centre is the same AC eddy that was present at the onset PB, and the slightly weaker one situated over Iceland is a second eddy coming from upstream after another wave breaking event. The negative PV anomaly is more widespread and stronger with the first AC eddy than the second one (6.12f). To the west of the UK and Ireland, a small region of less strong positive Z'_*, and weakly positive q'_*, is present that acts to squeeze the block from the west and give it its arrowhead-like shape at this time.

The MOGREPS-G ensemble mean (Fig. 6.12b, g) captures the eastern AC eddy and the block around it very accurately, however the new AC eddy is poorly rep-

Name	**Members**	**Description**
MOGREPS-G	0–18	All-member ensemble mean
Group D	0, 8, 11	Members that underpredict block area the most
Group E	9, 13, 17	Members that overpredict block strength the most, while also underpredicting block area
Group F	2, 4, 6, 7	Members that perform best at simulating the block, with smallest D

Table 6.2: Description of the groups analysed for the decay PB of the February 2019 block.

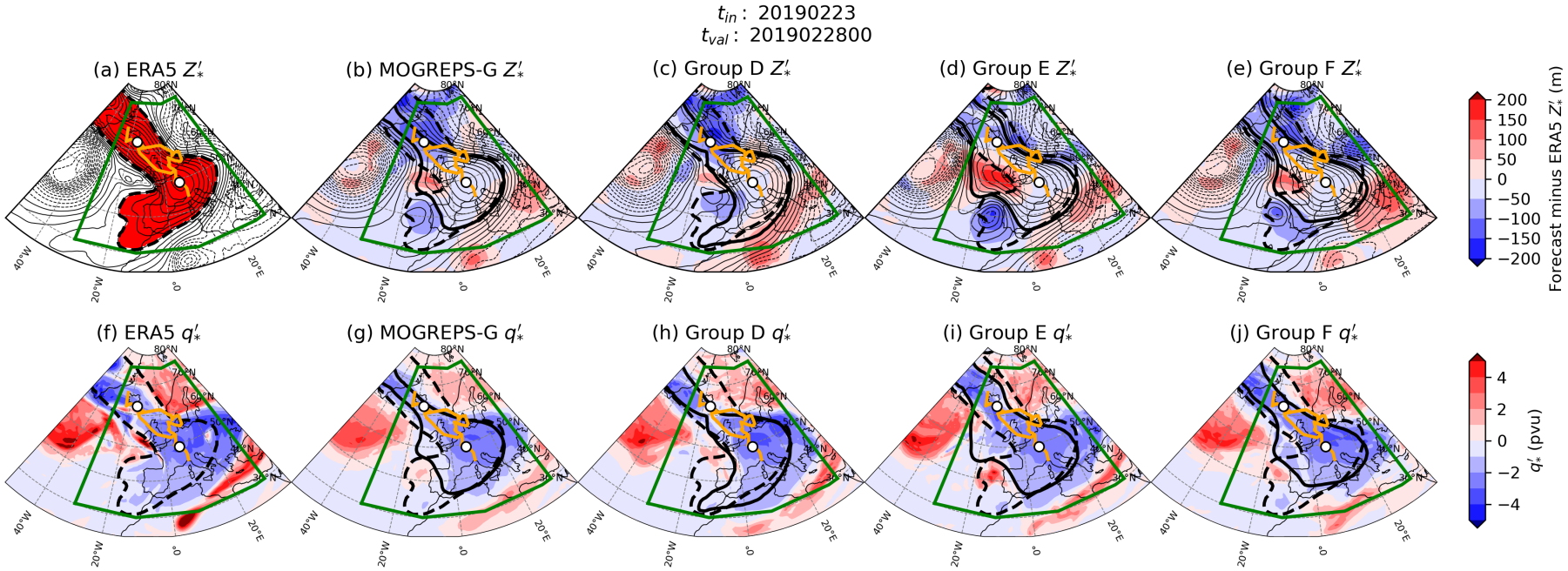

Figure 6.12: Z'_* (black, negatives dashed, every 25 m; top row) and q'_* (shading; bottom row) at 28 February 2019, 00 UTC, for (a, f) ERA5, and (b-e, g-j) forecasts initialised on 23 February 2019. Red shading in panel (a) shows the ERA5 instantaneous blocked points (where $Z'_* \geq 100$ m), and this contour is replicated in panels (b-j) by the thick dashed line. Results are also shown for ensemble means from (b, g) the entire MOGREPS-G ensemble, (c, h) Group A, (d, i) Group B, and (e, j) Group C. The solid thick black lines in (b-e, g-j) show the outline of instantaneously blocked points in that particular ensemble. Filled contours in (b-e) show the difference between the forecasted and ERA5 Z'_*. The orange line(s) in each panel show the path of any Z'_* tracks (from ERA5 only), with its position at the valid time shown by the white circle, and the green box shows the domain in which ZAL statistics are computed in.

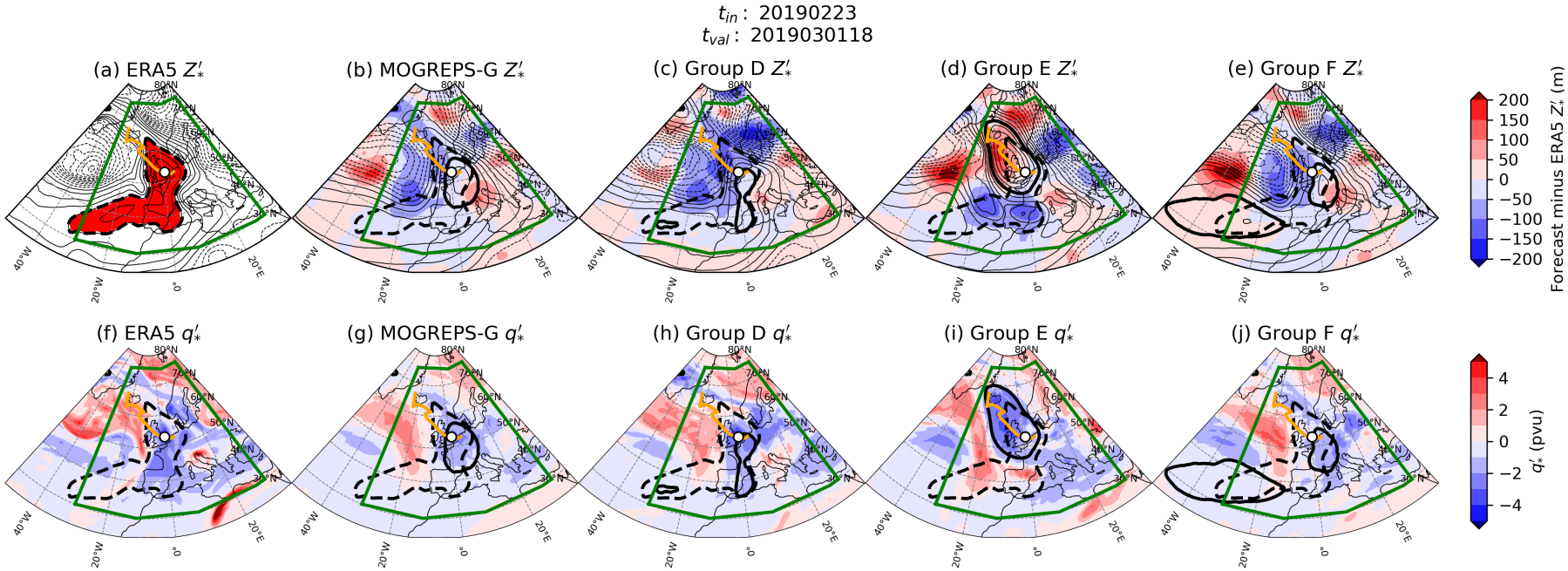

Figure 6.13: As in Fig. 6.12, but at a validity time of 1 March 2019, 18 UTC.

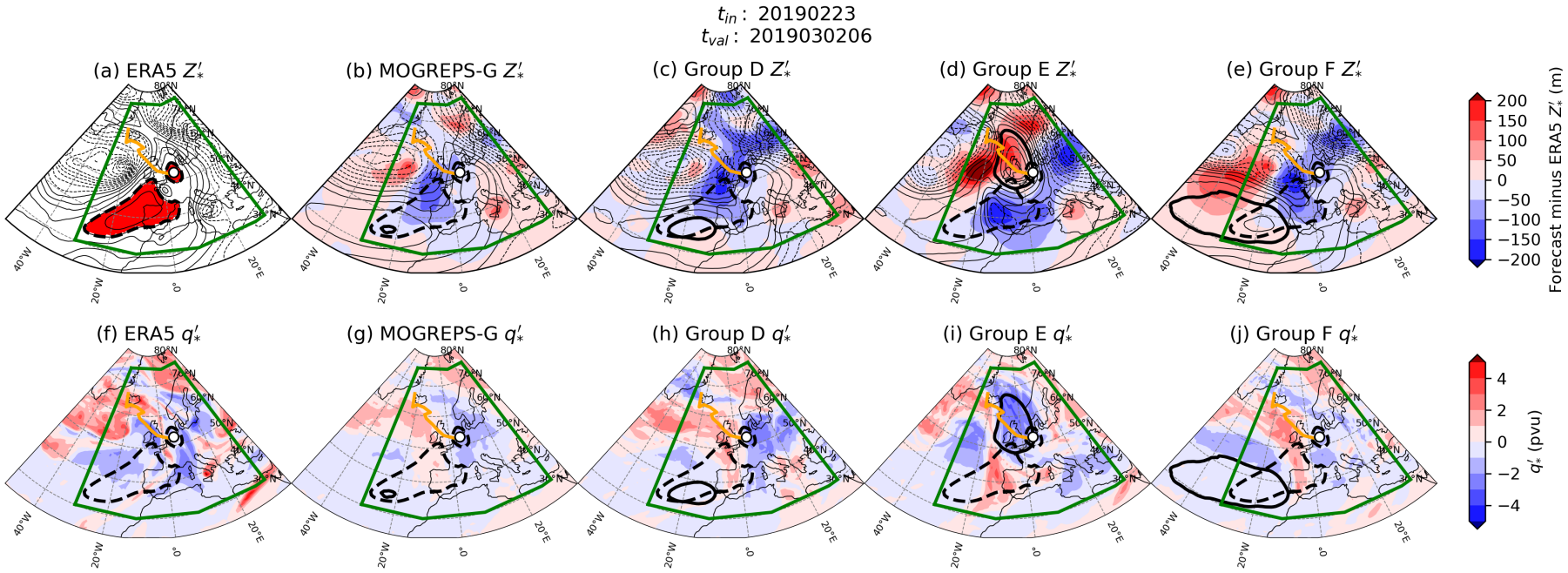

Figure 6.14: As in Fig. 6.12, but at a validity time of 2 March 2019, 06 UTC.

resented. It is about 100 m too weak and thus much of the northwestern portion of the block is missing from the ensemble mean. The southwestern portion and "arrowhead" shape of the block are also poorly represented in this group, due to the area of weaker Z500 anomalies being positioned too far to the south.

The anomalous Z500 field in the group that underestimates block area (Group D, Fig. 6.12c) also demonstrates that the smaller positive Z'_* values to the west of the UK are slightly too far south. The representation of the northwestern portion of the block in Group D is even poorer than that in the MOGREPS-G mean (Fig. 6.12c), with some parts exceeding an underestimation of 150 m. In Group D, the AC eddy does not break off from the wavebreaking event to the west, the edge of which can be seen to the east of Greenland. However, the eastern portion of this block (and the AC eddy here) is again represented very well by Group D, and the magnitude of q'_* is close to that in ERA5 (Fig. 6.12h).

Groups E (overprediction of strength, Fig. 6.12d, i) and F (the best forecasts at the time of the PB, Fig. 6.12e, j) are similar to the other two groups in that the arrowhead shape of the block is not predicted as well as in ERA5 due to the misplacing of the small-scale positive PV anomalies, but the eastern portion of the block is represented well. Both of these group means also slightly underestimate the strength, and therefore size, of the northwestern AC eddy, but to a lesser extent than the MOGREPS-G ensemble and Group D (e.g. compare Figs. 6.12c and d). Surprisingly, at this stage, the strength of the AC eddy is closest to ERA5 in the group that overpredicts block strength, rather than the best forecasts. However, for Group E models, the western extent and strength of the block along 50 °N are much poorer than Group D, with the small-scale Z'_* minimum being far too large in magnitude at 40°N.

By 1 March 2019, 18 UTC, the instantaneous block in ERA5 has reduced in size and magnitude, and the AC eddy has travelled to the east of the UK (Fig. 6.13a, f). The small region of smaller-magnitude Z'_* and positive q'_* has travelled through the block (not shown) and is now positioned over the north of Italy. The errors in the AC eddy representation 54 hours earlier have led to continued errors in block representation at this time, particularly in the MOGREPS-G and Group D means (Fig. 6.13b-c, g-h). The western extent of the blocks in these two representations is

too small and as a result the blocks are too small and too weak, both as a Z500 and also a PV anomaly. Even in Group F, where the block intensity and area are closest to ERA5, the southwestern portion of the block is almost entirely missing, but close to the instantaneous blocking threshold value. However, the main portion of the block, centred around the AC eddy, is represented somewhat better (within 25 m of the reanalysis), and certainly better than in Group D.

Despite the findings above, a good representation of the AC eddies in previous time steps does not necessarily lead to better later forecasts of blocks. Group E underpredicts the strength and size of the incoming AC eddy the least in the preceding 54 hours, but by 1 March 18 UTC the block in this group is too strong, too large, and centred too far northwest (Fig. 6.13d, i). This happens because the AC eddy is erroneously forecasted to intensify to the northwest of the UK and slow down, which allows the block to be re-centred in the northwest and re-intensify.

The misrepresentation of the AC eddy earlier in the forecast, and at the PB, leads to continued forecast errors until the end of the simulation (Fig. 6.14). Twelve hours later, the ERA5 block has continued its decay, with only a very small portion associated with the decaying AC eddy. A second, weak part of the block is in the southwest of the domain, but this also soon decays. The groups that underestimate the AC eddy's strength earlier in the forecast (MOGREPS-G ensemble mean, Groups D, F) have almost no instantaneous blocking around this eddy at all by this time (2 March, 06 UTC), with both the anomalous Z500 and PV field weaker than in ERA5. Meanwhile, Group E still overestimates the persistence, size, and intensity of the block after earlier re-intensifying the eddy.

6.4 March 2021

6.4.1 Mean ZAL

The mean ZAL for all t_{in} and h combinations for the March 2021 block are shown in Fig. 6.15. Like with the February 2019 block, the onset and decay of the March 2021 block are associated with enhanced uncertainty within the ensemble mean, and present themselves as PBs. In this case, the larger PB (PB3) is associated with the onset of the block, which is generally characterised by an underprediction of block area, implying an onset that was too slow. PB3 is most evident yet again when measuring the area of the block, while the strength of the block is much better simulated. The location error of the block's centre at onset is also rather large, but this positional error reduces more quickly than the area error. Though not shown here, the same PBs identified in Fig. 6.15 can also be identified by the RMSE and spread from the ensemble mean in the instantaneous block area (like that shown for the February 2019 case in Fig. 6.4).

The onset PB for the March 2021 block will be investigated further. As demonstrated in an earlier chapter, the onset of this block in ERA5 perfectly coincides with the arrival of an AC eddy centre, which therefore could be important for the accurate modelling of the block. The AC eddy responsible for the onset of

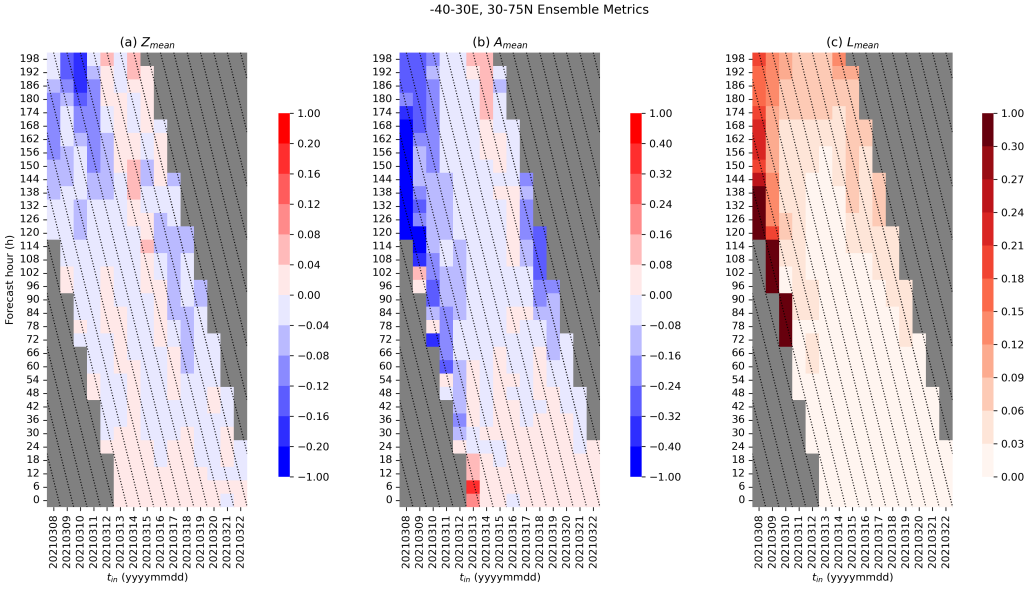

Figure 6.15: As in Fig. 6.3, but for the March 2021 block for forecasts initialised from 8–14 March, in the sector defined by 40°W–30°E, 30–75°N.

the block also has a long track, originating from eastern North America, so its representation across the Atlantic will also be analysed.

6.4.2 Block Onset Predictability Barrier

Timeseries of Z, A, and L, valid at block onset (14 March 12 UTC), for forecasts initialised from 8–14 March, for each ensemble member and the mean are shown in Fig. 6.16. These reveal that while the mean ZAL decreases with decreasing lead time, the spread within the ensemble remains consistently high for the first three forecasts in A, and even increases slightly for Z. This large spread is typical of a PB and demonstrates the large uncertainty in early forecasts in predicting the characteristics of the developing block. Five members from the 8 March forecast did not have any instantaneous blocking at all at this t_{val}, further highlighting the forecast uncertainty. For forecasts initialised on 11 March onwards (a lead time of below 84 hours), the ZAL spread quickly reduces, emphasising that the PB has been overcome as certainty increases. The spread in L begins high but decreases

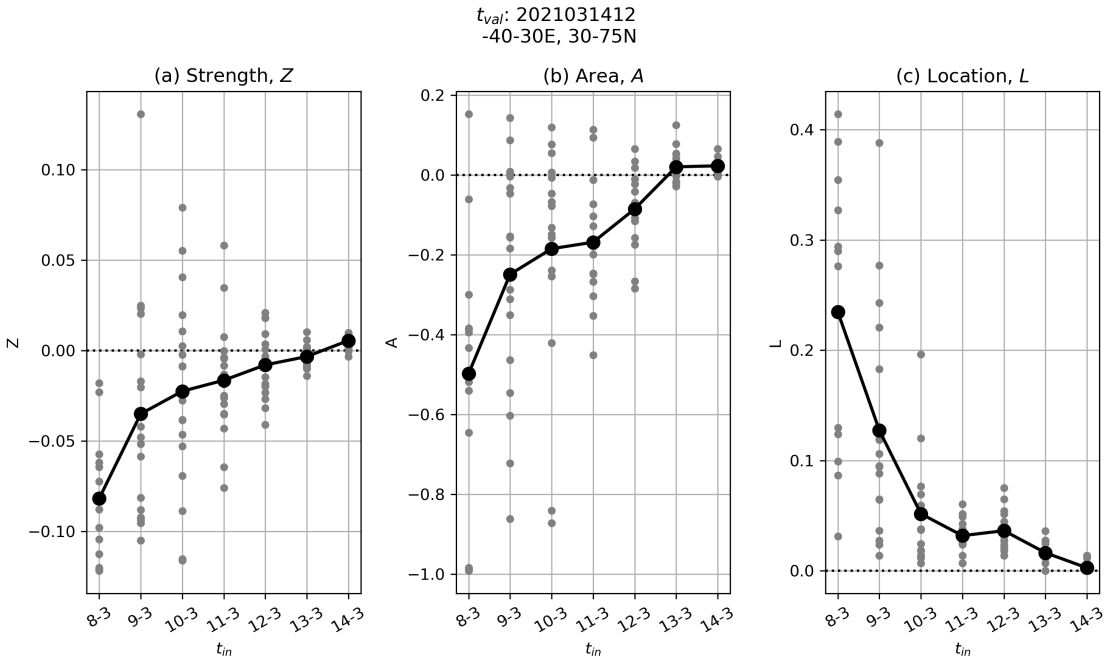

Figure 6.16: As in Fig. 6.5, but for a t_{val} of 2021-03-14 12 UTC. Note that five ensemble members from forecasts initialised on 2021-03-08 did not have any instantaneous block area, so ZAL statistics are not computed for these members, and as such that column (and the mean) only contains data from 13 members, rather than the full 18.

rapidly, at a faster rate than in Z and A.

Further analysis of the AC eddy associated with block onset will be performed on forecasts with a t_{in} of 8 March 2021. The ZAL diagram showing the mean, and the 13 members that predicted instantaneous blocking, for t_{in} of 8 March and t_{val} of 14 March 12 UTC is shown in Fig. 6.17. All 13 members shown on the ZAL diagram underestimate the strength of the block, mostly by a factor of 5–10%. Furthermore, the majority of ensemble members misplace the block (with a positional error well in excess of 25%) and vastly underpredict the area by up to 100% (i.e. no block). Only one member (4) overpredicts block area. These findings demonstrate that not only is the ensemble mistiming the onset of the block (shown by strength and intensity), but the location of onset is also incorrect.

Like before, the ZAL diagram is used to motivate the analysis of different members or groups of members and examine how their forecast evolves, with a particular focus on how representation of any AC eddies goes on to affect the forecast of the block. Along with the four members that had no block whatsoever,

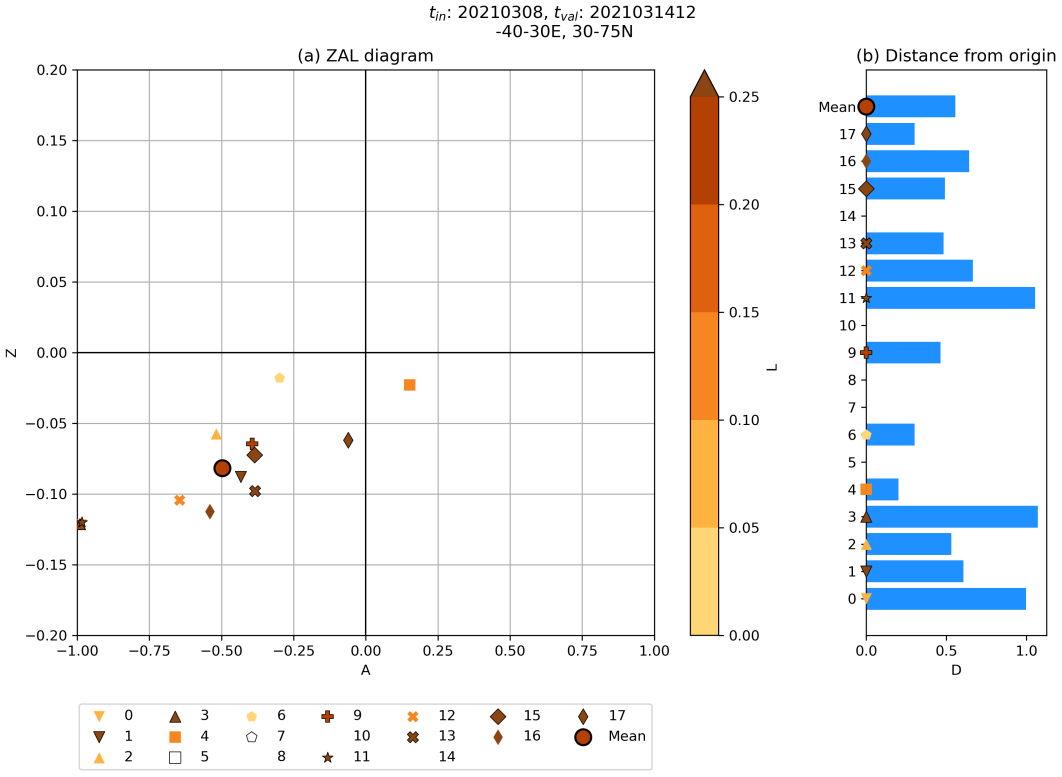

Figure 6.17: As in Fig. 6.6, but results are for a t_{in} of 8 March 2021 and a t_{val} of 14 March, 12 UTC, between 40°W–30°E, 30–75°N. Members 5, 7, 8, 10 and 14 had no instantaneous blocking in the domain, so are absent from the ZAL diagram.

Name	Members	Description
MOGREPS-G	0–18	All-member ensemble mean
Group G	3, *5*, *7*, *8*, *10*, 11, *14*	Members that either have no block at all (italic), or underpredict block area by nearly 100%
Group H	4, 6	Members that are closest to the origin
Group I	17	Member that predicted area well, but was still in the wrong place

Table 6.3: Description of the groups analysed for the onset PB in the March 2021 block.

the groups analysed for this combination of t_{in} and t_{val} are shown in Table 6.3.

In the analysis that follows, the Z500 and PV anomalies associated with the groups in Table 6.3 will be described firstly from the time of the PB (block onset), and then traced back in time centred on the representation of the AC eddy that begun the block. Figure 6.18 shows the Z_* and q'_* fields associated with these groups in Table 6.3 and ERA5 at 14 March 12 UTC. In ERA5 (Fig. 6.18a, f), the block begins as the result of the slowing down and northward-turning AC eddy in the East Atlantic from upstream, and there is a large cut-off low over much of Western and Northern Europe. The incipient block is characterised by positive Z500 and negative PV anomalies at this time.

The MOGREPS-G ensemble mean field and Group G mean fields (6.18b, c, g, h) have no instantaneous block at all in the domain of interest at the time of ERA5 block onset, and appear remarkably similar. The weakly anticyclonic region of Z'_* centred over Iberia is not strong enough to exceed the blocking threshold, and is not the same feature as shown by the ERA5 AC eddy (this is a weak stationary feature that has been here throughout). The Z'_* error in the region of the ERA5 AC eddy is very large and negative, signifying that there is no AC eddy at all, which could explain why the onset of the block was missed in these groups.

The members that were closest to the origin have the location of the block in the best position out of the groups analysed (Fig. 6.18d, i). As will become evident in later maps, this is the only group analysed where the upstream AC eddy from North America is still visible at this validation time, and has strengthened in a similar way at block onset to ERA5. While the strength of the block, as measured using Z'_* is close to that in ERA5, the magnitude of the negative q'_* within the

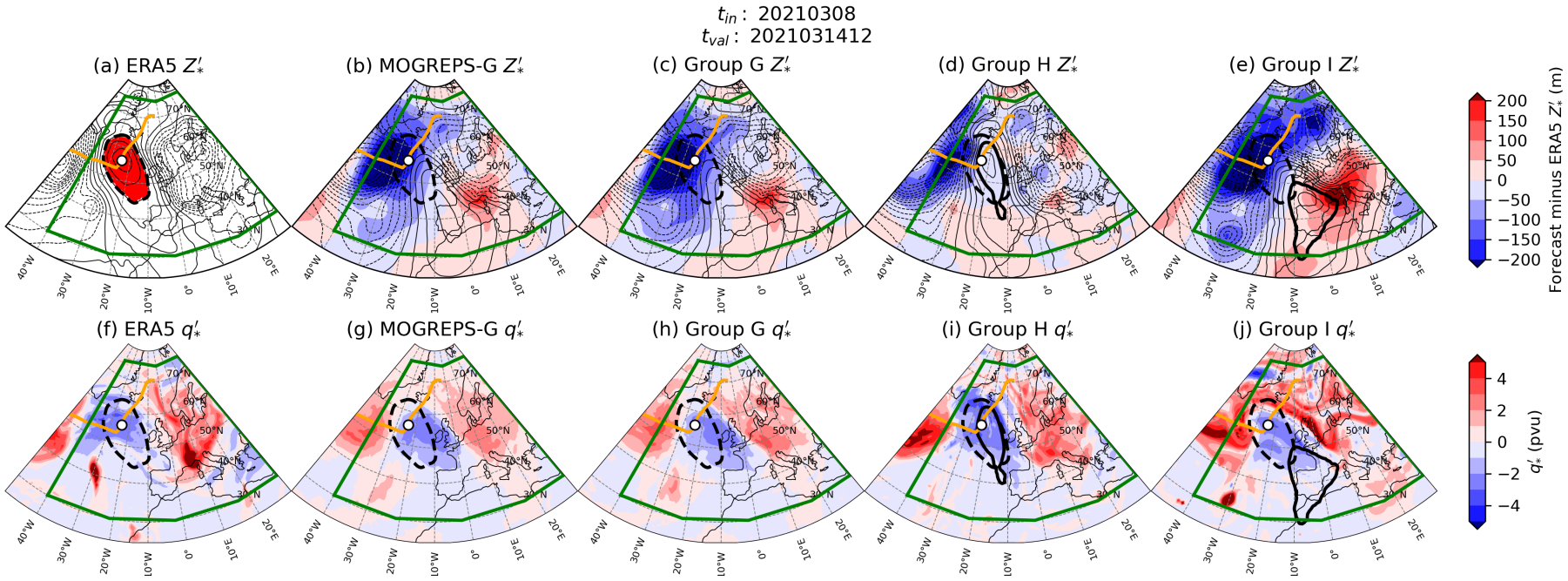

Figure 6.18: Z'_* (black, negatives dashed, every 25 m; top row) and q'_* (shading; bottom row) at 14 March 2021, 12 UTC, for (a, f) ERA5, and (b-e, g-j) forecasts initialised on 8 March 2021. Red shading in panel (a) shows the ERA5 instantaneous blocked points (where $Z'_* \geq 100$ m), and this contour is replicated in panels (b-j) by the thick dashed line. Results are also shown for ensemble means from (b, g) the entire MOGREPS-G ensemble, (c, h) Group A, (d, i) Group B, and (e, j) Group C. The solid thick black lines in (b-e, g-j) show the outline of instantaneously blocked points in that particular ensemble. Filled contours in (b-e) show the difference between the forecasted and ERA5 Z'_*. The orange line(s) in each panel show the path of any Z'_* tracks (from ERA5 only), with its position at the valid time shown by the white circle, and the green box shows the domain in which ZAL statistics are computed in.

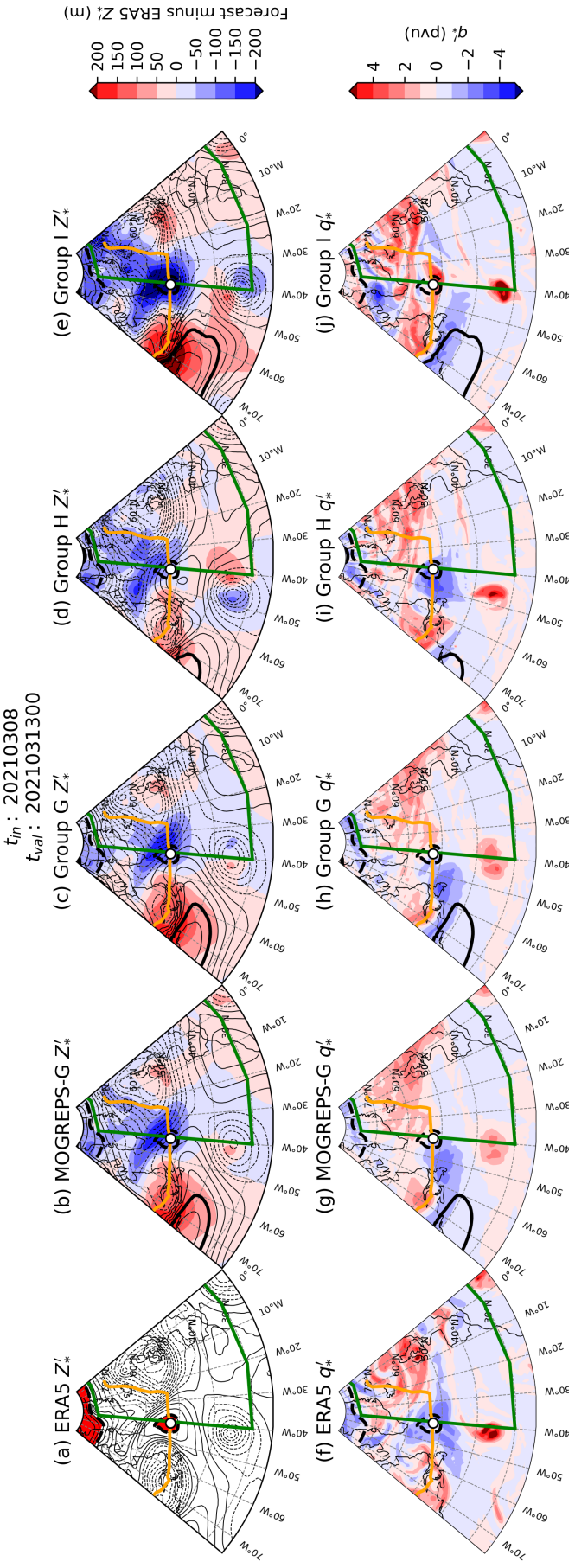

Figure 6.19: As in Fig. 6.18, but for a t_{val} of 00 UTC on 13 March 2021, 36 hours before the PB.

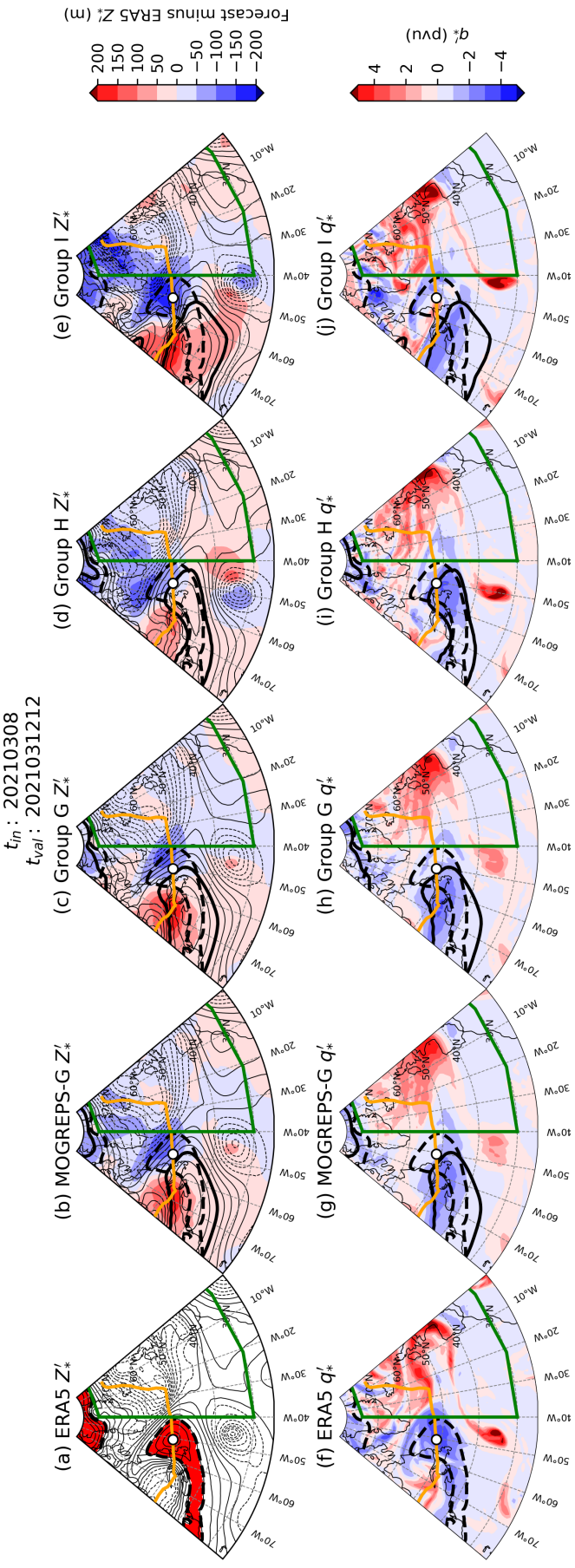

Figure 6.20: As in Fig. 6.18, but for a t_{val} of 12 UTC on 12 March 2021, 48 hours before the PB.

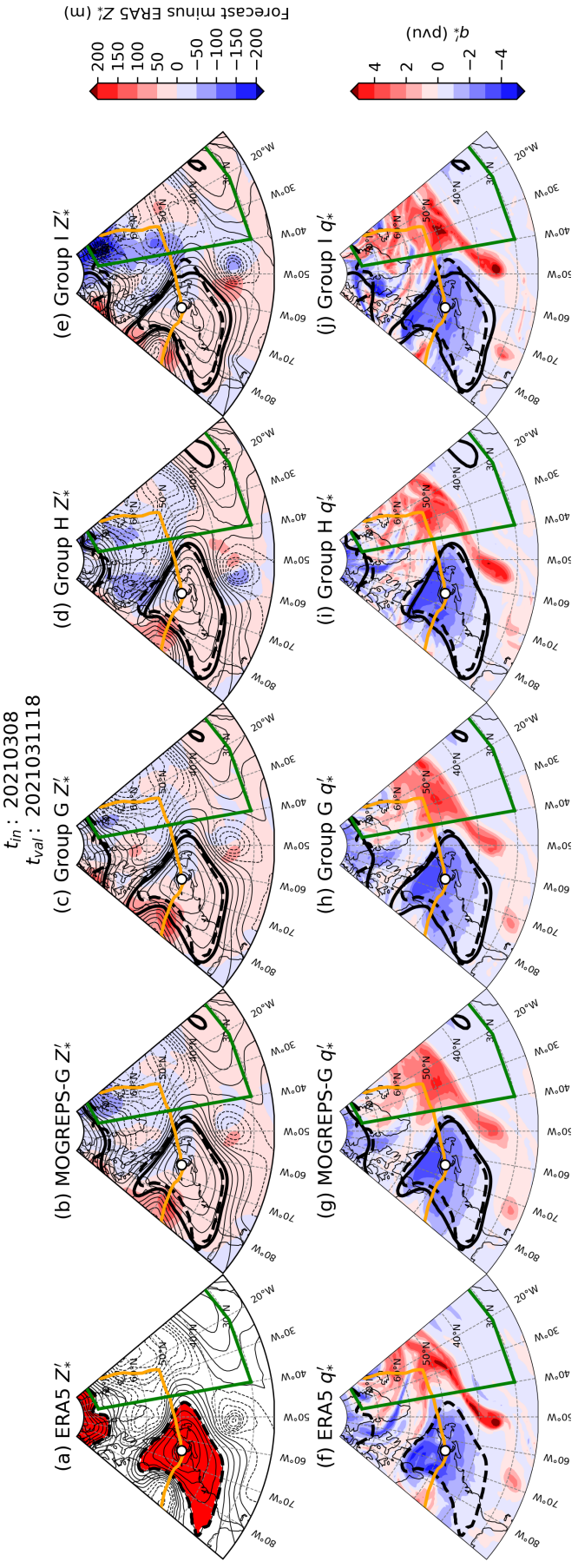

Figure 6.21: As in Fig. 6.18, but for a t_{val} of 18 UTC on 11 March 2021, 66 hours before the PB.

Group H block is higher than in the reanalysis. Furthermore, the large-magnitude underestimation of the Z500 anomaly just upstream of the block is also present in this realisation.

While the member in Group I has an accurate representation of the block area at onset, the block forms too far southeast and is not associated with the upstream AC eddy (Fig. 6.18e, j). Instead, like with MOGREPS-G and Group G, the anticyclonic region is a stationary feature centred over Iberia, that happens to intensify enough in this member to exceed the blocking threshold. The dipole of Z'_* errors in this member indicates that the flow over Western Europe is too zonal, compared to the ERA5 solution.

Now, the same groups will be followed backwards in time and the upstream Z500 and PV anomaly patterns examined to determine where, when, and why AC representation in these groups deviated from ERA5, which potentially led to the errors in forecasting the onset of the block. The times analysed are 00 UTC on 13 March (36 hours before onset, Fig. 6.19), 12 UTC on 12 March (48 hours before, Fig. 6.20) and 18 UTC on 11 March (66 hours before, Fig. 6.21). A day and a half before the PB, the ERA5 AC eddy is centred at about 40°W as a fairly small and weak feature, with an anomaly of approximately 100 m. It has its own maximum in the Z'_* field, with two further maxima to the southwest and southeast. However, this structure is only present in Group H (Fig. 6.21d, i). In MOGREPS-G and Group G, which again look very similar to each other, there are only two anticyclonic features: an instantaneous block over the eastern seaboard of the US with a weak anticyclonic anomaly extending northeastwards into the Atlantic (which also has a negative PV anomaly), and a weak anticyclonic anomaly over Iberia/Morocco. Where the AC eddy should be, there is a region of approximately zero Z500 and PV anomalies. The same broad pattern is also demonstrated in Group I (Fig. 6.21e, j), except the Z'_* underestimation where the AC eddy should be is even more pronounced in this case. Therefore, in the MOGREPS-G ensemble mean, Group G and Group I, the AC eddy was still missing 36 hours before block onset, potentially explaining the lack of blocking later. The only Group that has an anticyclonic pattern around the ERA5 AC eddy centre at this stage before onset is Group H, where even here the AC eddy is only about

half as intense as it is in reanalysis, however the PV anomaly is approximately correct in both structure and magnitude.

A further 12 hours back in time (48 hours before the PB, Fig. 6.20), the source of the ERA5 AC eddy becomes clear. The AC eddy broke off as a spawned eddy from a weak North American block to the southwest, and the only group that also captures this event is Group H (Fig. 6.20a, d, f, i). The MOGREPS-G ensemble mean, and Groups G and I at this stage do show instantaneous blocking in the same general region; however, it is too strong and too broad, and there is no separate Z500 anomaly maximum/PV anomaly minimum that becomes the European block's AC eddy. Thus, AC eddy misrepresentation is still prevalent in a large part of the entire ensemble 48 hours before the PB, and this uncertainty could be due to the uncertainty in the way in which an anticyclonic vortex is shed from the American block. Finally, going back to 66 hours before the onset of the Euro-Atlantic block (11 March 18 UTC, Fig. 6.21), the North American origin of the AC eddy being a North American block is even more evident, but at this time all four groups in the forecast represent the PV and Z500 anomaly fields reasonably accurately, within $\pm$ 0.5 pvu and 50 m respectively. Therefore, it can be concluded that forecast errors in representation of this North American block's spawned eddy (which become the Euro-Atlantic block's AC eddy) led to errors in how this eddy interacted with a block event further downstream.

6.5 Discussion and Conclusions

The purpose of this chapter was to examine whether the representation of AC eddies in forecasts can lead to errors in how blocks are predicted later in the forecast. To investigate this hypothesis, the ZAL metric was devised to quantify the extent to which the MOGREPS-G ensemble misrepresents the intensity, area, and location of instantaneous blocking in the February 2019 and March 2021 case studies. Constant validity times associated with higher intensity, areal, and positional errors for a range of initialisation and lead times (predictability barriers) were identified for the two cases. In both blocks, the PBs were associated with the timings of block onset and decay, while three of these four PBs also coincided

with the timing of AC eddy-block interactions. It is these PBs that were examined further, first by studying the characteristics of the ensemble at the PB itself (summarised in Sect. 6.5.1), and then by focusing on how the representation of the AC eddies potentially led to these PBs (summarised in Sect. 6.5.2).

6.5.1 Predictability Barrier Characteristics

The onset of the February 2019 block was almost exclusively predicted to be too large and slightly more intense by forecasts initialised 5.5–7.5 days before PB1. This was due to either the lack of decay from a preceding block in the area, or the forecasts predicting the onset of this block to be too early. The forecast with a 4.5-day lead time was somewhat of an outlier in that it had members that both over- and under-predicted block strength and area at PB1, and was therefore chosen as an appropriate set of forecasts to analyse in further detail. Block location at PB1 was generally well-predicted throughout the ensemble even at longer lead times (L_{mean} generally smaller than 0.10). This PB was also close to the time in which a tracked AC eddy arrived in the region, which had its origins from a wave-breaking event over Greenland.

The second PB in the February 2019 block (PB2) was associated with its decay and second AC eddy interaction. This was a more uncertain forecast period than PB1 since the spread and mean ZAL statistics remained high in magnitude for shorter lead times than in PB1. PB2 was associated with a general slight overestimation of block strength (by less than 4%) but quite a more severe underestimation of size. The spread in forecasted block area in particular was also large for lead times even as short as 3–4 days. The location error of the block at PB2 was also larger than PB1.

Finally, the onset of the March 2021 block, and its associated AC eddy interaction, was examined (PB3). This was probably the strongest PB analysed and manifested in large-magnitude mean area and positional errors in particular. The ensemble spread in predicted block area was strikingly large (exceeding 100%), with some members missing the block event entirely, while others had a slight overestimation of block area, especially at longer lead times.

6.5.2 AC Eddy Representation and Block Forecasts

The three PBs studied in this work were associated with errors in AC eddy representation in the forecasts, which led to inaccurate forecasts of the block. The eddies associated with PB1 and PB2 both came from wave breaking over Greenland, and in some cases this was misrepresented. This led to positional, timing, or size errors in the AC eddy in the period before the PB, which were consequently carried through to errors in how the block was represented at the time of the PB. For example, in the group of ensemble members that underpredicted block size, the AC eddy was too weak and/or slow on its approach to the block. Similarly, in cases where forecasts overpredicted block size, the preceding AC eddy was also stronger than the underprediction examples.

The representation of the AC eddies preceding PB1 and PB2 had notable impacts of the timing of block onset (PB1) and decay (PB2). It was found that the slow/weak AC eddy at PB1 led to late block onset, and weak (strong) AC eddies resulted in early (late) block decay at PB2. This can have important implications for forecasted surface conditions underneath the block. As mentioned in the previous chapter, this February 2019 block was responsible for record-breaking winter warmth and so incorrect forecasts concerning the persistence of the block, as the result of misrepresented AC eddy interactions, could be vital for the preparedness of the public for extreme temperatures and the impacts they cause. This would be even more crucial were the block to be responsible for bringing extreme winter cold or extreme summer heat. Therefore the accurate representation of transient anticyclonic features in forecasts could have an important role in determining the predicted persistence and therefore longevity of severe surface weather associated with blocks.

Additionally, the analysis of the AC eddy that led to PB3, during the onset of the March 2021 block, highlights the need for more research into how one blocking event may influence the dynamics of another one. The AC eddy that started the March 2021 block originated from over North America as another block's spawned eddy. The shedding of this eddy from the North American block, and its subsequent crossing of the Atlantic, was not modelled well by the majority of ensemble members from the initialisation time examined. As a result, most of

the ensemble members forecasted that the eddy did not cross the entire Atlantic and therefore most members had no block forming at all, or a block forming due to the wrong mechanism, namely the poleward extension of the Azores High, instead of the upstream eddy. Only a few members correctly predicted that the eddy would make it to the East Atlantic (and even then it was too weak), but these forecasts were the only ones to model the onset of the block at PB3.

While this work shows the clear importance of the representation of AC eddies to the representation of blocks in forecasts, the forecasting of other factors important to blocking dynamics have not been considered here. The previous chapter demonstrates that diabatic processes, while of lesser importance than adiabatic PV flux convergence/divergence, are also present during blocking episodes and are contributing towards the PV budget of the block. This is especially true at block onset (where diabatic processes promote blocking) and decay (where blocking is discouraged by diabatic processes), which also happens to be where the PBs are in the February 2019 and March 2021 blocks. Therefore, it is possible that the accuracy to which the diabatic processes are forecasted is also at least partly contributing to the PBs examined in this work. Further work is therefore necessary in order to determine the effect of the forecasting of diabatic processes towards block forecast uncertainty.

In Sect. 5.7, it was decided that further work should focus on tracking and defining AC eddies using q'_* instead of Z'_* as this may provide a more accurate quantification of the AC eddies. By extension, it is therefore reasonable to hypothesise that a more accurate counting of AC eddies (via a PV-based definition) could also lead to decreased uncertainty in the PBs. The maps of the groupings in Sects. 6.3, 6.4 suggest that, for the most part, the PV signature of blocking is fairly similar within the ensemble around the PBs, which would suggest that the PB is not as marked for a PV-based forecast, compared to a Z500-based one. This hypothesis could be tested in future by defining a ZAL-like forecast performance metric that uses q'_* instead of Z'_* and identifying PBs according to these metrics, following a similar procedure to that demonstrated in this Chapter. Then, the magnitude of the strength, areal, and positional errors in the predicted blocks could be compared between the Z500 and PV-based methods to determine whether changing

the way in which eddies and blocks are defined changes the error associated with forecasting their interactions.

As with the two previous work chapters, only the effect of anticyclonic eddies is studied, but *cyclonic* eddies are also likely to be influential in the predictability of blocking events too (Maddison et al., 2019). A clear example of this is given at PB2, where the block is split into two portions by a small-scale positive PV anomaly crossing from west to east through the middle of the block. This is also an important factor in determining the way in which this block decayed, so would require further investigation to study how this cyclonic feature is modelled and whether this lead to discrepancies in block decay.

To conclude, this work shows that AC eddy forecasts do affect the onward forecasts of blocks, but they are unlikely to be the only factor in determining an accurate blocking forecast. In reality, a complex combination of the representation of anticyclonic eddies, cyclonic eddies, and diabatic processes in forecasts are likely to contribute to the accuracy of block forecasts.

Chapter 7

Conclusions

Atmospheric blocking is responsible for a large range of hazardous surface weather conditions (Kautz et al., 2022), and therefore it is vital that such events are forecast accurately in the medium-range to allow for adequate mitigation. Unfortunately, the dynamics that result in blocking are still not completely known (Woollings et al., 2018) and this could lead to the fact that blocking situations are the least predictable weather patterns (Ferranti et al., 2015). However, many dynamical processes are known to be important, and one such phenomenon that had theoretically been proven to aid blocking dynamics is the interaction of blocks with transient synoptic-scale eddies (Shutts, 1983; Yamazaki and Itoh, 2013a; Luo et al., 2014). Despite this knowledge, a climatological study on the relationship between the two had been lacking.

This thesis addresses this research gap by examining the role that AC eddies have on the persistence of blocks in both the Euro-Atlantic and North Pacific. An attempt at quantifying the relative importance towards block maintenance of AC eddies and diabatic processes is also undertaken, to place the dynamics of block-eddy interactions into context with other processes known to be influential for blocking. Finally, the degree to which the accurate forecasting of AC eddies affects the accurate forecasting of blocks is analysed, to potentially highlight a reason as to why blocking is so unpredictable in medium-range NWP.

7.1 Research Questions

In Sect. 1.2, the main aims and research questions (RQs) of the thesis were posed. Throughout the rest of the thesis, the answers to these questions were subsequently obtained, and the main conclusions are now summarised here.

7.1.1 Is there a Relationship between AC Eddies and Block Persistence?

The first RQ sought to determine whether there was a relationship between AC eddies and the persistence of a block, since previous work (Yamazaki and Itoh, 2013a) had suggested that blocking anticyclones attract and absorb synoptic scale AC eddies. This question was examined in Sect. 4 through a climatological analysis of atmospheric blocking events and the AC eddies that coincide with them in both the Euro-Atlantic and North Pacific sectors. A novel definition of Z500 anomaly was devised and used to detect persistent regions of Eulerian anomalies (the blocks), and Lagrangian transient features (the AC eddies). This combined Eulerian-Lagrangian technique for analysing blocks has recently become more commonplace (e.g. Hauser et al., 2022, 2023) because it provides a more complete way to quantify the processes occurring in blocking. Using this method in this thesis, it was found that there is indeed a relationship between block persistence and AC eddies.

The most robust result from Sect. 4 was that there is a statistically significant positive correlation between the persistence of a block and the number of AC eddies it interacts with (Sect. 4.5.1). This relationship holds true for both the Euro-Atlantic and North Pacific at all times of year, albeit with a seasonal difference between the average number of absorbed AC eddies per block. These results perhaps indicate that the dynamics behind long blocks are different to those in shorter ones, as in Drouard et al. (2021). A less significant and more variable relationship, however, is found between the strength of the AC eddies and the length of the blocks they contribute to. Longer blocks are not always the result of stronger AC eddies, with the relation varying by time of year and location.

It was also shown that AC eddies increase block persistence by increasing

the strength and size of the block. The resulting larger, more intense blocking vortex takes longer to dissipate or requires more upstream forcing to be advected downstream, resulting in a more persistent block. In this sense, the correlation described above was not purely a statistical relationship. Some evidence of the SAM, where blocks attract AC eddies, was also found through the northward acceleration of the eddies in the few days before they enter the block.

An important caveat to the main conclusion in this section is that while it is true that *on average* longer blocks interact with more AC eddies, there is marked spread in the number of AC eddy interactions for a block of given persistence. This could suggest that AC eddies do not always have the same effect on the persistence of a block, and that other processes not thus far considered could also be important in determining how long a block lasts. This finding led to the formulation of RQ2, which is summarised in the next section.

7.1.2 For blocks with similar persistence but different AC eddy interactions, are their dynamics different?

To test this hypothesis, three case study blocks with similar persistence, but with 0, 1, and 2 AC eddies, were analysed in detail. A comparison between two dynamical processes in space and time in these blocks was performed: PV flux convergence, and diabatic modification of PV, the latter being obtained by analysis of diabatic tracer accumulations from the MetUM.

The three blocks analysed have both similarities and differences. All three are characterised by negative PV flux convergence and diabatic reduction in PV at onset. The AC eddies only contribute a large proportion of the total PV flux convergence within the block when they first enter (or when spawned eddies leave) since the interior of the block is associated with small PV gradients and light winds, therefore reducing PV flux convergence. Near the decay of the three blocks, there is positive PV flux convergence, which acts to end the blocking event.

The relative importance of diabatic processes and PV flux convergence is seen to vary from case to case, though it must be noted that a small sample of only three blocks was analysed. Therefore, it is impossible to determine whether

blocks with fewer AC eddies have a stronger influence towards their maintenance by diabatically-driven reduction in PV, and vice-versa. Out of the three studied here, the block with the highest AC eddy contribution also had the strongest contribution from diabatic processes towards block maintenance, and the case with zero AC eddies also had the strongest PV increase due to diabatic effects. However, the dominant diabatic process in each block also varies between cloud and convective parameterisations. To conclude, while it is hard to say whether blocks with fewer AC eddies have a stronger influence from diabatic processes than those with more eddies, it is probably more accurate to say that the dynamics of each blocking event are different anyway, regardless of AC eddy interactions or persistence.

7.1.3 Do errors in the forecasting of AC eddies lead to errors in forecasts of blocks?

This final RQ was investigated through identifying periods of increased uncertainty within the MOGREPS-G ensemble for certain blocking characteristics. Any periods that coincided with an AC eddy-block interaction were analysed in more detail. Predictability barriers (PBs) were found for two of the three case studies, which occurred at the onset and decay of the blocks. Three of these PBs were also close to the timings of AC eddy interactions, and were investigated further.

The PBs could be associated with an over- or underprediction of block strength or area, and also often a positional error, especially at longer lead times. These PBs remained at constant validity times, for multiple forecast initialisation times, and were associated with large spread of these block characteristics within the ensemble. Forecast confidence only increased at relatively short lead times.

The uncertainty could be explained by the misrepresentation of upstream AC eddies that went on to interact with the block at the validity time of the PB. In cases where the forecasted AC eddy was too small, weak, or slow, the corresponding block at the PB was also too small or weak. In one case, no block formed in the forecast at all as the result of an upstream AC eddy that was far too weak. Times of the onset and the decay of the block appeared to depend on the accuracy to which the AC eddies were represented in the forecast, but once the block

was mature, confidence in the forecast improved again regardless of how the AC eddy was earlier modelled. One PB investigation also revealed the possibility of an upstream block directly influencing the onset of another block downstream through spawning an eddy of its own which becomes an AC eddy that begins the downstream block.

7.2 Key Results from this Thesis

The overarching key result from this thesis is that **synoptic-scale, transient AC eddies are important for blocking dynamics**. This had long been suspected based on theoretical models and case study analysis by other authors (Shutts, 1983; Yamazaki and Itoh, 2013a; Luo et al., 2014), but this was for the first time able to be confirmed in a climatological study of blocks and their AC eddies (Sect. 4). Potential evidence was also found for the SAM (Yamazaki and Itoh, 2013a) from a climatological perspective, which goes to reinforce the case study of the SAM analysed in (Yamazaki and Itoh, 2013b).

Another key result from this work is that **accurate representation of AC eddies in forecasts can be important for accurate block onset or decay forecasts**. From the perspective of an operational meteorologist, this is a very important result. Since blocks can be associated with hazardous surface conditions (Sect. 2.3), it is prudent to accurately predict the strength, size, and location of a block accurately, with confidence, as far in advance as possible to allow for adequate time to mitigate against any potential impacts. However, the onset and decay of blocking events are often associated with increased uncertainty in the forecast (e.g. Ferranti et al., 2015), and confidence only increases at much shorter lead times (Sect. 6). This uncertainty can arise from uncertainty in how an AC eddy is forecast to evolve, and therefore it is necessary to accurately model AC eddies in order to accurately model block characteristics at longer lead times.

Additionally, this work shows that **an upstream block can influence another downstream block**. Maddison et al. (2019) demonstrated that forecasts of blocks are sensitive to the characteristics of upstream cyclones, but the final case study presented in Sect. 6.4 highlights that upstream anticyclones can also affect how

blocks are forecasted. In fact, this was a case where an upstream *blocking* anticyclone directly goes on to cause another downstream block (via a spawned eddy), and this interaction between two separate blocking events has not been noted before, to this author's knowledge.

7.3 Open Questions and Possible Future Research

Although the results presented in this thesis demonstrate the importance of AC eddies towards blocking dynamics, certain aspects are neglected from this work, which leads to the development of potential avenues for further research. These unanswered questions are discussed below.

An obvious question raised from the case study analysis in Sect. 5 is **does the same relationship between block persistence and AC eddies exist, if AC eddies and blocks were defined using the PV-based q'_* metric**, rather than from the Z500-based Z'_* field? The three case studies highlighted that not all distinct anticyclonic q'_* regions align with a corresponding distinct anticyclonic Z'_* area, suggesting that more AC eddies would be identified if they were defined using PV. This way of defining AC eddies (and blocks) would then be more inline with the work of Hauser et al. (2022, 2023) and would allow a much more thorough comparison between the results from those studies and this. An intriguing result from Hauser et al. (2023) was that the eddies associated with Greenland blocks have two pathways: directly from upstream; and eddies from upstream that "overshoot" Greenland and then retrogress back towards the region. In the work presented in this thesis, there was no evidence of any retrogression pathways for blocking for the PAC or ATL sectors, however it is very possible (and perhaps even expected given the observed behaviour of some blocking systems) that retrogression does occur in these regions too. Therefore, using a PV-based diagnostic for detecting blocking and eddies could potentially reveal a similar retrogression pathway for the Atlantic and Pacific sectors. Additionally, the SAM was originally explained from the perspective of PV and so defining blocks and eddies using PV would allow for a more vigorous test of the climatological relevance of the SAM.

The blocks examined in Sect. 5 actually showed some evidence that contradicted the SAM. In these blocks, positive q'_* streamers entered the block, which should have been repelled by the block according to the SAM. Therefore, **future work should also implement tracks of cyclonic transient eddies, as well as the anticyclonic ones**. By tracking eddies of both polarities, a much more complete verification of the SAM could be performed, to see whether on average, blocking anticyclones mostly absorb AC eddies, and mostly repel cyclonic eddies. In addition, a definition of a "blocking low", i.e., a persistent, quasi-stationary cyclone, like those in the equatorward portion of a dipole block, could also be implemented to test a similar hypothesis to that in Sect. 4 for blocking anticyclones: **do more persistent blocking lows absorb more cyclonic eddies that shorter ones?** This would also give the opportunity to test the validity of the SAM for large vortices of both polarities.

A third open question regarding the SAM that requires further investigation is **whether or not more persistent blocks absorb more AC eddies, simply because they would be expected to come across more given their longevity?** Is there a characteristic regular frequency of AC eddies in the mid-latitude jet stream which would therefore be expected to enter the region of a blocking event, whether or not the block was there? Or, is it the case that the block allows for more AC eddies to pass through the region because it is attracting them from further afield via the SAM?

Another aspect regarding synoptic-scale eddies and blocking dynamics that this thesis highlights is the interaction between two concurrent blocking systems (Sect. 6.4). However, **it is unclear how common two (or more) blocks influencing each other's onset/maintenance/decay is** via eddies shedding from one block and entering another. The case study in Sect. 6.4 suggests that such scenarios are not very predictable in medium-range weather forecasts, but it is unknown whether this is true for all eddies spawning from a pre-existing block, or whether there was something particular to the March 2021 case that made it unpredictable. Therefore, any future study on a block's spawned eddies should take into account both how common it is for one block to start another one, and whether such scenarios are inherently unpredictable.

The conclusions from Sect. 5 were vague in that it was only possible to deduce that the role of diabatic processes in blocks varies between each case, but not the extent to which this varies according to the number of AC eddy interactions a block has. One of the reasons for this was that it was only possible to examine three case studies in detail, due to the computing time and resources required for completing MetUM simulations with diabatic tracers. Additionally, the choices of example blocks to study were severely limited by the need to use a current version of the MetUM. Ideally, **a future study should examine more than just three blocks with similar persistence, with a wider range of numbers of contributing AC eddies**, in order to potentially be able to draw a more robust conclusion as to the relative importance of diabatic processes and AC eddies in blocks.

Finally, in a similar vein to Steinfeld and Pfahl (2019), **a climatological study of the importance of each parameterised process** (e.g. large-scale clouds, convection, radiation, etc.) in the MetUM towards blocking dynamics could be explored. Even from the small sample size in Sect. 5, it is clear that the dominant source of diabatic PV modification varies in space, time, and block event, but this current work does not investigate the potential reasons behind this. More work is needed to uncover why in certain blocks, the convection parameterisation is most important, whereas in others it appears that the large-scale cloud parameterisation is just as crucial for block development. This could depend on aspects such as season, location of the block, proximity of the block to a WCB, and intensity of the WCB.

Appendices

Appendix A

Appendix

A.1 Comparison of Δq_{PC2} and Δq_{LW} under the Original and Updated PC2 Scheme

As mentioned in Sect. 5.2.6, after the forecasts were run for the analysis in this thesis, the PC2 cloud scheme was fixed such that unrealistic opposing large-magnitude regions of Δq_{PC2} and Δq_{LW} were removed. An example cross-section of the Δq_{PC2} and Δq_{LW}, as resolved using the original and updated PC2 scheme, is shown in Fig. A.1, from a 60 hour forecast from 18 February 2019 at a latitude of 55°N.

Under the old PC2 scheme, localised maxima/minima in Δq_{LW} (Fig. A.1a) coincide with minima/maxima in Δq_{PC2} (Fig. A.1b), especially between -10 and 20°E (between the block) in the mid-troposphere. Large-magnitude regions of modified PV are also found in the boundary layer. With the updated PC2 scheme, these maxima/minima in the mid-troposphere are eliminated for both Δq_{SW} (Fig. A.1c) and Δq_{PC2} (Fig. A.1d), though the boundary layer remains unchanged for Δq_{PC2}.

Ideally, all case study analysis in Sect. 5 would have been performed using the updated PC2 scheme in the MetUM, but timing did not allow for this to happen. The effect of using the original PC2 scheme in the analysis is now briefly discussed. There would be very little effect on the block-mean total change to PV (Δq) by updating the PC2 scheme like this, because the small-scale structure produced by the original scheme is responsible for generally equal and op-

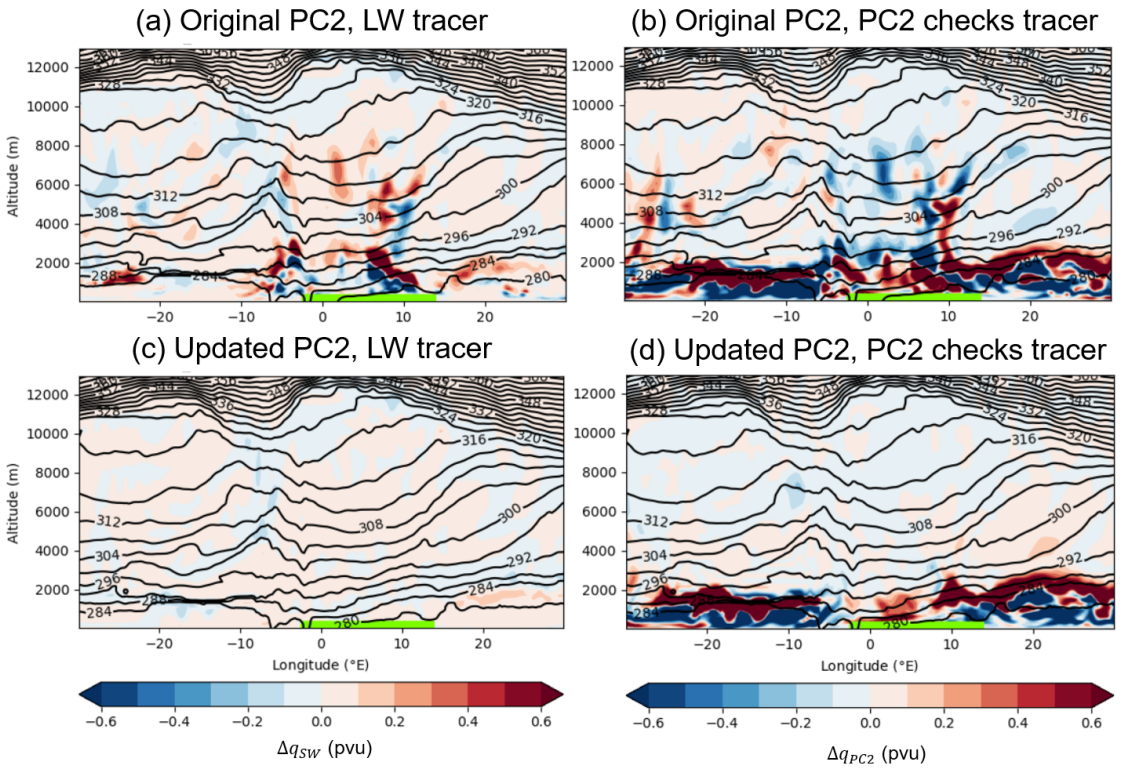

Figure A.1: Cross-sections, at 55°N, of Δq_{SW} (a, c), and Δq_{PC2} (b, d) under the original (top row) and updated (bottom row) PC2 scheme in the MetUM. The forecast was initialised on 18 February 2019 00 UTC, with a lead time of 60 h (validity time of 20 February 12 UTC). Isentropes are shown in black, and blocked longitudes in green.

posite Δq_{LW} and Δq_{PC2} patterns in the mid-troposphere (Fig. A.1a, b). Likewise, throughout the entire block, there are regions of both positive and negative change to PV for each tracer, and therefore the net effect of averaging over the block would be to smooth these out (such that the fields appear like those in the updated PC2 anyway, Fig. A.1c, d). Thus, it is expected that using the original PC2 scheme setting would not change the results or conclusions much in this work. However, it should be noted that the results presented for Δq_{rad} and Δq_{cloud} (which Δq_{LW} and Δq_{PC2} contribute to respectively) are a little more uncertain because of this.

The update to PC2 also produces minor changes to the meteorology in the forecasts (as seen by the 292 K isentrope west of -20°E, for example, in Fig. A.1). Therefore there could also be subtle changes to the forecasted Z500, Z'_* and q'_* of the blocks between the two PC2 setups. However, these changes are expected to be very small and therefore are not considered a significant source of error for the

analysis in Sect. 5. A full analysis of the changes that the updated PC2 scheme setting makes on the results in this thesis is out of scope for this study.

A.2 MOGREPS-G Blocking Tool

While working on the analysis for Chapter 3, an additional block identification tool was developed in association with Duncan Ackerley and Dan Suri at the Met Office. The aim of this tool was to quickly and easily identify how likely blocking is predicted to be over the Euro-Atlantic sector, for MOGREPS-G forecasts in near-real time, such that operational meteorologists can determine the likelihood of blocking in a matter of seconds. The tool uses my code for calculating the instantaneous Z'_* blocking index for each ensemble member, at every lead time. On the webpage, it is also possible to scroll back in time for forecasts of the same t_{val} but from forecasts initialised at previous t_{in}, to examine the previous model runs and determine how the signal for blocking may have changed through time.

The webpage contains four plots, which are briefly summarised below:

- A map containing the percentage of the ensemble mean forecast length that is instantaneously blocked at each grid point. This is designed as a top-level "overview" of blocking in the forecast. If percentages in the Euro-Atlantic are large, it would signal to operational meteorologists that blocking is likely at some stage in the medium-range and would suggest to them to look at additional output to obtain more information.
- A map containing the percentage of each member's forecast period that is instantaneously blocked, with a switch that allows for scrolling between different members.
- A map, at a certain t_{val} that is specified by the user, that shows the percentage of ensemble members that indicate instantaneous blocking in the NH. Buttons allow for the changing of t_{val} and t_{in}.
- Postage stamps showing either the MSLP, Z500, or Z'_*, along with the instantaneously blocked grid points, for each ensemble member. Again, buttons allow the user to change the t_{val} and t_{in} of the postage stamps.

While developing this real-time tool, it was realised that the postage stamps in particular would be useful in aiding the manual checks required for choosing similarly-evolving ensemble members that form the small groups (see Sect. 6.2.3). Therefore, webpages were created of the same data, but using MOGREPS-G output from forecasts initialised around the February 2019, March 2021, and August 2021 case studies. An example, used when analysing the onset of the March 2021 block (Sect. 6.4), is shown in Fig. A.2. Here, the rationale behind the choices of members that form part of groups G, H, and I (Table 6.3) is clear. The members in Group G (3, 5, 7, 8, 10, 11, 14) have a very small collection of blocked points, if any, over the Euro-Atlantic, but do have a weak Z'_* ridge in the vicinity of the UK. Members 4 and 6 (Group H) both have a block centred between Iceland and Ireland. Finally, member 17 (Group I) is an outlier in that the Z'_* ridge forecast in Group G is much stronger and is the result of an extension of the Azores high.

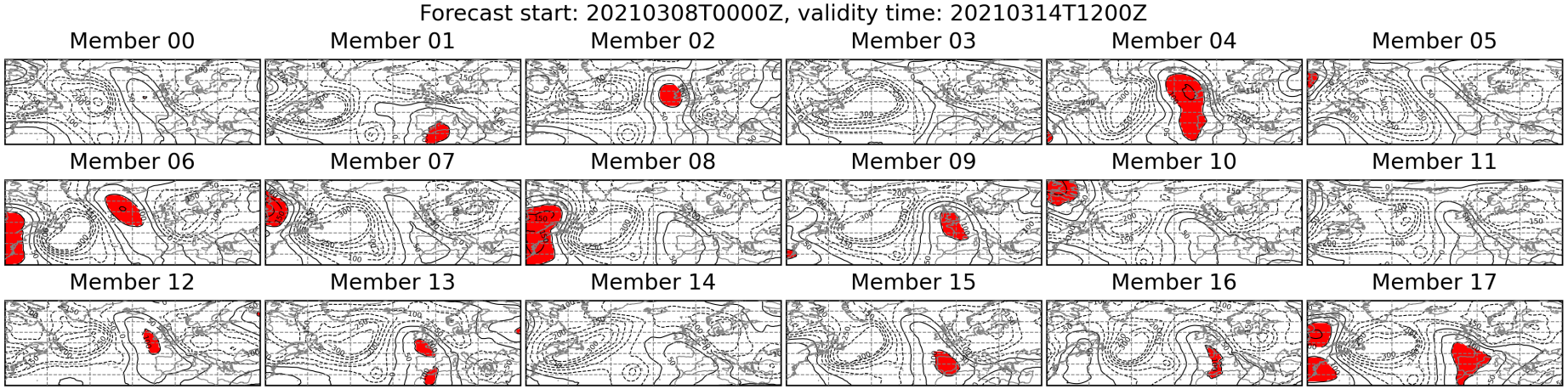

Figure A.2: Postage stamps for all 18 ensemble members, for PB3 (the March 2021 block onset case), from a forecast with a t_{in} of 8 March 2021 and a t_{val} of 12 UTC on 14 March. Z'_* is shown every 50 m in black contours (negatives dashed, and instantaneously blocked grid points are shown in red.

Bibliography

A. M. Altenhoff, O. Martius, M. Croci-Maspoli, C. Schwierz, and H. C. Davies. Linkage of atmospheric blocks and synoptic-scale Rossby waves: A climatological analysis. *Tellus A: Dynamic Meteorology and Oceanography*, 60(5):1053–1063, 2008.

C. Anagnostopoulou, K. Tolika, G. Lazoglou, and P. Maheras. The exceptionally cold January of 2017 over the Balkan Peninsula: A climatological and synoptic analysis. *Atmosphere*, 8(12):252, 2017.

J. A. Anstey, P. Davini, L. J. Gray, T. J. Woollings, N. Butchart, C. Cagnazzo, B. Christiansen, S. C. Hardiman, S. M. Osprey, and S. Yang. Multi-model analysis of Northern Hemisphere winter blocking: Model biases and the role of resolution. *Journal of Geophysical Research: Atmospheres*, 118(10):3956–3971, 2013.

O. Y. Antokhina, P. N. Antokhin, B. D. Belan, A. V. Gochakov, Y. V. Martynova, K. N. Pustovalov, L. D. Tarabukina, and E. V. Devyatova. Effects of Rossby Waves Breaking and Atmospheric Blocking Formation on the Extreme Forest Fire and Floods in Eastern Siberia 2019. *Fire*, 6(3):122, 2023.

A. Arakawa and V. R. Lamb. Computational design of the basic dynamical processes of the UCLA general circulation model. *General circulation models of the atmosphere*, 17(Supplement C):173–265, 1977.

J. Austin. The blocking of middle latitude westerly winds by planetary waves. *Quarterly Journal of the Royal Meteorological Society*, 106(448):327–350, 1980.

G. Azizi, H. Mohammadi, M. Karimi, A. A. Shamsipour, and I. Rousta. The relationship between the Arctic oscillation and North Atlantic blocking frequency. *Open J Atmos Clim Changes*, 2015.

E. A. Barnes, J. Slingo, and T. Woollings. A methodology for the comparison of blocking climatologies across indices, models and climate scenarios. *Climate dynamics*, 38(11):2467–2481, 2012.

D. Barriopedro, R. García-Herrera, A. R. Lupo, and E. Hernández. A climatology of Northern Hemisphere blocking. *Journal of climate*, 19(6):1042–1063, 2006.

D. Barriopedro, R. García-Herrera, and R. M. Trigo. Application of blocking diagnosis methods to general circulation models. Part I: A novel detection scheme. *Climate dynamics*, 35(7):1373–1391, 2010.

BBC Weather. Remembering the Beast from the East. `https://www.bbc.co.uk/weather/weather-watcher/47356036`, 2019. Accessed: 25 April 2024.

P. Berrisford, B. Hoskins, and E. Tyrlis. Blocking and Rossby wave breaking on the dynamical tropopause in the Southern Hemisphere. *Journal of the Atmospheric Sciences*, 64(8):2881–2898, 2007.

M. Bieli, S. Pfahl, and H. Wernli. A Lagrangian investigation of hot and cold temperature extremes in Europe. *Quarterly Journal of the Royal Meteorological Society*, 141(686):98–108, 2015.

C. H. Bishop, B. J. Etherton, and S. J. Majumdar. Adaptive sampling with the ensemble transform Kalman filter. Part I: Theoretical aspects. *Monthly weather review*, 129(3):420–436, 2001.

E. Black, M. Blackburn, G. Harrison, B. Hoskins, and J. Methven. Factors contributing to the summer 2003 European heatwave. *Weather*, 59(8):217–223, 2004.

H. Bloomfield, C. Suitters, and D. Drew. Meteorological drivers of European power system stress. *Journal of Renewable Energy*, 2020, 2020.

N. E. Bowler, A. Arribas, K. R. Mylne, K. B. Robertson, and S. E. Beare. The MOGREPS short-range ensemble prediction system. *Quarterly Journal of the Royal Meteorological Society: A journal of the atmospheric sciences, applied meteorology and physical oceanography*, 134(632):703–722, 2008.

L. Brunner, G. C. Hegerl, and A. K. Steiner. Connecting atmospheric blocking to European temperature extremes in spring. *Journal of Climate*, 30(2):585–594, 2017.

L. Brunner, N. Schaller, J. Anstey, J. Sillmann, and A. K. Steiner. Dependence of present and future European temperature extremes on the location of atmospheric blocking. *Geophysical research letters*, 45(12):6311–6320, 2018.

J. Cattiaux, R. Vautard, C. Cassou, P. Yiou, V. Masson-Delmotte, and F. Codron. Winter 2010 in Europe: A cold extreme in a warming climate. *Geophysical Research Letters*, 37(20), 2010.

H. Chappells, W. Medd, and E. Shove. Disruption and change: drought and the inconspicuous dynamics of garden lives. *Social & Cultural Geography*, 12(7): 701–715, 2011.

A. J. Charlton-Perez, R. W. Aldridge, C. M. Grams, and R. Lee. Winter pressures on the UK health system dominated by the Greenland Blocking weather regime. *Weather and Climate Extremes*, 25:100218, 2019.

J. Charney, J. Shukla, and K. Mo. Comparison of a barotropic blocking theory with observation. *Journal of Atmospheric Sciences*, 38(4):762–779, 1981.

J. G. Charney and N. Phillips. Numerical integration of the quasi-geostrophic equations for barotropic and simple baroclinic flows. *Journal of Atmospheric Sciences*, 10(2):71–99, 1953.

S. J. Colucci. Explosive cyclogenesis and large-scale circulation changes: Implications for atmospheric blocking. *Journal of Atmospheric Sciences*, 42(24):2701–2717, 1985.

M. Croci-Maspoli, C. Schwierz, and H. Davies. A multifaceted climatology of atmospheric blocking and its recent linear trend. *Journal of Climate*, 20(4):633–649, 2007.

P. Davini and F. D'Andrea. Northern Hemisphere atmospheric blocking representation in global climate models: Twenty years of improvements? *Journal of Climate*, 29(24):8823–8840, 2016.

P. Davini, C. Cagnazzo, S. Gualdi, and A. Navarra. Bidimensional diagnostics, variability, and trends of Northern Hemisphere blocking. *Journal of Climate*, 25 (19):6496–6509, 2012.

P. Davini, A. Weisheimer, M. Balmaseda, S. J. Johnson, F. Molteni, C. D. Roberts, R. Senan, and T. N. Stockdale. The representation of winter Northern Hemisphere atmospheric blocking in ECMWF seasonal prediction systems. *Quarterly Journal of the Royal Meteorological Society*, 147(735):1344–1363, 2021.

A. Dawson and T. Palmer. Simulating weather regimes: Impact of model resolution and stochastic parameterization. *Climate Dynamics*, 44:2177–2193, 2015.

C. Detring, A. Müller, L. Schielicke, P. Névir, and H. W. Rust. Atmospheric blocking types: Frequencies and transitions. *Weather and Climate Dynamics Discussions*, 2020:1–33, 2020.

Y. Diao, J. Li, and D. Luo. A new blocking index and its application: Blocking action in the Northern Hemisphere. *Journal of Climate*, 19(19):4819–4839, 2006.

R. M. Dole and N. D. Gordon. Persistent anomalies of the extratropical Northern Hemisphere wintertime circulation: Geographical distribution and regional persistence characteristics. *Monthly Weather Review*, 111(8):1567–1586, 1983.

A. Donohoe and D. S. Battisti. The amplitude asymmetry between synoptic cyclones and anticyclones: Implications for filtering methods in feature tracking. *Monthly weather review*, 137(11):3874–3887, 2009.

M. Drouard and T. Woollings. Contrasting mechanisms of summer blocking over western Eurasia. *Geophysical Research Letters*, 45(21):12–040, 2018.

M. Drouard, T. Woollings, D. M. Sexton, and C. F. McSweeney. Dynamical differences between short and long blocks in the Northern Hemisphere. *Journal of Geophysical Research: Atmospheres*, 126(10):e2020JD034082, 2021.

E. Dunn-Sigouin, S.-W. Son, and H. Lin. Evaluation of Northern Hemisphere blocking climatology in the global environment multiscale model. *Monthly Weather Review*, 141(2):707–727, 2013.

J. Edwards and A. Slingo. Studies with a flexible new radiation code. I: Choosing a configuration for a large-scale model. *Quarterly Journal of the Royal Meteorological Society*, 122(531):689–719, 1996.

H. Ertel. Ein neuer hydrofynamischer Wirbelsatz. *Meteor. Z.*, 59:277–282, 1942.

L. Ferranti, S. Corti, and M. Janousek. Flow-dependent verification of the ECMWF ensemble over the Euro-Atlantic sector. *Quarterly Journal of the Royal Meteorological Society*, 141(688):916–924, 2015.

A. H. Fink, T. Brücher, V. Ermert, A. Krüger, and J. G. Pinto. The European storm Kyrill in January 2007: synoptic evolution, meteorological impacts and some considerations with respect to climate change. *Natural Hazards and Earth System Sciences*, 9(2):405–423, 2009.

E. M. Fischer, S. I. Seneviratne, P. L. Vidale, D. Lüthi, and C. Schär. Soil moisture–atmosphere interactions during the 2003 European summer heat wave. *Journal of Climate*, 20(20):5081–5099, 2007.

G. Forzieri, A. Bianchi, F. B. e Silva, M. A. M. Herrera, A. Leblois, C. Lavalle, J. C. Aerts, and L. Feyen. Escalating impacts of climate extremes on critical infrastructures in europe. *Global environmental change*, 48:97–107, 2018.

R. García-Herrera and D. Barriopedro. Northern Hemisphere snow cover and atmospheric blocking variability. *Journal of Geophysical Research: Atmospheres*, 111(D21), 2006.

J. M. Garrido-Perez, C. Ordóñez, and R. Garcia-Herrera. Strong signatures of high-latitude blocks and subtropical ridges in winter PM10 over Europe. *Atmospheric Environment*, 167:49–60, 2017.

C. M. Grams, H. Binder, S. Pfahl, N. Piaget, and H. Wernli. Atmospheric processes triggering the central European floods in june 2013. *Natural Hazards and Earth System Sciences*, 14(7):1691–1702, 2014.

C. M. Grams, R. Beerli, S. Pfenninger, I. Staffell, and H. Wernli. Balancing Europe's wind-power output through spatial deployment informed by weather regimes. *Nature climate change*, 7(8):557–562, 2017.

S. Gray. Mechanisms of midlatitude cross-tropopause transport using a potential vorticity budget approach. *Journal of Geophysical Research: Atmospheres*, 111 (D17), 2006.

D. Gregory and P. Rowntree. A mass flux convection scheme with representation of cloud ensemble characteristics and stability-dependent closure. *Monthly Weather Review*, 118(7):1483–1506, 1990.

E. Hanna, T. E. Cropper, R. J. Hall, and J. Cappelen. Greenland Blocking Index 1851–2015: a regional climate change signal. *International Journal of Climatology*, 36(15):4847–4861, 2016.

D. L. Hartmann and S. J. Ghan. A statistical study of the dynamics of blocking. *Monthly weather review*, 108(8):1144–1159, 1980.

S. Hauser, F. Teubler, M. Riemer, P. Knippertz, and C. M. Grams. Towards a diagnostic framework unifying different perspectives on blocking dynamics: insight into a major blocking in the North Atlantic-European region. *Weather and Climate Dynamics Discussions*, 2022:1–36, 2022.

S. Hauser, F. Teubler, M. Riemer, P. Knippertz, and C. M. Grams. Life cycle dynamics of Greenland blocking from a potential vorticity perspective. *EGUsphere*, 2023:1–37, 2023.

M. Hawcroft, L. Shaffrey, K. Hodges, and H. Dacre. How much Northern Hemisphere precipitation is associated with extratropical cyclones? *Geophysical Research Letters*, 39(24), 2012.

P. H. Haynes and M. E. McIntyre. On the evolution of vorticity and potential vorticity in the presence of diabatic heating and frictional or other forces. *Journal of Atmospheric Sciences*, 44(5):828–841, 1987.

H. Hersbach, B. Bell, P. Berrisford, S. Hirahara, A. Horányi, J. Muñoz-Sabater, J. Nicolas, C. Peubey, R. Radu, D. Schepers, et al. The ERA5 global reanalysis. *Quarterly Journal of the Royal Meteorological Society*, 146(730):1999–2049, 2020.

K. Hodges. A general method for tracking analysis and its application to meteorological data. *Monthly Weather Review*, 122(11):2573–2586, 1994.

K. Hodges. Feature tracking on the unit sphere. *Monthly Weather Review*, 123(12): 3458–3465, 1995.

K. Hodges. Adaptive constraints for feature tracking. *Monthly Weather Review*, 127(6):1362–1373, 1999.

K. I. Hodges, R. W. Lee, and L. Bengtsson. A comparison of extratropical cyclones in recent reanalyses ERA-Interim, NASA MERRA, NCEP CFSR, and JRA-25. *Journal of Climate*, 24(18):4888–4906, 2011.

B. Hoskins and K. Hodges. The annual cycle of northern hemisphere storm tracks. Part I: Seasons. *Journal of Climate*, 32(6):1743–1760, 2019.

B. J. Hoskins, M. E. McIntyre, and A. W. Robertson. On the use and significance of isentropic potential vorticity maps. *Quarterly Journal of the Royal Meteorological Society*, 111(470):877–946, 1985.

G. Inverarity, W. Tennant, L. Anton, N. Bowler, A. Clayton, M. Jardak, A. Lorenc, F. Rawlins, S. Thompson, M. Thurlow, et al. Met Office MOGREPS-G initialisation using an ensemble of hybrid four-dimensional ensemble variational (En-4DEnVar) data assimilations. *Quarterly Journal of the Royal Meteorological Society*, 149(753):1138–1164, 2023.

L. Ioannidou and M. Yau. A climatology of the Northern Hemisphere winter anticyclones. *Journal of Geophysical Research: Atmospheres*, 113(D8), 2008.

P. James. An objective classification method for Hess and Brezowsky Grosswetterlagen over Europe. *Theoretical and Applied Climatology*, 88:17–42, 2007.

E. Kaas and G. Branstator. The relationship between a zonal index and blocking activity. *Journal of the atmospheric sciences*, 50(18):3061–3077, 1993.

A. Y. Karpechko, A. Charlton-Perez, M. Balmaseda, N. Tyrrell, and F. Vitart. Predicting sudden stratospheric warming 2018 and its climate impacts with a multimodel ensemble. *Geophysical Research Letters*, 45(24):13–538, 2018.

L.-A. Kautz, O. Martius, S. Pfahl, J. G. Pinto, A. M. Ramos, P. M. Sousa, and T. Woollings. Atmospheric blocking and weather extremes over the Euro-Atlantic sector–a review. *Weather and Climate Dynamics*, 3(1):305–336, 2022.

J. L. Knox and J. E. Hay. Blocking signatures in the Northern Hemisphere: Rationale and identification. *Atmosphere-Ocean*, 22(1):36–47, 1984.

S. H. Lee, M. K. Tippett, and L. M. Polvani. A new year-round weather regime classification for North America. *Journal of Climate*, 36(20):7091–7108, 2023.

B. Legras and M. Ghil. Persistent anomalies, blocking and variations in atmospheric predictability. *Journal of Atmospheric Sciences*, 42(5):433–471, 1985.

H. Lejenäs and H. Økland. Characteristics of Northern Hemisphere blocking as determined from a long time series of observational data. *Tellus A*, 35(5):350–362, 1983.

S. Lenggenhager and O. Martius. Quantifying the link between heavy precipitation and Northern Hemisphere blocking—A Lagrangian analysis. *Atmospheric science letters*, 21(10):e999, 2020.

M. Leutbecher and T. N. Palmer. Ensemble forecasting. *Journal of computational physics*, 227(7):3515–3539, 2008.

B. Li, S. Basu, S. J. Watson, and H. W. Russchenberg. A Brief Climatology of Dunkelflaute Events over and Surrounding the North and Baltic Sea Areas. *Energies*, 14(20):6508, 2021.

M. Li, Y. Yao, D. Luo, and L. Zhong. The linkage of the large-scale circulation pattern to a long-lived heatwave over Mideastern China in 2018. *Atmosphere*, 10(2):89, 2019.

P. Liu, Y. Zhu, Q. Zhang, J. Gottschalck, M. Zhang, C. Melhauser, W. Li, H. Guan, X. Zhou, D. Hou, et al. Climatology of tracked persistent maxima of 500-hPa geopotential height. *Climate Dynamics*, 51(1):701–717, 2018.

K. Lochbihler, G. Lenderink, and A. P. Siebesma. The spatial extent of rainfall events and its relation to precipitation scaling. *Geophysical Research Letters*, 44 (16):8629–8636, 2017.

A. Lock, A. Brown, M. Bush, G. Martin, and R. Smith. A new boundary layer mixing scheme. Part I: Scheme description and single-column model tests. *Monthly weather review*, 128(9):3187–3199, 2000.

B. Luo, D. Luo, A. Dai, I. Simmonds, and L. Wu. A connection of winter Eurasian cold anomaly to the modulation of Ural blocking by ENSO. *Geophysical Research Letters*, 48(17):e2021GL094304, 2021.

D. Luo. A barotropic envelope Rossby soliton model for block–eddy interaction. Part III: Wavenumber conservation theorems for isolated blocks and deformed eddies. *Journal of the atmospheric sciences*, 62(11):3839–3859, 2005.

D. Luo and J. Cha. The North Atlantic Oscillation and the North Atlantic jet variability: Precursors to NAO regimes and transitions. *Journal of the Atmospheric Sciences*, 69(12):3763–3787, 2012.

D. Luo, J. Cha, L. Zhong, and A. Dai. A nonlinear multiscale interaction model for atmospheric blocking: The eddy-blocking matching mechanism. *Quarterly Journal of the Royal Meteorological Society*, 140(683):1785–1808, 2014.

A. R. Lupo. A diagnosis of two blocking events that occurred simultaneously in the midlatitude Northern Hemisphere. *Monthly Weather Review*, 125(8):1801–1823, 1997.

J. Maddison, S. Gray, O. Martínez-Alvarado, and K. Williams. Upstream cyclone influence on the predictability of block onsets over the Euro-Atlantic region. *Monthly Weather Review*, 147(4):1277–1296, 2019.

J. W. Maddison, S. L. Gray, O. Martínez-Alvarado, and K. D. Williams. Impact of model upgrades on diabatic processes in extratropical cyclones and downstream forecast evolution. *Quarterly Journal of the Royal Meteorological Society*, 146(728):1322–1350, 2020.

E. Madonna, H. Wernli, H. Joos, and O. Martius. Warm conveyor belts in the ERA-Interim dataset (1979–2010). Part I: Climatology and potential vorticity evolution. *Journal of climate*, 27(1):3–26, 2014.

E. Madonna, M. Boettcher, C. M. Grams, H. Joos, O. Martius, and H. Wernli. Verification of North Atlantic warm conveyor belt outflows in ECMWF forecasts. *Quarterly Journal of the Royal Meteorological Society*, 141(689):1333–1344, 2015.

O. Martínez-Alvarado and R. Plant. Parametrized diabatic processes in numerical simulations of an extratropical cyclone. *Quarterly Journal of the Royal Meteorological Society*, 140(682):1742–1755, 2014.

G. Masato, B. J. Hoskins, and T. J. Woollings. Can the frequency of blocking be described by a red noise process? *Journal of the Atmospheric Sciences*, 66(7): 2143–2149, 2009.

G. Masato, B. Hoskins, and T. J. Woollings. Wave-breaking characteristics of mid-latitude blocking. *Quarterly Journal of the Royal Meteorological Society*, 138(666): 1285–1296, 2012.

G. Masato, B. J. Hoskins, and T. Woollings. Wave-breaking characteristics of Northern Hemisphere winter blocking: A two-dimensional approach. *Journal of climate*, 26(13):4535–4549, 2013a.

G. Masato, B. J. Hoskins, and T. Woollings. Winter and summer Northern Hemisphere blocking in CMIP5 models. *Journal of Climate*, 26(18):7044–7059, 2013b.

M. Matsueda. Blocking predictability in operational medium-range ensemble forecasts. *Sola*, 5:113–116, 2009.

J. C. McWilliams. An application of equivalent modons to atmospheric blocking. *Dynamics of Atmospheres and Oceans*, 5(1):43–66, 1980.

G. A. Meehl and C. Tebaldi. More intense, more frequent, and longer lasting heat waves in the 21st century. *Science*, 305(5686):994–997, 2004.

Met Office. Snow and low temperatures February to March 2018. `https://www.metoffice.gov.uk/binaries/content/assets/metofficegovuk/pdf/weather/learn-about/uk-past-events/interesting/2018/snow-and-low-temperatures-february-to-march-2018---met-office.pdf`, 2018. Accessed: 25 April 2024.

Met Office. UM vn12.1 user release notes. `https://code.metoffice.gov.uk/trac/um/wiki/ReleaseNotes12.1`, 2022. Accessed: 8 May 2024.

Met Office. Blocking patterns. https://www.metoffice.gov.uk/weather/learn-about/weather/how-weather-works/high-and-low-pressure/blocks, 2024a. Accessed: 25 April 2024.

Met Office. The heatwave of 2003. https://www.metoffice.gov.uk/weather/learn-about/weather/case-studies/heatwave#:~:text=Maximum%20temperatures,high%20which%20still%20stands%20today., 2024b. Accessed: 25 April 2024.

Met Office. Numerical weather prediction models. https://www.metoffice.gov.uk/research/approach/modelling-systems/unified-model/weather-forecasting, 2024c. Accessed: 9 May 2024.

P.-A. Michelangeli, R. Vautard, and B. Legras. Weather regimes: Recurrence and quasi stationarity. *Journal of the atmospheric sciences*, 52(8):1237–1256, 1995.

D. E. Miller and Z. Wang. Northern Hemisphere Winter Blocking: Differing Onset Mechanisms across Regions. *Journal of the Atmospheric Sciences*, 2022.

D. G. Miralles, P. Gentine, S. I. Seneviratne, and A. J. Teuling. Land–atmospheric feedbacks during droughts and heatwaves: state of the science and current challenges. *Annals of the New York Academy of Sciences*, 1436(1):19–35, 2019.

S. Mohr, J. Wandel, S. Lenggenhager, and O. Martius. Relationship between atmospheric blocking and warm-season thunderstorms over western and central Europe. *Quarterly Journal of the Royal Meteorological Society*, 145(724):3040–3056, 2019.

R. J. Murray and I. Simmonds. A numerical scheme for tracking cyclone centres from digital data. *Australian Meteorological Magazine*, 39(3):155–166, 1991.

N. Nakamura and C. S. Huang. Atmospheric blocking as a traffic jam in the jet stream. *Science*, 361(6397):42–47, 2018.

R. Neal, R. Dankers, A. Saulter, A. Lane, J. Millard, G. Robbins, and D. Price. Use of probabilistic medium-to long-range weather-pattern forecasts for identifying periods with an increased likelihood of coastal flooding around the UK. *Meteorological Applications*, 25(4):534–547, 2018.

C. Ordóñez, D. Barriopedro, R. García-Herrera, P. M. Sousa, and J. L. Schnell. Regional responses of surface ozone in Europe to the location of high-latitude blocks and subtropical ridges. *Atmospheric chemistry and physics*, 17(4):3111–3131, 2017.

J. Pasquier, S. Pfahl, and C. M. Grams. Modulation of atmospheric river occurrence and associated precipitation extremes in the North Atlantic region by European weather regimes. *Geophysical Research Letters*, 46(2):1014–1023, 2019.

M. Patterson, T. Bracegirdle, and T. Woollings. Southern Hemisphere atmospheric blocking in CMIP5 and future changes in the Australia-New Zealand sector. *Geophysical Research Letters*, 46(15):9281–9290, 2019.

Y. Peings. Ural blocking as a driver of early-winter stratospheric warmings. *Geophysical Research Letters*, 46(10):5460–5468, 2019.

J. L. Pelly and B. J. Hoskins. A new perspective on blocking. *Journal of the atmospheric sciences*, 60(5):743–755, 2003a.

J. L. Pelly and B. J. Hoskins. How well does the ECMWF ensemble prediction system predict blocking? *Quarterly Journal of the Royal Meteorological Society: A journal of the atmospheric sciences, applied meteorology and physical oceanography*, 129(590):1683–1702, 2003b.

A. Pepler, A. Dowdy, and P. Hope. A global climatology of surface anticyclones, their variability, associated drivers and long-term trends. *Climate Dynamics*, 52 (9):5397–5412, 2019.

S. Pfahl. Characterising the relationship between weather extremes in Europe and synoptic circulation features. *Natural Hazards and Earth System Sciences*, 14 (6):1461–1475, 2014.

S. Pfahl and H. Wernli. Quantifying the relevance of cyclones for precipitation extremes. *Journal of Climate*, 25(19):6770–6780, 2012.

S. Pfahl, C. Schwierz, M. Croci-Maspoli, C. M. Grams, and H. Wernli. Importance of latent heat release in ascending air streams for atmospheric blocking. *Nature Geoscience*, 8(8):610–614, 2015.

F. Rabier, E. Klinker, P. Courtier, and A. Hollingsworth. Sensitivity of forecast errors to initial conditions. *Quarterly Journal of the Royal Meteorological Society*, 122(529):121–150, 1996.

D. F. Rex. Blocking action in the middle troposphere and its effect upon regional climate. *Tellus*, 2(4):275–301, 1950.

J.-M. Robine, S. L. K. Cheung, S. Le Roy, H. Van Oyen, C. Griffiths, J.-P. Michel, and F. R. Herrmann. Death toll exceeded 70,000 in Europe during the summer of 2003. *Comptes Rendus. Biologies*, 331(2):171–178, 2008.

M. J. Rodwell, L. Magnusson, P. Bauer, P. Bechtold, M. Bonavita, C. Cardinali, M. Diamantakis, P. Earnshaw, A. Garcia-Mendez, L. Isaksen, et al. Characteristics of occasional poor medium-range weather forecasts for europe. *Bulletin of the American Meteorological Society*, 94(9):1393–1405, 2013.

M. Röthlisberger and O. Martius. Quantifying the local effect of Northern Hemisphere atmospheric blocks on the persistence of summer hot and dry spells. *Geophysical Research Letters*, 46(16):10101–10111, 2019.

L. Saffin, J. Methven, and S. Gray. The non-conservation of potential vorticity by a dynamical core compared with the effects of parametrized physical processes. *Quarterly Journal of the Royal Meteorological Society*, 142(696):1265–1275, 2016.

L. Saffin, S. Gray, J. Methven, and K. Williams. Processes maintaining tropopause sharpness in numerical models. *Journal of Geophysical Research: Atmospheres*, 122 (18):9611–9627, 2017.

C. Sánchez, J. Methven, S. Gray, and M. Cullen. Linking rapid forecast error growth to diabatic processes. *Quarterly Journal of the Royal Meteorological Society*, 146(732):3548–3569, 2020.

A. A. Scaife, T. Woollings, J. Knight, G. Martin, and T. Hinton. Atmospheric blocking and mean biases in climate models. *Journal of Climate*, 23(23):6143–6152, 2010.

S. C. Scherrer, M. Croci-Maspoli, C. Schwierz, and C. Appenzeller. Two-dimensional indices of atmospheric blocking and their statistical relationship

with winter climate patterns in the Euro-Atlantic region. *International Journal of Climatology: A Journal of the Royal Meteorological Society*, 26(2):233–249, 2006.

R. Schiemann, M.-E. Demory, L. C. Shaffrey, J. Strachan, P. L. Vidale, M. S. Mizielinski, M. J. Roberts, M. Matsueda, M. F. Wehner, and T. Jung. The resolution sensitivity of Northern Hemisphere blocking in four 25-km atmospheric global circulation models. *Journal of Climate*, 30(1):337–358, 2017.

R. Schiemann, P. Athanasiadis, D. Barriopedro, F. Doblas-Reyes, K. Lohmann, M. J. Roberts, D. V. Sein, C. D. Roberts, L. Terray, and P. L. Vidale. Northern Hemisphere blocking simulation in current climate models: Evaluating progress from the Climate Model Intercomparison Project Phase 5 to 6 and sensitivity to resolution. *Weather and Climate Dynamics*, 1(1):277–292, 2020.

C. Schwierz, M. Croci-Maspoli, and H. Davies. Perspicacious indicators of atmospheric blocking. *Geophysical research letters*, 31(6), 2004.

F. Schwing, T. Murphree, and P. Green. The Northern Oscillation Index (NOI): a new climate index for the northeast Pacific. *Progress in oceanography*, 53(2-4): 115–139, 2002.

T. Selz, M. Riemer, and G. C. Craig. The transition from practical to intrinsic predictability of midlatitude weather. *Journal of the Atmospheric Sciences*, 79(8): 2013–2030, 2022.

J. Shukla and K. Mo. Seasonal and geographical variation of blocking. *Monthly Weather Review*, 111(2):388–402, 1983.

G. Shutts. The propagation of eddies in diffluent jetstreams: Eddy vorticity forcing of 'blocking' flow fields. *Quarterly Journal of the Royal Meteorological Society*, 109(462):737–761, 1983.

J. Sillmann and M. Croci-Maspoli. Present and future atmospheric blocking and its impact on European mean and extreme climate. *Geophysical Research Letters*, 36(10), 2009.

I. Simmonds, R. J. Murray, and R. Leighton. A refinement of cyclone tracking methods with data from FROST. *Aust. Meteor. Mag*, 48:35–49, 1999.

E. T. Smith and S. C. Sheridan. Where do cold air outbreaks occur, and how have they changed over time? *Geophysical Research Letters*, 47(13):e2020GL086983, 2020.

P. M. Sousa, R. M. Trigo, D. Barriopedro, P. M. Soares, A. M. Ramos, and M. L. Liberato. Responses of European precipitation distributions and regimes to different blocking locations. *Climate dynamics*, 48(3):1141–1160, 2017.

P. M. Sousa, R. M. Trigo, D. Barriopedro, P. M. Soares, and J. A. Santos. European temperature responses to blocking and ridge regional patterns. *Climate Dynamics*, 50(1):457–477, 2018.

P. M. Sousa, D. Barriopedro, R. García-Herrera, T. Woollings, and R. M. Trigo. A new combined detection algorithm for blocking and subtropical ridges. *Journal of Climate*, 34(18):7735–7758, 2021.

M. Sprenger and H. Wernli. The LAGRANTO Lagrangian analysis tool–version 2.0. *Geoscientific Model Development*, 8(8):2569–2586, 2015.

D. Steinfeld and S. Pfahl. The role of latent heating in atmospheric blocking dynamics: a global climatology. *Climate Dynamics*, 53(9):6159–6180, 2019.

D. Steinfeld, M. Boettcher, R. Forbes, and S. Pfahl. The sensitivity of atmospheric blocking to upstream latent heating–numerical experiments. *Weather and Climate Dynamics*, 1(2):405–426, 2020.

M. T. Stoelinga. A potential vorticity-based study of the role of diabatic heating and friction in a numerically simulated baroclinic cyclone. *Monthly weather review*, 124(5):849–874, 1996.

P. Stucki, R. Rickli, S. Brönnimann, O. Martius, H. Wanner, D. Grebner, and J. Luterbacher. Weather patterns and hydro-climatological precursors of extreme floods in Switzerland since 1868. *Meteorologische Zeitschrift*, 21(6):531–550, 2012.

C. C. Suitters, O. Martínez-Alvarado, K. I. Hodges, R. K. Schiemann, and D. Ackerley. Transient anticyclonic eddies and their relationship to atmospheric block persistence. *Weather and Climate Dynamics*, 4(3):683–700, 2023.

Q. Sun, C. Miao, M. Hanel, A. G. Borthwick, Q. Duan, D. Ji, and H. Li. Global heat stress on health, wildfires, and agricultural crops under different levels of climate warming. *Environment international*, 128:125–136, 2019.

F. Teubler and M. Riemer. Dynamics of Rossby wave packets in a quantitative potential vorticity–potential temperature framework. *Journal of the Atmospheric Sciences*, 73(3):1063–1081, 2016.

J. Thuburn. ENDGame: The new dynamical core of the Met Office weather and climate prediction model. *UK success stories in Industrial Mathematics*, pages 27–33, 2016.

S. Tibaldi and F. Molteni. On the operational predictability of blocking. *Tellus A*, 42(3):343–365, 1990.

M. Toulabi Nejad, Z. Hejazizadeh, A. R. Lupo, and M. Saligheh. Spatio-temporal distribution of atmospheric blocking events in the Northern and Southern Hemispheres. *Theoretical and Applied Climatology*, 150(1):491–505, 2022.

K. E. Trenberth and J. T. Fasullo. Climate extremes and climate change: The Russian heat wave and other climate extremes of 2010. *Journal of Geophysical Research: Atmospheres*, 117(D17), 2012.

E. Tyrlis and B. Hoskins. Aspects of a Northern Hemisphere atmospheric blocking climatology. *Journal of the atmospheric sciences*, 65(5):1638–1652, 2008.

E. Tyrlis, J. Bader, E. Manzini, and D. Matei. Reconciling different methods of high-latitude blocking detection. *Quarterly Journal of the Royal Meteorological Society*, 147(735):1070–1096, 2021.

UK Centre for Ecology and Hydrology. The hot summer - 2003. `https://www.ceh.ac.uk/our-science/projects/hot-summer-2003`, 2024. Accessed: 25 April 2024.

K. van der Wiel, H. C. Bloomfield, R. W. Lee, L. P. Stoop, R. Blackport, J. A. Screen, and F. M. Selten. The influence of weather regimes on European renewable energy production and demand. *Environmental Research Letters*, 14(9):094010, 2019.

J. van Mourik, H. de Vries, and M. Baatsen. The movement of atmospheric blocking systems: can we still assume quasi-stationarity? *EGUsphere*, 2024:1–26, 2024.

A. Van Niekerk and S. Vosper. Towards a more "scale-aware" orographic gravity wave drag parametrization: description and initial testing. *Quarterly Journal of the Royal Meteorological Society*, 147(739):3243–3262, 2021.

R. Vautard. Multiple weather regimes over the North Atlantic: Analysis of precursors and successors. *Monthly weather review*, 118(10):2056–2081, 1990.

M. H. Visbeck, J. W. Hurrell, L. Polvani, and H. M. Cullen. The North Atlantic Oscillation: past, present, and future. *Proceedings of the National Academy of Sciences*, 98(23):12876–12877, 2001.

E. Vogel, M. G. Donat, L. V. Alexander, M. Meinshausen, D. K. Ray, D. Karoly, N. Meinshausen, and K. Frieler. The effects of climate extremes on global agricultural yields. *Environmental Research Letters*, 14(5):054010, 2019.

L. J. Wachowicz, J. R. Preece, T. L. Mote, B. S. Barrett, and G. R. Henderson. Historical trends of seasonal Greenland blocking under different blocking metrics. *International Journal of Climatology*, 41:E3263–E3278, 2021.

D. Walters, A. J. Baran, I. Boutle, M. Brooks, P. Earnshaw, J. Edwards, K. Furtado, P. Hill, A. Lock, J. Manners, et al. The Met Office Unified Model global atmosphere 7.0/7.1 and JULES global land 7.0 configurations. *Geoscientific Model Development*, 12(5):1909–1963, 2019.

L. Wang, W. Chen, W. Zhou, J. C. Chan, D. Barriopedro, and R. Huang. Effect of the climate shift around mid 1970s on the relationship between wintertime Ural blocking circulation and East Asian climate. *International Journal of Climatology: A Journal of the Royal Meteorological Society*, 30(1):153–158, 2010.

H. Wernli, M. Paulat, M. Hagen, and C. Frei. SAL—A novel quality measure for the verification of quantitative precipitation forecasts. *Monthly Weather Review*, 136(11):4470–4487, 2008.

J. M. Wiedenmann, A. R. Lupo, I. I. Mokhov, and E. A. Tikhonova. The climatology of blocking anticyclones for the Northern and Southern Hemispheres: Block intensity as a diagnostic. *Journal of climate*, 15(23):3459–3473, 2002.

D. R. Wilson and S. P. Ballard. A microphysically based precipitation scheme for the UK Meteorological Office Unified Model. *Quarterly Journal of the Royal Meteorological Society*, 125(557):1607–1636, 1999.

D. R. Wilson, A. C. Bushell, A. M. Kerr-Munslow, J. D. Price, and C. J. Morcrette. PC2: A prognostic cloud fraction and condensation scheme. I: Scheme description. *Quarterly Journal of the Royal Meteorological Society: A journal of the atmospheric sciences, applied meteorology and physical oceanography*, 134(637):2093–2107, 2008.

N. Wood, A. Staniforth, A. White, T. Allen, M. Diamantakis, M. Gross, T. Melvin, C. Smith, S. Vosper, M. Zerroukat, et al. An inherently mass-conserving semi-implicit semi-Lagrangian discretization of the deep-atmosphere global non-hydrostatic equations. *Quarterly Journal of the Royal Meteorological Society*, 140 (682):1505–1520, 2014.

T. Woollings, B. Hoskins, M. Blackburn, and P. Berrisford. A new Rossby wave–breaking interpretation of the North Atlantic Oscillation. *Journal of the Atmospheric Sciences*, 65(2):609–626, 2008.

T. Woollings, D. Barriopedro, J. Methven, S.-W. Son, O. Martius, B. Harvey, J. Sillmann, A. R. Lupo, and S. Seneviratne. Blocking and its response to climate change. *Current climate change reports*, 4:287–300, 2018.

A. Yamazaki and H. Itoh. Selective absorption mechanism for the maintenance of blocking. *Geophysical research letters*, 36(5), 2009.

A. Yamazaki and H. Itoh. Vortex–vortex interactions for the maintenance of blocking. Part I: The selective absorption mechanism and a case study. *Journal of the Atmospheric Sciences*, 70(3):725–742, 2013a.

A. Yamazaki and H. Itoh. Vortex–vortex interactions for the maintenance of

blocking. Part II: Numerical experiments. *Journal of the Atmospheric Sciences*, 70(3):743–766, 2013b.

M. Young and J. Galvin. The record-breaking warm spell of February 2019 in Britain, the Channel Islands, France and the Netherlands. *Weather*, 75(2):36–45, 2020.

G. Zappa, G. Masato, L. Shaffrey, T. Woollings, and K. Hodges. Linking Northern Hemisphere blocking and storm track biases in the CMIP5 climate models. *Geophysical Research Letters*, 41(1):135–139, 2014.

P. Zschenderlein, A. H. Fink, S. Pfahl, and H. Wernli. Processes determining heat waves across different European climates. *Quarterly Journal of the Royal Meteorological Society*, 145(724):2973–2989, 2019.